Low-Frequency Macroscopic Instabilities of a Fully Ionized Magnetoplasma

by

Thomas Dale Rognlien

SUIPR Report No. 487

October 1972

NASA Grant NGL 05-020-176

INSTITUTE FOR PLASMA RESEARCH
STANFORD UNIVERSITY, STANFORD, CALIFORNIA

LOW-FREQUENCY MACROSCOPIC INSTABILITIES OF A FULLY IONIZED MAGNETOPLASMA

by

Thomas Dale Rognlien

NASA Grant NGL 05-020-176

SUIPR Report No. 487

October 1972

Institute for Plasma Research
Stanford University
Stanford, California

ABSTRACT

This thesis describes a series of studies of low-frequency quasi-static instabilities in a fully ionized plasma. The plasma is assumed to be immersed in a uniform magnetic field, and is either uniform or has a number density gradient perpendicular to the magnetic field. A moment equation description of the ion and electron dynamics is used; collisions are assumed to have a strong effect on electron motion along the magnetic field. Before considering specific modes, a stability analysis is developed which allows a classification of wave growth characteristics to be made for a bounded system from solutions to the dispersion relation for an infinite system. Also, a method is given for calculating the normal mode frequencies and wave profiles by using the reflection coefficients at the boundaries.

For wave propagation perpendicular to the magnetic field, the flute wave is studied in cylindrical geometry. The destabilizing effect of a radial electric field is considered by solving a differential equation. Both analytic and numerical solutions are given which include the eigen-frequencies and eigenfunctions. The effect of the plasma column being radially bounded is investigated, and results of previous workers are generalized. The transition to Kelvin-Helmholtz instability is illustrated for sharp rotational shear of the column. In addition, two instabilities observed in a hollow cathode arc discharge experiment carried out at Stanford are identified as flute instabilities.

For propagation at an angle to the magnetic field, resistive drift waves driven unstable by a density gradient are considered in rectangular geometry. A general dispersion relation is derived which includes ion axial motion, electron heat transfer, and electron axial drift. Comparison is made with dispersion relations of other authors, and the effects of these terms on the wave solutions are illustrated; both frequency and values of the first order variables are given. The solutions are interpreted for bounded systems, using the method presented in the thesis. This provides a proper explanation of some experimental results obtained elsewhere from a drift wave experiment in a Q-machine. The characteristics of an entropy or temperature wave are also studied.

For propagation parallel to the magnetic field, the stability of ion-acoustic waves is studied; frequency and values of the first order variables are again given. The destabilizing effect of electron drift is investigated, and it is shown that an estimate of the threshold drift for instability given by other investigators is too large if $T_i < T_e$, due to collisional energy exchange between electrons and ions. Further, instability is found in the absence of an electron drift when $2T_i \lesssim T_e$, again due to collisional energy exchange. Normal mode solutions for a bounded plasma are also given. These results are valid for a plasma in which the temperature difference is maintained by an external source. In addition, the case of a plasma equilibrating in time $(T_i \rightarrow T_e)$ is considered, and it is found that here ion-acoustic instability should not grow to a significant amplitude.

CONTENTS

		Page
1.	INTRODUCTION	1
	1.1 Stability Analysis	3
	1.2 Low-Frequency Instabilities	6
	1.2.1 Waves Propagating Perpendicular to the Magnetic Field	6
	1.2.2 Waves Propagating at an Angle to the Magnetic Field	7
	1.2.3 Waves Propagating Parallel to the Magnetic Field	9
2.	STABILITY ANALYSIS FOR BOUNDED MEDIA	11
	2.1 Waves in an Infinite Medium	12
	2.1.1 Basic Model	12
	2.1.2 Natural Response	13
	2.1.3 Forced Response	20
	2.2 Waves in a Bounded Medium	21
	2.2.1 Physical Model	21
	2.2.2 Mathematical Model	24
	2.2.3 Natural Response	30
	2.2.4 Forced Response	35
	2.2.5 Axial Profiles	36
	2.2.6 Extension to $D(\omega,k)$ of Higher Order in k	40
3.	WAVES PROPAGATING PERPENDICULAR TO THE MAGNETIC FIELD	42
	3.1 Basic Theory	42
	3.1.1 Steady State Plasma	42
	3.1.2 Perturbed Plasma	48
	3.2 Waves for Uniform Rotation	53
	3.2.1 Solutions for Radially Unbounded Columns	53
	3.2.2 Solutions for Radially Bounded Columns	56
	3.3 Waves for Nonuniform Rotation	63
	3.3.1 Numerical Procedure	63
	3.3.2 Solutions for Gradual Shear	65
	3.3.3 Solutions for Abrupt Shear	72
	3.4 Comparison with Hollow Cathode Arc Experiment	76
	3.4.1 Experimental Measurements	76
	3.4.2 Comparison between Theory and Experiment	81

CONTENTS (Cont'd)

		Page
4.	WAVES PROPAGATING AT AN ANGLE TO THE MAGNETIC FIELD	89
	4.1 Basic Theory	90
	4.1.1 Steady State Plasma	90
	4.1.2 Perturbed Plasma	93
	4.1.3 Comment on the Slab Model	98
	4.2 Solutions to the Isothermal Dispersion Relation	100
	4.2.1 Basic Drift Wave Characteristics	100
	4.2.2 Effect of Ion Axial Motion	106
	4.3 Solutions to the Non-Isothermal Dispersion Relation	107
	4.3.1 Effect of Electron Heat Transfer on Drift Waves	107
	4.3.2 Entropy Wave	113
	4.3.3 Effect of Electron Axial Drift	115
	4.4 Comparison with Experiment	120
	4.4.1 Experiment of Rowberg and Wong	120
	4.4.2 Normal Mode Interpretation	125
	4.4.3 Comparison with Measured Results	127
5.	WAVES PROPAGATING PARALLEL TO THE MAGNETIC FIELD	130
	5.1 Basic Theory: The Maintained Plasma	131
	5.1.1 Steady State Plasma	131
	5.1.2 Perturbed Plasma	133
	5.2 Solutions to the Dispersion Relation	136
	5.2.1 Effect of Unequal Electron and Ion Temperatures	136
	5.2.2 Effect of an Electron Drift	143
	5.2.3 Normal Mode Solutions	149
	5.3 Initial Value Problem: The Equilibrating Plasma	151
	5.3.1 Steady State Plasma	151
	5.3.2 Perturbed Plasma	152
	5.3.3 Almost Time-harmonic Solutions	154
	5.4 Applications	156

CONTENTS (Cont'd)

	Page
6. CONCLUSIONS	158
6.1 Review of the Research	158
6.2 Suggestions for Future Work	161
APPENDIX A: RESPONSE OF A BOUNDED SYSTEM TO AN ARBITRARILY POSITIONED SOURCE	163
APPENDIX B: ION VELOCITY DUE TO A RADIAL ELECTRIC FIELD IN CYLINDRICAL GEOMETRY	167
APPENDIX C: EFFECT OF ELECTRON TEMPERATURE FLUCTUATIONS ON WAVES PROPAGATING PERPENDICULAR TO THE MAGNETIC FIELD	172
APPENDIX D: ION VISCOSITY TENSOR INCLUDING ION-ION COLLISIONS	175
REFERENCES	177

TABLES

Table		Page
4.1	Comparison of various drift wave dispersion relations	98

ILLUSTRATIONS

Figure		Page
2.1	(a) The loci of the zeros of $D(\omega,k)$ in the k-plane when $Im(\omega)$ increases for constant $Re(\omega)$. (b) The corresponding path taken by ω is shown by the dotted line. The solid lines in (b) represent ω_α(k real) contours	14
2.2	Map (or loci) of several LIP's from Fig. 2.3 into the k-plane via $D(\omega_L,k) = 0$, showing the FIP and its deformation to include the same poles of $G(\omega_L,k)$ as the LIP is raised. Two poles collide at the saddle point (ω_s,k_s), pinching the FIP between them	16
2.3	Map of k into the ω-plane via $D(\omega,k) = 0$ for $k_i = 0$, k_{si}, showing the branch point (ω_s,k_s), and the LIP's corresponding to Fig. 2.2, but with σ_3 deformed around the branch point	17
2.4	Development of a localized perturbation as a function of time ($t_1 < t_2 < t_3 < t_4$) for (a) absolute instability, and (b) convective instability	19
2.5	Bounded system with reflection coefficients ρ_1 and ρ_2, defined in Eq. (2.12), and source $s(t,z)$	23
2.6	Bounded system ($-L/2 \le z \le L/2$) modeled as an infinite system with image sources given by Eqs. (2.14) and (2.15). Shaded area contains the reciprocal medium .	25
2.7	Equivalent models with respect to the response in the bounded region ($-L/2 \le z \le L/2$) for a source at $z = -5L$. Source $\bar{f}_{-5}$ is given by Eq. (2.19)	27
2.8	Map of k into the ω-plane via $D(\omega,k) = 0$, when $D(\omega,k)$ is even and quadratic in k. The two sheets are represented by $\pm$ signs, and the normal mode frequencies denoted by ω_n. The cases of convective and absolute instability for the unbounded system are indicated by the full line ω_r-axis and the chain-dot ω_r-axis, respectively	34
3.1	(a) Model of the cylindrical plasma column immersed in a magnetic field B, showing the coordinate system. (b) Radial profiles of number density and electric field in the column	44
3.2	Values of p for (a) the (1,q) mode, and (b) the (2,q) mode, as $X_b (= r_b^2/r_0^2)$ is varied. ——, actual value; ----, asymptotic value	58

Figure		Page
3.3	The real frequency, W_r, and the growth rate, $-W_i$, of (a) the (1,0) mode, and (b) the (2,0) mode, for $W_E = 1.5$ as the boundary position is varied. ——, W_r; ----, $-W_i$	60
3.4	Loci of the eigenfrequencies [Eq. (3.35)] in the W-plane for $X_b = 4$, as W_E is varied. Complex conjugate solutions are omitted. ——, (1,0) mode; ----, (2,0) mode	62
3.5	Rotation frequency profile, W_E, due to the electric field, as given by Eq. (3.48)	65
3.6	Locus of the eigenfrequency of the (1,0) mode for $X_b = 4$. ——, as s is varied in Eq. (3.48); ----, as constant W_E is varied for uniform rotation	67
3.7	Locus of the eigenfrequency of the (2,0) mode, with conditions as in Fig. 3.6	68
3.8	Computed eigenfunctions of the (1,0) mode for (a) uniform rotation (s = 0), and (b) nonuniform rotation with s = -2.5. —— $e\phi_1/T_i$, ---- n_1/n_0	70
3.9	Computed eigenfunctions of the (2,0) mode for the conditions of Fig. 3.8	71
3.10	Rotation frequency profile, W_E, due to the electric field, as given by Eq. (3.50)	73
3.11	Locus of the eigenfrequency of the (1,0) mode with $X_b = 4$. ——, as a is varied in Eq. (3.50); -·-·-·-, with centrifugal effect neglected; ----, for uniform rotation	74
3.12	Locus of the eigenfrequency of the (2,0) mode, with conditions as for Fig. 3.11	75
3.13	Computed eigenfunctions for (a) the (1,0) mode, and (b) the (2,0) mode, corresponding to eigenfrequencies for a = 2.0 in Figs. 3.11 and 3.12. —— $e\phi_1/T_i$; ---- n_1/n_0	77
3.14	Measured radial variations of (a) potential, ϕ_1, and (b) density, n_1, for the m = 1 instability. ——, amplitude; ----, phase	79
3.15	Measured radial variations of (a) potential, ϕ_1, and (b) density, n_1, for the m = -1 instability. ——, amplitude; ----, phase	80

Figure		Page
3.16	Estimated electric field profiles as determined from measured profiles of ϕ_f and T_e, together with Eq. (3.51). ----, m = 1 instability present; ——, m = -1 instability present	82
3.17	Profiles of W_E for (a) the m = 1 mode, and (b) the m = -1 mode, used in the calculation of the eigenfunctions	84
3.18	Calculated eigenfunctions of (a) potential, ϕ_1, and (b) density, n_1, for the m = 1 mode. Comparison to be made with Fig. 3.14. ——, amplitude; ----, phase . .	85
3.19	Calculated eigenfunctions of (a) potential, ϕ_1, and (b) density, n_1, for the m = -1 mode. Comparison to be made with Fig. 3.15. ——, amplitude; ----, phase.	87
4.1	Model of the plasma in rectangular geometry, showing the DC quantities and the direction of wave propagation	90
4.2	Rectangular slab model with coordinates (x,y,z) applied to cylindrical geometry with coordinates (r,θ,z)	99
4.3	Map of K into the w-plane via Eq. (4.26) for conditions of Rowberg and Wong's experiment: m_i = 39.1 AMU; n = 6.7 × 10^{10} cm^{-3}; T_0 = 0.19 eV; B = 1.6 kG; m = 2; $k_y = k_x$ = 1.43 cm^{-1}; χ = -0.80 cm^{-1}; ν_{ei} = 2.0 × 10^7 sec^{-1}; ν_{ii} = 5.2 × 10^4 sec^{-1}; ω_D = 1.36 × 10^4 sec^{-1}; ω_{ci} = 3.92 × 10^5 sec^{-1}; ν_e = 7.5 × 10^2; ν_i = 3.8; b = 0.124. The lowest axial mode (λ_z = 3.6L, L = 60 cm) is shown by crosses. The drift wave branch is indicated by (I) and the flute wave branch by (II). ——, K_i = constant; ----, K_r = constant	103
4.4	Amplitude and phase of $\phi_{ln} = (e\phi_1/T_0)/(n_1/n_0)$ for the drift wave branch in Fig. 4.3 as K_r is varied for several K_i values	105
4.5	Partial map of K into the w-plane via Eq. (4.32) which includes ion axial motion. Branch III is the ion-acoustic wave, and parameters are as in Fig. 4.3. ——, K_i = constant; ----, K_r = constant	108

Figure		Page
4.6	Partial map of K into the w-plane via Eq. (4.24) for the non-isothermal theory. Branch IV is the entropy wave. Parameters as in Fig. 4.3. ——, K_i = constant; ----, K_r = constant; -·-·-·-, isothermal theory as in Fig. 4.5	110
4.7	Amplitude and phase of (a) ϕ_{1n}, and (b) T_{eln}, for the drift wave branch in Fig. 4.6	111 112
4.8	Amplitude and phase of ϕ_{1n} and T_{eln} for the entropy wave branch in Fig. 4.6	114
4.9	Partial map of K into the w-plane via Eq. (4.24) with values of K_r shown on the curves ($K_i = 0$). Parameters are as in Fig. 4.3. ——, $v_{ez0} = 5(T_0/m_i)^{\frac{1}{2}}$; ----, $v_{ez0} = 0$	116
4.10	Amplitude and phase of (a) ϕ_{1n}, and (b) T_{eln}, for the drift wave branch in Fig. 4.9 with $v_{ez0} = 5(T_0/m_i)^{\frac{1}{2}}$.	117 118
4.11	Map of the difference $(K^+ - K^-)$ into the w-plane via Eq. (4.24) for the drift wave with $v_{ez0} = 5(T_0/m_i)^{\frac{1}{2}}$, as in Fig. 4.9. There are branch points at w_{s1} and w_{s2}. ——, $(K_i^+ - K_i^-)$ = constant; ----, $(K_r^+ - K_i^-)$ = constant; -·-·-·-, $v_{ez0} = 0$, $(K_i^+ - K_i^-) = 0$	121
4.12	Axial profile of wave for lowest axial mode. (a) Electron-rich sheaths, $\lambda_z \approx 2L$. (b) Ion-rich sheaths, $\lambda_z > 2L$	123
4.13	Amplitude and phase of axial normal mode for various magnitudes of the reflection coefficient ρ, with k_{zr} = 1.67 cm^{-1}	126
4.14	Comparison of drift wave growth rates for (a) isothermal theory neglecting ion axial motion [Eq. (4.26)], (b) isothermal theory including ion axial motion [Eq. (4.32)], and (c) non-isothermal theory including ion axial motion [Eq. (4.24)]. Parameters as in Fig. 4.3. ——, theory; ----, Rowberg and Wong's experimental data	128
5.1	Model of the plasma in rectangular geometry showing the DC quantities and the direction of propagation . .	131
5.2	Map of the real $\varkappa$ contour into the Ω-plane via Eq. (5.16) for the ion-acoustic wave branch with various temperature ratios, R_T, and R_m = 1837, corresponding to a hydrogen plasma	139

Figure		Page
5.3	Values of (a) amplitude, and (b) phase, of the normalized variables ϕ_{1n}, T_{eln}, and T_{iln} for the conditions in Fig. 5.2 with $R_T = 1/2, 1/10$	141 142
5.4	Map of the real $\varkappa$ contour into the Ω-plane via Eq. (5.16) for the ion-acoustic wave branch with the parameters as in Fig. 5.2. ——, $v_{e0} = 4(T_{e0}/m_i)^{\frac{1}{2}}$; ----, $v_{e0} = 0$	146
5.5	Values of (a) amplitude, and (b) phase, of the normalized variables ϕ_{1n}, T_{eln}, and T_{iln} for the ion-acoustic wave in Fig. 5.4 with $v_{e0} = 4(T_{e0}/m_i)^{\frac{1}{2}}$. ——, $R_T = 1/2$; ----, $R_T = 1/10$. Curves for $R_T = 1/10$ are omitted if they essentially coincide with $R_T = 1/2$ curves	147 148
5.6	Map of the difference $(\varkappa^+ - \varkappa^-)$ into the Ω-plane via Eq. (5.16) for $R_T = 1/10$. The curves are not dependent on V for the range considered $(0 \leq V \leq 4)$. .	150
5.7	Relaxation of electron and ion temperatures given by Eq. (5.30). ——, V = 0; ----, V(0) = 3	152
6.1	Map of K real into the w-plane via Eq. (4.24) for the conditions in Fig. 4.3. Branch I is the drift wave for small K, while branches I and III evolve into a pair of ion-acoustic waves for large K. Branch II denotes the flute wave	159
A.1	Bounded system $(-L/2 \leq z \leq L/2)$ modeled as an infinite system with image sources as given in Eqs. (2.14) and (2.15). Shaded area contains the reciprocal medium	164
B.1	Fluid velocity components due to a radial electric field ($v_E = -E/B$) from Eqs. (B.4) and (B.5). ——, v_θ; -·-·-·-, v_r; ----, v_θ from Eq. (B.6)	169

LIST OF SYMBOLS

Symbol		Page where first used
	(1) Latin Alphabet	
$A(z)$	spatial dependence of normal mode	29
$\bar{A}(z)$	spatial dependence defined by Eq. (2.36)	36
a	parameter in Eq. (3.50)	72
a_n	coefficients of a series	64
$\underset{\sim}{B}$	magnetic field	1
$b(\omega)$	coefficient in Eq. (2.9)	22
b	$k_\perp^2 \rho_i^2$	94
C_r	resistivity coefficient	91
C_t	thermal force coefficient	91
$C_{e\chi}$	electron thermal conductivity coefficient	93
C_i	ion viscosity coefficient	94
C_s	$(T_0/m_i)^{\frac{1}{2}}$, $\sim$ ion-acoustic speed	115
$C_{i\eta, e\eta}$	ion and electron viscosity coefficients	132
$c(\omega)$	coefficient in Eq. (2.9)	22
c	parameter in Eq. (3.51)	81
$D(\omega, k)$	dispersion function	4
$\underset{\sim}{E}$	electric field	1
$-e$	charge of an electron	43
$F(\omega, z)$	function defined by Eq. (2.4)	13
$\tilde{F}(\omega, z)$	analytic continuation of $F(\omega, z)$	15
$f(t)$	temporal dependence of source $s(t,z)$	12
$f(\omega)$	Laplace transform of $f(t)$	12
f_n	image source	24
$\bar{f}_n$	modified image source	28
$G(\omega, k)$	Green's function, $[D(\omega, k)]^{-1}$	12
$g(z)$	spatial dependence of source $s(t,z)$	12
$g(k)$	Fourier transform of $g(z)$	12
$H(\omega, \rho_1, \rho_2, L, n)$	function defined by Eq. (2.29)	31
h	function defined by Eq. (3.30)	53

Symbol		Page where first used
i	$(-1)^{\frac{1}{2}}$	3
$\hat{i}_{r,\theta}$	unit vectors in the radial and azimuthal directions, respectively	45
$\hat{i}_{x,y,z}$	unit vectors in the x-,y-, and z-directions, respectively	91
j	function defined by Eq. (3.45)	64
K	normalized axial wavenumber, $(T_0 k_z^2/m_e \omega_D)^{\frac{1}{2}}$	100
$\underset{\sim}{k}$	vector wavenumber	4
k_s	k at a saddle point of $D(\omega,k) = 0$ in the k-plane	18
k^+, k^-	roots of $D(\omega,k) = 0$	15
L	length of bounded system	21
ℓ	$m/2$	53
$M_{h,\ell}(X)$	solution to Whittaker's equation	54
$M(\ell-h+1/2,\ 1+2\ell, X)$	Kummer's function	54
m	azimuthal mode number; also particle mass	5;170
$m_{i,e}$	ion and electron mass, respectively	43
n	number density	43
P	constant defined by Eq. (A.9)	166
p	function defined by Eq. (3.34)	54
q	radial mode number	54
R_m^2	mass ratio, m_i/m_e	134
R_T	temperature ratio, T_{i0}/T_{e0}	134
r	displacement along r-axis	5
r_0	scale length of a Gaussian profile	43
r_b	radial position of boundary	53
Δr	slab thickness	99
$S_{i,e}$	external ion and electron heat source or sink terms, respectively	132
$s(t,z)$	localized source	12
s	slope of W_E profile	65
$T_{e,i,n}$	temperature of electrons, ions, and neutrals, respectively	9
T_0	common electron and ion temperature in Section 4	90
T_{eln}	normalized first order electron temperature, $(T_{e1}/T_{e0})/(n_1/n_0)$	109

Symbol		Page where first used
T_{iln}	normalized first order ion temperature, $(T_{i1}/T_{i0})/(n_1/n_0)$	140
t	time	4
U	sheath potential	122
U_w	end-plate work function	124
U_I	ionization potential of neutrals	124
u_z	relative axial velocity of the electrons with respect to that of the ions	91
V	normalized drift velocity, $v_{e0}/(T_{e0}/m_i)^{\frac{1}{2}}$	134
v_G	generalized group velocity	33
$\underset{\sim}{v}_i$	ion velocity	43
v_0	velocity defined by Eq. (3.7)	45
$\underset{\sim}{v}_e$	electron velocity	47
v_D	diamagnetic drift velocity	92
v_{E0}	$\underset{\sim}{E}_0 \times \underset{\sim}{B}$ drift velocity	92
v_{ith}	ion thermal velocity	124
$\underset{\sim}{\overleftrightarrow{W}}$	tensor defined by Eqs. (3.4) and (3.5)	45
W	normalized frequency, ω/ω_{Di}	59
W_E	normalized rotation frequency, ω_E/ω_{Di}	61
w	normalized frequency, $\omega/\omega_D (= W/m)$	100
$w_{s1,s2}$	branch points in the w-plane	119
X	normalized radius squared, $(r/r_0)^2$	53
X_b	measure of radial boundary position, $(r_b/r_0)^2$	56
x	displacement along x-axis	5
y	displacement along y-axis	5
y(r)	dummy variable	63
Ze	charge of an ion	132
z	displacement along z-axis	5

(2) Greek Alphabet

α	order of $D(\omega,k)$ in ω	12
$\alpha_{1,2}$	constants defined by Eqs. (2.21) and (2.22)	29
$\bar{\alpha}_{1,2}$	constants defined by Eqs. (2.34) and (2.35)	35

Symbol		Page where first used
α_{ij}	coefficients of Eqs. (4.16), (4.22), and (4.23).	95
β	order of $D(\omega,k)$ in k; also particle pressure divided by magnetic pressure	12;48
$\beta_{1,2}$	constants defined by Eq. (2.52); also coefficients defined by Eq. (4.33)	39;106
β_0	coefficient defined by Eq. (4.33)	106
$\Gamma_{0,1,2}$	coefficients defined by Eq. (5.35)	154
γ	$(n_1/n_0 + e\phi_1/T_i)$; also constant in Eq. (5.24) .	50;138
γ_{ij}	coefficients of Eqs. (5.10), (5.12), and (5.14).	134
$\Delta_{1,2,3}$	correction terms for ion velocity	50
Δ	1 if n is odd; 0 if n is even	163
δ	impulse or delta-function; also probability of an ion being lost to the end-plate	13;125
$\delta_{\ell,k}$	Kronecker delta	175
$\eta_{0,1,2,3}$	coefficients in the ion viscosity tensor	175
θ	azimuthal angle	53
$\theta_{1,2}$	phase angle of reflection coefficients	23
$\varkappa$	normalized wavenumber, $k\lambda_e$	134
λ_z	axial wavelength	120
λ_e	electron mean-free-path	134
ν_{ii}	ion-ion collision frequency	45
ν_{ei}	electron-ion collision frequency	91
$\nu_{i,e}$	normalized collision frequencies, ν_{ii}/ω_D and ν_{ei}/ω_D, respectively	100
ξ	$(n_1/n_0 - e\phi_1/T_e)$	48
π	3.14159...	12
$\overleftrightarrow{\pi}_i$	ion viscosity tensor	43
$\rho_{1,2}$	reflection coefficients	23
ρ_i	ion gyroradius or Larmor radius	46
σ	$\mathrm{Im}(\omega)$ on the Laplace integral path	12
σ_0	a σ below the lowest ω_α(k real) contour	15
τ	normalized time, $2\nu_{ei}t/R_m^2$	151
ϕ	phase angle defined in Eq. (2.42)	38
ϕ_1	first order potential	48

Symbol		Page where first used
$\phi_{f,s}$	floating and space potentials, respectively . . .	78
ϕ_{1n}	normalized first order potential, $(e\phi_1/T_0)/(n_1/n_0)$	104
$\chi(z)$	phase angle of normal mode profile	37
χ_r	inverse scale length of rotational shear	46
χ	inverse scale length of density gradient	91
Ψ	first order variable, $\phi_1/r\omega_1 B$	52
ψ	a first order variable	12
Ω	normalized frequency, ω/ν_{ei}	134
ω_{pi}	ion plasma frequency	1
ω_{ci}	ion cyclotron frequency	1
ω	angular frequency	4
ω_s	ω at a saddle point of $D(\omega,k) = 0$ in the k-plane	18
ω_0	source frequency	20
ω_n	normal mode frequency	30
ω_{Di}	ion diamagnetic frequency, $(2m/r_0^2)(T_i/eB)$ . . .	49
ω_E	rotation frequency, $-E_0/rB$	49
ω_1	frequency, $\omega - m\omega_E$; also $\omega - k_y v_{E0}$	51;94
ω_2	frequency, $\omega - m\omega_E + m\omega_{Di}$	51
ω_D	diamagnetic frequency, $k_y v_D$	94
ω_{iD}	temporal damping decrement	124

(3) Subscripts

D	diamagnetic	49
E	due to the electric field	49
e	electron	9
i	ion; imaginary part of	1;18
L	Laplace contour	13
n	integer index	24
r	real part of; also radial component	15;45
x	x-direction component	3
y	y-direction component	5
z	z-direction component, parallel to the magnetic field	91

Symbol		Page where first used
θ	azimuthal component	45
0	zero order	45
1	first order	48
$\perp$	component perpendicular to the magnetic field . . .	43

ACKNOWLEDGMENTS

I wish to thank my research supervisor, Professor F. W. Crawford, for his advice and encouragement during the course of this research, and for his constructive comments on this manuscript. I am indebted to Dr. S. A. Self for the hours he made available for discussions, for many suggestions throughout the research, and for useful comments on the manuscript. Both of these gentlemen have had a strong influence on the development of my understanding of plasma physics. I also thank Professor G. S. Kino for reading and commenting on the manuscript.

I would like to express my appreciation to D. B. Ilić for supplying the experimental results quoted in Section 3.4.1, and to Dr. J. M. Larsen and L. Wigton for advice and assistance with some of the computer programming. I am grateful to Jane Johnston and Mildred Nilsson for doing an excellent job of typing, and to Gary McDonough for his assistance with administrative matters. My wife, Jude, has been involved at all stages of this work, typing most of the rough draft, serving as editor, and being a constant companion; I give her special thanks.

Finally, I wish to thank the National Science Foundation for financial support during my graduate studies.

1. INTRODUCTION

The primary purpose of this research is to obtain the characteristics of quasistatic instabilities in a fully ionized plasma. These instabilities will be studied in the low-frequency range below the ion plasma frequency, ω_{pi}, and generally below the ion cyclotron frequency, ω_{ci} ($\omega_{ci} < \omega_{pi}$ in all plasmas of interest here), when a static magnetic field is present. The instabilities considered arise in plasmas for which a moment equation description of the ion and electron dynamics is appropriate. This applies to those plasmas in which the effects of particle motion are localized spatially, typically by a magnetic field for motion perpendicular to the field, and by collisions for motion parallel to the field. Specific criteria will be discussed in Sections 3 and 4.

It will be useful to keep in mind the following features of these instabilities. First, the motion of the ions is usually the more involved; that of the electrons is simply described as the motion of an inertialess fluid. This is in contrast to high-frequency instabilities and waves with frequencies of the order of the electron plasma or cyclotron frequencies, where the ions can be assumed to form a stationary background, since their mass is much larger than that of the electrons. Second, for a plasma configuration to be unstable, one should be able to identify a source of energy for the instability. This source often takes the form of a drift motion of the particles, as arises, for example, when a DC electric field is present. For an electric field perpendicular to the magnetic field, an $\underset{\sim}{E} \times \underset{\sim}{B}/B^2$ Hall drift velocity arises for both electrons and ions; for an electric field parallel to the magnetic field, a parallel drift arises with the velocity of the electrons being much larger than that of the ions. The kinetic energy available from these particle drifts may also be supplemented by the potential energy which arises from plasma inhomogeneities, such as a pressure gradient. Sometimes a combination of these sources is needed for instability, as we shall see in Section 3.

Interest in low-frequency instabilities arises from studies of both man-made and naturally occurring plasmas. For man-made plasmas, the most ambitious goal has been to confine a hot, dense plasma long enough to

attain controlled thermonuclear fusion.[1] In the late 1950's, confinement of particles by a magnetic field seemed promising, but it was found that increasing the magnetic field strength did not always lead to the expected increased confinement either for weakly ionized plasmas[2] or for fully ionized plasmas.[3] The cause of this was later identified as plasma instabilities,[4,5] which arose due to the combined effects of a density gradient and particle drifts. Growth of these instabilities leads to an increase in the flow of plasma (both ions and electrons) to the wall, over what occurs for a stable configuration. This is known as "anomalous" diffusion. In this connection, it is important to note that it is the low-frequency instabilities, affecting both ion and electron motion, which are potentially harmful to plasma confinement; the high-frequency instabilities have little effect on the ions, unless they couple nonlinearly to low-frequency waves.

From the 1960's to the present, there have followed extensive investigations of plasma instabilities, both theoretical and experimental. Investigators turned to devices such as the Q-machine,[6] and the positive column,[7] to study the basic wave properties of plasmas without the greater complexities of fusion study devices. The interest in collisional plasmas has come from these lower temperature devices, where Coulomb collisions and/or charged particle-neutral collisions can have an important effect on stability. However, even in fusion study devices such as the stellarator, instabilities in the initial plasma heating stage may be described by collisional theory.[8] Furthermore, it has been argued very recently[9] that collisional instabilities may occur in high temperature fusion devices such as the Tokamak, where the required localization of particles is caused by small-scale turbulence rather than classical particle collisions. Thus, there are a number of man-made plasmas in which low-frequency collisional instabilities may arise.

For naturally occurring plasmas, the ionosphere exhibits several phenomena which are believed to be produced by low-frequency plasma instabilities. Spread-F, which is the spreading of the height of the F-layer on ionosonde records, has been observed since 1938,[10] and is associated with irregularities in the plasma density of the F-layer. A

number of theories have been proposed to explain its origin, and though none is conclusive, it is believed to be due to plasma instability.[11] Farley[12] has identified an instability which arises in the equatorial electrojet as being due to a relative Hall particle drift in a weakly ionized plasma. Finally, plasma instability is thought to be responsible for the enhanced energy transfer between electrons and ions (i.e., over collisional effects) required to obtain agreement between theoretical and measured values of electron and ion temperatures in the solar wind.[13]

We shall now consider a more detailed review of the subject matter of this work. In Section 1.1, a discussion is given of the method by which plasma stability is determined; Section 1.2 contains a discussion of the low-frequency instabilities to be studied.

1.1 Stability Analysis

In order to determine the stability of various plasma configurations, a linear perturbation analysis is carried out on the equations which describe the configuration. Infinite rectangular geometry is often used, and for spatial directions x_j, along which the plasma is uniform, a spatial dependence of $\exp(-ik_j x_j)$ is assumed, where k_j is the wavenumber in the x_j-direction. This corresponds to considering a single wavenumber component in a Fourier transform for an unbounded system, or a single mode, if a finite plasma with periodic boundaries is assumed. Thus, k is usually taken as real. For directions in which the plasma is not uniform, a general spatial dependence of the variables must be allowed for, which leads to a differential equation in that coordinate when the perturbed equations are combined. However, an $\exp(-ik_x x)$ spatial dependence can also be assumed in a direction where the inhomogeneity is not too strong, the condition usually being taken as $k_x \gg C^{-1}\,\partial C/\partial x$, where C is the inhomogeneous steady state parameter. This is known as the local approximation, and is discussed in greater detail in Section 4.1.3.

Similarly, the perturbed variables are assumed to have a time dependence of $\exp i\omega t$ when the zero order plasma properties are constant in time, which is equivalent to Fourier transforming in time. In combining and solving the perturbed equations, including the

differential equations appropriate to inhomogeneous plasmas, a dispersion relation, $D(\omega,\underset{\sim}{k}) = 0$, is obtained. This specifies the relation between ω and $\underset{\sim}{k}$ for perturbations varying as $\exp i(\omega t - \underset{\sim}{k}\cdot\underset{\sim}{r})$.

The stability of the plasma configuration is determined by studying the characteristics of $D(\omega,\underset{\sim}{k}) = 0$. Most often, ω is considered to be the dependent complex variable, with $\underset{\sim}{k}$ being the independent real variable. If some value of $\underset{\sim}{k}$ yields a value of ω with a negative imaginary part, and if a monochromatic plane wave could be set up with that spatial dependence, it would grow in time, and the plasma would be unstable. Presumably the plane wave with the minimum imaginary part of ω for a real $\underset{\sim}{k}$ would be dominant after a long time.

On the other hand, to describe the propagation of a wave away from some point in space, it would seem more appropriate to solve $D(\omega,\underset{\sim}{k}) = 0$ for real ω and complex $\underset{\sim}{k}$, the implication being that the instabilities grow in space rather than in time. An additional ambiguity which arises is that, for active systems, it is not clear whether the imaginary part of $\underset{\sim}{k}$ corresponds to growth in one direction or decay in the opposite direction. These difficulties were first clearly pointed out in the early 1950's by Pierce[14] and Twiss[15] in connection with plasma streaming instabilities. Twiss indicated that the difficulty lay in the formulation of the problem, and that two types of instabilities could arise if the more realistic problem of response of the system to a localized disturbance was considered. This approach to the stability analysis has received much attention in the last fifteen years.[16-21]

In 1958, Sturrock[16] considered this type of problem for the response of a system described by two coupled modes to a localized disturbance switched on at time $t = 0$. He showed how to distinguish, purely from the topology of the conformal mappings of $D(\omega,\underset{\sim}{k}) = 0$, between two types of instabilities: the absolute instability which grows in time, and the convective instability which grows in space. These definitions will be made more precise in Section 2.1. Since the source is switched on at time $t = 0$, the analysis must be for an initial value problem, so the Laplace transform is used in time. The time variation of $\exp i\omega t$ can still be assumed, but the inversion of the Laplace and Fourier transforms must be performed to determine the response, which will be a wave packet rather

than a plane wave. The medium is still described by a dispersion relation $D(\omega,\underset{\sim}{k}) = 0$, and the expression $[D(\omega,\underset{\sim}{k})]^{-1}$ may be considered the transform of the Green's function for the system, as seen in Section 2.1. Subsequently, a number of workers have developed these ideas to varying degrees of generality.[17-21] However, all of these analyses apply to media which are infinite and uniform in the directions that the Fourier transform is applied, and, since all physical systems are bounded, leave open the question of how to interpret the behavior of bounded systems from wave solutions obtained for infinite media. The answer to this question for certain systems is the major contribution of Section 2.

There are situations in which one may argue the validity of using the results obtained from an infinite model directly in explaining the behavior of a physical system. In these cases, the boundaries should have no appreciable effect on the waves, something which is often tacitly assumed, but rarely shown, in comparisons between theory and experiment. If the boundaries could be made effectively reflectionless, the system would appear infinite as far as the waves are concerned. This can be achieved, for example, with ion-acoustic and drift waves on a long discharge column,[22] where the axial magnetic field lines diverge slowly at the ends of the column, and the electrodes are located well beyond the uniform field region. The waves are effectively absorbed in the boundary region. Also, in applying the theories to practical geometries, periodic boundary conditions may be used for coordinates which close on themselves. For instance, drift modes derived in rectangular coordinates (x,y,z) are adapted to cylindrical geometry (r,θ,z) by identifying k_y with m/a for waves varying as $\exp(-im\theta)$, where m is the azimuthal mode number, and a is the radius at which the wave is localized (see Section 4). However, as we shall see in Sections 3 - 5, the effect of the boundaries can be important for plasma stability.

One approach to including the effect of boundaries is to consider each particular experimental configuration separately, and apply the appropriate boundary conditions determined by detailed physical considerations. This approach has been taken by a number of authors,[23-28] but the analysis is often quite involved, and the results only applicable

to the specific problem. It is, however, the only completely satisfactory way to solve the problem of a bounded plasma. There are two reasons for this. First, boundaries can support surface waves which are not accounted for in the infinite plasma dispersion relation; second, the boundaries will in general couple the linearly independent modes of the infinite plasma dispersion relation together, along with the surface waves, in order to satisfy the appropriate boundary conditions.

There are systems for which it is sufficient to use a less detailed approach to determine the effect of boundaries. For example, in ideal acoustic or electromagnetic resonators, there are no surface waves, and the normal modes can be interpreted in terms of the dispersion relation for the waves of an infinite system. Also, the effect of a lossy boundary, or one which couples linearly independent modes, is often accounted for by ascribing a reflection coefficient to the boundary for the dominant wave of the system. Since there are many existing theories of plasma waves in an infinite medium, it would be useful to develop a similar technique in which the infinite system dispersion relation can be used to determine the behavior of bounded plasma systems. We treat this problem in Section 2, and show, subject to certain restrictions, how to interpret such theories for bounded systems.

1.2 Low-Frequency Instabilities

1.2.1 Waves Propagating Perpendicular to the Magnetic Field

In 1954, Kruskal and Schwarzschild[29] used the single-fluid MHD equations to show that a plasma supported against gravity by a magnetic field can be unstable to flute-like perturbation on the plasma boundary (i.e., no variation along the magnetic field direction). The instability is analogous to the Rayleigh-Taylor instability of ordinary hydrodynamics, which develops when a heavy fluid is supported against gravity by a lighter fluid. Several years later, Rosenbluth and Longmire[30] considered the same instability using the guiding-center equations for the particles, and gave a clear physical explanation of how it develops. A kinetic treatment of this flute wave[31] revealed that the finite ion Larmor radius has a stabilizing effect, a point confirmed both by a moment equation approach including collisionless viscosity,[32,33] and by

the guiding-center equations.[34,35] The stabilization is due basically to the ions sampling the perturbed electric field over their gyro-orbits.

The form of this instability studied in Section 3 arises in a plasma column immersed in an axial magnetic field, which may rotate due to a radial electric field. The inertia or centrifugal force effect on the ions is analogous to a gravitational force, and the radial density varies continuously, but decreases with radius. When the electric field is a linear function of radius and the density profile is Gaussian, the column rotates uniformly, and one obtains a second order differential equation in combining the perturbed equations.[31,33] For nonuniform rotation, Rosenbluth and Simon[36] give the resulting second order differential equation as obtained from a new set of moment equations derived from kinetic theory. To derive these moment equations, quantities are ordered in a manner more consistent with a finite ion Larmor radius than are the usual moment equations. However, it turns out that this differential equation can also be derived from the usual moment equations, which is the approach used in Section 3.

We consider solutions to this equation for both uniform rotation, when analytical results are obtained, and for nonuniform rotation, when numerical methods are used. Particular attention is paid to the radial extent of the column, as this has a strong influence on the stability of the waves. The effect of nonuniform rotation due to the radial electric field is considered for the lower order azimuthal modes, including the transition to rotation with a sharp shear. For this latter case, the additional destabilizing mechanism of velocity shear can lead to a Kelvin-Helmholtz instability.[37,38] Finally, two low-frequency instabilities in a hollow cathode arc discharge experiment are identified as the type of flute wave studied here.

1.2.2 Waves Propagating at an Angle to the Magnetic Field

When the preceding problem is generalized to allow propagation at an angle to the magnetic field, a new instability can develop in the presence of a density gradient alone. This is the collisional drift wave first discussed by Moiseev and Sagdeev[39] in 1963, and by Chen[40,41] in 1964-65. The drift wave propagates in the direction of the electron

diamagnetic drift, and the axial (i.e., along the magnetic field) resistivity of the electrons can maintain a phase shift between the perturbed density and potential to produce instability. The dispersion relation describing this wave is usually derived from the moment equations, although it can be treated from kinetic theory by using an appropriate collision term.[42] There is also a counterpart to this instability for a collisionless plasma, where resonant particle effects replace resistivity in maintaining a phase shift between the perturbed density and potential.[42]

In the early treatments of collisional drift waves, it was found that any density gradient could produce instability, so it was sometimes referred to as a "universal" instability. However, including the effect of collisional viscosity (ion-ion collisions) can stabilize the instability, as discussed by Hendel et al.[43] Another modification to the drift wave arises when ion and electron heat conduction are included in the theory, as shown by Galeev et al.,[44] and by Tsai et al.[45] The effect of ion heat conduction is very small, but that of the electrons can be significant. In fact, the inclusion of the electron heat conduction along the magnetic field is needed to obtain a destabilizing effect from an axial electron drift (a current) for the drift wave.[8,28] This is in contrast to the drift wave found for weakly ionized plasmas, where charged-neutral particle collisions are important, and an isothermal theory reveals a destabilizing effect due to axial electron drift.[46]

In Section 4, we first derive a general dispersion relation for the drift waves, and then systematically examine the various approximations to it which give the dispersion relations of other authors. The effects of these approximations are illustrated for parameters appropriate to a Q-machine experiment, using the procedure obtained in Section 2 for determining the stability of bounded plasmas. These results allow us to correctly explain a recent drift wave experiment in a Q-machine.[47]

1.2.3 Waves Propagating Parallel to the Magnetic Field

When one restricts the direction of propagation of the waves to lie along the magnetic field, they become ion-acoustic waves of the type first studied by Tonks and Langmuir in 1929.[48] These waves are similar to sound waves in a neutral gas, except that there are Coulomb forces present; these cause the waves to be driven by a combination of the electron and ion pressures, while the inertia is due to the ions. Kinetic treatments[49-52] of these waves for a collisionless plasma in the early 1960's indicate stability in the absence of electron drift. The waves are Landau damped by the electrons and ions, the latter predominating except when $T_i \ll T_e$. In the presence of electron drift, resonant particle effects can produce instability when Landau amplification by the electrons offsets Landau damping by the ions. For a weakly ionized magnetoplasma, with $T_i \ll T_e$, Self[46] has discussed ion-acoustic instability due to electron drift, using the moment equations with the isothermal assumption. In this case, the destabilizing effect of drift results from electron-neutral collisions, and offsets ion-neutral collisional damping.

For fully ionized collisional plasmas, Coppi and Mazzucato[8] have found ion-acoustic instability due to electron drift only if electron heat conduction is included, as for collisional drift waves. In Section 5, we treat this instability in detail, and show, in addition, that electron viscosity and collisional energy transfer between electrons and ions at different temperatures ($T_i < T_e$) can also produce instability. Electron drift is required to make the electron viscosity destabilizing, but a temperature difference can produce instability without electron drift. This latter effect is analogous to a neutral sound wave instability in a weakly ionized plasma studied by Ingard and Schulz[53] which is driven by collisional energy transfer between electrons and neutrals with $T_n < T_e$. Schulz[54] also suggested the occurrence of this type of instability in fully ionized plasmas, as studied in Section 5. Again, the analysis of these waves includes a description of their behavior in bounded systems using the methods of Section 2.

In conclusion, it should be noted that we follow the classification of the wave types by the direction of propagation because of

historical development, and for simplicity of the analysis. As the angle of propagation with respect to the magnetic field is varied continuously, one wave type may evolve into another, or one wave type may become more unstable than another. As far as possible, we shall point out the connections between the wave types in the study to follow, particularly in Section 4.

2. STABILITY ANALYSIS FOR BOUNDED MEDIA

In this section, we give a formal procedure for interpreting the solutions to the dispersion relation of a system,

$$D(\omega,\underset{\sim}{k}) = 0 \ , \tag{2.1}$$

where $D(\omega,\underset{\sim}{k})$ is the dispersion function. This dispersion function is obtained by perturbing to first order the equation describing the system, and then eliminating the perturbed variables among these equations. The presence of the wavenumber $\underset{\sim}{k}$ implies that the equations have been Fourier transformed along the direction of $\underset{\sim}{k}$, and that the system is infinite in this direction. Similarly, the equations have been Fourier or Laplace transformed in time, so Eq. (2.1) describes the relation between ω and $\underset{\sim}{k}$ for linear perturbations varying as $\exp i(\omega t - \underset{\sim}{k}\cdot\underset{\sim}{r})$. The system is said to be unstable if a real $\underset{\sim}{k}$ yields a complex ω with a negative imaginary part, i.e., $\mathrm{Im}(\omega) < 0$, for the perturbation then grows in time. For an infinite system, $\underset{\sim}{k}$ is assumed to take on any real value.

As mentioned in Section 1, a number of authors have already considered improvements to this method of stability analysis. Most of these follow Sturrock,[16] who has clearly pointed out the importance of considering the perturbation to be localized in space, i.e., a wave packet, rather than a physically unrealizable monochromatic plane wave. In this case, $[D(\omega,\underset{\sim}{k})]^{-1}$ acts like the Laplace-Fourier transform of the Green's function for an initial value problem, and one must invert the Laplace and Fourier transforms to determine the wave packet response. The system is still unstable if any real $\underset{\sim}{k}$ yields an $\mathrm{Im}(\omega) < 0$, but the characteristics of the instability may be changed. We shall review this procedure for infinite systems in Section 2.1.

In using the results obtained from an infinite system to interpret experimental results, one must use caution, for all real systems are bounded. Thus, in Section 2.2, we consider the stability analysis for bounded systems which can be treated as a section of an infinite system. Strictly this is applicable to media which can be described by the fluid

equations, as discussed in Section 2.2.1. In such a case, Eq. (2.1) still describes the medium, but the boundary conditions now restrict the values of $\underset{\sim}{k}$.

2.1 Waves in an Infinite Medium

2.1.1 Basic Model

We consider a time-invariant system of general cylindrical form, infinite and uniform along z. It is assumed that the transverse eigenvalue problem has been solved for the perturbed equations, so that the perturbations now vary as $\exp i(\omega t - kz)$. A single linearly independent transverse eigenmode is considered with a dispersion relation of the form of Eq. (2.1) when the vector on the wavenumber is dropped, i.e., $D(\omega,k) = 0$. For simplicity, $D(\omega,k)$ is taken to be a polynomial of order α in ω and of order β in k, as is the case for the fluid treatment of plasmas. Derfler[17] discusses cases when $D(\omega,\underset{\sim}{k})$ is a double-valued function as arises, in general, in the kinetic theory of hot plasmas.

We consider the initially quiescent system to be excited by a localized source, $s(t,z)$, following the approach of Briggs.[19] The source has the form $s(t,z) = g(z)f(t)$, where $g(z) = 0$ for $|z| > d$, and $f(t) = 0$ for $t < 0$. To find the spatial and temporal response of the system to such a source, we must perform the inverse Laplace and Fourier transforms. The system response can thus be written[19]

$$\psi(t,z) = \left(\frac{1}{2\pi}\right)^2 \int_{-\infty}^{\infty} \int_{-\infty+i\sigma}^{\infty+i\sigma} G(\omega,k)\, f(\omega)\, g(k) \exp i(\omega t - kz)\, d\omega dk \,. \qquad (2.2)$$

Here ψ represents any first order variable, $f(\omega)$ is the Laplace transform of $f(t)$, $g(k)$ is the Fourier transform of $g(z)$, and $G(\omega,k) = [D(\omega,k)]^{-1}$ is the Laplace-Fourier transform of the Green's function. The Fourier integral path (FIP) is taken along the real k-axis, while the Laplace integral path (LIP) is taken below all singularities of the integrand, i.e., σ sufficiently negative, as dictated by causality. The response can be written in a more useful form if we interchange the order of integration. This yields

$$\psi(t,z) = \frac{1}{2\pi} \int_{-\infty+i\sigma}^{\infty+i\sigma} F(\omega,z)\, f(\omega) \exp i\omega t \, d\omega \,, \qquad (2.3)$$

where

$$F(\omega,z) = \frac{1}{2\pi} \int_{-\infty}^{\infty} G(\omega,k)\, g(k) \exp(-ikz)\, dk \,. \qquad (2.4)$$

Equations (2.3) and (2.4) give the required mathematical formalism for finding the response of the system to some source. We will apply it to the two most general questions of interest. The first question relates to determining the natural response of the system; that is, what is the response to an impulse source in space and time? If the natural response eventually grows indefinitely in time at a given position, the system cannot reach a linear steady state. On the other hand, if the response eventually decays at a given position, one may inquire into the second question, which relates to the forced response of the system; that is, what is the response to a localized steady sinusoidal source switched on at $t = 0$?

2.1.2 Natural Response

To study the natural response of the system, we let $f(t) = \delta(t)$, where $\delta(t)$ is the impulse (or delta-) function. In order to use contour integration in evaluating the integrals of Eqs. (2.3) and (2.4), we shall be interested in the singularities of the integrands. Consider first the evaluation of $F(\omega,z)$ for any $\omega = \omega_L$ on the LIP. Since $g(z)$ is localized, then, for any physically realizable form, $g(k)$ is an entire function, i.e., it has no singularities in the finite k-plane. Thus, the only possible singularities in the integrand of Eq. (2.4) are those of $G(\omega,k)$. In the simple cases to which the present discussion is limited, these singularities of G will be poles at the zeros of $D(\omega,k)$. A sketch of these zeros in the k-plane is shown in Fig. 2.1(a). The dotted lines indicate the loci of the zeros as $\mathrm{Im}(\omega)$ is increased for constant $\mathrm{Re}(\omega)$, as shown by the corresponding dotted line in Fig. 2.1(b). As ω traverses the LIP, one of these zeros may appear on the real k-axis. This corresponds to the LIP intersecting one of the ω_α (k real) contours, where ω_α is a solution to $D(\omega,k) = 0$, as shown in

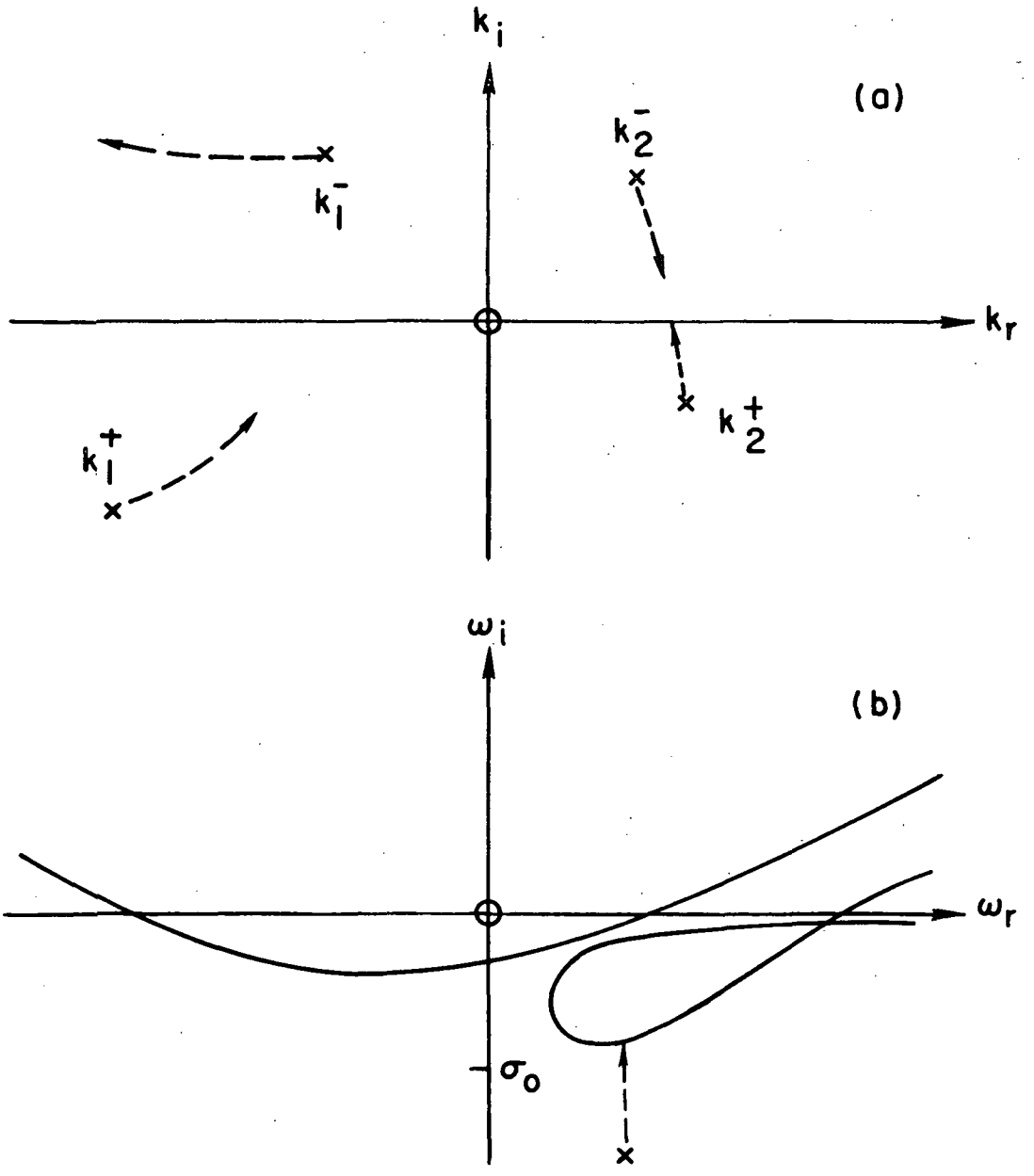

Fig. 2.1 (a) The loci of the zeros of $D(\omega,k)$ in the k-plane when $Im(\omega)$ increases for constant $Re(\omega)$. (b) The corresponding path taken by ω is shown by the dotted line. Solid lines in (b) represent ω_α(k real) contours.

Fig. 2.1(b). However there is then an ambiguity in the k-integration as to which direction to integrate around this pole on the real k-axis. This is resolved by initially taking the LIP low enough in the ω-plane so that the zeros of $D(\omega_L,k)$ are off the real k-axis; that is, $\sigma = \sigma_0$, where σ_0 is less than the minimum imaginary value of ω_α(k real). Only then do we unambiguously satisfy causality, which is proved as follows. With $\mathrm{Im}(\omega) < \sigma_0$, we may label the zeros of $D(\omega,k)$ in the k-plane as k^+ or k^-, depending on whether or not they appear in the lower or upper half planes, respectively, as shown in Fig. 2.1(a). $F(\omega,z)$ can now be evaluated by contour integration, with the contours being closed in the lower half k-plane for $z > 0$ and in the upper half k-plane for $z < 0$. It is clear that $F(\omega,z)$ is nonsingular for any ω below σ_0 in the ω-plane. Causality is thus assured, since, for the ω-plane integration in Eq. (2.3), we may close the contour in the lower half plane for $t < 0$, enclosing no poles [$f(\omega) = 1$ here], and thus giving $\psi(t,z) = 0$ for $t < 0$. As we shall see, the asymptotic natural response does not depend on the explicit evaulation of $F(\omega,z)$ for these simple poles, although we will need to return to this evaluation for the forced response in Section 2.1.3.

In order to find the asymptotic time response of the system, we wish to deform the LIP as far as possible upward, where it will become clear that the asymptotic response is governed by the lowest singularity of $F(\omega,z)$. As the LIP is raised in the ω-plane, e.g., $\sigma \to \sigma_1$, the poles due to $G(\omega_L,k)$ will cross the real k-axis when the LIP intersects the lowest branch of ω_α(k real). When this happens the function F must be redefined as its analytic continuation, $\tilde{F}$, as the FIP is deformed to continue to include the same poles as before. This is illustrated in Fig. 2.2, where we show, along with the deformed FIP, the loci of two poles of $G(\omega_L,k)$ in the k-plane for several LIP's. The poles may be compared with k_2^+ and k_2^- in Fig. 2.1(a). These loci are the contours of $\omega_L = \omega_r + i\sigma$, as shown in Fig. 2.3, in the map of ω_L into the k-plane via $D(\omega_L,k) = 0$. Also shown in Fig. 2.3 is a branch of the ω_α (k real) contour [see Fig. 2.1(b)].

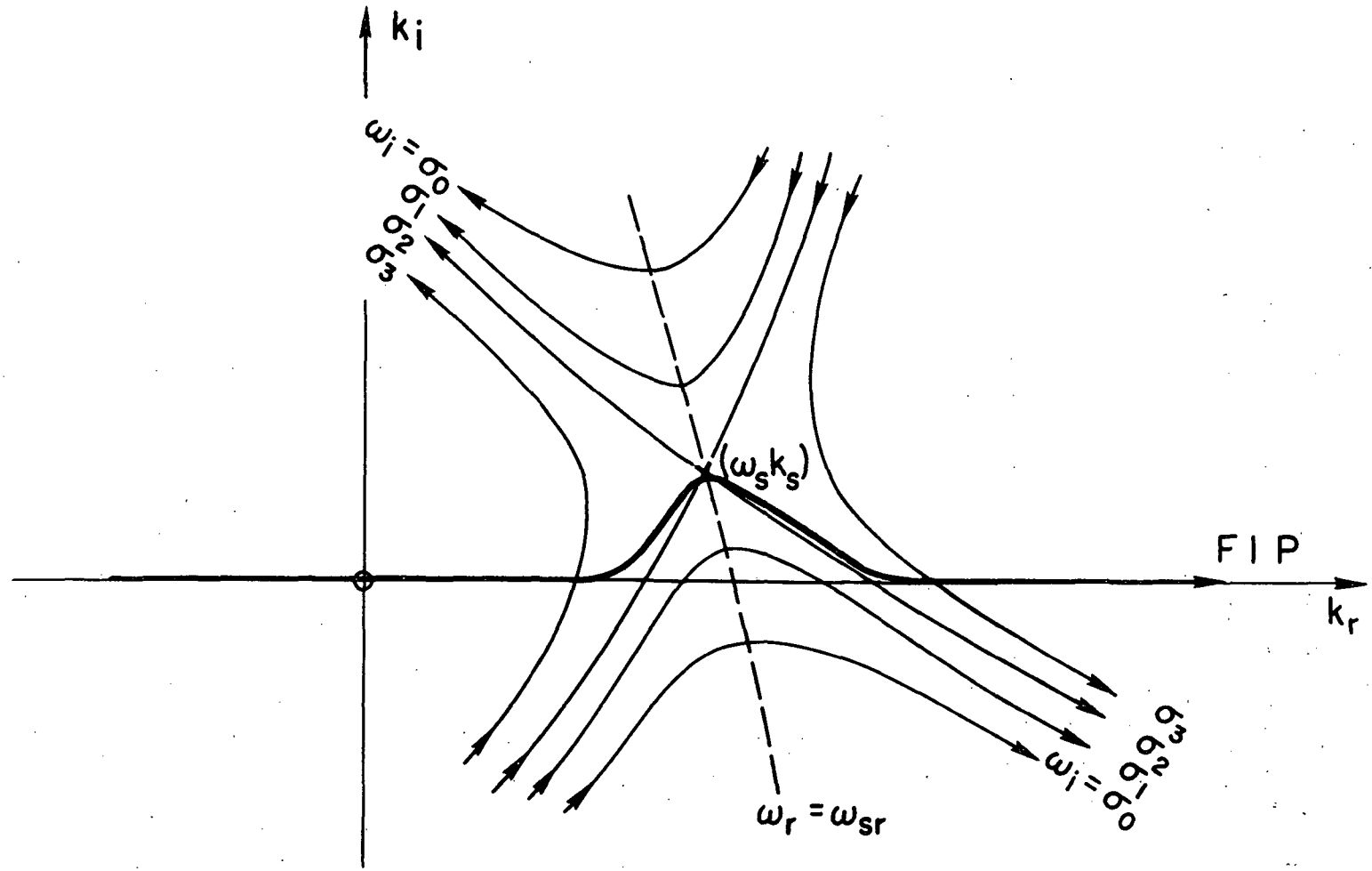

Fig. 2.2 Map (or loci) of several LIP's from Fig. 2.3 into the k-plane via $D(\omega_L, k) = 0$, showing the FIP and its deformation to include the same poles of $G(\omega_L, k)$ as the LIP is raised. Two poles collide at the saddle point (ω_s, k_s), pinching the FIP between them.

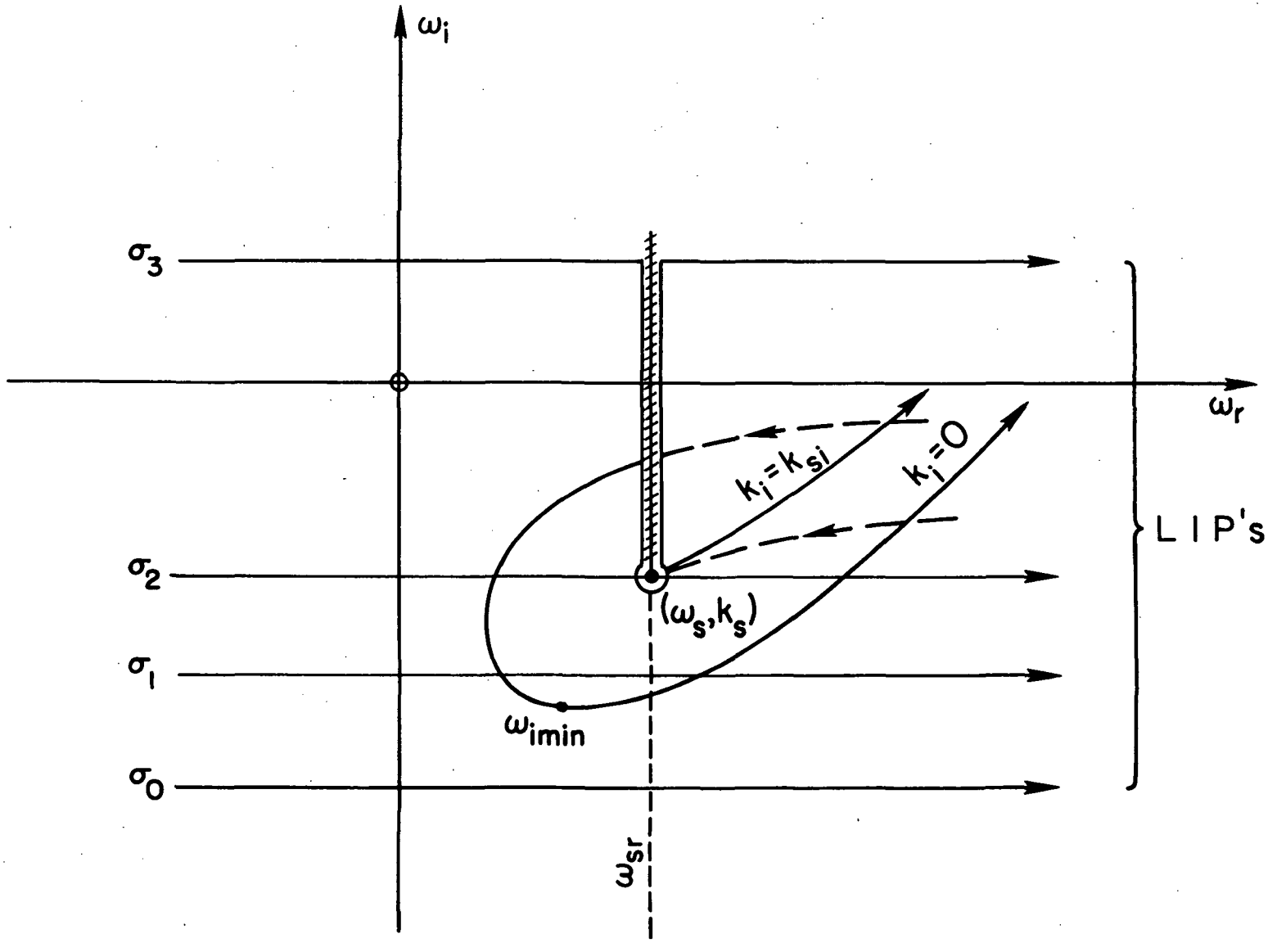

Fig. 2.3 Map of k into the ω-plane via $D(\omega,k) = 0$ for $k_i = 0, k_{si}$, showing the branch point (ω_s, k_s), and the LIP's corresponding to Fig. 2.2, but with σ_3 deformed around the branch point.

The LIP may be continuously raised ($\sigma \to \sigma_2$) until two poles of $G(\omega_L, k)$ collide or merge through the FIP, pinching it between them, as shown in Fig. 2.2. When this happens, at (ω_s, k_s), we have a double root $k_s(\omega_s)$ of $D(\omega,k) = 0$, i.e., a saddle point of $\omega(k)$ in the map of ω into the k-plane or, equivalently, a branch point of $k(\omega)$ in the map of k into the ω-plane via $D(\omega,k) = 0$. In raising the LIP still further ($\sigma \to \sigma_3$), it must be deformed around the branch cut of which the branch point (ω_s, k_s) forms one end point, as shown in Fig. 2.3. The asymptotic response is clearly governed by the lowest such branch point in the ω-plane and can be evaluated as[19]

$$\psi(z,t) \longrightarrow \frac{g(k_s)}{\left[2\pi i\left(\frac{\partial^2 D}{\partial k^2}\right)\left(\frac{\partial D}{\partial \omega}\right)\right]^{1/2}_{\omega_s, k_s}} \frac{\exp i(\omega_s t - k_s z)}{t^{1/2}} \qquad (t \to \infty) . \tag{2.5}$$

In general, saddle points of $\omega(k)$, i.e., the branch points of $k(\omega)$, are given by the simultaneous solution of $D(\omega,k) = 0$ and $\partial D/\partial k = 0$. However, not all such saddle/branch points are relevant to the stability analysis, but only those which correspond to the merging of roots $k(\omega)$ for $D(\omega,k) = 0$ from opposite half k-planes, and thus pinch the FIP. If the lowest such branch point (ω_s, k_s) lies in the lower half plane ($\omega_{si} < 0$), the response eventually increases without limit (in a linear analysis) at all finite z, as described by Eq. (2.5), and the system is by definition <u>absolutely</u> unstable. On the other hand, if the lowest such branch point lies in the upper half plane ($\omega_{si} > 0$), the response eventually decays to zero at all finite z, according to Eq. (2.5). In this case, if the system supports instabilities, i.e., if any ω_α(k real) contour dips below the real ω-axis, it is <u>convectively</u> unstable, and the perturbation grows but convects away. In all cases, the asymptotic response has an exponential envelope in space (except near the front of the disturbance) given by $\exp(-k_{si} z)$.

The essential difference between absolute instabilities and convective instabilities is shown in Fig. 2.4. For a system which is absolutely unstable, any random noise will grow and saturate in a

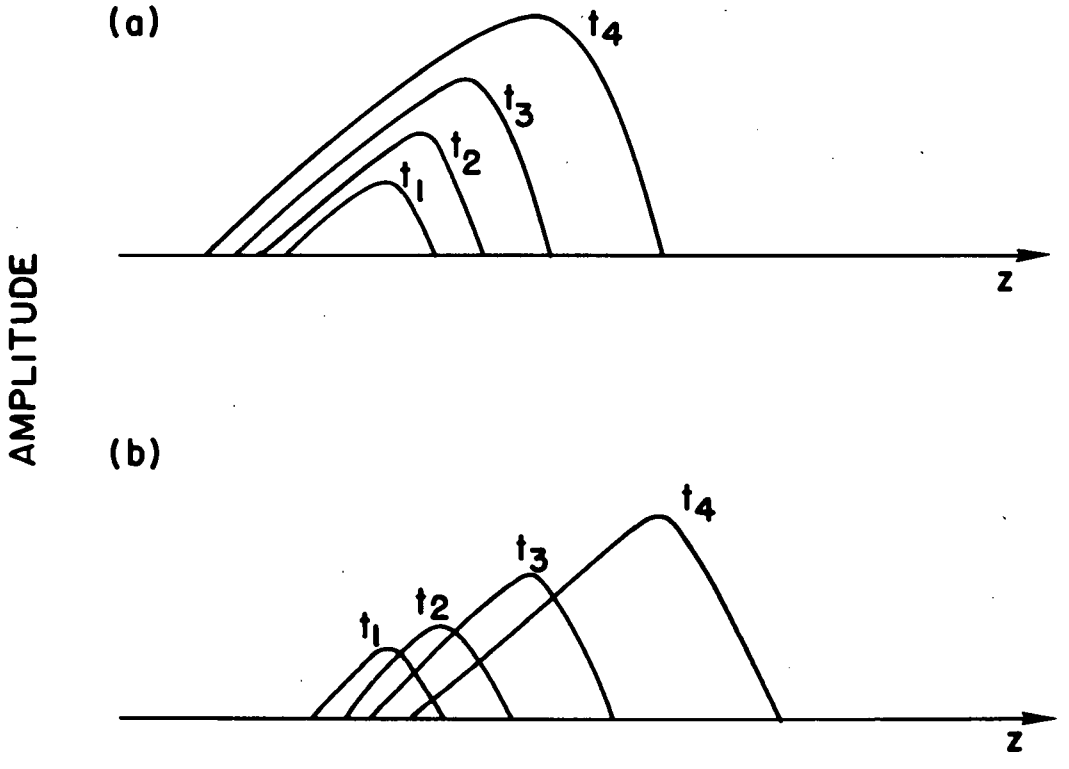

Fig. 2.4 Development of a localized perturbation as a function of time ($t_1 < t_2 < t_3 < t_4$) for (a) absolute instability, and (b) convective instability.

nonlinear state, so that further linear analysis is not appropriate. However, since for convectively unstable or stable systems the natural response eventually decays, one may consider the response to a continuous forcing function. We might expect a convectively unstable system to exhibit spatial amplification. A more detailed explanation of the convective instability is given in the next subsection.

2.1.3 Forced Response

We consider a localized sinusoidal source switched on at $t = 0$, i.e., $s(t,z) = \delta(z) \exp i\omega_0 t$ for $t > 0$, where ω is real. This gives $g(k) = 1$, and $f(\omega) = [i(\omega-\omega_0)]^{-1}$. We are again interested in the asymptotic response, so the LIP is moved upward to evaluate Eq. (2.3). The system is assumed free of absolute instabilities, so that any branch points in the ω-plane due to the colliding of poles are in the upper half ω-plane. The first singularity encountered in the integrand of Eq. (2.3) by moving the LIP upward is due to $f(\omega)$ at $\omega = \omega_0$ on the real ω-axis. The asymptotic response is thus determined by $\tilde{F}(\omega_0,z)$.

To evaluate $\tilde{F}(\omega_0,z)$, which is the analytic continuation of Eq. (2.4), we use contour integration as mentioned in Section 2.1.2. The integration contour is closed in the upper half k-plane for $z < 0$ and in the lower half k-plane for $z > 0$. The poles of $G(\omega_0,k)$ included in the upper half plane and lower half plane contours occur at $k = k_\beta^-(\omega_0)$ and $k = k_\beta^+(\omega_0)$, respectively. It is important to note that some of the $k_\beta^-(\omega_0)$ may actually be in the lower half plane and some of the $k_\beta^+(\omega_0)$ in the upper half plane. These are the poles which cross the real k-axis as the LIP is raised from σ_0 to the real ω-axis. In defining $\tilde{F}(\omega_0,z)$ as the analytic continuation of $F(\omega_0,z)$, the contour along the real k-axis is deformed to always include the same poles as when $\sigma = \sigma_0$ (see Fig. 2.2); that is, the positions of the poles on the initial σ_0 contour determine whether they appear in the response for $z > 0$ or $z < 0$.

By the theory of residues, Eq. (2.4) can be evaluated as

$$\tilde{F}(\omega_0, z < 0) = \sum_{\beta} \frac{i \exp(-ik_\beta^- z)}{\left[\frac{\partial D(\omega_0, k)}{\partial k}\right]_{k=k_\beta^-}} , \qquad (2.6)$$

$$\tilde{F}(\omega_0, z > 0) = \sum_{\beta} \frac{i \exp(-ik_\beta^+ z)}{\left[\frac{\partial D(\omega_0, k)}{\partial k}\right]_{k=k_\beta^+}} , \qquad (2.7)$$

where, for simplicity, we have only considered simple poles. From Eq. (2.2), we see that the asymptotic response is

$$\psi(t,z) \longrightarrow \tilde{F}(\omega_0, z) \exp i\omega_0 t \qquad (t \to \infty) . \qquad (2.8)$$

Note that if any of the $k_\beta^\pm$ have crossed the real k-axis as the LIP was moved upward from σ_0 to the real ω-axis, they now appear as spatially amplifying waves in the response. This is the condition under which a system is convectively unstable. If none of the $k_\beta^\pm$ has crossed the real k-axis, all of the waves decay away from the source, and the system is stable. In general, several waves will be excited by the source (different β's), but, as $|z|$ increases, the wave with the smallest spatial damping rate or largest spatial growth rate will ultimately dominate.

2.2 Waves in a Bounded Medium

2.2.1 Physical Model

In this subsection, we discuss the response of a uniform cylindrical system, as in Section 2.1.1, but now of finite length, L, with arbitrary terminations at $z = -L/2$ and $z = L/2$. The response will be determined from the appropriate roots of the linear dispersion relation of an infinite system containing the same medium, together with the boundary conditions.

The conditions under which it is valid to treat the finite system as a terminated length of an infinite system need some discussion. Briefly, it is valid for ordinary dielectrics and cold plasmas and also, subject to conditions discussed later, for fluids and plasmas treated via fluid equations. It is not, however, in general valid for collisionless plasmas treated by kinetic equations. The reason for the distinction between dielectric or fluid treatments on the one hand, and kinetic treatments on the other, is that in the former the particle dynamics used to calculate the charge, ρ, and current, $\underset{\sim}{J}$, in Maxwell's equations are determined purely by the local fields $\underset{\sim}{E}$ and $\underset{\sim}{B}$, whereas in the latter, ρ and $\underset{\sim}{J}$ are determined via integrals over the particle trajectories, including earlier encounters with the boundaries.[23-26] Thus in a cold or fluid model, a boundary imposes conditions on the fields and fluid variables only at the boundary, whereas in a kinetic model, the effect of the boundary conditions on the particles is felt on the particle dynamics throughout the system.

For simplicity, we assume that the dispersion relation is quadratic in k, which can be written as

$$D(\omega,k) \equiv k^2 + b(\omega)k + c(\omega) = 0 \ , \tag{2.9}$$

or

$$D(\omega,k) \equiv [k - k^+(\omega)][k - k^-(\omega)] = 0 \ . \tag{2.10}$$

These can be solved to yield the relation

$$k^+ - k^- = \pm \left[b^2(\omega) - 4c(\omega)\right]^{1/2} \ . \tag{2.11}$$

The roots k^+ and k^- are taken to be excited on opposite sides of a source. More explicitly, from the analysis of Section 2.1.3, k^+ and k^- must lie in the lower and upper half k-planes, respectively, as $\omega_i \to -\infty$. There are special cases for which both waves are excited on the same side of a source. For example, a cold beam-plasma system with $D \equiv 1 - \omega_p^2/\omega^2 - \omega_b^2/(\omega - kv_0)^2$ has two k roots corresponding to waves excited on the downstream side. Here ω_p and ω_b are the plasma frequencies of the background plasma and beam, respectively, and v_0 is

the beam velocity. In such cases, the downstream boundary can produce no effect upstream, so the waves act as though the boundary were not present. Finally, the case when a dispersion relation is of higher order than quadratic in k is discussed in Section 2.2.5.

The boundaries are described by complex reflection coefficients, ρ_1 and ρ_2, for the boundaries at $z = -L/2$ and $z = L/2$, respectively, as shown in Fig. 2.5. Specifically, ρ_1 and ρ_2 give the ratio of the reflected wave to the incident wave at the boundary, and have the forms

$$\rho_1 = |\rho_1| \exp \pm i\theta_1 \ , \quad \rho_2 = |\rho_2| \exp \pm i\theta_2 \ , \qquad (2.12)$$

where $0 \leq |\rho_{1,2}| \leq 1$ and $-\pi < \theta_{1,2} \leq \pi$. It is assumed that the phase of the reflected wave is given, either from physical arguments or by experiment, as leading or lagging the incident wave by a certain angle $|\theta|$, and the convention is adopted that $\theta > 0$ when the reflected wave leads and $\theta < 0$ when it lags. In order to preserve this convention, irrespective of the sign of ω_r, the alternate signs are introduced in Eqs. (2.12), and should be taken as + or - for $\omega_r \gtrless 0$, respectively. Also, ρ_1 and ρ_2 may be functions of the frequency, ω, although this dependence will not be shown explicitly in what is to follow.

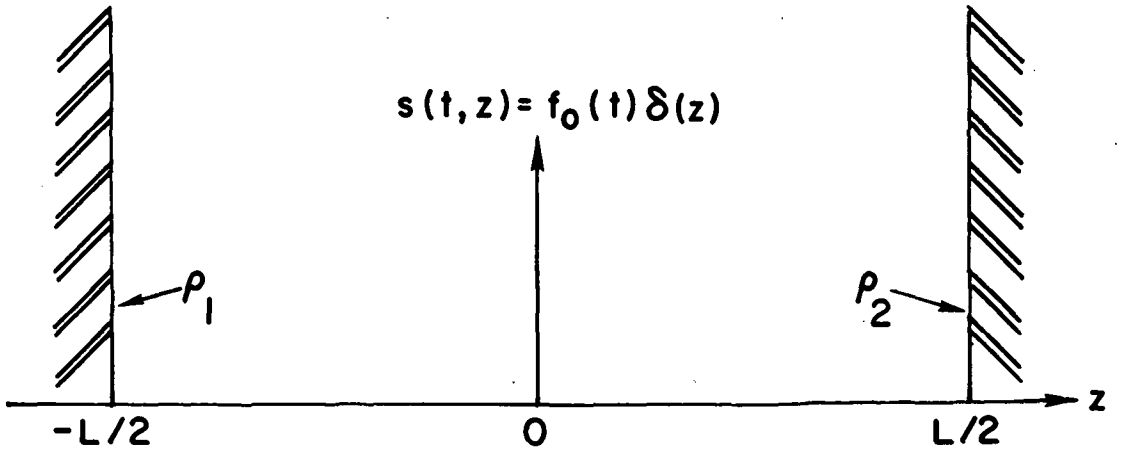

Fig. 2.5 Bounded system with reflection coefficients ρ_1 and ρ_2, defined in Eq. (2.12), and source $s(t,z)$.

For simplicity, we consider the source to be localized at the origin, i.e., $s(t,z) = f(t)\delta(z)$, since the form of the asymptotic natural response is independent of the position of the source. This is proved in Appendix A, where we derive the response of a system to an arbitrarily positioned source. The results of this more general analysis will be used in Section 2.2.4 to study the forced response.

2.2.2 Mathematical Model

If we are to use the methods of Section 2.1 in evaluating the response of a bounded system to some source, our model must be modified. We have to account for the waves reflected from the boundaries, and produce a spatially infinite and uniform model to use the Fourier transform method of Section 2.1. The reflected waves can be accounted for by using an infinite train of image sources, each one representing a reflected wave. This is akin to the method of images used in electrostatics. Care must be exercised, though, as waves from these image sources must sometimes propagate as k^- waves, and sometimes as k^+ waves, to model the system properly.

As an intermediate step, we define the reciprocal medium as the medium with the dispersion relation

$$D(\omega,-k) = 0. \tag{2.13}$$

The bounded system can now be modeled as in Fig. 2.6, where we have included the image sources. The clear area denotes the regular medium, and the shaded area denotes the reciprocal medium. These areas alternate spatially at odd multiples of $L/2$. It is understood that the boundaries between the media have no effect other than to convert a k^- wave into a k^+ wave and *vice versa*. This, of course, does not correspond to a physically realizable model, since in that case there would be reflections from the boundaries between the different media. However, for the bounded system, this effect is included in the reflection coefficients, ρ_1 and ρ_2, and, in our model, we choose to account for the reflection coefficients in determining the amplitudes and phases of the image sources. So, given the initial source $f_0(t)$, a general expression for the source $f_n(t)$, where n is an integer, can be written as

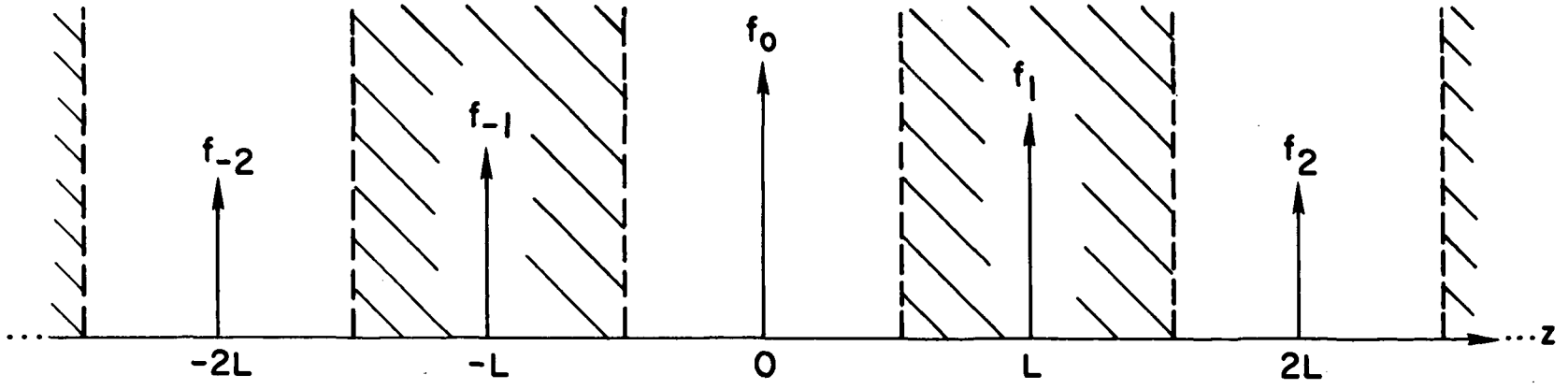

Fig. 2.6 Bounded system ($-L/2 \leq z \leq L/2$) modeled as an infinite system with image sources given by Eqs. (2.14) and (2.15). Shaded area contains the reciprocal medium.

$$f_n(t) = |\rho_1| \exp(\pm i\theta_1)\, f_{n-1}(t) \qquad (2.14)$$

if n is odd and positive, or even and negative. Otherwise, we have

$$f_n(t) = |\rho_2| \exp(\pm i\theta_2)\, f_{n-1}(t) , \qquad (2.15)$$

where the sources are located at $z = nL$. The response to each of these sources in the bounded region ($-L/2 \le z \le L/2$) corresponds to a reflected wave of the original system. Just how to find these responses, and how to reduce the model to one that is uniform in space, is discussed below.

To evaluate the response due to the image sources, each source can be considered separately and the results added together, which is valid due to linearity. Since we are now only considering one source at a time, as far as the response in the bounded region ($-L/2 \le z \le L/2$) is concerned, all the regions of the reciprocal medium between the source and the bounded region can be combined, beginning at the image source (remember that the interfaces between the media do not produce reflections). The procedure will then be to find the response to the image source in the reciprocal medium up to the position where the combined reciprocal medium ends. From this position on to the bounded region, the wave will be treated as propagating in the regular medium.

As an example of this procedure, we shall evaluate the response of the image source at $z = -5L$. The essential steps are shown in Fig. 2.7(a-c). In part (a) the basic model is shown, while in part (b) all the regions of the reciprocal medium between the source and the bounded region have been combined, beginning at the image source. Next, we find the response at the position where the reciprocal medium ends, i.e., at $z = -5L/2$. We do this by assuming that all space is filled with the reciprocal medium, and use the analysis for an infinite system given in Section 2.1. The response is thus given by Eqs. (2.3) and (2.4). For the source at $z = -5L$, the functions in the integrands of Eqs. (2.3) and (2.4) have the form $G(k) = \exp(-i5kL)$ and, from Eqs. (2.14) and (2.15), $f_{-5}(\omega) = |\rho_1|^3 |\rho_2|^2 \exp[\pm i(3\theta_1+2\theta_2)]\, f_0(\omega)$. Also, $G(\omega,k) = [D(\omega,-k)]^{-1}$, i.e., we have the reciprocal medium. The response

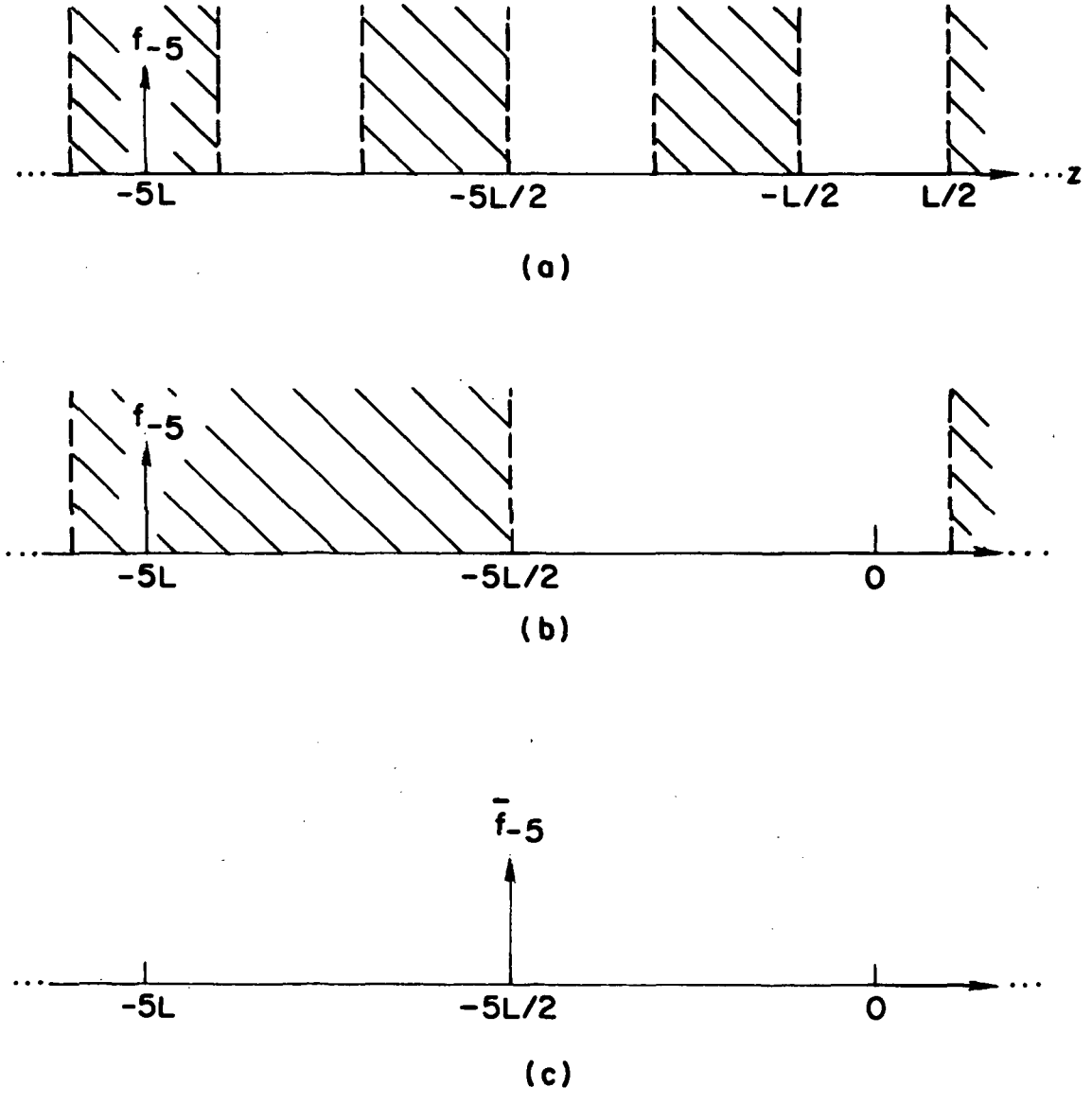

Fig. 2.7 Equivalent models with respect to the response in the bounded region ($-L/2 \leq z \leq L/2$) for a source at $z = -5L$. Source $\bar{f}_{-5}$ is given by Eq. (2.19).

at $z = -5L/2$ is then

$$\psi(t,-5/2L) = \frac{1}{2\pi}\int_{-\infty+i\sigma_0}^{\infty+i\sigma_0} F(\omega,-5L/2)|\rho_1|^3|\rho_2|^2 \exp i[\omega t\pm(3\theta_1+2\theta_2)]f_0(\omega)d\omega, \tag{2.16}$$

where the k-integration has been performed to obtain

$$F(\omega,-5L/2) = \frac{1}{2\pi}\int_{-\infty}^{\infty} \frac{\exp(-i5kL/2)}{(k+k^+)(k+k^-)}\, dk = \frac{-i \exp i5k^-L/2}{k^+ - k^-} . \tag{2.17}$$

The wave is now to propagate from $z = -5L/2$ to the bounded region in the regular medium. This portion of the wave's propagation is accounted for by considering the wave response of Eq. (2.16) to act like a source for the region to the right of $z = -5L/2$. It is in just this sense that the interface between the media is said to convert a k^- wave to a k^+ wave with no reflection. This source is determined by finding a source which, when placed at $z = -5L/2$, produces the same response there as given by Eq. (2.16). This source, shown in Fig. 2.7(c), has the value $\bar{f}_{-5} = \exp(i5k^-L/2)\,\bar{f}_{-5}$. Again, Eqs. (2.3) and (2.4) are used to find the response to the new source. We assume all space is filled with the regular medium, so that $G(\omega,k) = [D(\omega,k)]^{-1}$, and, with the source at $z = -5L/2$, $G(k) = \exp(-i5kL/2)$. Equation (2.4) then gives

$$F(\omega,z) = \frac{-i \exp[-ik^+(z+5L/2)]}{k^+ - k^-} . \tag{2.18}$$

Finally, this can be inserted in Eq. (2.3), along with the source term $\bar{f}_{-5}(\omega)$, to give the response in the bounded region.

To generalize this approach to any image source, note that the exponential factor relating $\bar{f}_{-5}$ and f_{-5} simply accounts for the wave initially propagating from $z = -5L$ to $z = -5L/2$ as a k^- wave. It is thus reasonable, and can be shown, that any source f_n at $z = nL$ can be replaced by a source $\bar{f}_n$ at $z = nL/2$ with

$$\overline{f_n} = \exp(-ink^{\pm}L/2) f_n \quad , \tag{2.19}$$

where $k^{\pm}$ is used for $n \gtrless 0$.

This gives the spatially uniform model we have sought. It consists of an infinite train of image sources at $z = nL/2$, whose values are given by $\overline{f}_n$ from Eq. (2.19). These sources are subject to the regular medium only, so the analysis of Section 2.1 may be used to evaluate the response to each source. The total response of the bounded region is found by adding all of these responses together to obtain

$$\psi(t,z) = \frac{1}{2\pi} \int_{-\infty+i\sigma_0}^{\infty+i\sigma_0} \frac{-i f_0(\omega)}{k^+ - k^-} \left\{ \exp(-ik^{\pm}z) + A(z) \sum_{m=1}^{\infty} \exp[-im(\alpha_1+\alpha_2)] \right\} \exp i\omega t \, d\omega, \tag{2.20}$$

where $k^{\pm}$ is used for $z \gtrless 0$. The other quantities in Eq. (2.20) are

$$\alpha_1 = (k^+ - k^-)\frac{L}{2} \mp \theta_1 + i \ell n|\rho_1| \quad , \tag{2.21}$$

$$\alpha_2 = (k^+ - k^-)\frac{L}{2} \mp \theta_2 + i \ell n|\rho_2| \quad , \tag{2.22}$$

and

$$A(z) = [(1 + \exp i\alpha_1) \exp(-ik^-z) + (1 + \exp i\alpha_2) \exp(-ik^+z)] \, . \tag{2.23}$$

Equations (2.20) - (2.23) give the basic mathematical equations needed to evaluate the response of a bounded system to a localized source at $z = 0$.

It should be emphasized that Eq. (2.20) gives the response for any time t, just as Eq. (2.2) gives the response of an infinite system for any time t. Thus, the finite speed of propagation of the reflected waves is taken into account. However, it is the asymptotic response which is most readily evaluated, and of most general interest, so we shall concentrate on it.

We shall consider the same two basic problems treated for the infinite plasma. First, the response of the system is found for a source which is an impulse in time. If this natural response eventually grows indefinitely in time, the system is unstable, and the linear analysis has given as much information as possible. If the response eventually decays, we may consider the second problem, i.e., the response to a steady sinusoidal source switched on at $t = 0$.

2.2.3 Natural Response

For this case, the source is an impulse in time, i.e., $f(t) = \delta(t)$, so that $f_0(\omega) = 1$ in Eq. (2.20). The first step in determining the response is to evaluate the infinite series in Eq. (2.20) as a geometric progression, which gives

$$\sum_{m=1}^{\infty} \exp\left[-im(\alpha_1 + \alpha_2)\right] = \frac{1}{\exp i(\alpha_1+\alpha_2)-1} , \qquad (2.24)$$

for $Im(\alpha_1+\alpha_2) < 0$. Thus, initially the LIP must be taken low enough in the ω-plane that the condition $Im(\alpha_1+\alpha_2) < 0$ is satisfied, in addition to the requirement that the LIP be below the branch point which occurs when $k^+ = k^-$. This is located at $\omega = \omega_s$, and is just the branch point we found for the infinite system (Section 2.1.2) when the k-integration contour was pinched by colliding poles (k^+ and k^- here).

To evaluate the asymptotic response of the system, the LIP in Eq. (2.20) is raised upward, and, as in Section 2.1.2, deformed around the branch points of the integrand. In doing so, the function in Eq. (2.24) is analytically continued in order to include the region for $Im(\alpha_1+\alpha_2) \geq 0$. The response will be governed by the lowest branch point in the ω-plane. In addition to the branch point at ω_s when $k^+ = k^-$, there are also branch points of the integrand when the function in Eq. (2.24) is singular, say at $\omega = \omega_n$. This occurs when

$$\alpha_1 + \alpha_2 = 2n\pi , \qquad (2.25)$$

where n is an integer.

Now if ω_s is the lowest branch point, Eq. (2.20) can be evaluated by using Eq. (2.11). The result, as in Eq. (2.5), has the form

$$\psi(t,z) \propto \frac{\exp i(\omega_s t - k_s z)}{t^{1/2}} \qquad (t \to \infty) , \qquad (2.26)$$

where $k_s = k^+(\omega_s) = k^-(\omega_s)$. For this case, the boundaries have no effect on the spatial form or time dependence of the response.

If, on the other hand, the lowest branch point is at ω_n, Eq. (2.24) indicates that it will be, in general, a simple pole. The response may then be written as

$$\psi(t,z) \to A(z) \exp i\omega_n t \qquad (t \to \infty) , \qquad (2.27)$$

where $A(z)$ is given by Eq. (2.23). This response is due to the constructive interference of reflected waves, and may be termed a normal mode of the system. To see this more clearly, we rewrite Eq. (2.25) as

$$(k^+ - k^-)L = [2n\pi \pm (\theta_1 + \theta_2)] - i[\ell n|\rho_1||\rho_2|] , \qquad (2.28)$$

where Eqs. (2.21) and (2.22) have been used. This equation states that for the normal modes the phase shift around the loop must be an integral multiple of 2π, and that the loop gain must be unity. It should be noted that the ω_n's and the spatial dependence of the corresponding modes are functions of the reflection coefficients.

The normal mode frequencies, ω_n, are found by eliminating $(k^+ - k^-)$ between Eqs. (2.11) and (2.28), and solving for ω. Hence, the ω_n's are given by solutions to

$$H(\omega,\rho_1,\rho_2,L,n) \equiv \left\{[2n\pi \pm (\theta_1+\theta_2)] - i\,\ell n|\rho_1||\rho_2|\right\}^2 L^{-2} - b^2(\omega) + 4c(\omega) = 0 . \qquad (2.29)$$

If the system is reciprocal, i.e., $D(\omega,k)$ is even in k, then $k^+ = -k^-$, and Eq. (2.29) reduces to

$$H(\omega,\rho_1,\rho_2,L,n) \equiv \left\{[2n\pi \pm (\theta_1+\theta_2)] - i\,\ell n\,|\rho_1||\rho_2|\right\}^2 L^{-2} + 4c(\omega) = 0. \tag{2.30}$$

Recall that, in the above analysis, ρ_1 and ρ_2 may be functions of ω. If such a dependence exists, it must be included in Eqs. (2.29) and (2.30) to solve for the frequencies ω_n. In Eqs. (2.29) and (2.30), the whole range of n values ($n = 0, \pm1, \pm2$, etc.) is allowed; with the + sign on $(\theta_1+\theta_2)$, only roots with $\omega_r > 0$ are admitted, while with the - sign on $(\theta_1+\theta_2)$, only roots with $\omega_r < 0$ are admitted. Even with this limitation, Eqs. (2.29) and (2.30) may still give extraneous roots because they were derived by squaring Eqs. (2.11) and (2.28) to remove the sign ambiguity in Eq. (2.11). To distinguish these roots, the dispersion relation must be solved for each admitted root of Eq. (2.29) or Eq. (2.30) to give k^+ and k^- separately, identifying them by the prescription that $k_i^+ < 0$ and $k_i^- > 0$ for $\omega_i < \sigma_0$. Only those roots giving $(k^+ - k^-)$ with the correct sign to satisfy Eq. (2.28) are proper ω_n roots.

It is possible to make some general observations about these normal modes without solving a specific problem. For an ω below the lowest $\omega_\alpha(k \text{ real})$ contour, i.e., $\omega_i < \sigma_0$, we have $(k_i^+ - k_i^-) < 0$. However, Eq. (2.28) demands $(k_i^+ - k_i^-) \geq 0$ since $\ell n\,|\rho_1||\rho_2| \leq 0$, so all of the ω_n's must be on or above the lowest $\omega_\alpha(k \text{ real})$ contour. Also, for $|\rho_{1,2}| \neq 1$, at least one of the roots $k^\pm$ must, in general, correspond to a spatially amplifying wave. For perfect reflections, $|\rho_1| = |\rho_2| = 1$, so the spatial growth rate of the amplifying wave equals the spatial damping rate of the attenuated wave. For a symmetric medium ($D(\omega,k)$ even in k), Eq. (2.28) can be satisfied by purely real $k^\pm$, for perfect reflections.

In order to find the more detailed loci of the ω_n's as the reflection coefficients are varied, consider the solutions to $D(\omega,k) = 0$ for small changes in ω and k, i.e., $\delta\omega$ and δk, about some solution

(ω_1, k_1). These parameters are related by

$$\frac{\delta\omega}{\delta k} = v_{G1} \quad , \tag{2.31}$$

where $v_{G1} = d\omega/dk\big|_{\omega_1, k_1}$ is the generalized group velocity, usually defined for simply propagating waves when ω and k are purely real. Using Eq. (2.31), we find for the normal modes

$$\delta(k_i^+ - k_i^-) = \delta\omega_{ni} \, \mathrm{Re}\left(\frac{1}{v_G^+} - \frac{1}{v_G^-}\right) \quad , \tag{2.32}$$

where $\delta\omega_{ni}$ is the change in the growth (or damping) rate of the normal mode. From Eq. (2.28), we see that an incremental decrease in the magnitude of the reflection coefficients gives $\delta(k_i^+ - k_i^-) > 0$. Thus, the corresponding sign of $\delta\omega_{ni}$ depends on the sign of $\mathrm{Re}(1/v_G^+ - 1/v_G^-)$. In general, for the waves studied in Sections 4 and 5, we have $\mathrm{Re}(1/v_G^+ - 1/v_G^-) > 0$, so the effect of decreasing $|\rho_1||\rho_2|$ is to damp the normal modes.

Some of these results are illustrated in Fig. 2.8, where the location of various branch points (ω_s and ω_n's) are shown in the ω-plane for a symmetric medium with $\mathrm{Re}(1/v_G^+ - 1/v_G^-) > 0$. Note that in general, for low loss reflections, it is possible to have an ω_n lower than ω_s, except in the special case when ω_s is the lowest point on the ω_α(k real) contour. As the reflections are made more lossy, the normal mode frequencies will migrate upward, eventually leaving ω_s as the lowest branch point. If ω_s is in the lower half plane, the natural response will eventually grow in time, due either to a normal mode at ω_n or an absolute instability at ω_s, depending on the reflection coefficients. If, on the other hand, ω_s is in the upper half plane, but the ω_α(k real) contour still extends below the real ω-axis (as for a convective instability), we may find a decaying or a growing natural response, depending on whether or not the reflections are lossy enough to move all of the ω_n's into the upper half plane.

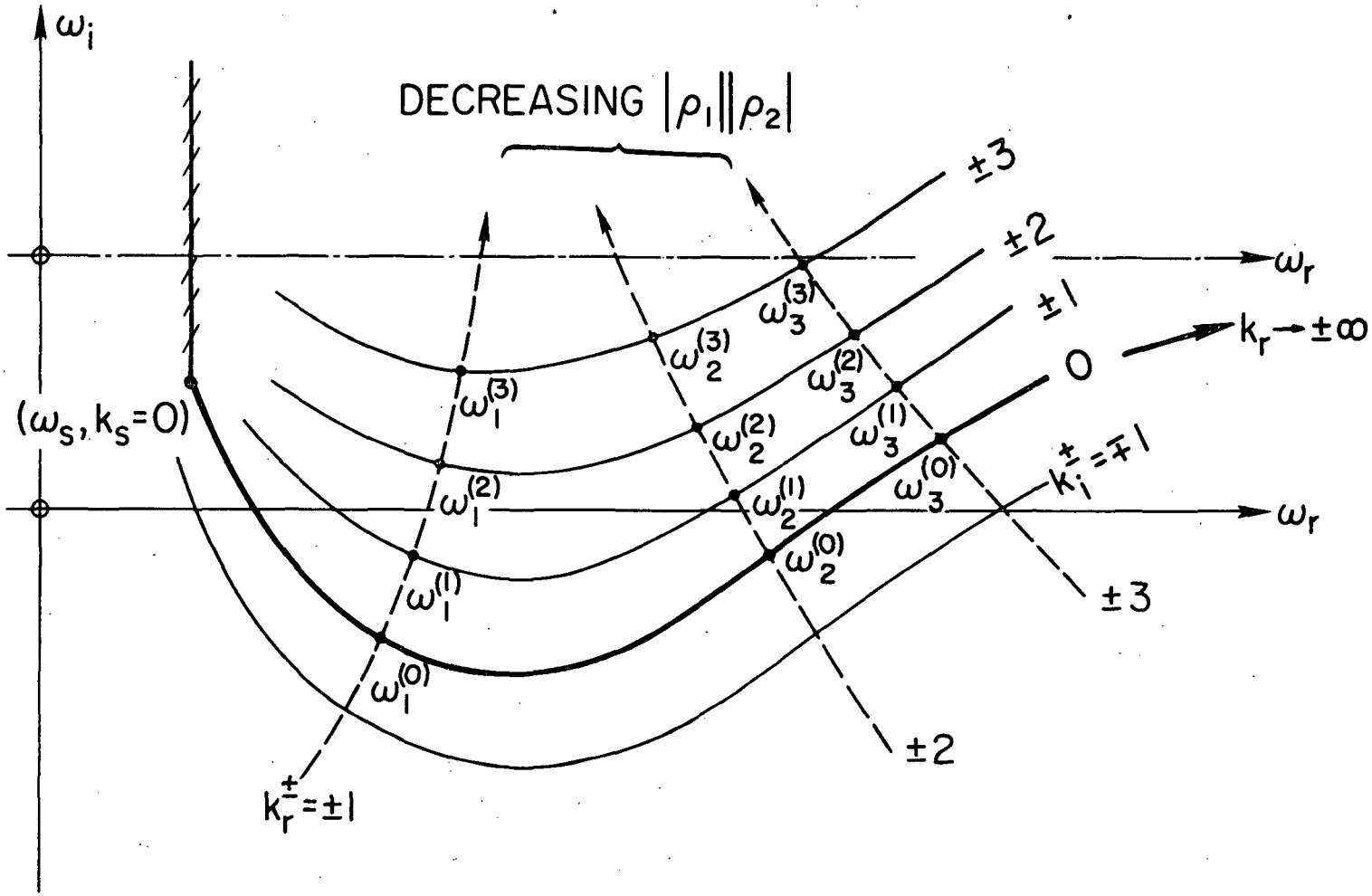

Fig. 2.8 Map of k into the ω-plane via $D(\omega,k) = 0$, when $D(\omega,k)$ is even and quadratic in k. The two sheets are represented by $\pm$ signs, and the normal mode frequencies denoted by ω_n. The cases of convective and absolute instability for the unbounded system are indicated by the full line ω_r-axis and the chain-dot ω_r-axis, respectively.

It should be noted that if a medium supports two waves which, in some parameter range, have $\mathrm{Re}(1/v_G^+ - 1/v_G^-) < 0$, an incremental increase in the reflection losses will have a destabilizing effect on the normal modes. For nearly lossless media, such a change in the sign of $\mathrm{Re}(1/v_G^+ - 1/v_G^-)$ may occur when one or both of the waves have negative small signal energy.[55] The destabilizing effect of loss is then analogous to that found in a resistive-wall amplifier.[56] Of course, any such system would have to comply with the model used in this section. However, we shall not pursue such a study here. In any event, as mentioned earlier, all of the ω_n's must still be above the lowest ω_α(k real) contour.

2.2.4 Forced Response

In the last subsection, we found that if all the normal mode frequencies, ω_n, and the branch point, ω_s, are in the upper half ω-plane, the natural response of the bounded system will eventually decay. For this case, the forced response of the system to a localized sinusoidal source may be considered. We again take $f_0(t) = \exp i\omega_0 t$ for $t > 0$, where ω_0 is real, as shown in Section 2.1.3. Its Laplace transform is $f_0(\omega) = [i(\omega-\omega_0)]^{-1}$. In studying the natural response, the source was taken at $z = 0$ since the form of the asymptotic natural response is not dependent on the source position, as shown in Appendix A. However, the form of the forced response is dependent on the source position, so we use the result of Appendix A for a localized source at an arbitrary position, z_0, where $-L/2 \le z_0 \le L/2$. For the sinusoidal source, this gives the response

$$\psi(t,z) = \frac{1}{2\pi}\int_{-\infty+i\sigma_0}^{\infty+i\sigma_0} - \frac{\left\{\exp[-ik^{\pm}(z-z_0)]\ \bar{A}(z)\sum_{m=1}^{\infty}\exp[-im(\bar{\alpha}_1+\bar{\alpha}_2)]\right\}}{(k^+ - k^-)(\omega - \omega_0)} \exp i\omega t\, d\omega, \tag{2.33}$$

where $k^{\pm}$ is used for $z \gtrless z_0$. The other quantities in Eq. (2.33) are

$$\bar{\alpha}_1 = (k^+ - k^-)\left(\frac{L}{2} + z_0\right) \mp \theta_1 + i\,\ell n|\rho_1|\ , \tag{2.34}$$

$$\bar{\alpha}_2 = (k^+ - k^-)\left(\frac{L}{2} - z_0\right) \mp \theta_2 + i\,\ell n|\rho_2|\ , \tag{2.35}$$

and

$$\bar{A}(z) = \left\{(1 + \exp i\bar{\alpha}_1) \exp[- ik^-(z-z_0)] + (1 + \exp i\bar{\alpha}_2) \exp[- ik^+(z-z_0)]\right\} : \tag{2.36}$$

Note from Eqs. (2.21) and (2.22) that

$$\bar{\alpha}_1 + \bar{\alpha}_2 = \alpha_1 + \alpha_2 \quad , \tag{2.37}$$

so Eq. (2.24) may be used to evaluate the infinite series again. As the LIP of Eq. (2.32) is moved upward to evaluate the asymptotic response, the first branch point encountered is at $\omega = \omega_0$ on the real ω-axis, due to $f_0(\omega)$. The asymptotic response determined by this branch point is

$$\Psi(t,z) \to \left\{\exp[- ik^{\pm}(z-z_0)] + \frac{\bar{A}(z)}{\exp i(\alpha_1+\alpha_2) - 1}\right\}_{\omega=\omega_0} \exp i\omega_0 t \quad (t \to \infty). \tag{2.38}$$

The first term of this response is due to the initial wave propagating away from the source at z_0, while the second term is due to the sum of the reflected waves. If ω_0 is very close to a normal mode frequency, ω_n, the second term is very large and can dominate. This is the usual case in exciting resonant cavities, since their normal mode or resonant frequencies are nearly on the real ω-axis due to very small reflection losses. On the other hand, certain systems, including many bounded plasmas, have more lossy boundaries, in which case one must use both terms in Eq. (2.38) to determine the spatial form of the response. In the case that the reflections become so lossy as to approximate an infinite system, the response is given by the first term alone, as one would also find from Eqs. (2.6) - (2.8) of Section 2.1.

2.2.5 Axial Profiles

In the last several subsections, we have been mainly concerned with the asymptotic time response of bounded systems. However, the

results we have obtained also contain information on the axial profile of the asymptotic response. In this subsection, the axial profiles for natural and forced responses are compared.

Before giving the axial profile for the natural response, it should be mentioned that in the case that the natural response grows in time, the asymptotic amplitude is actually determined by the nonlinear saturation of the waves, whereas our analysis has been linear. However, it is often assumed, and observed experimentally, that for weakly unstable plasmas, the nonlinear steady state is determined by the form of the linear asymptotic response. Thus, the axial profile should be a useful check with theory, even for many unstable systems.

Natural response profiles: There are two types of natural responses to consider. One occurs when the lowest branch point in the ω-plane is at ω_s, due to the colliding of poles k^+ and k^-, and is given by Eq. (2.28). For this case, the amplitude has the form

$$|\psi(z)|^2 \propto \exp 2\, k_{si} z \quad , \tag{2.39}$$

while the phase angle of ψ, $\chi(z)$, varies as

$$\chi(z) \propto - k_{sr} z \quad . \tag{2.40}$$

This is just the form the response would take for an infinite system, so the boundaries have no significant effect.

The second type of response occurs when a normal mode frequency at ω_n is the lowest branch point. The natural response is then given by Eq. (2.27), which yields an axial profile with

$$|\psi(z)|^2 \propto |\rho_1| \exp 2\, k_i^+ z + |\rho_2| \exp 2\, k_i^- z + 2\, |\rho_1|^{1/2} |\rho_2|^{1/2} \exp (k_i^+ + k_i^-) z \cos[2\phi - (k_r^+ - k_r^-) z] \quad , \tag{2.41}$$

$$\tan \chi(z) \propto \frac{[|\rho_1|^{1/2} \exp k_i^+ z \sin(\phi - k_r^+ z) - |\rho_2|^{1/2} \exp k_i^- z \sin(\phi + k_r^- z)]}{[|\rho_1|^{1/2} \exp k_i^+ z \cos(\phi - k_r^+ z) + |\rho_2|^{1/2} \exp k_i^- z \cos(\phi + k_r^- z)]} , \tag{2.42}$$

where $2\phi = n\pi \pm (\theta_1 - \theta_2)/2$. This profile depends not only on the dispersion relation, but also on the system length and reflection coefficients. There are some special cases for which these expressions can be simplified.

Case 1: The dispersion function, $D(\omega,k)$, is even in k. We then have a symmetric medium, so Eq. (2.28) can be written as

$$\begin{aligned} k_i L \equiv k_i^+ L = - k_i^- L &= \frac{1}{2} \ell n \, |\rho_1||\rho_2| \ , \\ k_r L \equiv k_r^+ L = - k_r^- L &= [n\pi \pm (\theta_1 + \theta_2)/2] \ . \end{aligned} \tag{2.43}$$

This reduces Eqs. (2.41) and (2.42) to

$$|\psi(z)|^2 \propto |\rho_1| \exp 2 k_i z + |\rho_2| \exp(-2k_i z) + 2|\rho_1|^{1/2}|\rho_2|^{1/2} \cos 2(\phi - k_r z), \tag{2.44}$$

$$\tan \chi(z) \propto \frac{[|\rho_1|^{1/2} \exp k_i z - |\rho_2|^{1/2} \exp(- k_i z)]}{[|\rho_1|^{1/2} \exp k_i z + |\rho_2|^{1/2} \exp(- k_i z)]} \tan(\phi - k_r z) . \tag{2.45}$$

Since k_r and k_i are determined when ρ_1, ρ_2, L, and n are specified, the mode pattern is now determined purely by the system length and terminations, and is independent of the form of the infinite dispersion relation.

Case 2: In addition to $D(\omega,k)$ being even in k, the terminations are identical. This means $|\rho_1| = |\rho_2| = |\rho|$ and $\theta_1 = \theta_2 = \theta$, so that $\phi = n\pi/2$. Equations (2.44) and (2.45) thus become

$$\begin{aligned} |\psi(z)|^2 &\propto [\cosh 2 k_i z + \cos(n\pi - 2k_r z)] \\ &\propto \cosh [2(\ell n \, |\rho|) z/L] + \cos [2(n\pi \pm \theta) \, z/L - n\pi] \ , \end{aligned} \tag{2.46}$$

$$\tan \chi(z) \propto \tanh k_i z \tan\left(\frac{n\pi}{2} - k_r z\right)$$

$$\propto - \tanh k_i z \tan[(n\pi \pm \theta)\, z/L - n\pi/2] \quad . \tag{2.47}$$

Case 3: In addition to the conditions for Cases 1 and 2, the terminations are lossless. Thus, $|\rho_1| = |\rho_2| = 1$, or $k_i = 0$, so Eqs. (2.46) and (2.47) reduce to

$$|\psi(z)|^2 \propto \cos^2[(n\pi \pm \theta)z/L - n\pi/2] \quad , \tag{2.48}$$

$$\chi(z) \to 0 \quad . \tag{2.49}$$

In this case, the mode patterns are pure standing waves with cosine or sine forms about the center for n even or odd, respectively.

Forced response profiles: If a system's natural response eventually decays, we may consider the form of the forced response as given by Eq. (2.38) for a localized sinusoidal source. The axial profile is made up of a combination of the initial wave from the source, and the sum of its reflections from the boundaries. This profile has the amplitude and phase given by

$$|\psi(z)|^2 \propto \exp 2k_i^{\pm} z + |\rho_{2,1}|^2 \exp(k_i^+ - k_i^-)L \exp 2\, k_i^{\mp} z$$

$$+ 2|\rho_{2,1}| \exp(k_i^+ - k_i^-)\, \frac{L}{2} \exp(k_i^+ + k_i^-)z \cos[2\beta_{2,1} - (k_r^+ - k_r^-)z] \, , \tag{2.50}$$

$$\tan \chi(z) \propto \pm \left[\frac{\exp k_i^{\pm} z \sin(\beta_{2,1} \mp k_r^{\pm} z) - |\rho_{2,1}| \exp(k_i^+ - k_i^-)\frac{L}{2} \exp k_i^{\mp} z \sin(\beta_{2,1} \pm k_r^{\mp} z)}{\exp k_i^{\pm} z \cos(\beta_{2,1} \mp k_r^{\pm} z) + |\rho_{2,1}| \exp(k_i^+ - k_i^-)\frac{L}{2} \exp k_i^{\mp} z \cos(\beta_{2,1} \pm k_r^{\mp} z)} \right], \tag{2.51}$$

where the upper superscripts and left subscripts are used for $z > z'$, and vice versa for $z < z'$. The new constants in these equations are

$$2\beta_2 = (k_r^+ - k_r^-)\, \frac{L}{2} \mp \theta_2, \qquad 2\beta_1 = -(k_r^+ - k_r^-)\, \frac{L}{2} \pm \theta_1 \quad . \tag{2.52}$$

If $|\rho_1| = |\rho_2| = 0$, the system acts as if it were infinite, and we simply have the profile of a k^+ wave propagating to the right of the source, and a k^- wave to the left. On the other hand, if ω_0 (the source frequency) is very close to a normal mode frequency, ω_n, we may use the additional condition

$$(k^+ - k^-)L \approx [2n\pi \pm (\theta_1 + \theta_2)] - i[\ell n|\rho_1||\rho_2|] \quad , \tag{2.53}$$

as in Eq. (2.28). Then Eqs. (2.50) and (2.51) can be reduced to Eqs. (2.41) and (2.42) to give the normal mode profile.

2.2.6 Extension to $D(\omega,k)$ of Higher Order in k

Up to this point, we have assumed $D(\omega,k)$ to be quadratic in k. When the dispersion relation is of order $\beta > 2$ in k, the various roots $k(\omega)$ can all be identified, for $\omega_i \to -\infty$, as waves excited on the + or - sides of an excitation point. Often β will be even, and there will be pairs of roots $k_\beta^{\pm}(\omega)$ corresponding to waves excited on either side for each wave type. For instance, for a two component plasma treated by the first two moment equations, we have $\beta = 4$; there is a pair of pressure waves associated primarily with the electrons (Langmuir waves), and another pair associated primarily with the ions (ion-acoustic waves). We then need to define a set of reflection coefficients, ρ_{ee}, ρ_{ii}, ρ_{ie}, and ρ_{ei}, for each termination, to account for the fact that upon reflection a wave of a given type can excite not only the same type, but also the other type. In principle, one could model this situation by again using a series of image sources to represent the reflections. In practice, however, this procedure is hardly tractable.

Many cases of practical interest correspond to the situation where one pair of waves is dominant, and the others are strongly attenuated and excited only very locally to the terminations. Over most of the system, only the dominant waves have appreciable amplitude, and may be amplifying or only weakly attenuated. The situation is analogous to that in ordinary electromagnetic waveguides[57] used in a frequency range where only the lowest transverse eigenmode propagates freely.

Evanescent higher order transverse eigenmodes are excited locally to the termination, and the impedance or reflection coefficient for the dominant mode is measured at a point sufficiently far from the termination that the evanescent modes are negligible. The locally excited higher order modes, which are necessary to satisfy the boundary conditions in a full treatment of the problem via Maxwell's equations, contribute to the reflection coefficient for the dominant waves.

In the present case, we can combine the effects of the evanescent modes with those of surface waves, if any, into the reflection coefficient of the dominant wave. The theory of the previous section is then applicable as far as Eq. (2.28), which determines $(k^+ - k^-)$ for the dominant waves. The only problem that arises is to solve the dispersion relation for the normal mode frequencies, ω_n, for the allowed $(k^+ - k^-)$ values. It is clear that the problem is determined, but it is difficult to give a general method when $\beta > 2$. In practice, however, there should be no difficulty in solving particular problems either graphically or numerically.

The reflection coefficients can be determined most simply by measurements. In Section 2.2.5, we have given the axial wave profile for both the normal modes and an externally driven system. Since these are functions of the reflection coefficients, careful measurements of the axial profile would allow one to determine the reflection coefficient values. For cases where measurements are not available, the reflection coefficients must be determined from physical considerations. A combination of these approaches is used in Section 4. There we illustrate how varying the reflection coefficients effects the normal mode growth rate and axial profile for drift waves.

3. WAVES PROPAGATING PERPENDICULAR TO THE MAGNETIC FIELD

In this section, we begin the study of low-frequency instabilities by investigating waves which propagate perpendicular to a uniform magnetic field in an inhomogeneous plasma column. These waves can be driven unstable by Hall drifts, i.e., $\underset{\sim}{E}_0 \times \underset{\sim}{B}$ drifts, of the electrons and ions due to a radial electric field. The instabilities belong to a general class of flute-type instabilities[30] which arise when electrons and ions drift at different speeds. For the analysis of the column, we use cylindrical geometry rather than rectangular slab geometry. There are two reasons for this: first, the centrifugal force on the ions, which arises in cylindrical geometry, can cause instability; second, we pay particular attention to the lower order azimuthal modes, which are not, in general, localized at some radial position in the column. Consequently, the waves are described by a differential equation, which is derived in Section 3.1. Solutions to this equation, as specified by the boundary conditions for the column, determine the wave characteristics.

For the case of uniform rotation of the column, the electric field must be a linear function of radius. The instability which arises is usually called a centrifugal flute mode, and has been studied, for example, by Rosenbluth *et al.*,[31] and by Chen.[33] We treat this case in Section 3.2, and determine the effect of the column being radially bounded. If the electric field is other than a linear function of radius, the column rotation is nonuniform, i.e., there is shear in the angular rotation velocity. We consider the effect of this shear in Section 3.3, and illustrate how, for abrupt shear, the instability resembles a Kelvin-Helmholtz instability.[37,38] In Section 3.4, we proceed to identify some instabilities in a hollow cathode arc discharge as being of the type discussed here.

3.1 Basic Theory

3.1.1 Steady State Plasma

The model we use is an infinitely long cylindrical plasma column immersed in a uniform axial magnetic field. The plasma is taken to be fully ionized with singly charged ions. The model is shown in

Fig. 3.1 together with the cylindrical coordinate system used. We assume an arbitrary form for the DC radial electric field, a Gaussian radial number density profile, and no axial variations. The number density thus has the form

$$n(r) = N \exp(-r^2/r_0^2) \quad . \tag{3.1}$$

One can extend this model to consider other number density profiles. However, it is most often the electric field profile which can take on various shapes in plasma discharges, while many of the number density profiles can be approximated by Gaussian curves. Thus, we consider this case in detail.

The equations used to describe this fully ionized plasma are two-species moment equations given by Braginskii.[58] For the plasma to be accurately described by these equations, the particles of the plasma must be sufficiently localized, so that the plasma acts nearly like a fluid, the small variation from this state being accounted for by transport effects included in the theory. For particle motion across the magnetic field, this localization is provided by the magnetic field, and requires the Larmor radii of the particles to be small compared to the zero and first order scale lengths of the physical quantities (density, electric field, etc.). For particle motion along the magnetic field, the localization must be provided by particle collisions, and requires the mean-free-path to be small compared to the scale lengths of the physical quantities. This latter condition will be of more concern in Section 4, when we consider waves propagating at an angle to the magnetic field, so that axial variations are important; in this chapter, the equations describe only variations perpendicular to the magnetic field.

For the ions, we use the continuity equation

$$\frac{\partial n}{\partial t} + \nabla_\perp \cdot (n \underset{\sim}{v}_{i\perp}) = 0 \quad , \tag{3.2}$$

and the momentum transfer equation with the isothermal assumption

$$nm_i \frac{d\underset{\sim}{v}_{i\perp}}{dt} = - T_i \nabla_\perp n - \nabla_\perp \cdot \overleftrightarrow{\underset{\sim}{\pi}}_{i\perp} + en (\underset{\sim}{E} + \underset{\sim}{v}_{i\perp} \times \underset{\sim}{B}) \quad . \tag{3.3}$$

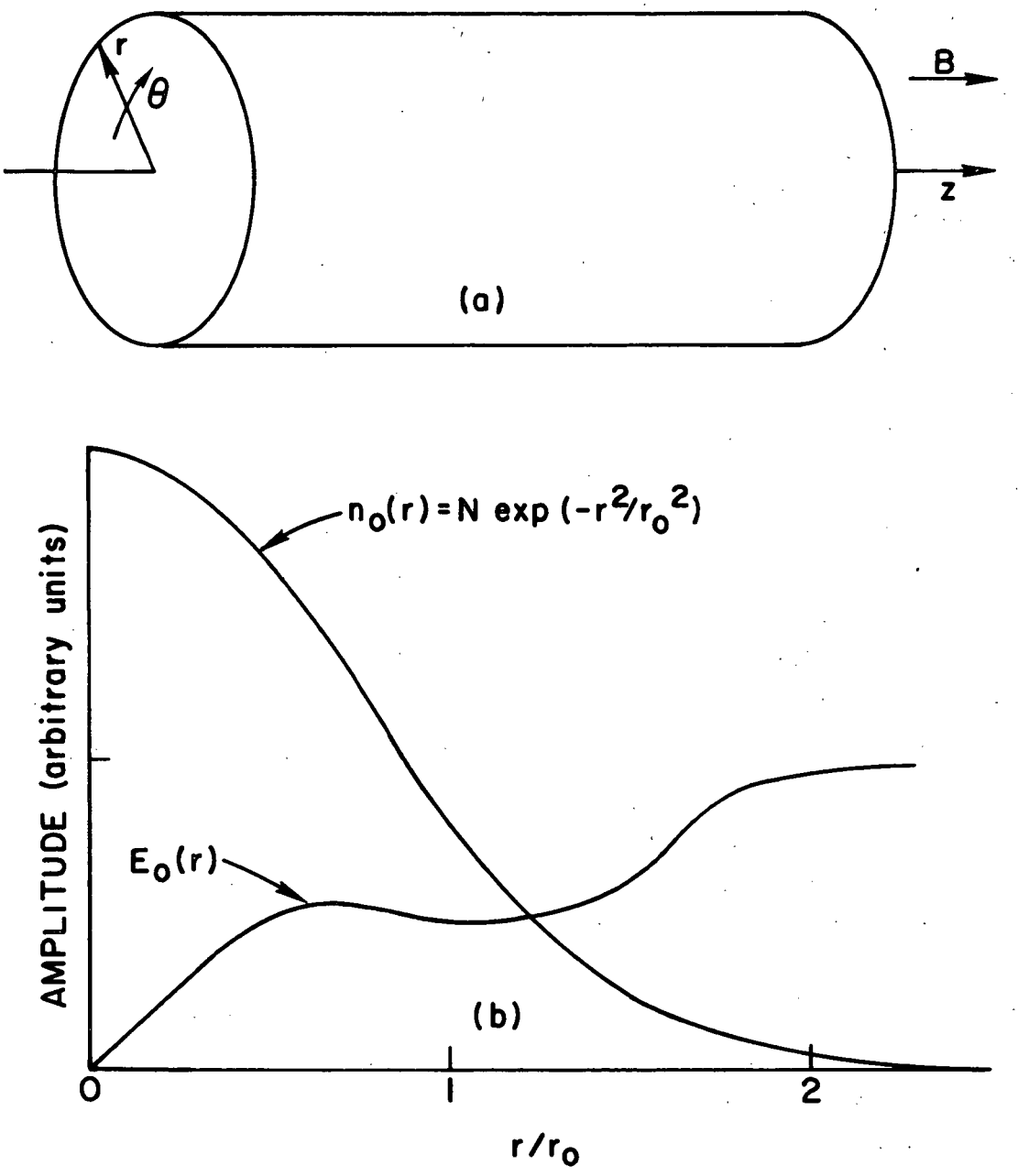

Fig. 3.1 (a) Model of the cylindrical plasma column immersed in a magnetic field B , showing the coordinate system. (b) Radial profiles of number density and electric field in the column.

Here, n is the number density for both ions and electrons, m_i is the ion mass, $\underset{\sim}{v}_{i\perp}$ is the ion macroscopic velocity, T_i is the ion temperature in energy units, $\underset{\sim}{\pi}_{i\perp}$ is the traceless viscosity tensor, -e is the charge of an electron, $\underset{\sim}{E}$ is the electric field, and $\underset{\sim}{B}$ is the magnetic field. MKS units are implied throughout. We assume that $\omega_{ci} \gg \nu_{ii}$, where ω_{ci} is the ion cyclotron frequency and ν_{ii} is the ion-ion collision frequency. Thus, ion-ion collisions are neglected, and the collisionless viscosity tensor is used in order to account for finite ion Larmor radius effects, as discussed by Chen.[41] The form of this viscosity tensor in cylindrical coordinates is[33]

$$\underset{\sim}{\overleftrightarrow{\pi}}_{i\perp} = - \frac{nT_i}{\omega_{ci}} \underset{\sim}{\overleftrightarrow{W}} , \quad \underset{\sim}{\overleftrightarrow{W}} = \begin{pmatrix} W_{rr} & W_{r\theta} \\ W_{\theta r} & W_{\theta\theta} \end{pmatrix} , \tag{3.4}$$

where the tensor components are

$$W_{rr} = - W_{\theta\theta} = \frac{1}{2} \left(r \frac{\partial (v_{i\theta}/r)}{\partial r} + \frac{1}{r} \frac{\partial v_{ir}}{\partial \theta} \right) ,$$

$$W_{r\theta} = W_{\theta r} = \frac{1}{2} \left(r \frac{\partial (v_{ir}/r)}{\partial r} - \frac{1}{r} \frac{\partial v_{i\theta}}{\partial \theta} \right) . \tag{3.5}$$

Finally, in the analysis to follow, care must be taken to properly differentiate the unit vectors for cylindrical geometry, $\hat{\underset{\sim}{i}}_r$ and $\hat{\underset{\sim}{i}}_\theta$. Their nonzero derivatives are

$$\frac{\partial \hat{i}_r}{\partial \theta} = \hat{i}_\theta , \quad \frac{\partial \hat{i}_\theta}{\partial \theta} = - \hat{i}_r . \tag{3.6}$$

We begin by solving Eq. (3.3) for the zero order ion velocity. First, it is assumed that the inertia and viscosity terms are small compared to the other terms in Eq. (3.3), which gives the solution

$$\underset{\sim}{v}_{i\perp 0} \approx - \left(\frac{2r}{r_0^2} \frac{T_i}{eB} + \frac{E_0}{B} \right) \hat{\underset{\sim}{i}}_\theta \equiv v_0 \hat{\underset{\sim}{i}}_\theta . \tag{3.7}$$

This approximation is then used to find the correction due to inertia and viscosity. The result is

$$\underset{\sim}{v}_{i\perp 0} = \left\{ v_0 - \frac{v_0^2}{r\omega_{ci}} + \rho_i^2 \left[\left(\frac{r^2}{r_0^2} - \frac{3}{2} \right) \left(\frac{v_0}{r} \right)' - \frac{r}{2} \left(\frac{v_0}{r} \right)'' \right] \right\} , \qquad (3.8)$$

where $\rho_i \left[= (T_i/m_i)^{1/2}/\omega_{ci} \right]$ is the ion gyroradius (or Larmor radius), and the prime denotes differentiation with respect to r. The first correction term is due to inertia, and represents the centrifugal force. This always acts radially outward, so it aids or opposes the force of the radial electric field, depending on the latter's direction. For this correction to be small, the rotation frequency $(= v_0/r)$ must be much less than ω_{ci}. Solutions to Eq. (3.3) for larger rotation frequencies are discussed in Appendix B. The remaining correction terms in Eq. (3.8) arise from ion viscosity, i.e., from the effect of the finite ion Larmor radius. These terms are nonzero when there is rotational shear due to an electric field which is other than a linear function of radius, since from Eq. (3.7)

$$\left(\frac{v_0}{r} \right)' = \left(\frac{E_0}{Br} \right)' . \qquad (3.9)$$

This correction is small if the scale length of the rotational shear,

$$\frac{1}{\chi_r} = \frac{(v_0/r)}{(v_0/r)'} , \qquad (3.10)$$

is large compared to the ion gyroradius in the sense that

$$\rho_i \chi_r \left(\frac{\rho_i}{r} \right) \ll 1 , \qquad (3.11)$$

and if the rate of change of shear, $(v_0/r)''$, is not too large over a gyroradius.

The equations and analysis for the electrons are somewhat simpler due to their smaller mass. We neglect both electron inertia and

finite Larmor radius effects, since these terms appear in the momentum transfer equation multiplied by the mass, as seen from Eqs. (3.3) and (3.4). The continuity equation for the electrons is unaffected by this, being

$$\frac{\partial n}{\partial t} + \nabla_\perp \cdot (n \underset{\sim}{v}_{e\perp}) = 0 \quad , \tag{3.12}$$

while the momentum transfer equation becomes

$$0 = - T_e \nabla_\perp n - en(\underset{\sim}{E} + \underset{\sim}{v}_{e\perp} \times \underset{\sim}{B}) \quad , \tag{3.13}$$

where the symbols are analogous to those for the ions. We have also made the isothermal assumption for the electrons since, as is proved in Appendix C, not making this assumption results in exactly the same first order wave equation as we derive in Section 3.1.2. Equation (3.13) can be solved to yield the zero order electron velocity

$$\underset{\sim}{v}_{e\perp 0} = \left(\frac{2r}{r_0^2} \frac{T_e}{eB} - \frac{E_0}{B} \right) \underset{\sim}{\hat{i}}_\theta \quad . \tag{3.14}$$

We thus have a steady state in which the electron fluid rotates about the axis at a velocity given by Eq. (3.14), while the ion fluid rotates at the velocity given by Eq. (3.8). It should be noted that each drift is made up of a diamagnetic drift term and an $\underset{\sim}{E}_0 \times \underset{\sim}{B}$ drift term; these are the first and second terms, respectively, in Eqs. (3.7) and (3.14). But only the $\underset{\sim}{E}_0 \times \underset{\sim}{B}$ drift represents a true particle drift; the diamagnetic term describes momentum transport due to a density gradient for particles gyrating about a fixed point. As we shall see in Section 3.2.1, the diamagnetic drift cannot produce instability, while the $\underset{\sim}{E}_0 \times \underset{\sim}{B}$ drift can. In the next section, the perturbation analysis of the equations describing the plasma column is considered in order to determine the stability of this configuration.

3.1.2 Perturbed Plasma

To perform a linear perturbation analysis on the equations describing the plasma, i.e., Eqs. (3.2), (3.3), (3.12), and (3.13), we assume that the variables n, $\underset{\sim}{v}_i$, $\underset{\sim}{v}_e$, and $\underset{\sim}{E}$ all have the general form

$$n(r) = n_0(r) + n_1(r) \exp i(\omega t - m\theta) , \tag{3.15}$$

where the subscripts 0 and 1 stand for zero order and first order quantities, respectively, with $n_1 \ll n_0$. Also, ω is the wave frequency of the perturbation, which is equivalent to Fourier or Laplace transforming in time (see Section 2), and m is the azimuthal mode number, which is a positive or negative integer or zero. No axial variation is assumed since we are considering perturbations or waves which only propagate, or have spatial variations, perpendicular to the magnetic field. Before perturbing the equations, it is useful to make some further assumptions about the waves. We take $\beta \ll 1$, where β [$= nT/(B^2/2\mu_0)$ in MKS units] is the ratio of the particle pressure to magnetic field pressure. We thus neglect perturbations in the magnetic field, and assume that the waves are quasistatic, i.e., $\underset{\sim}{E}_1 = -\nabla_\perp \phi_1$, where ϕ_1 is the first order potential. In defining the number density, n, following Eq. (3.3), it was implied that the ion and electron densities are equal, even to first order. This is known as the quasineutrality assumption, and is valid for frequencies, ω, much less than the ion plasma frequency, ω_{pi}. In addition, we take $\omega \ll \omega_{ci}$, and, since $\omega_{ci} < \omega_{pi}$ for most plasmas of interest, this condition implies that quasineutrality is well satisfied.

We begin by perturbing the electron equations. The first order electron velocity comes directly from the momentum transfer equation, Eq. (3.13), and is

$$\underset{\sim}{v}_{e\perp 1} = -\frac{T_e}{eB}\left(\frac{im}{r}\xi \hat{\underset{\sim}{i}}_r + \xi' \hat{\underset{\sim}{i}}_\theta\right) , \tag{3.16}$$

where $\xi = (n_1/n_0 - e\phi_1/T_e)$. If this relation is substituted in the first order continuity equation, Eq. (3.12), we obtain

$$\frac{2m}{r_0^2}\ \frac{T_e}{eB}\left(\frac{e\phi_1}{T_e}\right) = \left(\omega + m\,\frac{E_0}{Br}\right)\left(\frac{n_1}{n_0}\right)\ , \tag{3.17}$$

which can also be written as

$$\frac{e\phi_1}{T_i} = \frac{\omega - m\,\omega_E}{m\,\omega_{Di}}\ \left(\frac{n_1}{n_0}\right)\ . \tag{3.18}$$

Here $-\omega_{Di}$ $[= -(2m/r_0^2)(T_i/eB)]$ is the ion diamagnetic frequency, which is not a function of radius since the density profile is Gaussian, and ω_E $[= -E_0/rB]$ is the rotation frequency due to the electric field. Note that Eq. (3.18) is independent of the electron temperature, so the waves themselves are not affected by the electron temperature. The physical reason for this is that the electron temperature only enters the equations via the pressure term, nT_e, of the momentum transfer equation. This term gives rise to a diamagnetic drift velocity, which describes momentum transport, but not true particle drift. When the electron velocity is substituted in the continuity equation, this term cancels out since it does not describe particle transport. In Appendix C, we prove that the electron temperature cancels out of the continuity equation to all orders, and also that, despite this, there may be electron temperature fluctuations associated with the waves. It should be emphasized that this cancellation does not occur if axial variation is considered, as for the waves studied in Section 4; nor does it occur for the ions, since we include ion inertia and viscosity. Another simplification arises in that Eq. (3.18) contains no derivatives, and thus gives the relationship between the potential perturbation and the density perturbation directly, once the frequency ω is known. The calculation of this frequency is, of course, one of our objectives. To obtain a second relation between n_1 and ϕ_1, we consider the ion equations.

As for the zero order ion velocity, the first order ion velocity is solved by iteration of Eq. (3.3). We use the zero order momentum transfer equation, multiplied by n_1/n_0, to simplify the first order equation, which amounts to using the equality

$$m_i n_1 (\underset{\sim}{v}_{i\perp 0} \cdot \nabla_\perp)\underset{\sim}{v}_{i\perp 0} - \frac{n_1 T_i}{\omega_{ci}} \nabla_\perp \cdot \overleftrightarrow{\underset{\sim}{W}}_0 - n_1 e(\underset{\sim}{E}_0 + \underset{\sim}{v}_{i\perp 0} \times \underset{\sim}{B})$$

$$= - \frac{T_i n_1}{n_0} \nabla_\perp n_0 + \frac{T_i}{\omega_{ci}} \frac{n_1}{n_0} (\overleftrightarrow{\underset{\sim}{W}}_0 \cdot \nabla_\perp) n_0 \, . \qquad (3.19)$$

This leads to the first order ion momentum transfer equation

$$m_i n_0 \left[\frac{\partial \underset{\sim}{v}_{i\perp 1}}{\partial t} + (\underset{\sim}{v}_{i\perp 1} \cdot \nabla_\perp) \underset{\sim}{v}_{i\perp 0} + (\underset{\sim}{v}_{i\perp 0} \cdot \nabla_\perp)\underset{\sim}{v}_{i\perp 1} \right] - \frac{T_i}{\omega_{ci}} \left[n_0 \nabla_\perp \cdot \overleftrightarrow{\underset{\sim}{W}}_0 + \right.$$

$$\left. (\overleftrightarrow{\underset{\sim}{W}}_1 \cdot \nabla_\perp) n_0 + \frac{n_1}{n_0} (\overleftrightarrow{\underset{\sim}{W}}_0 \cdot \nabla_\perp) n_0 - (\overleftrightarrow{\underset{\sim}{W}}_0 \cdot \nabla_\perp) n_1 \right] =$$

$$T_i \left[\frac{n_1}{n_0} \nabla_\perp n_0 - \nabla_\perp n_1 \right] + n_0 e(-\nabla_\perp \phi_1 + \underset{\sim}{v}_{i\perp 1} \times \underset{\sim}{B}) \, . \qquad (3.20)$$

As a first approximation, we neglect the terms on the left-hand side of Eq. (3.20) as small, and find

$$\underset{\sim}{v}_{i\perp 1} \approx \frac{T_i}{eB} \left(\frac{im}{r} \gamma \, \underset{\sim}{\hat{i}}_r + \gamma' \, \underset{\sim}{\hat{i}}_\theta \right) , \qquad (3.21)$$

where

$$\gamma = \left(\frac{n_1}{n_0} + \frac{e\phi_1}{T_i} \right) \, . \qquad (3.22)$$

Using this approximation to find the corrections due to the inertia and viscosity terms, i.e., the left-hand side of Eq. (3.20), yields

$$\underset{\sim}{v}_{i\perp 1} = \frac{T_{i0}}{eB} \left\{ \left[\frac{im}{r} \gamma \, \underset{\sim}{\hat{i}}_r + \gamma' \, \underset{\sim}{\hat{i}}_\theta \right] + \frac{1}{\omega_{ci}} \left[\underset{\sim}{\Delta}_1 + \underset{\sim}{\Delta}_2 + \underset{\sim}{\Delta}_3 \right] \right\} . \qquad (3.23)$$

Here $\underset{\sim}{\Delta}_1$ is due to ion inertia, $\underset{\sim}{\Delta}_2$ is due to zero order viscosity, and $\underset{\sim}{\Delta}_3$ is due to first order viscosity. These are given by

$$\underset{\sim}{\Delta}_1 = - i \left\{ \left[\left(\omega - \frac{m v_0}{r} \right) \gamma' + \frac{m}{r} \left(v_0' + \frac{v_0}{r} \right) \gamma \right] \underset{\sim}{\hat{i}}_r + \right.$$

$$\left. \left[2 \frac{v_0}{r} \gamma' + \frac{m}{r} \left(\omega - \frac{m v_0}{r} \right) \gamma \right] \underset{\sim}{\hat{i}}_\theta \right\} ,$$

$$\underset{\sim}{\Delta}_2 = \frac{im}{2}\left(\frac{v_0}{r}\right)'\left(\frac{n_1}{n_0}\right)\hat{\underset{\sim}{i}}_r - \frac{r}{2}\left(\frac{v_0}{r}\right)'\left(\frac{n_1}{n_0}\right)'\hat{\underset{\sim}{i}}_\theta \ , \tag{3.24}$$

$$\underset{\sim}{\Delta}_3 = \frac{T_{i0}}{eB}\left\{ im\left[-\frac{\gamma''}{2r} + \left(\frac{2}{r_0^2} - \frac{1}{2r^2}\right)\gamma' + \left(\frac{m^2}{2r^3} - \frac{2}{rr_0^2}\right)\gamma\right]\hat{\underset{\sim}{i}}_r \right.$$

$$\left. + \left[-\frac{\gamma'''}{2} + \left(\frac{1}{2r^2} - \frac{1}{r_0^2}\right)\gamma'' + \left(\frac{1}{rr_0^2} - \frac{m^2+1}{2r^3}\right)\gamma' + \frac{m^2}{r^2}\left(\frac{1}{r^2} - \frac{1}{r_0^2}\right)\gamma\right]\hat{\underset{\sim}{i}}_\theta \right\} .$$

To eliminate the ion velocity variable, we insert Eq. (3.23) into the continuity equation, i.e., Eq. (3.2). In doing so, Eq. (3.18) is used to express n_1/n_0 in terms of γ, as defined in Eq. (3.22). This leads to a second order differential equation in γ, which is less lengthy than one might expect from Eq. (3.23), as a large number of terms cancel out, including the third order derivatives of γ. The equation is

$$\gamma'' + \left[\left(\frac{1}{r} - \frac{2r}{r_0^2}\right) - m^2\frac{\omega_{Di}\omega_E'}{\omega_1\omega_2}\right]\gamma' - \frac{m^2}{r^2}\gamma +$$

$$\frac{1}{\omega_1}\left[-\frac{2}{r_0^2}\left(m(2\omega_E - \omega_{Di}) + m^2\frac{(\omega_E - \omega_{Di})^2}{\omega_2} + \frac{r\omega_1 m\omega_E'}{\omega_2}\right) + \frac{m\omega_E'}{r\omega_2}\right.$$

$$\left. + \left(\frac{2\omega_1 m\omega_E'}{r\omega_2} + \frac{\omega_1 m\omega_E''}{\omega_2} - \frac{m\omega_{Di}(m\omega_E')^2}{\omega_2^2}\right)\right]\gamma = 0 \ , \tag{3.25}$$

where $\omega_1 = \omega - m\omega_E$ and $\omega_2 = \omega - m\omega_E + m\omega_{Di}$. For the case of uniform rotation, $\omega_E' = 0$, and this equation reduces to that derived by Chen,[33] and by Chu *et al.*,[59] who used the moment equations, while Rosenbluth *et al.*[31] have derived an equivalent equation from kinetic theory. Equation (3.25) takes on a shorter form, and contains only first derivatives of ω_E, if we transform the variable γ to Ψ, where

$$\Psi = \frac{\phi_1}{r\omega_1 B} = \frac{T_i}{eB} \frac{1}{r\omega_2} \gamma \quad . \tag{3.26}$$

We then have the differential equation

$$\Psi'' + \left[\left(\frac{3}{r} - \frac{2r}{r_0^2}\right) - 2m\omega_E' \frac{(\omega - m\omega_E + m\omega_{Di}/2)}{\omega_1\omega_2}\right]\Psi'$$

$$- \left[\frac{m^2-1}{r^2} + \frac{2}{r_0^2} \frac{\omega^2}{\omega_1\omega_2}\right]\Psi = 0 \quad . \tag{3.27}$$

This agrees with the equation for nonuniform rotation derived by Rosenbluth and Simon,[36] when the density profile is assumed Gaussian as in our model. They used a special set of moment equations obtained directly from kinetic theory, while we have derived the equation using the more conventional moment equations.[58]

Now that we have the basic differential equation for the waves, the problem becomes one of solving it for the eigenfrequencies, ω, and the eigenfunctions, Ψ, and thus n_1 and ϕ_1 by Eqs. (3.18) and (3.26). A symmetry property of Eq. (3.27) which is useful to note is that if a given set of parameters yields an eigenfrequency ω and an eigenfunction Ψ, then by changing ω_E to $(\omega_{Di}-\omega_E)$, we obtain the eigenfrequency $-\omega^*$ for the eigenfunction Ψ^*, where the * denotes the complex conjugate. This can be proved by making the substitution of $\omega_E \rightarrow (\omega_{Di}-\omega_E)$ in Eq. (3.27), and then taking the complex conjugate of the equation. The asymmetry of the transformation with respect to the approximate total ion rotation frequency, $(\omega_E-\omega_{Di})$, can be traced back to the Coriolis force which arises from the first order inertia term in cylindrical geometry, as discussed by Chen.[33] Note also that there are complex conjugate solutions to the equation, i.e., if ω is an eigenfrequency for the eigenfunction Ψ, then ω^* is an eigenfrequency for the eigenfunction Ψ^*. We have assumed an exp $i\omega t$ time dependence, so the waves are unstable for $\omega_i < 0$, where $\omega_i = \mathrm{Im}(\omega)$. Thus, since both ω and ω^* are solutions, there is stability only if ω is real.

Before we can find explicit solutions to Eq. (3.27), two boundary conditions must be specified. Since the equation has a regular singularity at the origin, we use the nonsingular solution, and thus need only the boundary condition at the outer radial boundary, say at $r = r_b$. When r_b is not infinite, we take this to be $\phi_1(r_b) = 0$. This can be justified on physical grounds when the plasma column is enclosed by a conducting cylinder, or when a conducting ring of radius r_b is placed at one end of the column, e.g., an aperture limiter in a Q-machine,[60] since the conductivity of the plasma along the magnetic field is much larger than across the field. By Eq. (3.18), $\phi_1(r_b) = 0$ also demands $n_1(r_b) = 0$, while Eq. (3.26) gives the boundary condition in the variable Ψ, i.e., $\Psi(r_b) = 0$. For the case $r_b = \infty$, the boundary condition is more involved, and is discussed in the next subsection.

We now consider the behavior of these waves by solving Eq. (3.27) for uniform rotation, for which analytic solutions are obtained, and then for the more general case of nonuniform rotation, for which the equation must be solved numerically.

3.2 Waves for Uniform Rotation

3.2.1 Solutions for Radially Unbounded Columns

For uniform rotation, ω_E = constant, which implies that the electric field, E_0, is a linear function of radius. For this case, it is convenient to transform Eq. (3.27) by the following change of variables:[31]

$$X = \left(\frac{r}{r_0}\right)^2 \quad , \quad \Psi(r) = \frac{1}{X} \exp\left(\frac{X}{2}\right) M(X) \; . \tag{3.28}$$

We then obtain Whittaker's equation[61]

$$\frac{d^2M}{dX^2} + \left\{ -\frac{1}{4} + \frac{h}{X} + \frac{1-4\ell^2}{4X^2} \right\} M = 0 \quad , \tag{3.29}$$

where

$$h = 1 - \frac{\omega^2}{2\omega_1\omega_2} \quad , \tag{3.30}$$

and $\ell = m/2$. The nonsingular solution to this equation can be written as

$$M_{h,\ell}(X) = X^{\ell + \frac{1}{2}} \exp(-\frac{X}{2})\, M(\ell - h + \frac{1}{2},\ 1 + 2\ell, X)\ , \qquad (3.31)$$

where $M(\ell - h + 1/2,\ 1 + 2\ell, X)$ is the confluent hypergeometric function known as Kummer's function.

In previous studies of these waves, the normal modes are defined as those for which $M_{h,\ell}(X)$ decreases like $\exp(-X/2)$ as $X \to \infty$.[31,33,36,59] It should be noted from Eqs. (3.26) and (3.28) that ϕ_1 does not decrease as $r \to \infty$ for this case, but rather is a constant or increases as some power of r. However, we shall see in Section 3.2.2 that these modes indeed give the asymptotic behavior of the normal modes of a bounded column as $r_b \to \infty$. The form of ϕ_1 for $r_b \to \infty$ results from the model being of an unbounded, uniformly rotating plasma column, as discussed by Chu et al.[59] We thus proceed to investigate these normal modes. For $M_{h,\ell}(X)$ to decay exponentially at large values of X, the power series representing Kummer's function must be terminated after a finite number of terms, as determined by the radial mode number.[33] This condition can be written as

$$h = \ell + q + \frac{1}{2}\ , \qquad (3.32)$$

where $q = 0,1,2, \ldots$ is the radial mode number. Using the definition for $\ell (= m/2)$, Eq. (3.32) can be put in a more standard form if we let $h = 2p - 1$, in which case we obtain the condition

$$p = m + 2q\ . \qquad (3.33)$$

The set (m,q) denotes the azimuthal and radial mode numbers for a specific mode, which now directly specify p. The equation for the eigenfrequency thus becomes

$$p = 1 - \frac{\omega^2}{\omega_1 \omega_2}\ , \qquad (3.34)$$

which yields the solutions

$$\omega = m(\omega_E - \frac{\omega_{Di}}{2})(1 - \frac{1}{p}) \left[1 \pm i \left(\frac{(\omega_E - \omega_{Di}/2)^2 - p\omega_{Di}^2/4}{(\omega_E - \omega_{Di}/2)^2 (p-1)} \right)^{\frac{1}{2}} \right] \quad (3.35)$$

The symmetry of the solutions discussed in Section 3.1.2 is apparent. The transformation $\omega_E \rightarrow (\omega_{Di} - \omega_E)$ leads to an eigenfrequency having the same growth rate, but the negative of the real frequency, ω_r, of the original mode. The negative real frequency is interpreted physically as a mode whose phase velocity is in the opposite direction to the positive frequency mode. Equivalently, we may assume ω_r to always be positive and the azimuthal mode number, m, to take on the negative sign. The magnitude of ω_r is determined by the factor $m(\omega_E - \omega_{Di}/2)$, and, for large electric fields, is determined by the $\underset{\sim}{E}_0 \times \underset{\sim}{B}$ rotation, i.e., ω_E.

For the (1,0) mode, we have $p = 1$, which gives the solution $\omega = 0$; that is, this mode is always stable. For all other modes, the waves are unstable if the radicand in Eq. (3.35) is positive, which requires

$$\left| \frac{\omega_E}{\omega_{Di}} - \frac{1}{2} \right| > \frac{p^{\frac{1}{2}}}{2} . \quad (3.36)$$

Since $p > 1$ for these modes, the rotation due to the electric field must be sufficiently large to overcome finite Larmor radius stabilization, as manifested by the right-hand side of Eq. (3.36). Thus, as p increases for the higher order azimuthal and radial modes, increasingly large electric fields are required for instability.

The basic mechanism which drives these waves unstable is the charge separation caused by the difference in the ion and electron $\underset{\sim}{E}_0 \times \underset{\sim}{B}$ drifts due to ion inertia. This is explained from a particle orbit point of view by Rosenbluth and Longmire,[30] who use a gravity term in rectangular geometry, which simulates inertial effects of a rotating plasma or curvature of magnetic field lines. The inertial effect appears in Eq. (3.8) for the ion velocity as the correction term $v_0^2/r\omega_{ci}$. This term can be traced through to the final differential equation, i.e., Eq. (3.25) or Eq. (3.27). However, it is identified most easily in

Eq. (3.25), since $v_0^2/r^2 = (\omega_E - \omega_{Di})^2$, and this term is seen to be the last term in Eq. (3.25) when $\omega_E' = \omega_E'' = 0$. If we neglect this term, the eigenfrequencies become

$$\omega = m\omega_E + m\frac{(\omega_{Di} - 2\omega_E)}{p} \quad , \tag{3.37}$$

which are always real. As p becomes large for higher order modes, these waves correspond to perturbations being convected around the column at the $\underset{\sim}{E}_0 \times \underset{\sim}{B}$ velocity. Clearly, the inertial effect of the ions is needed for instability.

The waves also need a density gradient for instability. This may be shown by letting $r_0 \to \infty$, so that the density becomes uniform. Initially, we assume that the waves go to zero at a large, but finite radius, such that $r_b \ll r_0$. The condition now put on the constant p for Kummer's function to go to zero at r_b for the first radial mode is[33]

$$p = (1+m)(\frac{1}{2} + \frac{1}{X_b}) \quad , \tag{3.38}$$

where $X_b = (r_b/r_0)^2$. Thus, as $r_0 \to \infty$, we have $1/X_b \to \infty$ and $p \to \infty$, which is also true for higher order radial modes. From Eq. (3.35), we find that in this limit

$$\omega = m(\omega_E \pm \omega_{Di}) \quad , \tag{3.39}$$

and all the modes are stable. It should be emphasized that r_b is considered to be very large, and that $X_b \to \infty$ only because we take $r_0 \to \infty$ faster than $r_b \to \infty$. The different behavior of p seen in Eqs. (3.33) and (3.38) will become clear in the next subsection.

3.2.2 Solutions for Radially Bounded Columns

We now consider in more detail the solutions to Eq. (3.29) and the eigenfrequencies given by Eq. (3.35). In particular, we shall use the more realistic model of a radially bounded plasma column. For rectangular geometry, Lehnert[62] has found that the presence of a boundary can have a stabilizing effect on this type of instability. In addition, for cylindrical geometry, Chen[63] has shown from numerical

solutions to Eq. (3.29) for the special case of $r_b = \sqrt{2}\, r_0$ that the eigenfrequencies obtained can be quite different from those found for an unbounded column. Most dramatic is the fact that the (1,0) mode can be unstable for a boundary at this finite radial position. We consider a more systematic approach to this problem in cylindrical geometry by extending the analytic determination of the eigenfrequencies to the case of a bounded column. The behavior of the numerical solutions obtained by Chen then becomes clear, and the results are generalized to include the effect of a boundary at any radial position.

The approach is to find the zeroes of Kummer's function for finite radial boundaries, and relate these to the parameter appearing in Eq. (3.35). Curves of these functions are available,[64] and by writing the solution [Eq. (3.31)] in the form $M[(m-p)/2,\ 1+m,\ X]$, we may find the precise value of p as a function of the position of the outer radial boundary, measured by $X_b [= (r_b/r_0)^2]$. We have done this for the two lowest order radial and azimuthal modes, and compared the results with the asymptotic value of p given by Eq. (3.33). The results are shown in Fig. 3.2. The curves approach the asymptotic values of p at large X_b, but for moderate values of X_b they can be quite different. For example, as X_b becomes less than $\sim$ 2-3, p increases quite rapidly approaching the form given by Eq. (3.38) for the (m,0) modes when $X_b \ll 1$. The actual value of p for any mode is always larger than the asymptotic value; in particular, $p > 1$ for the (1,0) mode. Equation (3.35) thus gives the result that the (1,0) mode can be unstable for a finite radial boundary, as found numerically by Chen[63] for $X_b = 2$. In general, the eigenfrequencies for various radial positions of the boundary can now be found by using Fig. 3.2 in conjunction with Eq. (3.35).

In using these results, it should be noted that the position of the boundary also determines which mode will have the highest growth rate for a given electric field. By differentiating the expression for growth rate [Eq. (3.35)] with respect to p, we find the maximum growth rate of a mode occurs for

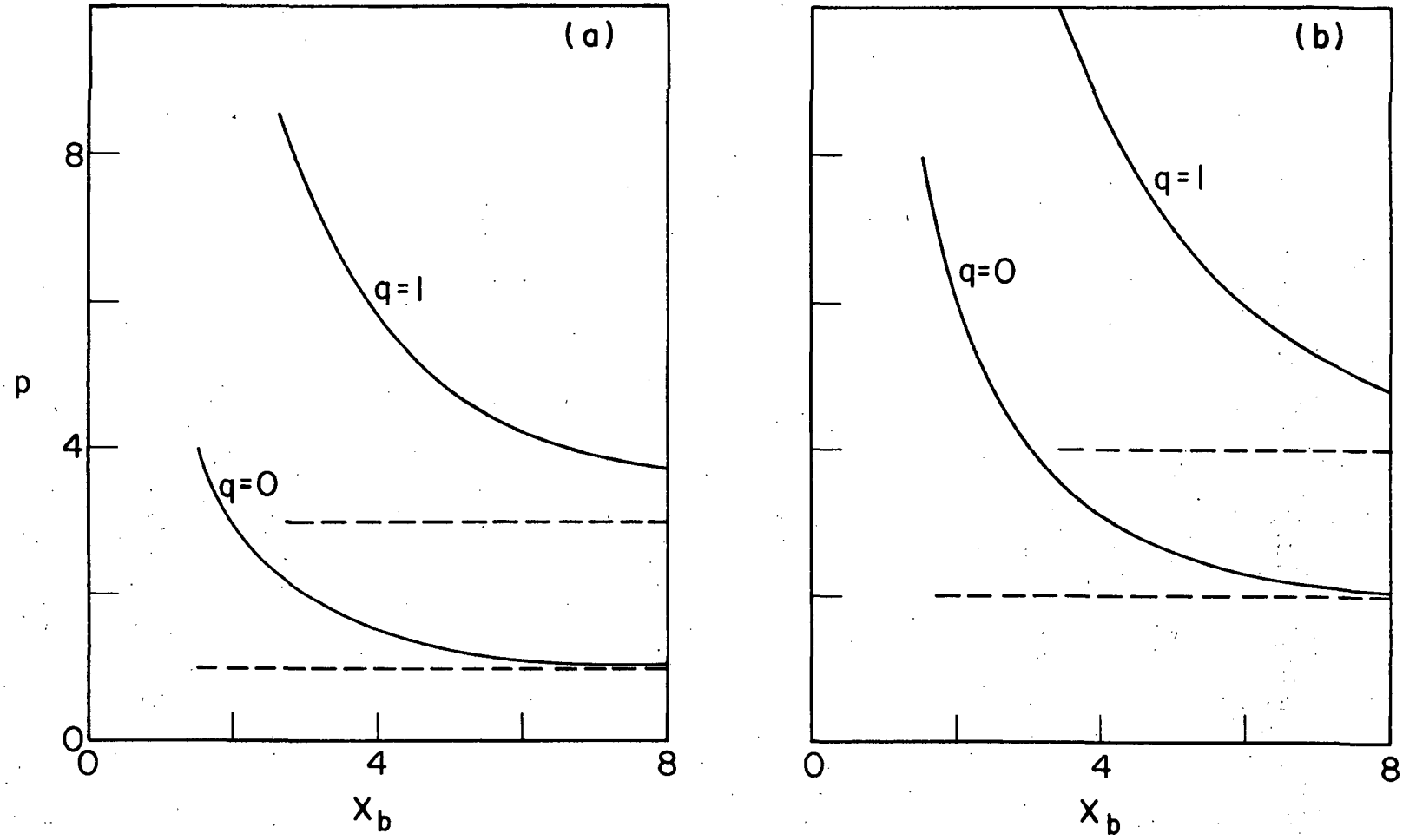

Fig. 3.2 Values of p for (a) the (1,q) mode, and (b) the (2,q) mode, as $X_b(=r_b^2/r_0^2)$ is varied. ——— , actual value; ---- , asymptotic value.

$$p = \frac{2}{\left[1 + \dfrac{\omega_{Di}^2}{4(\omega_E - \omega_{Di}/2)^2}\right]} , \qquad (3.40)$$

where the second term in the denominator must be larger than p for instability, by Eq. (3.36). Thus, the maximum growth rate is obtained for $1 < p < 2$. The only mode which can satisfy this condition is the (1,0) mode, as seen from Fig. 3.2. By substituting Eq. (3.40) in Eq. (3.35), we find that the maximum growth rate for this mode is

$$-\omega_i = \frac{\omega_E}{2} \frac{(\omega_E - \omega_{Di})}{(\omega_E - \omega_{Di}/2)} . \qquad (3.41)$$

These equations also give that $|-\omega_i| = |\omega_r|$ at maximum growth, which indicates that this is a large growth rate. Thus, the (1,0) mode changes from being stable for an unbounded column to having a possible growth rate given by Eq. (3.41) for a bounded column. The behavior of the eigenfrequency for other positions of the radial boundary is illustrated in Fig. 3.3(a). Here the real frequency and the growth rate of the (1,0) mode are plotted for $\omega_E = 1.5\ \omega_{Di}$ as X_b is varied. It is convenient for this and following figures to normalize all frequencies to ω_{Di}. These normalized frequencies are denoted by W's, with the appropriate subscript. The maximum growth rate as given by Eq. (3.41) is thus $-W_i = 0.375$. We also see that the real frequency rises rapidly for decreasing X_b; it increases nearly four times as the boundary radius is reduced from $X_b = 6(r_b = 2.45r_0)$ to $X_b = 4(r_0 = 2.0r_0)$. Both W_r and $-W_i$ tend to zero, the unbounded column solutions, for large X_b, although $-W_i$ decreases more slowly than W_r.

None of the other modes can satisfy Eq. (3.40) for the maximum growth rate because their p's are too large. Thus, since p increases for bounded columns over its value for an unbounded column, the effect of the boundary is stabilizing. This is in basic agreement with the stabilization found by Lehnert[62] for rectangular geometry, when

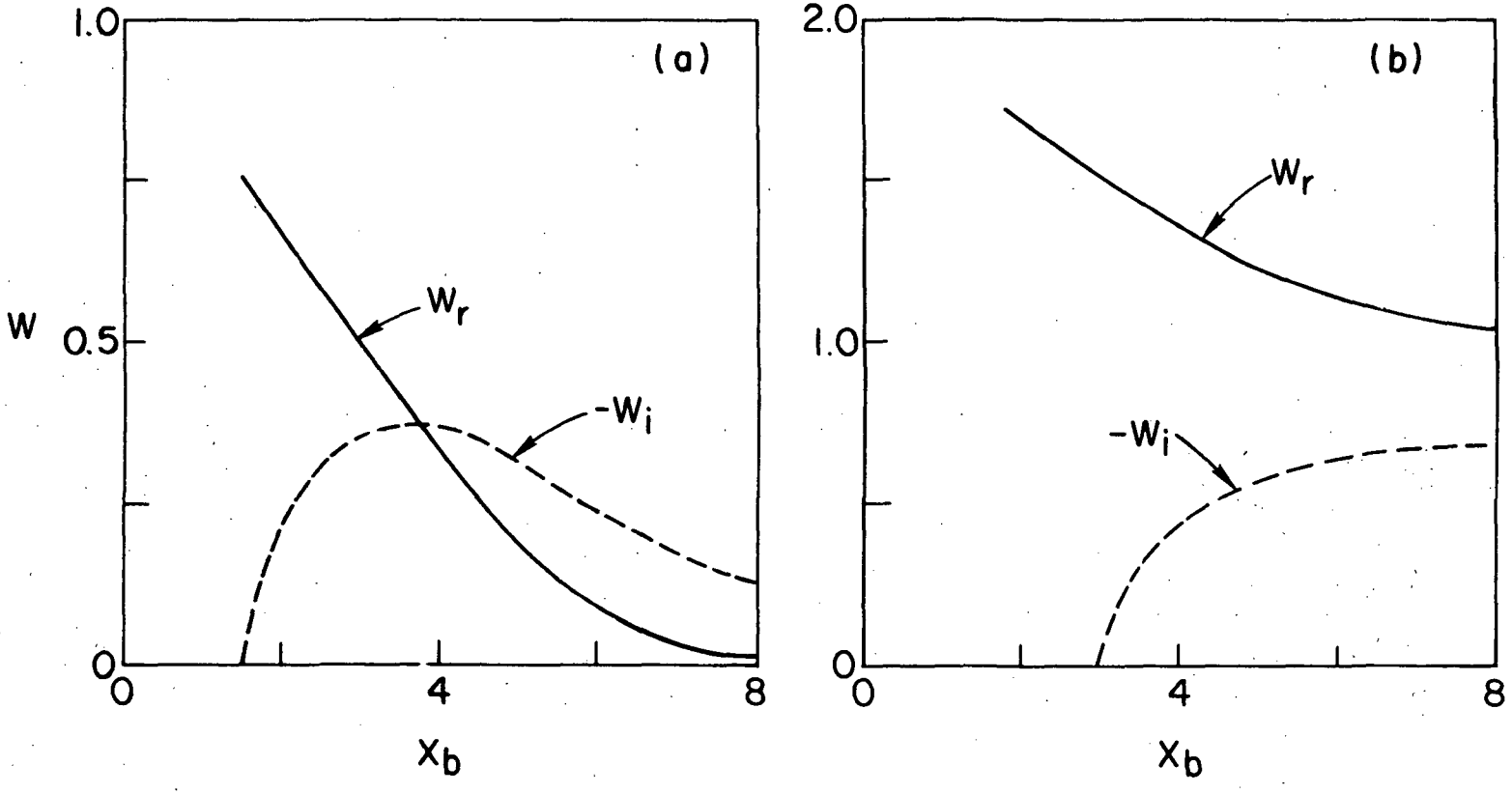

Fig. 3.3 The real frequency, W_r, and the growth rate, $-W_i$, of (a) the (1,0) mode, and (b) the (2,0) mode, for $W_E = 1.5$ as the boundary position is varied. ——— , W_r ; ---- , $-W_i$.

a boundary is introduced. The stabilization for cylindrical geometry is illustrated in Fig. 3.3(b) for the (2,0) mode with $W_E = 1.5$ again [note the scale change from Fig. 3.3(a)]. The frequency begins near its unbounded column value of $W = 1.00 - i0.707$ at large X_b. As the boundary radius decreases, the real frequency W_r increases, and the growth rate $-W_i$ decreases, finally going to zero at $X_b = 3$. Thus, the (1,0) mode can be more unstable than the (2,0) mode, and all other modes, say at $X_b = 3$, due to the fact that it is the first mode to go unstable as X_b is increased. This can be verified from Eq. (3.36), and the fact that the (1,0) mode has the lowest p values (see Fig. 3.2). On the other hand, for larger X_b, say $X_b = 4$, the (2,0) mode is more unstable. Thus, in general, one must solve Eq. (3.35) to determine the relative growth rates of the various modes.

Finally, we illustrate the effect of varying the magnitude of the rotation frequency, W_E, due to the electric field for the (1,0) and (2,0) modes. The radial boundary is taken at $X_b = 4$, which corresponds to the number density at the boundary being 2% of the number density on the axis. From Fig. 3.2, we have $p = 1.5$ for the (1,0) mode, and $p = 3.1$ for the (2,0) mode. These values of p are used in Eq. (3.35) for the eigenfrequencies. The loci these eigenfrequencies trace in the W-plane as W_E is varied are shown in Fig. 3.4, where the complex conjugate solutions are omitted. Again the symmetry of the eigenfrequencies with respect to the transformation $W_E \rightarrow (1-W_E)$ [or $\omega_E \rightarrow (\omega_D - \omega_E)$] is clearly evident. The stabilization of the modes due to finite ion Larmor radius effects occurs for small values of $|W_E|$ not satisfying Eq. (3.36); values of W_E for marginal stability are shown on the W_r-axis. The (1,0) mode is more unstable than the (2,0) mode for small values of $|W_E|$, since it goes unstable first as $|W_E|$ is increased. However, for larger values of $|W_E|$, the (2,0) mode becomes more unstable. This behavior is similar to that found above as the boundary position parameter, X_b, is increased (see Fig. 3.3).

We have stressed the characteristics of the lower order modes, (1,0) and (2,0), primarily because they are most affected by the column being bounded. We see from Eq. (3.35) that the real frequencies are not strongly affected for $p \gg 1$, which applies for the higher order

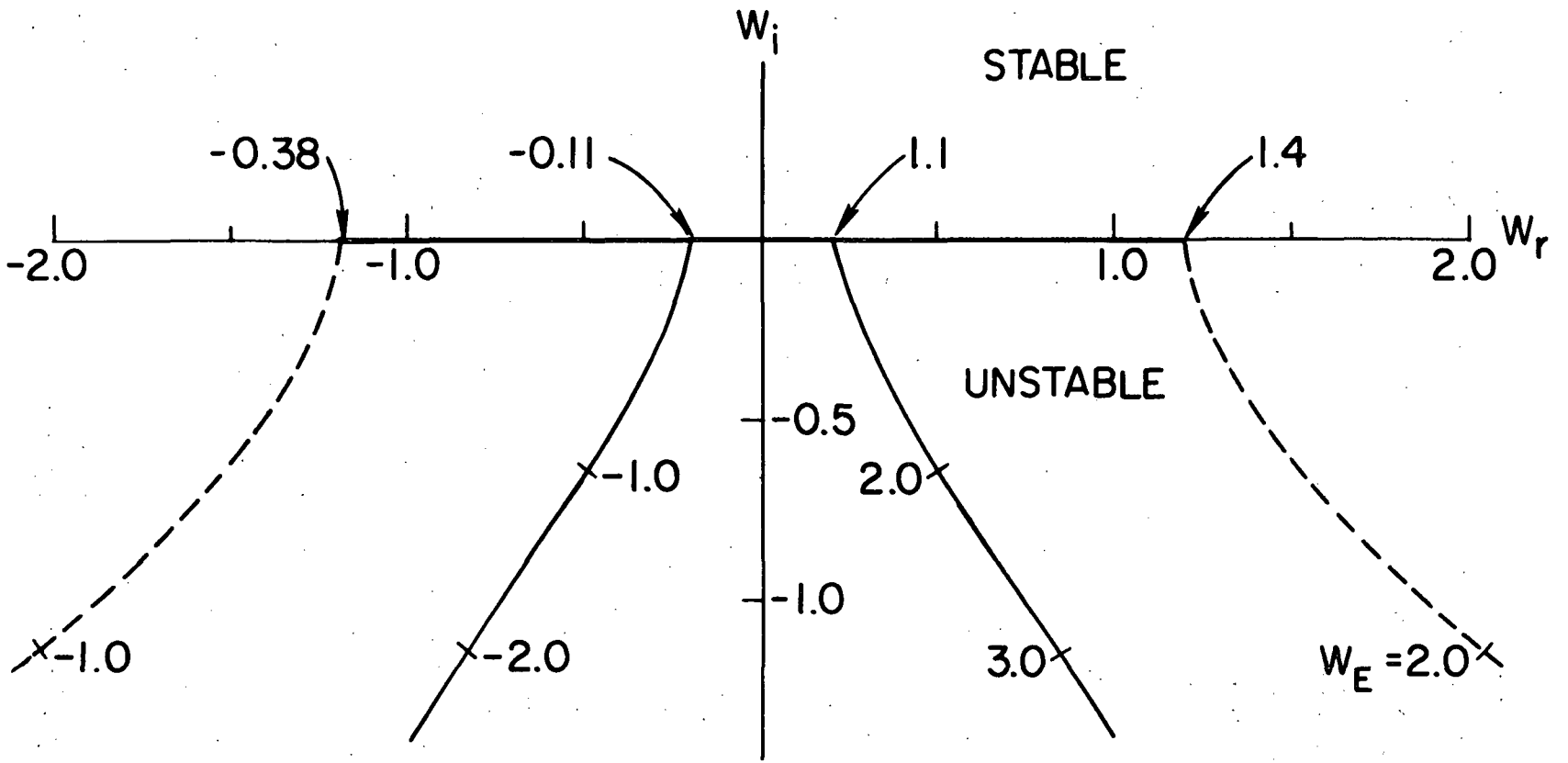

Fig. 3.4 Loci of the eigenfrequencies [Eq. (3.35)] in the W-plane for $X_b = 4$, as W_E is varied. Complex conjugate solutions are omitted. ——— , (1,0) mode; ---- , (2,0) mode.

modes. Also, it is the growth rate of the (1,0) mode which is most dramatically affected by the boundary, and this mode is first to go unstable as $|W_E|$ is increased. Since the value of W_E required for marginal stability, as given by Eq. (3.36), depends on $p^{\frac{1}{2}}$, the results for the (2,0) mode, along with Eq. (3.33), should allow one to estimate the marginal stability point for higher order modes quite well.

Having considered the behavior of the instabilities for a uniformly rotating plasma column, we now consider the case when the rotation is nonuniform.

3.3 Waves for Nonuniform Rotation

3.3.1 Numerical Procedure

We may still use the basic differential equation derived in Section 3.1.2, i.e., Eq. (3.27); however, since ω_E is no longer constant for nonuniform rotation, the equation must be solved numerically. The fact that we already have analytic solutions for uniform rotation with finite boundaries is helpful here, since we may check the validity of our numerical procedure by solving this special case first.

To solve Eq. (3.27) numerically, we have modified a predictor-corrector computer program for solving differential equations to allow complex eigenfunctions. Since the equation is linear and of second order, the procedure consists of solving a set of two linear first order differential equations of the form

$$\Psi'(r) = y(r) \quad , \tag{3.42}$$

$$y'(r) = -\left[\left(\frac{3}{r} - \frac{2r}{r_0^2}\right) - 2m\,\omega_E' \frac{(\omega - m\omega_E + m\omega_{Di}/2)}{\omega_1\omega_2}\right] y(r)$$

$$+ \left[\frac{m^2-1}{r^2} + \frac{2}{r_0^2}\,\frac{\omega^2}{\omega_1\omega_2}\right]\Psi(r) \quad , \tag{3.43}$$

which are equivalent to Eq. (3.27).

We know that Eq. (3.27) has a regular singularity at the origin, so care must be taken to eliminate the singular solution from

our procedure, i.e., to satisfy the boundary condition at the origin. To do this, we find the form of the nonsingular solution near the origin by expanding the equation about this point by the method of Frobenius.[65] The solution is assumed to have the form

$$\Psi(r) = \sum_{n=0}^{\infty} a_n r^{n+j} , \tag{3.44}$$

where j is to be determined. This solution is used in Eq. (3.27), and coefficients of like powers of r are grouped together. We find that in order to satisfy this equation, j must take on one of the two values

$$j = -1 \pm m . \tag{3.45}$$

For $m \geq 1$, the minus sign corresponds to the singular solution, so the nonsingular solution has the form

$$\Psi(r) \approx a_0 r^{m-1} \tag{3.46}$$

near the origin. Thus, we begin the numerical integration of Eqs. (3.42) and (3.43) very close to the origin, specifying the initial conditions in the ratio required by Eq. (3.46), i.e.,

$$\frac{\Psi'(r)}{\Psi(r)} = \frac{m - 1}{r} . \tag{3.47}$$

The full procedure, then, is to choose an eigenfrequency, ω, and integrate the differential equation outward. We also integrate the equation inward from the outer boundary, assuming $\Psi(r_b) = 0$ and any finite value of $\Psi'(r_b)$ as starting values. The values of Ψ'/Ψ obtained from each integration are compared at some intermediate position. If they agree, we have chosen a proper eigenfrequency, and also have computed the eigenfunction. If they do not agree, we must choose another eigenfrequency. An interpolation procedure is then used to converge to a proper eigenfrequency.

3.3.2 Solutions for Gradual Shear

The first case we consider is a gradual shear in the rotation frequency, W_E, due to the electric field. We take the form

$$W_E = 2.0 + s\left(\frac{r}{r_0} - 1.0\right) \quad , \tag{3.48}$$

where s assumes various values. This is shown in Fig. 3.5, where the radial boundary is taken at $X_b = 4$. This form for the profile of W_E is used to illustrate the effect of deviations from uniform rotation as might be encountered in experimental devices. For $s = 0$, we have uniform rotation, so that the electric field is a linear function of radius. As s becomes negative, the electric field becomes larger close to the origin, but decreases toward the outer boundary, r_b, and becomes negative there for large $-s$. It is this case which has the most dramatic effect on the eigenfrequencies, so we study it in detail. Again we stress the similarities and differences of the charcteristics of the lowest order (1,0) mode and the higher order modes as illustrated by the (2,0) mode.

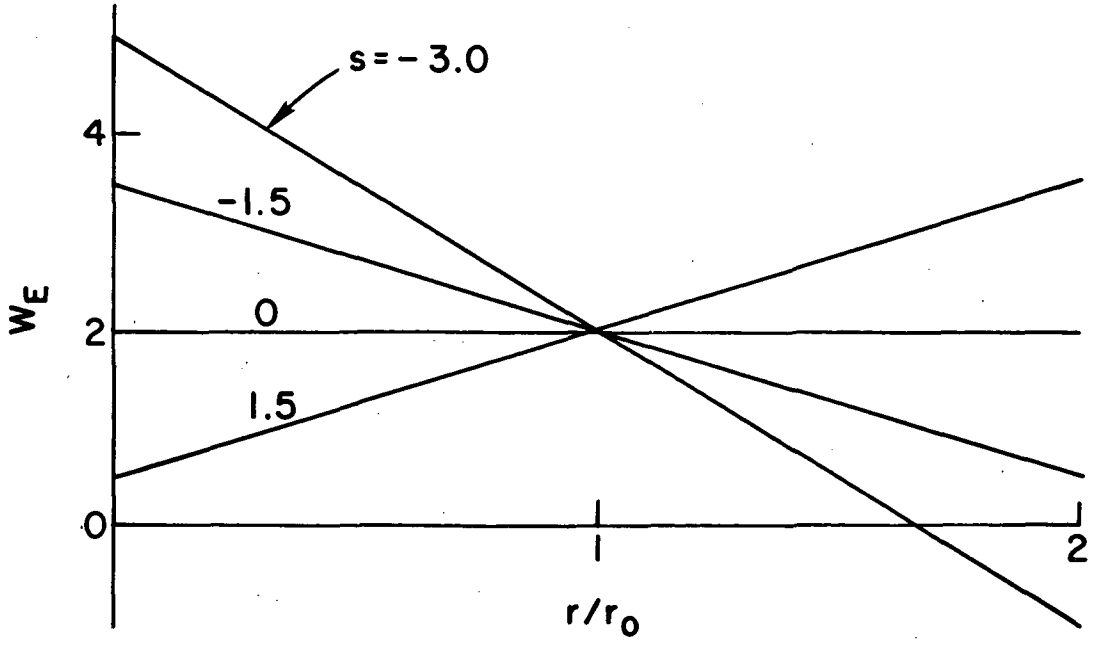

Fig. 3.5 Rotation frequency profile, W_E, due to the electric field, as given by Eq. (3.48).

In Figs. 3.6 and 3.7, we show the loci of the eigenfrequencies in the W-plane for these two modes as s is varied, and compare them to the loci for uniform rotation, when W_E takes on various constant values (see Fig. 3.4 for reference). The response of the two modes to the non-uniform rotation is quite different. The (1,0) mode (Fig. 3.6) has eigenfrequencies which change very rapidly as s becomes negative; the real part of the frequency becomes negative, corresponding to an $m = -1$ mode, when only a small outer region of the column has a negative W_E. In this connection, it should be noted from Eq. (3.7) that the total ion rotation frequency is $\sim (W_E - 1)$. There is a region between $s \approx -1.7$ and $s \approx -2.1$ for which the eigenfrequency appears to become real, corresponding to stabilization. However, one is then faced with a second singularity in Eq. (3.27) at the position where ω_2 $(= \omega - m\omega_E + m\omega_D)$ becomes zero, and possibly a third where ω_1 $(= \omega - m\omega_E)$ becomes zero. Numerically, we could not find solutions between $s \approx -1.7$ and $s \approx -2.1$, either on the real W-axis, or off it. Physically, we can argue that either the solutions are nonexistent in this region, i.e., there are no nonsingular eigenfunctions, or that the waves are stable (W real), and the singularities of the equation prevented us from finding numerical solutions. The stability of the plasma is not affected in either case. Another possibility is that the solutions continue into the upper half W-plane. This is not likely for two reasons: first, there should then be no singularities making numerical solutions unattainable; second, there are complex conjugate solutions, which would mean the plasma column is actually unstable between $s \approx -1.7$ and $s \approx -2.1$. This is not a very reasonable result in view of the finite Larmor radius stabilization for uniform rotation. For $s > 0$, the results are less interesting, as the main effect is to increase the growth rate and real frequency. The results for both $s < 0$ and $s > 0$ can be understood in terms of the eigenfrequency of this mode being very sensitive to, and primarily determined by, the rotation of the outer portion of the column.

Constrasted with the behavior of the (1,0) mode is that of the (2,0) mode, as shown in Fig. 3.7. As s takes on negative values, the

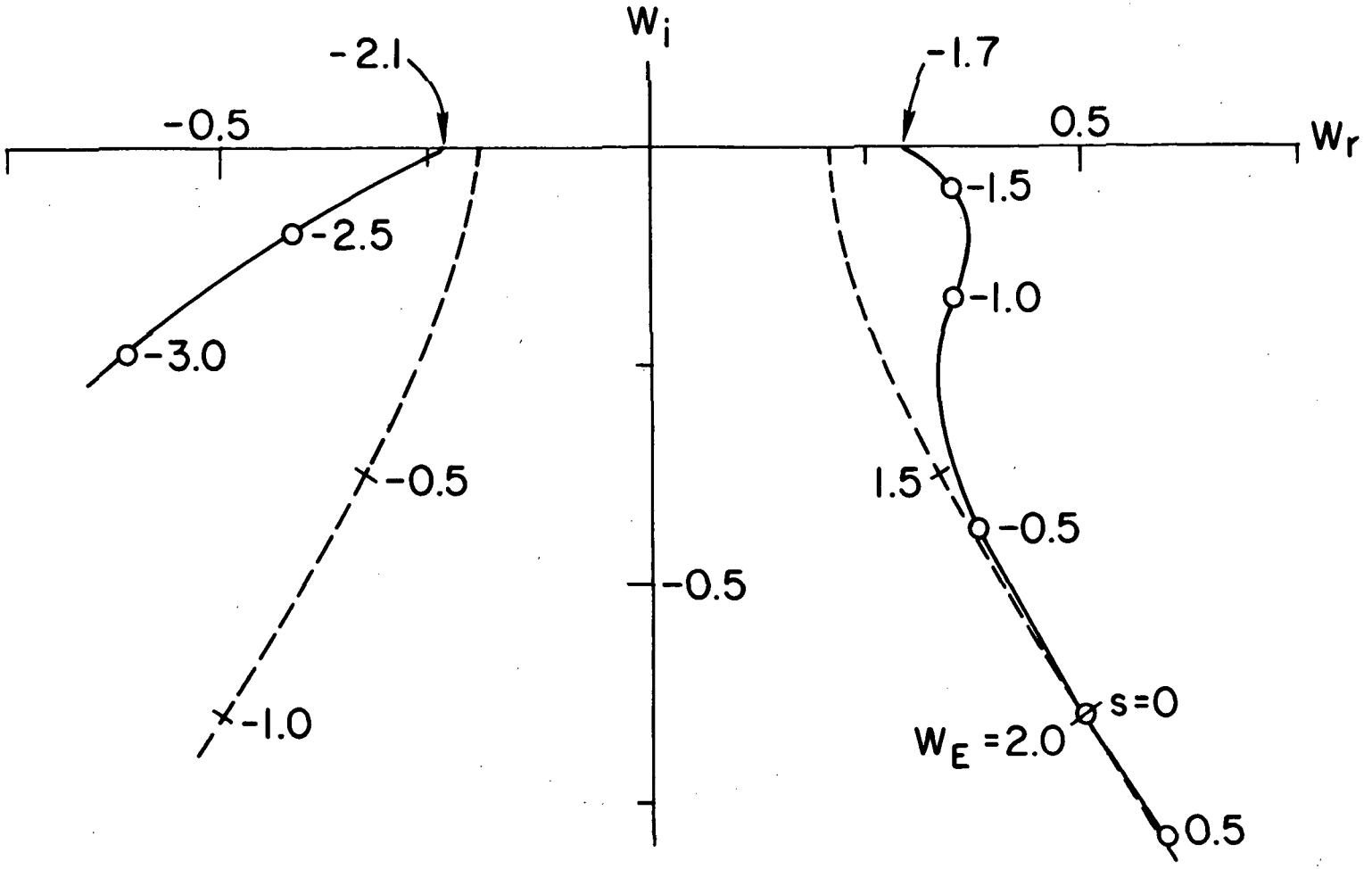

Fig. 3.6 Locus of the eigenfrequency of the (1,0) mode for $X_b = 4$. ——— , as s is varied in Eq. (3.48); ---- , as constant W_E is varied for uniform rotation.

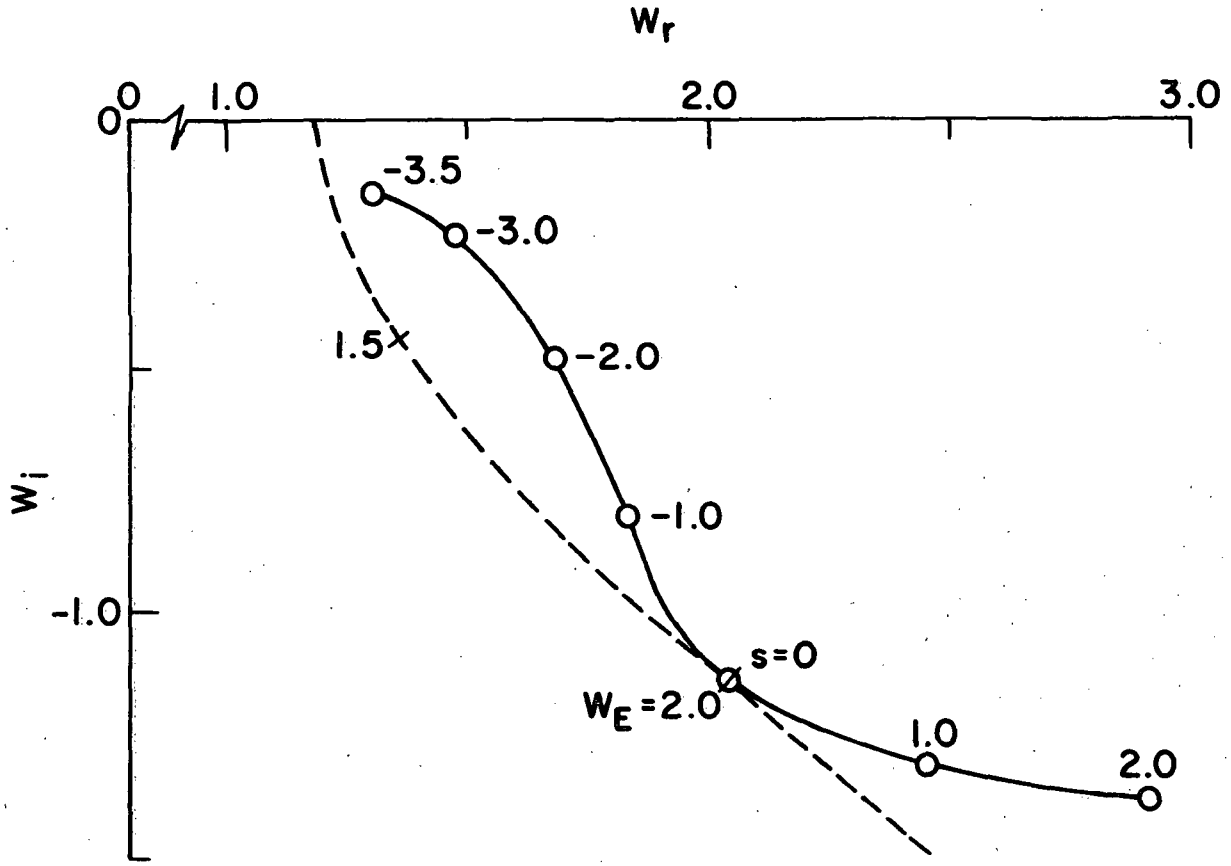

Fig. 3.7 Locus of the eigenfrequency of the (2,0) mode, with conditions as in Fig. 3.6.

eigenfrequency changes quite slowly, and remains well into the right half plane. The growth rate of the mode is reduced, but it remains unstable for the values of s considered. The effect of having $s > 0$ is similar to that for the (1,0) mode, in that it increases the growth rate and real frequency, although the effect on the growth rate is not as strong.

The general behavior shown by these modes can be deduced from approximate solutions based on quadratic forms, as given by Perkins and Jassby.[38] However, direct comparison with the solutions is not quantitatively useful due to some ill-defined quantities in their theory. Further, the use of quadratic forms depends on the shapes of the eigenfunctions, which are not given by the theory and must be guessed. Our solutions, on the other hand, do give the eigenfunctions.

It is interesting to compare the changes in the eigenfunctions of the (1,0) and (2,0) modes as s is varied. These are shown in Figs. 3.8 and 3.9 for the case of uniform rotation ($s = 0$), and for nonuniform rotation with $s = -2.5$ see Eq. (3.48) . We plot the wave variables of experimental interest, $e\phi_1/T_i$ and n_1/n_0, showing their relative amplitudes and phases. The behavior of Ψ can be found from the plot of n_1/n_0 since, from Eqs. (3.18) and (3.26),

$$\Psi(r) \propto \frac{1}{r} \frac{n_1}{n_0} \quad . \tag{3.49}$$

For uniform rotation, note that both modes have significant amplitudes throughout the bounded region. However, the (2,0) mode is somewhat more concentrated toward the outer boundary, a trend which continues with higher order m modes, as shown numerically by Chen.[64] This is consistent with the fact that Ψ varies as r^{m-1} near the origin as shown in Eq. (3.46). Once the eigenfrequency, W, is known, the relative phase shift between $e\phi_1/T_i$ and n_1/n_0 can be calculated directly from Eq. (3.18), since the eigenfunctions have no phase shift radially for uniform rotation. The relative phase shift is quite large, $\sim 180^o$, for this mode.

For nonuniform rotation ($s = -2.5$), the most significant effect is the localization of the eigenfunction for the (2,0) mode, while

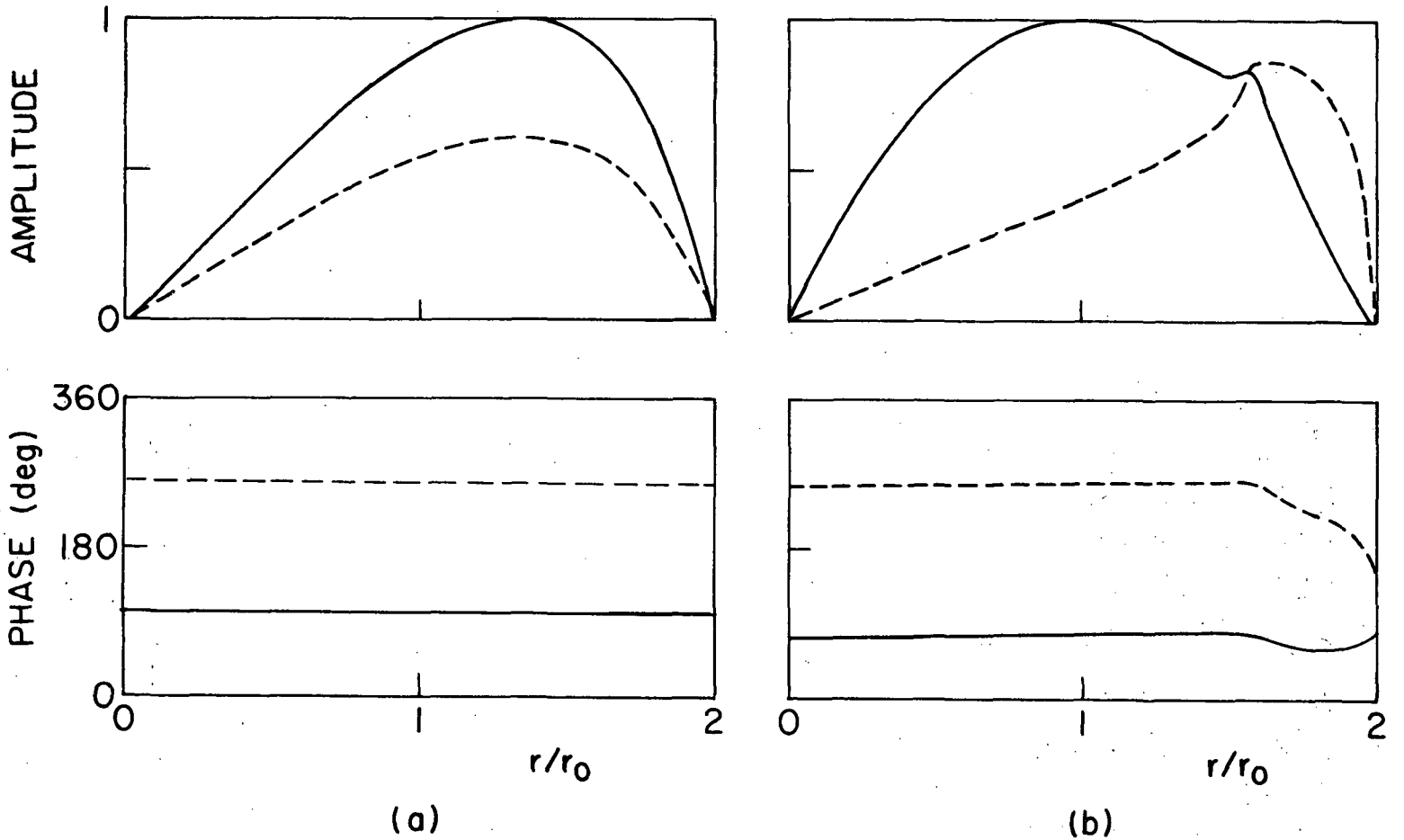

Fig. 3.8 Computed eigenfunctions of the (1,0) mode for (a) uniform rotation (s = 0), and (b) nonuniform rotation with s = -2.5. —— $e\phi_1/T_i$; ---- n_1/n_0 .

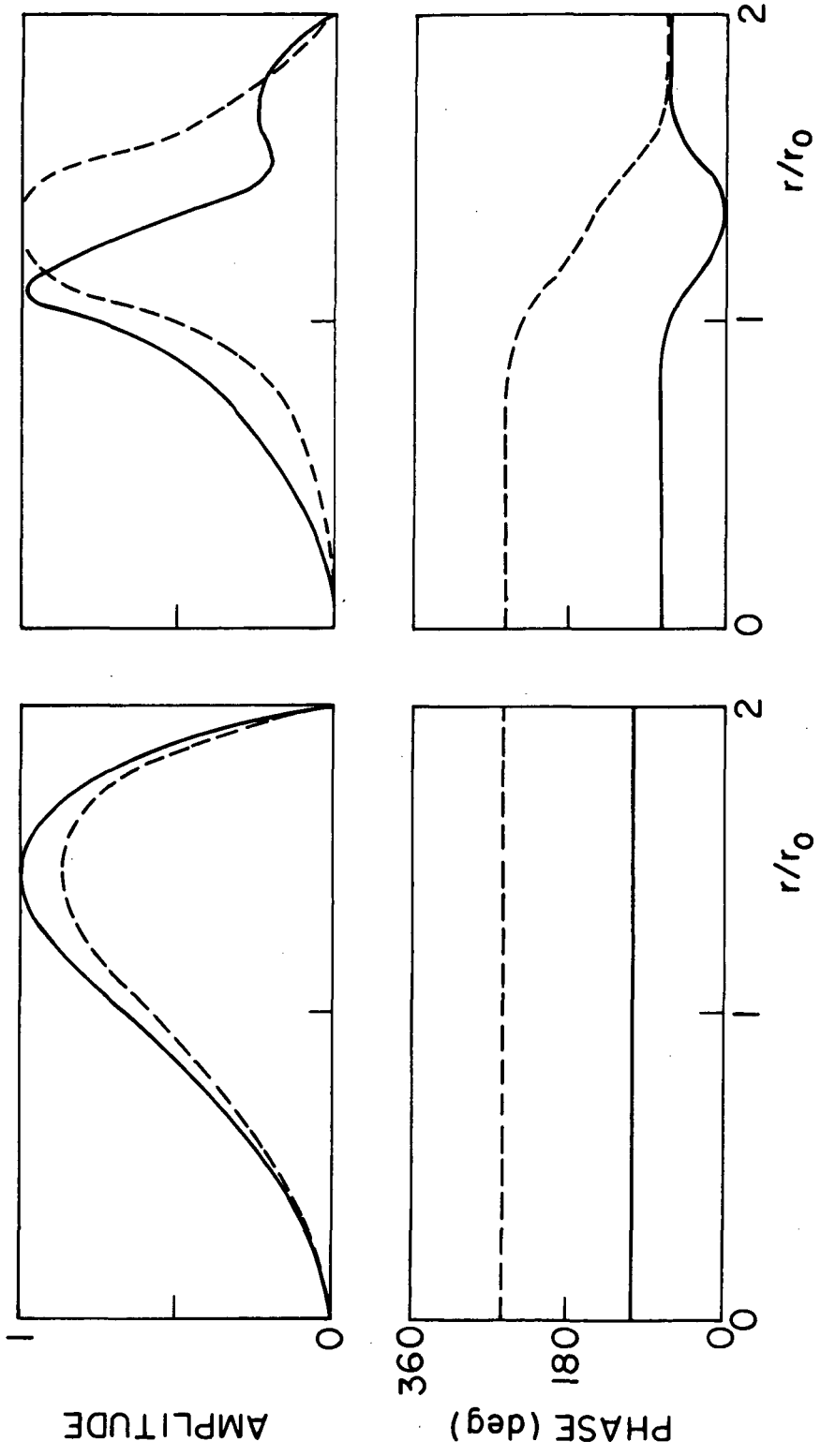

Fig. 3.9 Computed eigenfunctions of the (2,0) mode for the conditions of Fig. 3.8.

the (1,0) mode remains quite spread out. This can be understood physically as follows. The shear in the rotation frequency means that the wave cannot remain in phase radially as it propagates azimuthally. This effect is accentuated for higher m numbers due to the fact that they have increasingly rapid azimuthal phase variations. It is just this type of localization for higher order modes which allows us to use rectangular **slab** geometry in Section 4 to discuss drift waves. We would not expect this approximation to work well for $m = 1$ modes, however. This has been confirmed experimentally for drift waves.[43] Also note the sizeable radial phase shifts which now appear for the eigenfunction. These provide a convenient parameter for comparison between theory and experiment, as we shall see in Section 3.4. Finally, the eigenfunction n_1/n_0 for the (1,0) mode has quite a sharp variation near $r = 1.5r_0$. Since the eigenfrequency for this case is quite close to the W_r-axis (see Fig. 3.6), it illustrates the numerical difficulties experienced as the W_r-axis is approached, in that the eigenfunction appears to be becoming singular.

3.3.3 Solutions for Abrupt Shear

We consider the effects of abrupt shear by allowing W_E to take on the form

$$W_E = 2 - a \qquad (r/r_0 \leq 1.2) ,$$

$$W_E = 5a(r/r_0 - 1.4) + 2 \qquad (1.2 \leq r/r_0 \leq 1.4) ,$$

$$W_E = 2 \qquad (r/r_0 \geq 1.4) . \qquad (3.50)$$

A set of these profiles is shown in Fig. 3.10, where a is allowed to take on various values, and the radial boundary is at $X_b = 4$. For $a = 0$, we have uniform rotation, while, as a increases, the shear becomes more abrupt.

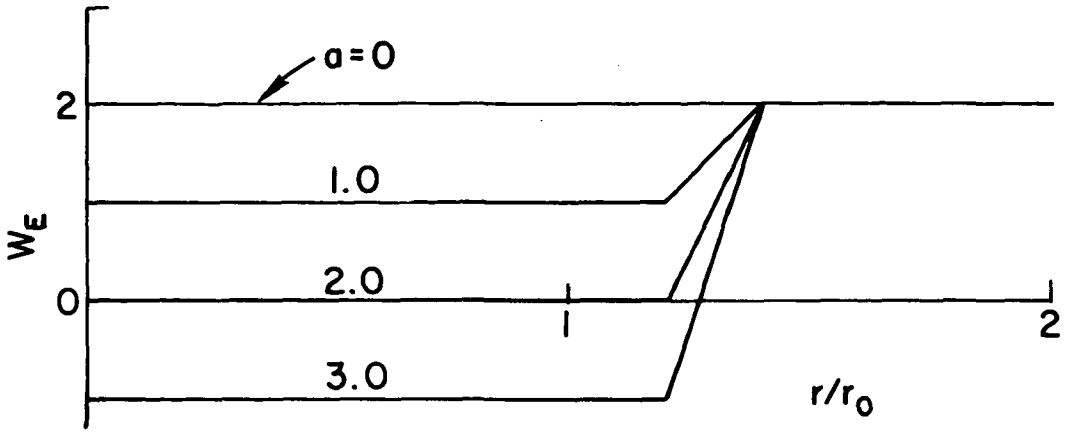

Fig. 3.10 Rotation frequency profile, W_E , due to the electric field, as given by Eq. (3.50).

The loci of the eigenfrequencies of the (1,0) mode and (2,0) mode as a is varied are shown by the full lines in Figs. 3.11 and 3.12, respectively. Also shown for comparison are the loci for uniform rotation as W_E is varied (dashed line) and the loci for the profile given by Eq. (3.50), but with the zero order ion inertia or centrifugal force term neglected in the differential equation (chain-dot line). The effect of neglecting the centrifugal force term was discussed in Section 3.2.1 for uniform rotation, where Eq. (3.37) gives the real eigenfrequencies which result. Again, the centrifugal force term is more easily identified in Eq. (3.25), where it is the $(\omega_E-\omega_{Di})^2$ term, than in Eq. (3.27). The solutions in Fig. 3.11 for the (1,0) mode show that the various profiles of W_E have very little effect on the eigenfrequency. The solutions when the centrifugal force effect is neglected show that the shear can cause instability for the (1,0) mode, but there is no apparent correlation between the two curves. Thus, for this mode, it is necessary to solve the full differential equation, including the centrifugal force effect. As for gradual shear, the behavior of the solution can be explained as the eigenfrequency being primarily determined by the rotation of the outer portion of the column.

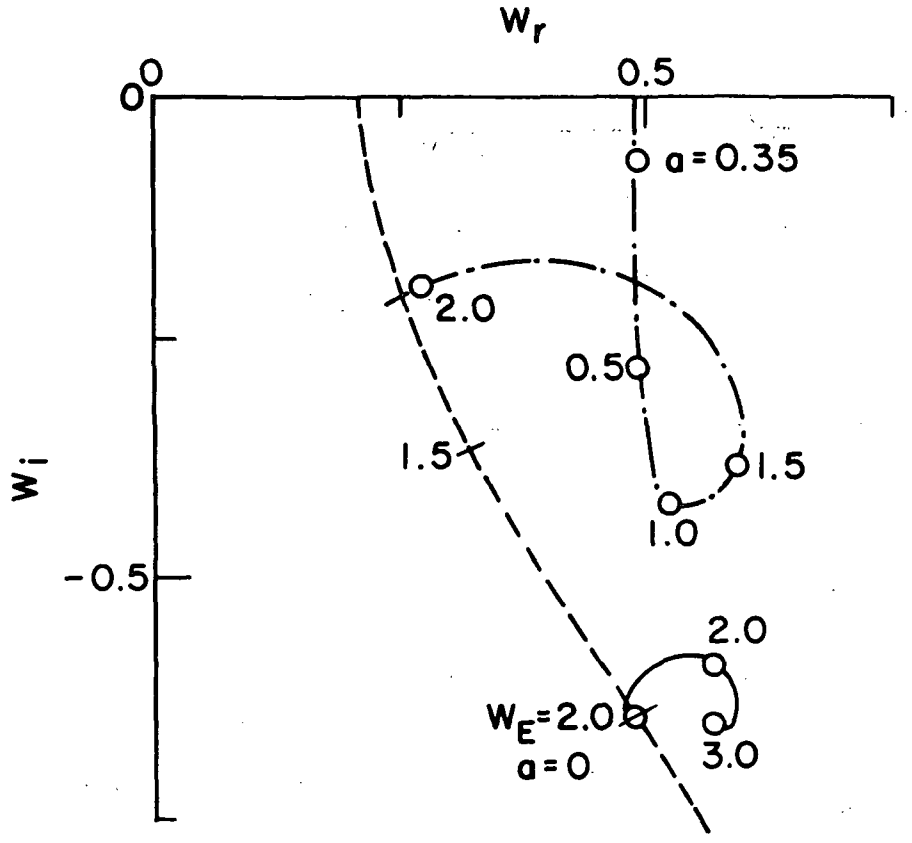

Fig. 3.11 Locus of the eigenfrequency of the (1,0) mode with $X_b = 4$. ——— , as a is varied in Eq. (3.50); -·-·-·-· , with centrifugal effect neglected; ---- , for uniform rotation.

The behavior of the (2,0) mode, as shown in Fig. 3.12, is quite different from that of the (1,0) mode. As the profile of W_E changes from uniform rotation, the growth rate of the (2,0) mode begins to decrease, but then, for $a > 1.0$, it increases. In comparing this with the solution when the centrifugal force effect is neglected, it is seen that the curves are very similar for large shears. Thus, the increase in the growth rate seems associated with the velocity shear rather than the centrifugal force. In this respect, the instability has become more like a Kelvin-Helmholtz instability.[37,38] The curves in Fig. 3.12 illustrate the transition from centrifugal instability for uniform rotation (a = 0) to instability driven primarily by velocity

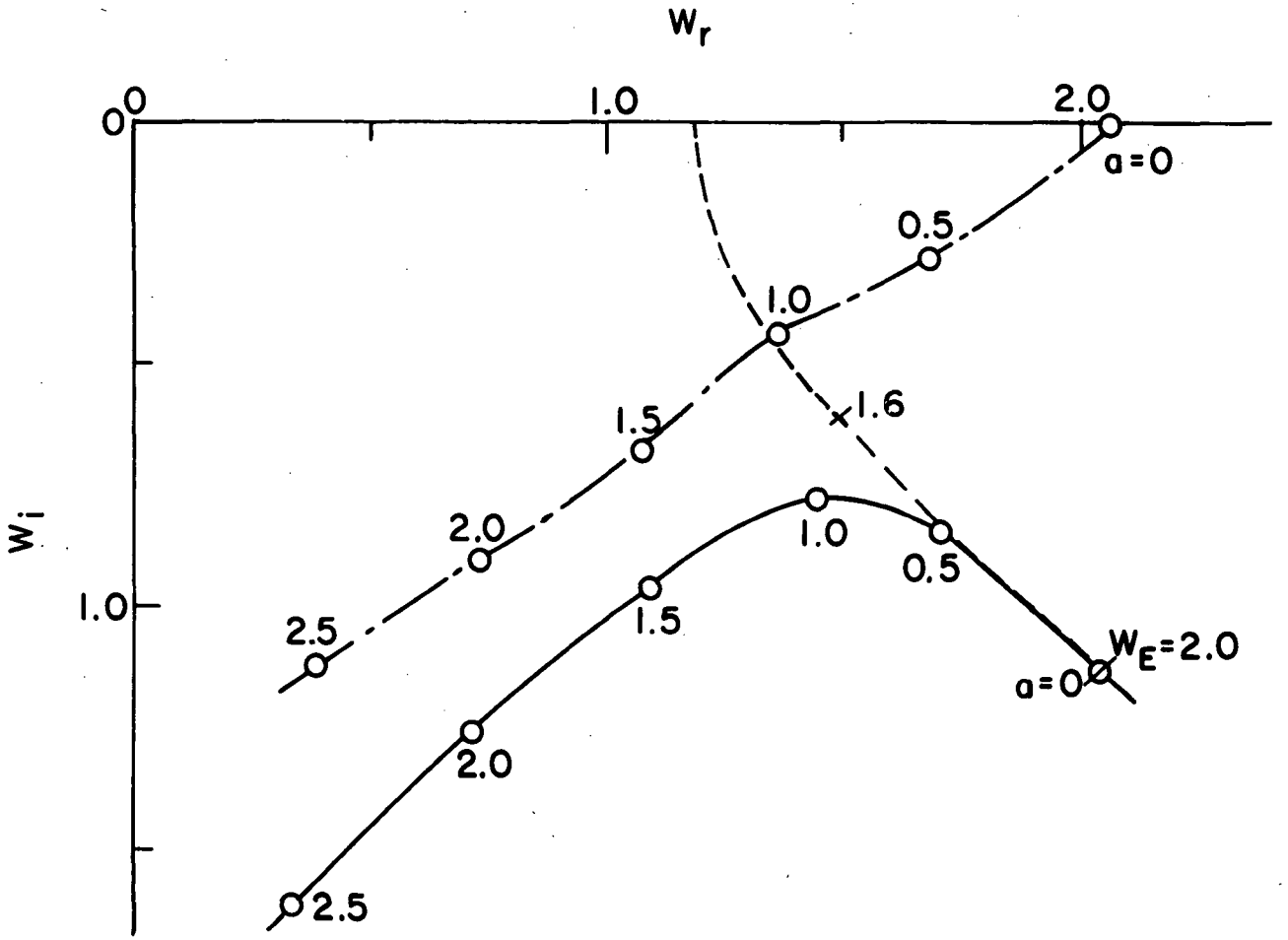

Fig. 3.12 Locus of the eigenfrequency of the (2,0) mode, with conditions as for Fig. 3.11.

shear (say $a = 2$). The behavior of the (2,0) mode is representative of the higher order azimuthal modes which can also exhibit Kelvin-Helmholtz type instability.[37,38]

The forms of the eigenfunctions of the (1,0) and (2,0) modes for abrupt shear are shown in Fig. 3.13. They correspond to $a = 2$ for the W_E profile in Fig. 3.10. Despite the different behavior of the eigenfrequencies for the two modes, their eigenfunctions are quite similar. The shear has little effect on n_1/n_0, while it has a pronounced effect on $e\phi_1/T_i$. These eigenfunctions may be compared with those shown in Figs. 3.8 and 3.9 for uniform rotation ($a = 0$), and for gradual shear. In the latter case, both n_1/n_0 and $e\phi_1/T_i$ are significantly affected by the shear. It should be noted that, by Eq. (3.49), Ψ is nearly constant through the shear region for abrupt shear since n_1/n_0 is nearly constant in this region. This is a basic assumption used in several approximate analyses of the Kelvin-Helmholtz instability, one by Kent *et al.*,[37] and the other by Perkins and Jassby.[38]

In conclusion, we emphasize that the solutions found in this and the previous subsections, for the profiles of W_E shown in Figs. 3.5 and 3.10, also give solutions for the profiles $(1 - W_E)$. This is due to the symmetry property of Eq. (3.27), as mentioned in Section 3.1.2. The new eigenfrequencies are $-W^*$, and the eigenfunctions are Ψ^*. This is a particularly useful result, since it doubles the number of profiles of W_E for which we have numerical solutions.

3.4 Comparison with Hollow Cathode Arc Experiment

3.4.1 Experimental Measurements

We now turn to use the results of the earlier parts of this section to explain some experimental measurements of low-frequency instabilities in a plasma discharge. The experimental results have been obtained by D. B. Ilić, at Stanford University, on a hollow cathode arc discharge of the type described by Lidsky *et al.*[66] The details of the experiment are available in a recent report.[67] To summarize, a cylindrical discharge tube of 10 cm diameter pyrex glass is immersed in an axial magnetic field uniform to ±2% over one meter and variable to 2.5 kG. The discharge itself is produced between a cathode of 3 mm diameter tungsten

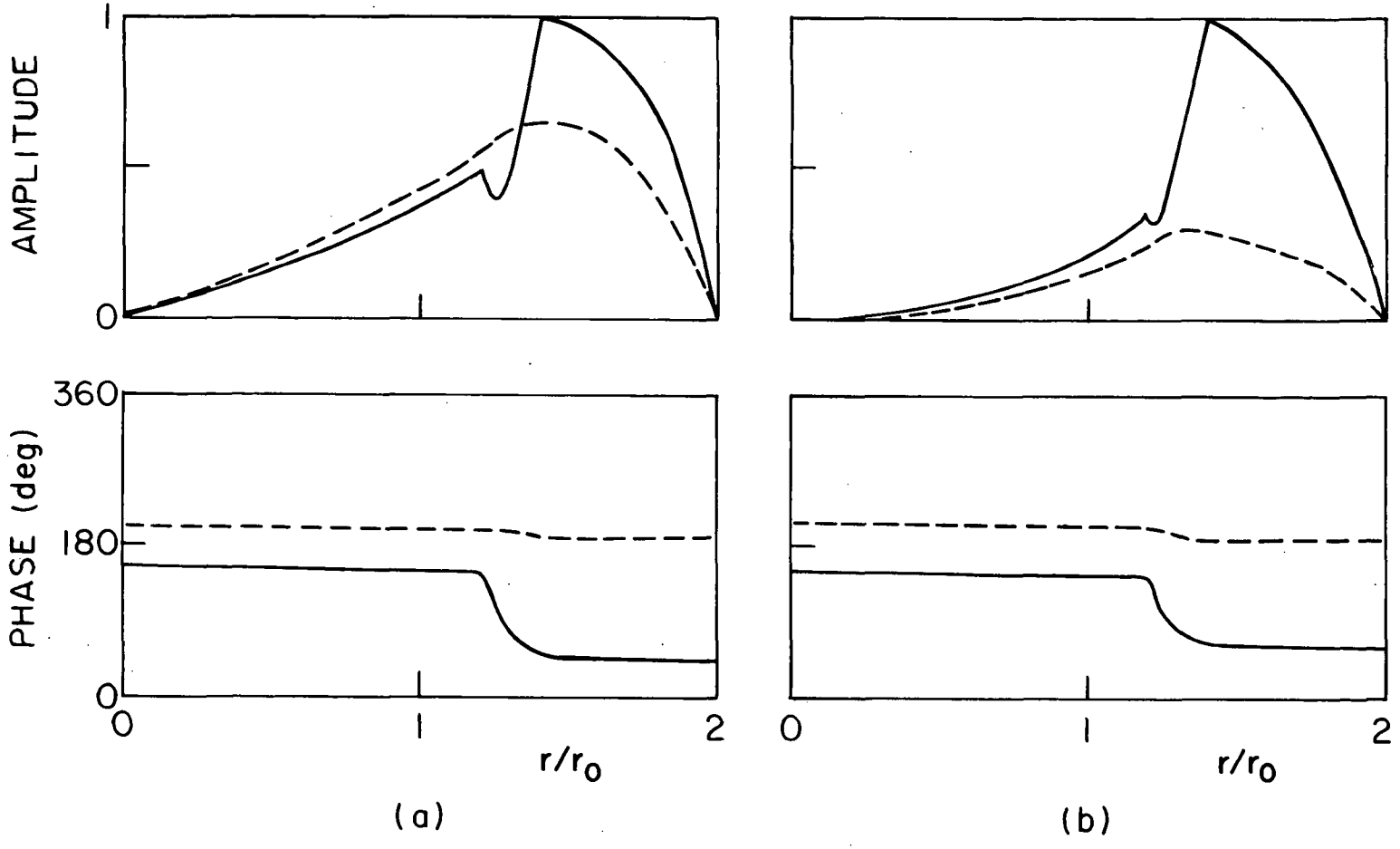

Fig. 3.13 Computed eigenfunctions for (a) the (1,0) mode, and (b) the (2,0) mode, corresponding to eigenfrequencies for a = 2.0 in Figs. 3.11 and 3.12. —— $e\phi_1/T_i$; ---- n_1/n_0 .

tubing impregnated with barium-oxide, and a 2.5 cm diameter copper anode, at opposite ends of the discharge tube. The discharge runs at a voltage of $\sim$ 50V and a current of $\sim$ 10 A. The argon plasma produced has a peak density of $\sim 10^{13}$ particles/cm^3 and an electron temperature of $\sim$ 5 eV at a background pressure of $\sim 1 \times 10^{-4}$ Torr. At this pressure, the plasma can be taken to be fully ionized with singly charged ions. Langmuir probe measurements of plasma density and electron temperature show that both decrease radially. The density profile can be approximated by a Gaussian profile, while, as we saw in Section 3.1.2, the variation of electron temperature is not of direct importance to the waves being studied. However, we shall see below that this temperature variation is needed in order to calculate the DC radial electric field in the plasma.

The profile of the radial electric field can be changed by varying the potential on a hollow copper cylinder, which comes in contact with the plasma since it is located just inside the discharge tube at the cathode end. This copper cylinder is also used as an anode when igniting the discharge, and is thus known as the starting anode. As the electric field profile is changed in this manner, two separate low-frequency instabilities can develop: one is an $m = 1$ mode at a frequency of $\sim$ 9 kHz, which appears when the starting anode is left floating; the other is an $m = -1$ mode at $\sim$ 7 kHz, which appears when the starting anode is grounded to the cathode. The starting anode assumes a voltage of $\sim$ 50 V when left floating, and, for a range of starting anode potentials between this value and O V (grounded), both modes are stabilized. There is no axial variation detected for either mode, and the ion cyclotron frequency has a value $f_{ci} = 50$ kHz ($B = 1.3$ kG). The measured radial eigenfunctions of density, n_1, and potential, ϕ_1, for these modes are shown in Figs. 3.14 and 3.15. The potential measurements were obtained from an electrically floating Langmuir probe, while the density was obtained from measurements of the ion saturation current to the probe. We shall compare these measurements with theory in Section 3.4.2, but first the form of the electric field profile needs to be determined for each mode.

To find the electric field, we must correct the measured floating potential, ϕ_f, as obtained from the Langmuir probe, in order to obtain the space potential, ϕ_s. The standard procedure is to take[68]

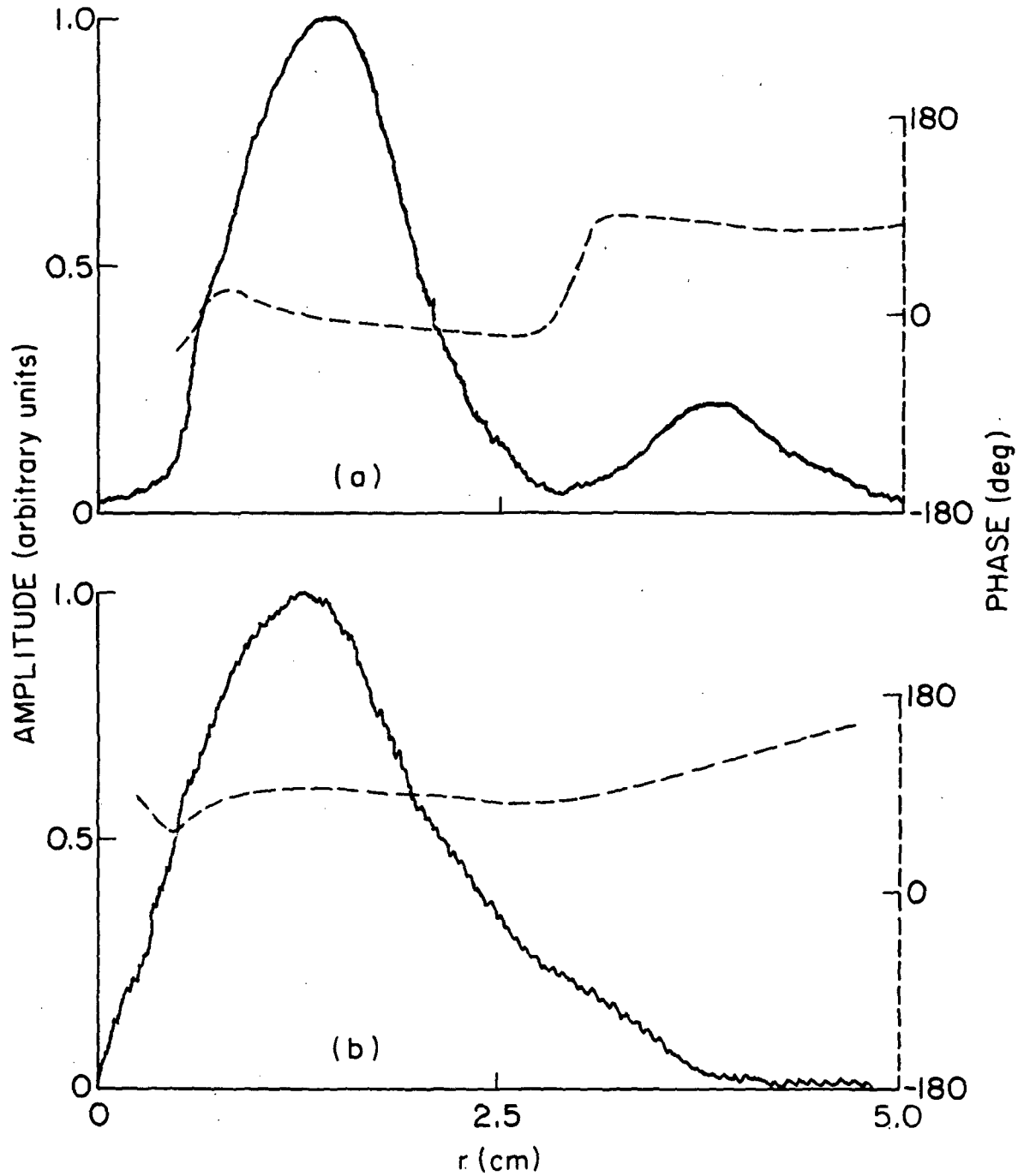

Fig. 3.14 Measured radial variations of (a) potential, ϕ_1, and (b) density, n_1, for the m = 1 instability. ——, amplitude; ----, phase.

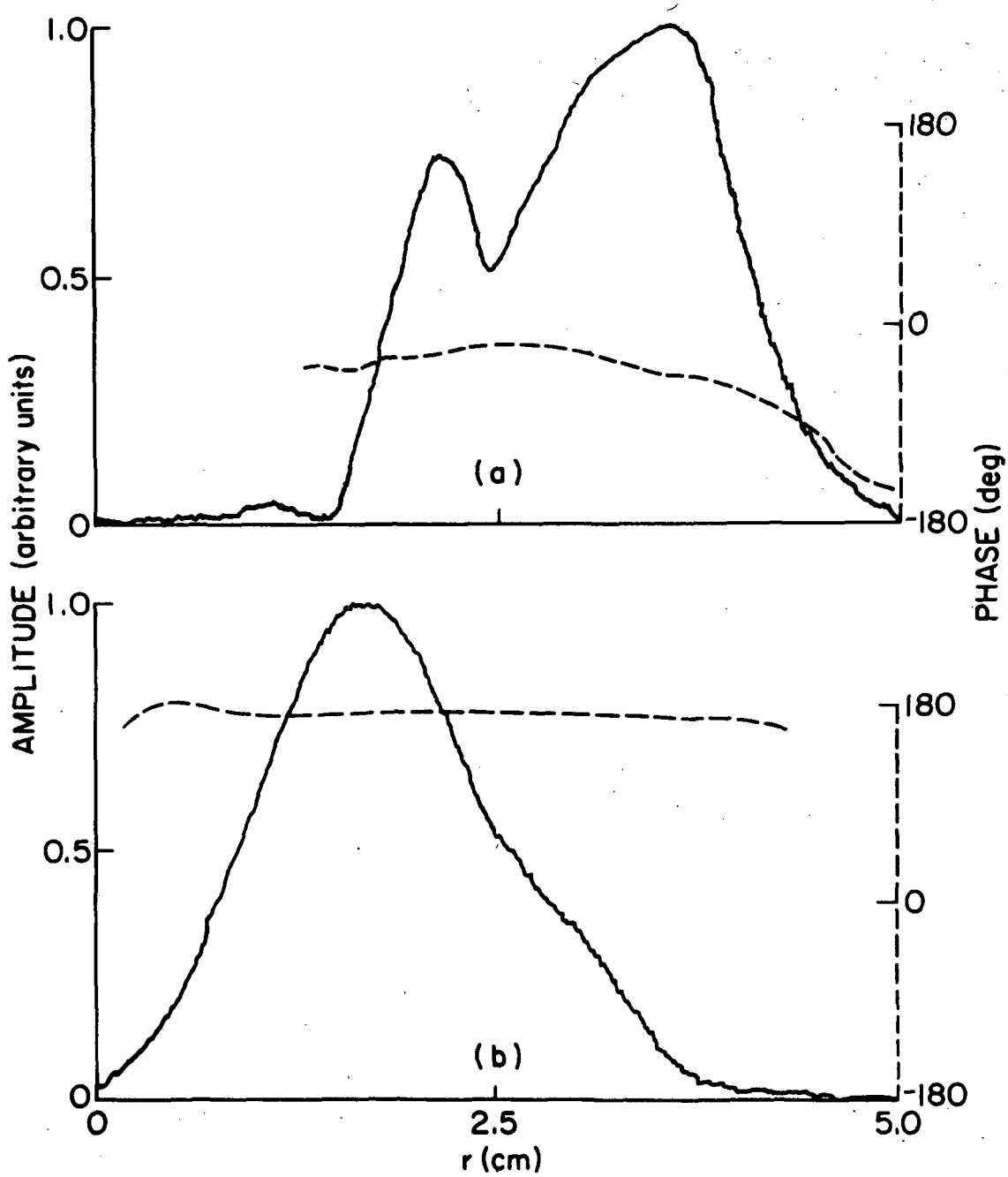

Fig. 3.15 Measured radial variations of (a) potential, ϕ_1, and (b) density, n_1, for the m = -1 instability. ——, amplitude; ----, phase.

$$\phi_s = \phi_f + c\,\frac{T_e}{e} \quad , \tag{3.51}$$

where T_e/e is the electron temperature in volts, and c is a constant. Thus, the form of the electron temperature profile affects the electric field E [$= d\phi_s/dr$]. There is no precise value calculated for the constant c in Eq. (3.51), although a value of around 4 is often taken.[68] We have taken values of $c = 4$ and $c = 2$, and compared the results in Fig. 3.16, where $-E/r$ is plotted as a function of radius. The quantity $-E/r$ is used since a negative electric field corresponds to an $\underset{\sim}{E}_0 \times \underset{\sim}{B}$ velocity in the right-hand sense. It should be stressed that these curves should be considered only approximate, as they depend quite sensitively on the electron temperature measurements and the validity of the probe theory. We have not attempted to extend the determination of the electric field to very near the axis, as there are large gradients in temperature and potential, and the measurements are less certain there. From the approximate profiles in Fig. 3.16, we see that, for the $m = 1$ mode, the electric field is mostly negative, and varies rapidly in a region about half-way to the wall. On the other hand, for the $m = -1$ mode, the electric field is positive and smaller, and does not have any rapid variations.

3.4.2 Comparison between Theory and Experiment

Comparison between theory and experiment is complicated by the difficulty of obtaining reliable measurements of the electric field, as mentioned in Section 3.4.1. However, the measurements are consistent as to the basic forms of the electric field, and using approximations to them, we can explain both the $m = 1$ and $m = -1$ instabilities observed experimentally, including good correlations between measured and computed eigenfunctions of density and potential.

The instabilities can be explained by referring to the wave solutions for uniform rotation in Section 3.2.2. For a negative electric field, the rotation of the column due to the $\underset{\sim}{E}_0 \times \underset{\sim}{B}$ drift is positive, i.e., in the right-hand sense, and, for a large enough rotation to overcome finite ion Larmor radius stabilization, the column becomes unstable in the $m = 1$ mode (see Fig. 3.4). This is what is observed when the starting anode is left floating, and the radial electric field

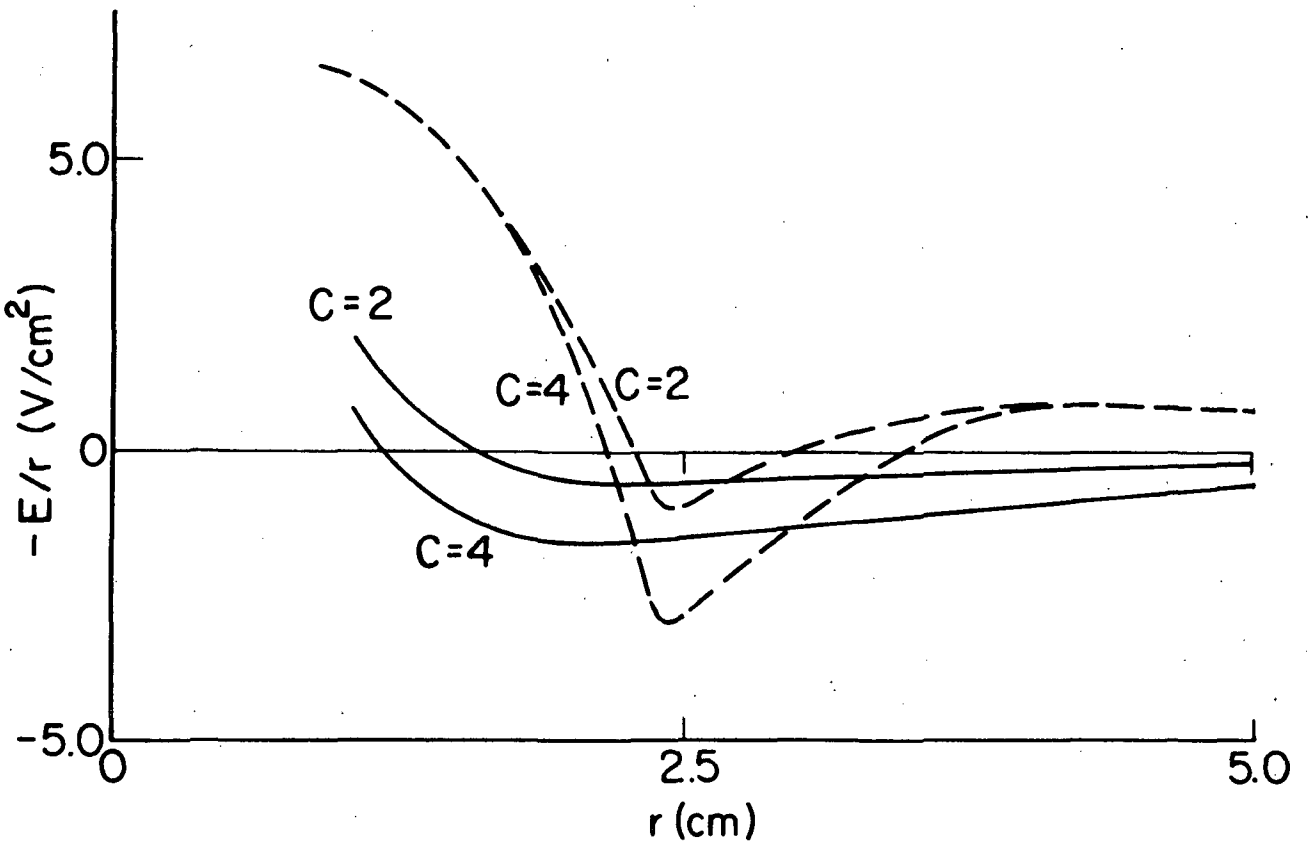

Fig. 3.16 Estimated electric field profiles as determined from measured profiles of ϕ_f and T_e, together with Eq. (3.51). ----, m = 1 instability present; ——, m = -1 instability present.

is negative. As the potential of the starting anode is lowered, the $m = 1$ mode stabilizes, as one would expect from finite ion Larmor radius effects as the electric field decreases (see Fig. 3.4). When the starting anode potential is depressed further, the sign of the electric field becomes positive, in which case the $m = -1$ mode should become unstable, which is observed experimentally. It should be stressed that the electric field strength required to make the $m = -1$ mode unstable is much less than that required to make the $m = 1$ mode unstable. This can be seen clearly from Fig. 3.4 or Eq. (3.36).

To compare the theory and experiment in more detail, we have computed the eigenfunctions of density and potential as described in Section 3.3.1. The experimental parameters used in this calculation include $r_b = 5$ cm, a Gaussian number density profile with $r_0 = 2.2$ cm, and an ion temperature of 3 eV. The density profile is a good approximation to the measured data, and, although the ion temperature was not directly measured, there has been experimental evidence for values of this order.[69] The possible origin of this large ion temperature is discussed later in this subsection. Due to uncertainty in the electric field measurements, the choice of the electric field profile used in the calculation is guided by the shape of the experimental curves in Fig. 3.16, and the profile which gives the best agreement between the theoretical and experimental eigenfunctions. The profiles selected are shown in Fig. 3.17. For reference, the initial slope of the electric field for the $m = 1$ mode of Fig. 3.17 is $4\ V/cm^2$.

The computed eigenfunctions for the perturbed potential, ϕ_1, and perturbed density, n_1, for the $m = 1$ mode are shown in Fig. 3.18. They are to be compared to the measured eigenfunctions shown in Fig. 3.14. The forms of the two sets of curves are very similar. The potential amplitude has a two-humped profile for both the theoretical and the experimental curves, the inner maximum being larger. There is also a large phase shift associated with the minimum in the potential curve. Given that n_1/n_0 varies slowly with radius [Figs. 3.1 and 3.18(b)], we can see from Eq. (3.18) that the potential profiles are controlled by the value of $(\omega-\omega_E)$. Thus, the minimum in $|\phi_1|$, and the large phase shift, occur where $(\omega-\omega_E)$ has a minimum. There is also

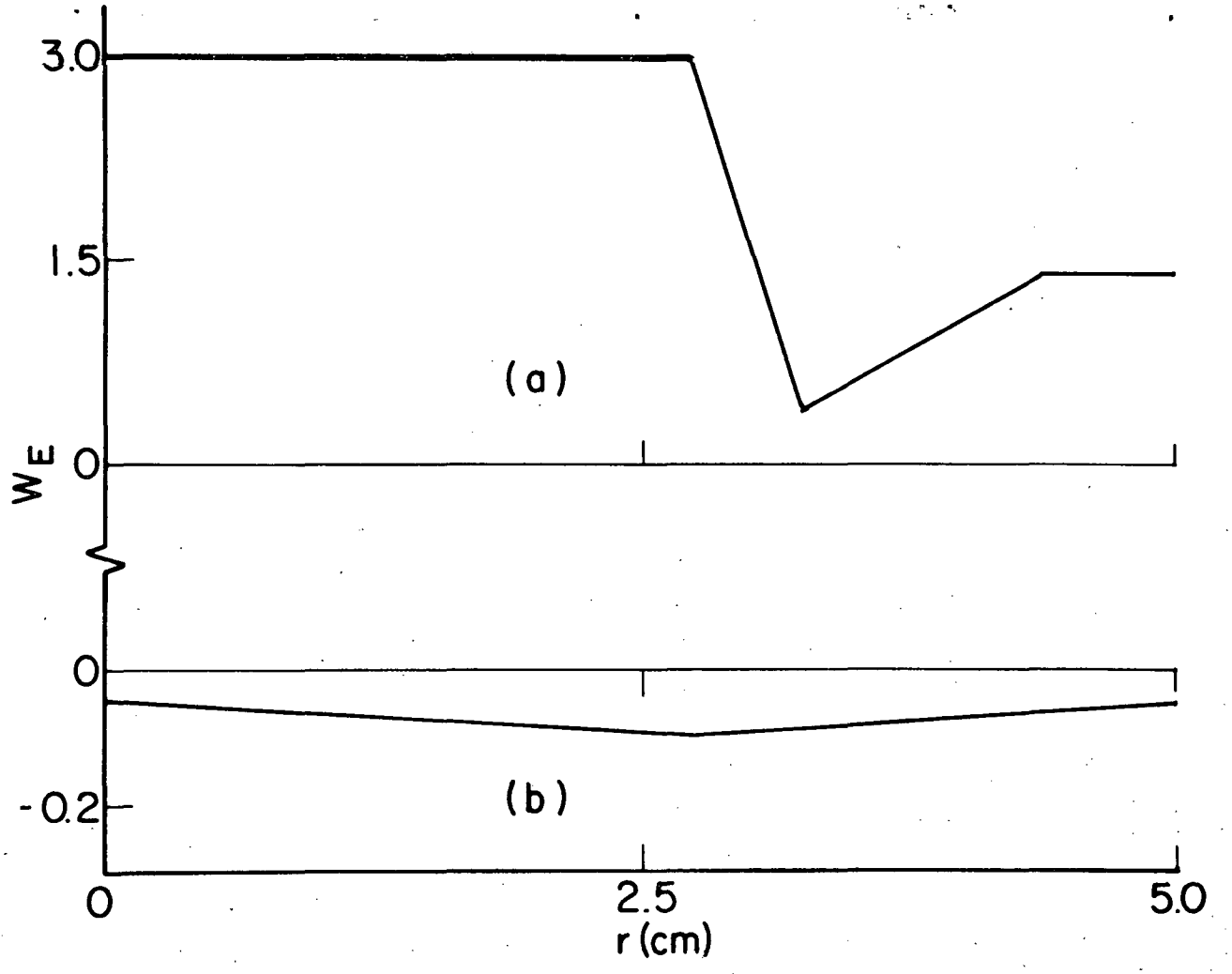

Fig. 3.17 Profiles of W_E for (a) the m = 1 mode, and (b) the m = -1 mode, used in the calculation of the eigenfunctions.

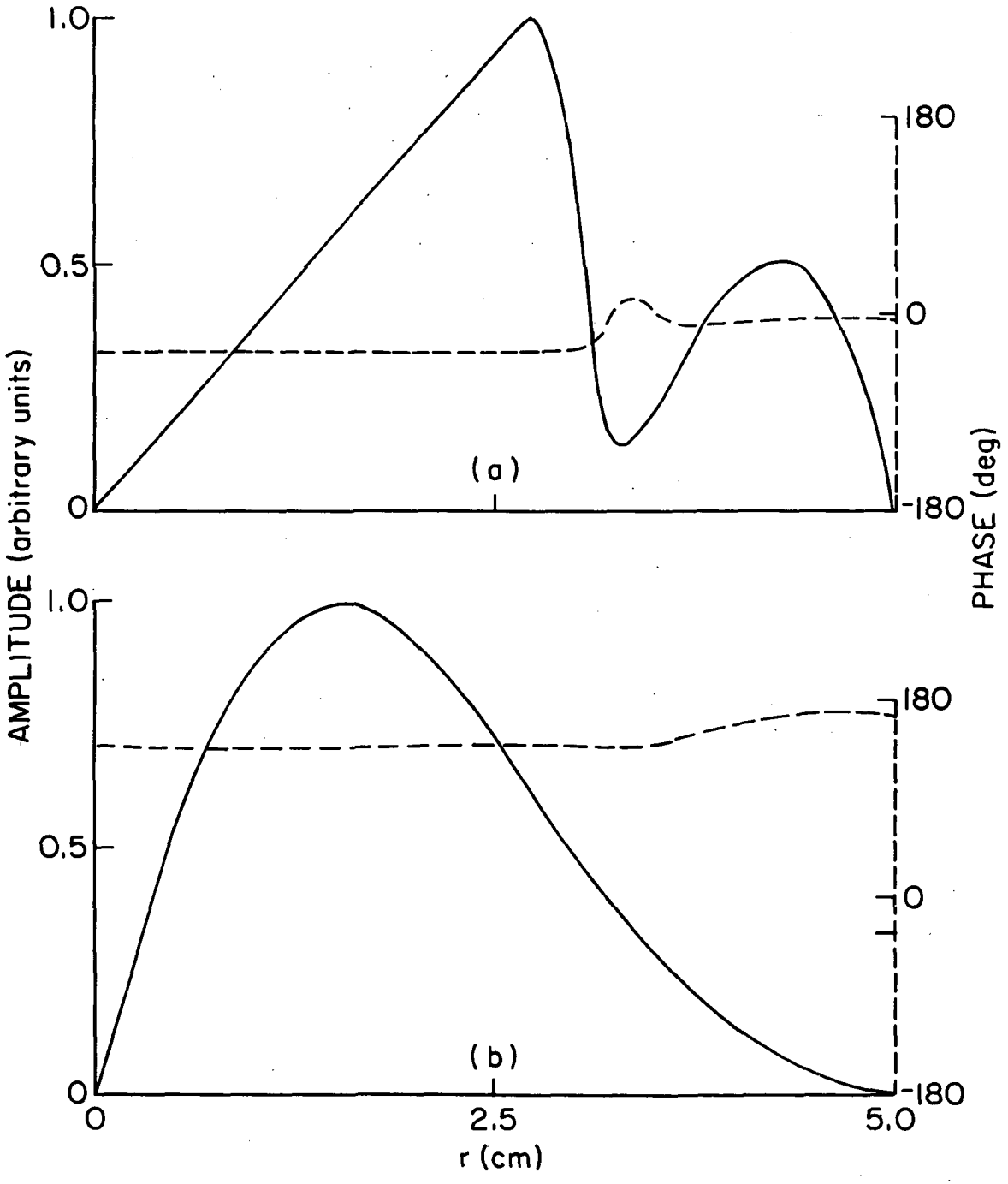

Fig. 3.18 Calculated eigenfunctions of (a) potential, ϕ_1, and (b) density, n_1, for the m = 1 mode. Comparison to be made with Fig. 3.14. —— amplitude; ---- phase.

good agreement with the profile of n_1. It has a single maximum close to the center of the column and a gradual phase shift near the outer boundary. The phase shift between n_1 and ϕ_1 is in fair agreement with theory, the theoretical value being about 25% higher than the experimental value. The computed eigenfrequency is $\omega = (0.18 - i\ 0.24)\omega_{Di}$, which gives a real frequency of ~ 3 kHz as compared to an observed value of ~ 9 kHz. However, as we saw in Section 3.2.2, the position of the radial boundary has a strong influence on the frequency of the $m = 1$ mode (see Fig. 3.3). Also, from the solutions in Section 3.3, it is apparent that the frequency of this mode is sensitive to the value of the electric field near the other radial boundary, a parameter which could not be measured accurately. Thus, we do not consider the frequency discrepancy as serious.

For the $m = -1$ mode, a small, positive electric field will cause instability, which is indeed the type of profile observed for this mode. The electric field profile taken for the $m = -1$ mode, shown in Fig. 3.17, implies nearly uniform rotation. Thus, increasing the magnitude of W_E has only a small effect on the eigenfunctions, as can be seen from the solutions in Section 3.2.2. The other experimental parameters are the same as for the $m = 1$ mode. The computed eigenfunctions are shown in Fig. 3.19, and should be compared with the experimental curves of Fig. 3.15. In contrast to the $m = 1$ mode, both the experimental and theoretical potential profiles now have a single maximum located nearer the outer boundary. The phase shift is more spread out, and can again be attributed to the behavior of $(\omega-\omega_E)$, as seen from Eq. (3.18). The density fluctuation has its maximum amplitude nearer the center, with only a gradual phase shift radially. The phase shift between n_1 and ϕ_1 is only about half of that measured. The computed eigenfrequency is $\omega = (-0.10 - i\ 0.05)\omega_{Di}$, which gives a real frequency of ~ 2 kHz compared to an observed value of ~ 7 kHz. This is consistent with the low value of frequency calculated for the $m = 1$ mode as discussed above.

From these results, it is seen that the theory of this section can reproduce the salient features of the two instabilities observed in the HCD. The discrepancies between the theory and the

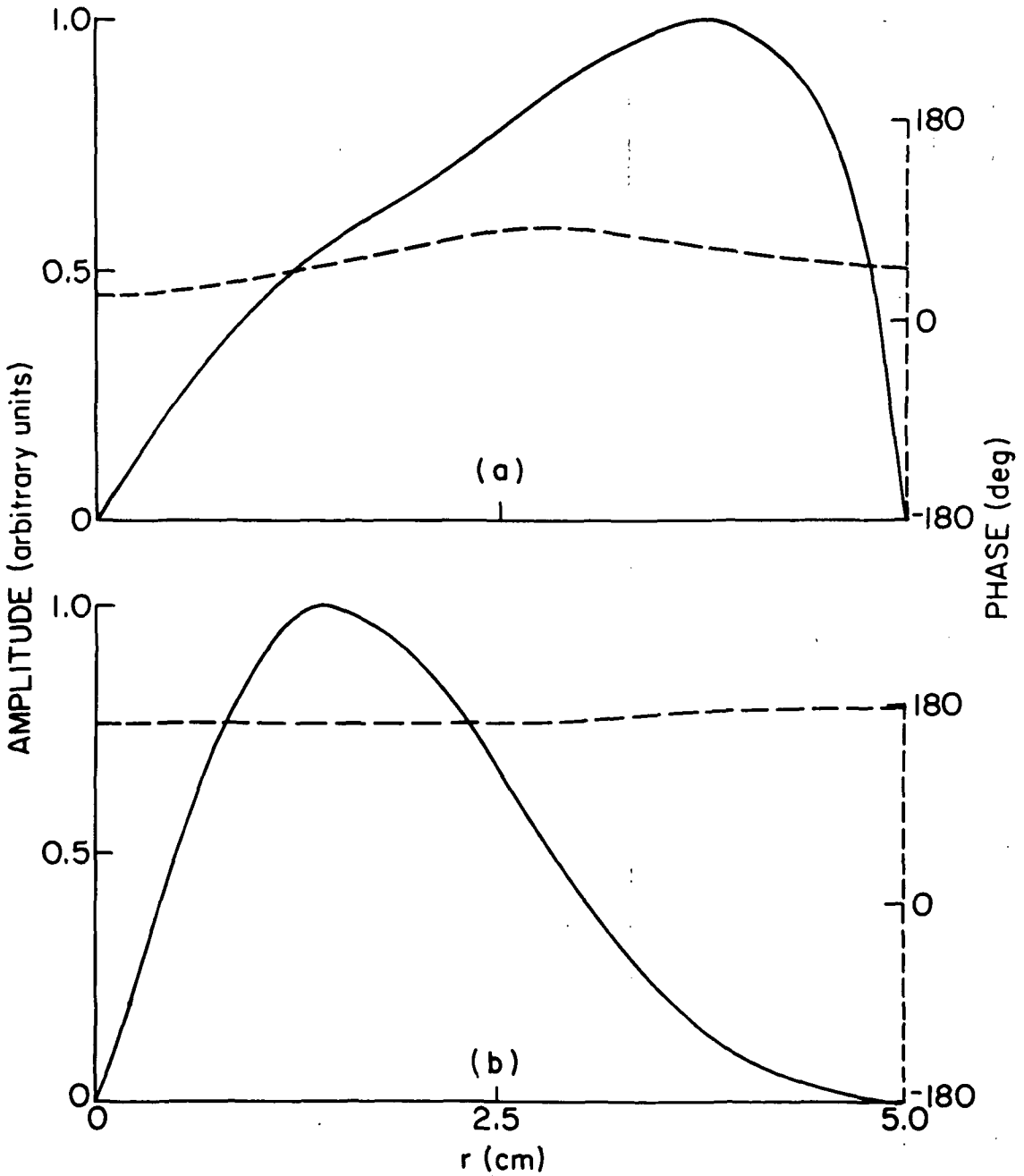

Fig. 3.19 Calculated eigenfunctions of (a) potential, ϕ_1, and (b) density, n_1, for the m = -1 mode. Comparison to be made with Fig. 3.15. —— amplitude; ---- phase.

experiment are in the precise values of certain quantities, particularly frequency and phase shift, rather than the qualitative behavior of the instabilities. In part, this may be due to the fact that the instabilities measured are nonlinearly saturated, while the theory considers only linear effects. In addition, a strong radial electric field (up to ~ 10 V/cm) is present in the experiment; for the parameters of the experiment, this implies that the $\underset{\sim}{E}_0 \times \underset{\sim}{B}$ velocity is of the order of the ion thermal velocity. Thus, the ions do not act strictly like a guiding-center fluid; we believe it is this effect which causes the ion temperature to appear to be as high as $\sim$ 3eV, and gives the observed finite Larmor radius stabilization. Although a more precise determination of this effect would require a kinetic theory to accurately describe the ion orbits, we believe that the experimental and theoretical agreement shown here demonstrates that fluid theory accounts for the basic features of the instability. Good agreement has also been found between observed and calculated eigenfunctions for Kelvin-Helmholtz instabilities in other experiments[38], where the fluid description of the ions is not strictly justifiable. In this connection, it may be noted that while the rotation of the column is nonuniform, especially for the $m = 1$ mode, we regard the velocity shear as modifying the simple centrifugal flute mode for uniform rotation, rather than giving rise to a Kelvin-Helmholtz type instability due to velocity shear. This is supported by our study of the effect of sharp velocity shear on the $m = 1$ mode in Section 3.3.3.

There have been other reports of low-frequency instabilities in the HCD, but the theories given to explain them have in general employed rectangular geometry, neglecting cylindrical geometry effects. These are discussed elsewhere.[67] However, it is clear from the theory of this section that cylindrical geometry effects are very important in the low-pressure HCD, due to the large $\underset{\sim}{E}_0 \times \underset{\sim}{B}$ rotation. Thus, in describing instabilities, these effects must be included.

4. WAVES PROPAGATING AT AN ANGLE TO THE MAGNETIC FIELD

The flute waves studied in Section 3 are generally most unstable due to centrifugal effects for propagation perpendicular to the magnetic field. As the waves propagate at an angle to the magnetic field, their characteristics are modified, and they can be unstable in the absence of cylindrical geometry effects. This transition region has been studied by Chen.[63]

When propagation is at an angle to the magnetic field, the nonzero axial wavenumber, k_z, allows for a phase shift between the potential and density fluctuations of the waves. This phase shift facilitates the release of potential energy associated with a density gradient perpendicular to the magnetic field. These unstable waves are usually called drift waves, and they can occur in both collisionless and collisional plasmas.[42] For these waves, the phase velocity perpendicular to both the magnetic field and the density gradient is close to the electron diamagnetic velocity, while the phase velocity along the magnetic field is between the ion and the electron thermal velocities.

In this section, we shall only consider collisional drift waves, also known as resistive drift waves. They were first studied by Moiseev and Sagdeev[39] in 1963, and by Chen[40,41] in 1964-65. Since these early papers, a number of theories have appeared which include various effects neglected previously, in order to obtain better correlation with experimental observation of these instabilities, most notably in Q-machines. These effects include ion collisional viscosity, first order axial motion of the ions, electron heat flow, and zero order axial drift (current) of the electrons. In Section 4.1, we derive the complete dispersion relation, including all of these effects, and compare it with the theories to date. In doing so, we use rectangular geometry, and assume weak gradients. This allows us to Fourier transform in space, which leads to an algebraic dispersion relation.

In Sections 4.2 and 4.3, we solve this dispersion relation for parameters appropriate to a Q-machine experiment, using various common approximations, and show what effects they have on the solutions. We pay particular attention to the manner in which we interpret the solutions

for axially bounded systems, as prescribed in Section 2. Section 4.3 also contains a discussion of the entropy wave,[45] which can be unstable for certain parameter ranges. In Section 4.4, we make direct comparison with some measurements of drift waves from a Q-machine experiment,[47] to illustrate the practical importance of both the common approximations to the dispersion relation, and the interpretation of the solutions.

4.1 Basic Theory

4.1.1 Steady State Plasma

The model we use in this section is a fully ionized plasma in rectangular geometry, with a uniform magnetic field in the z-direction, and a number density gradient in the x-direction. The model is shown in Fig. 4.1. The plasma is uniform in the y- and z-directions, and the ions are singly ionized. There may be a uniform DC electric field in the x-direction and/or z-direction. For reference, the z-direction will be known as the axial or parallel direction. The electrons and ions have a common uniform temperature, T_0, as is approximately true, for example, in Q-machines and also in the nighttime ionosphere.

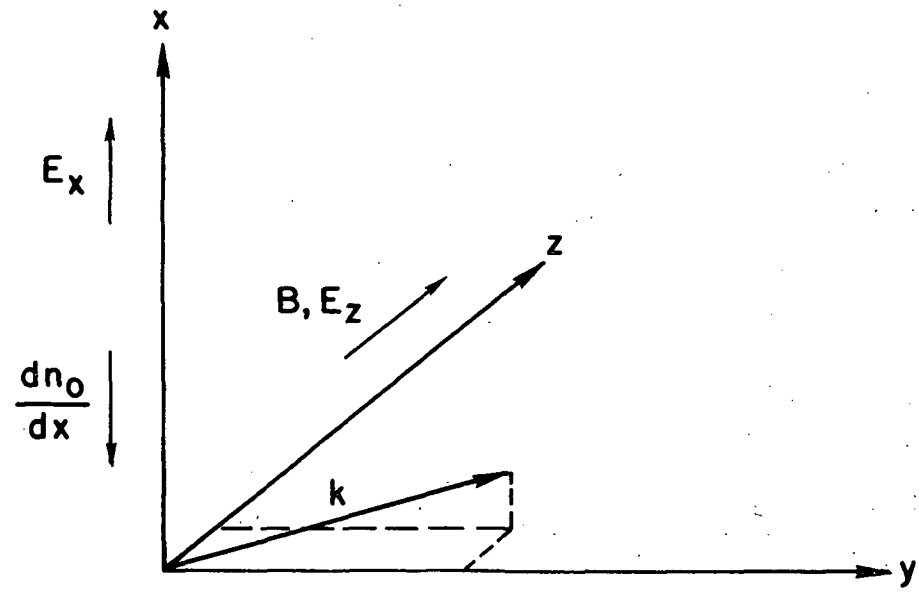

Fig. 4.1 Model of the plasma in rectangular geometry, showing the DC quantities and the direction of wave propagation.

We use the two-species moment equations given by Braginskii.[58] These will be very similar to those used in Section 3, except that we will include the effect of ion-ion collisions in the ion viscosity tensor, and allow for particle motion along the magnetic field. The particle localization necessary for a fluid approach is again caused by the magnetic field for motion across the magnetic field, and by particle Coulomb collisions for motion along the magnetic field. For the ions, we make the isothermal assumption; as has been shown by Tsai et al.,[45] inclusion of an ion energy equation has very little effect on the drift waves. The basic equations for the ions are consequently the continuity equation,

$$\frac{\partial n}{\partial t} + \nabla \cdot (n \underset{\sim}{v}_i) = 0 \quad , \tag{4.1}$$

the perpendicular momentum transfer equation,

$$nm_i \frac{d}{dt} \underset{\sim}{v}_{i\perp} = - T_i \nabla_\perp n - (\nabla \cdot \overleftrightarrow{\pi}_i)_\perp + en(\underset{\sim}{E}_\perp + \underset{\sim}{v}_{i\perp} \times \underset{\sim}{B}) \quad , \tag{4.2}$$

and the parallel momentum transfer equation,

$$nm_i \frac{d}{dt} v_{iz} = - T_i \frac{\partial n}{\partial z} - (\nabla \cdot \overleftrightarrow{\pi}_i)_z + enE_z + C_r m_e n \nu_{ei} u_z + C_t n \frac{\partial T_e}{\partial z} \quad . \tag{4.3}$$

Here $u_z = v_{ez} - v_{iz}$, $C_r = 0.51$, and ν_{ei} is the electron-ion collision frequency for momentum transfer, which accounts for the parallel resistivity. The last term in Eq. (4.3) is the thermal force term with $C_t = 0.71$. The other symbols are analogous to those defined in Section 3, except that $\overleftrightarrow{\pi}_i$ now includes ion-ion collisions. The explicit form of the viscosity tensor is now quite lengthy and is given in Appendix D, where it is assumed that $\omega_{ci}^2 \gg \nu_{ii}^2$, with ν_{ii} being the ion-ion collision frequency. Also in Appendix D are the definitions for ν_{ei} and ν_{ii}.

For the zero order ion velocity, we solve Eq. (4.2) with the assumption that $\chi = (\partial n_0/\partial x)/n_0$ is a constant, which leads to

$$\underset{\sim}{v}_{i\perp 0} = - (v_D - v_{E\Theta}) \underset{\sim}{\hat{i}}_y \quad . \tag{4.4}$$

Here $v_D[= - T_0\chi/eB]$ is the diamagnetic drift speed (note that $\chi < 0$ if the density decreases with x) and $v_{E0}[= - E_{x0}/B]$ is the $\underset{\sim}{E}_0 \times \underset{\sim}{B}$ drift speed. In this zero order solution, the effect of viscosity is neglected as being small; no inertia term arises since rectangular geometry is used. The appropriateness of taking χ constant and also neglecting possible cylindrical geometry effects for interpreting experimental results is discussed in Section 4.1.3. In any event, unlike the flute waves studied in Section 3, drift waves do not depend on zero order ion inertia for instability; the charge separation needed for instability is provided by electron resistivity along the magnetic field lines.[40] Finally, zero order axial velocities can arise due to the electric field E_{z0}. However, due to much larger inertia of the ions, their DC drift is much smaller than that of the electrons, so we may take $v_{iz0} = 0$.

We do not make the isothermal assumption for the electrons, since axial heat flow may be important. There are then three basic equations for the electrons: continuity, momentum transfer, and heat transfer. The continuity equation is

$$\frac{\partial n}{\partial t} + \nabla \cdot (n\underset{\sim}{v}_e) = 0 \ . \tag{4.5}$$

Neglecting inertia and resistivity terms compared to the $\underset{\sim}{v}_{e\perp} \times \underset{\sim}{B}$ term, the perpendicular momentum transfer equation is

$$0 = - \nabla_\perp (nT_e) - en(\underset{\sim}{E}_\perp + \underset{\sim}{v}_{e\perp} \times \underset{\sim}{B}) \ . \tag{4.6}$$

Including resistivity, the parallel momentum transfer equation is

$$0 = - \frac{\partial}{\partial z} (nT_e) - enE_z - C_r m_e n \nu_{ei} u_z - C_t n \frac{\partial}{\partial z} T_e \ . \tag{4.7}$$

Finally, the heat transfer equation is

$$\frac{3}{2} n \frac{dT_e}{dt} - T_e \frac{dn}{dt} - \frac{5}{2} \nabla_\perp \cdot \frac{nT_e}{eB} (\hat{\underset{\sim}{i}}_z \times \nabla_\perp T_e) - \frac{\partial}{\partial z} \left(\frac{C_e \chi \, nT_e}{m_e \nu_{ei}} \frac{\partial T_e}{\partial z} - C_t n T_e u_z \right) = m_e C_r \nu_{ei} n u_z^2 + C_t n u_z \frac{\partial T_e}{\partial z} \ , \tag{4.8}$$

where $C_{e\chi} = 3.2$ is the electron thermal conductivity coefficient.

To find the zero order electron motion, we solve Eqs. (4.6) and (4.7). Equation (4.6) yields

$$\underset{\sim}{v}_{e\perp 0} = (v_D + v_{E0})\, \hat{\underset{\sim}{i}}_y \quad , \tag{4.9}$$

where v_D and v_{E0} are defined in Eq. (4.4). Since we have taken $v_{iz0} = 0$, Eq. (4.7) can be used to obtain

$$v_{ez0} = - \frac{e\, E_{z0}}{m_e C_r \nu_{ei}} \quad . \tag{4.10}$$

We thus see that the zero order motions of the ions and electrons are closely analogous to those found in Section 3 [Eqs. (3.4) and (3.14)], i.e., there is a diamagnetic drift term and an $\underset{\sim}{E}_0 \times \underset{\sim}{B}$ drift term. However, we now also allow for motion along the magnetic field. As we shall see from the perturbed equations, it is the first order axial motion of the electrons which can lead to instability, while the zero order axial motion (or current) may aid or oppose this instability.

4.1.2 Perturbed Plasma

Following the procedure in Section 3, we perturb the equations describing the plasma configuration about the zero order state found in the previous subsection. The variables n, $\underset{\sim}{E}$, $\underset{\sim}{v}_i$, $\underset{\sim}{v}_e$, and T_e are assumed to have the general form

$$n(x,y,z) = n_0(x) + n_1 \exp i(\omega t - k_x x - k_y y - k_z z) \quad , \tag{4.11}$$

where, of all the zero order variables, only n_0 varies with x. The first order variation implies that the equations have been Laplace transformed in time and Fourier transformed in space. For this spatial variation to be accurate, k_x must be assumed large compared to χ, the inverse of the density gradient scale length. This is associated with the local approximation, which is discussed in Section 4.1.3. Furthermore, we neglect all odd powers of k_x in the dispersion relation. This is to simulate normal mode type behavior in the x-direction (or radial

direction in cylindrical geometry).[45,59] Finally, the waves are assumed to propagate at large angles to the magnetic field, such that $k_\perp \gg k_z$, where $k_\perp^2 = k_x^2 + k_y^2$. The remaining assumptions are the same as for the flute waves in Section 3, i.e., the waves are low frequency ($\omega \ll \omega_{ci}$), quasistatic ($\underset{\sim}{E}_1 = -\nabla\phi_1$), and quasineutral ($n_{el} = n_{i1}$).

First, we perturb the ion equations [Eqs. (4.1) - (4.3)]. To find the perpendicular ion velocity, we evaluate the ion viscosity term using Appendix D, keeping only the significant terms subject to the assumptions mentioned above. This gives

$$-\frac{1}{n_0 m_i}(\nabla\cdot\overleftrightarrow{\pi}_i)_{\perp 1} = \left(\frac{i\omega_D}{2} - C_i b\nu_{ii}\right)\underset{\sim}{v}_{i\perp 1} + \frac{b\omega_{ci}}{2}\,\hat{\underset{\sim}{i}}_z \times \underset{\sim}{v}_{i\perp 1} \quad , \tag{4.12}$$

where $C_i = 3/10$, $b = k_\perp^2\rho_i^2$, and $\omega_D = k_y v_D$ is the diamagnetic frequency. Using Eq. (4.12) in Eq. (4.2) then yields

$$\underset{\sim}{v}_{i\perp 1} = \frac{1}{1-b}\left\{\frac{T_0}{m_i\omega_{ci}}\left[-i\,\hat{\underset{\sim}{i}}_z \times \underset{\sim}{k}_\perp(1-\frac{b}{2}) - \frac{\underset{\sim}{k}_\perp}{\omega_{ci}}(\omega_1 + \frac{\omega_D}{2} - iC_i b\nu_{ii})\right]\right.$$
$$\left.\left(\frac{n_1}{n_0} + \frac{e\phi_1}{T_0}\right) + v_D\left[(1-\frac{b}{2})\hat{\underset{\sim}{i}}_y - \frac{i}{\omega_{ci}}(\omega_1 + \frac{\omega_D}{2} - iC_i b\nu_{ii})\hat{\underset{\sim}{i}}_x\right]\frac{n_1}{n_0}\right\}, \tag{4.13}$$

where $\omega_1 = \omega - k_y v_{E0}$ in analogy with the ω_1 used in Section 3. Unlike in the iterative method of solution used to find the ion velocity in Section 3, we do not assume the inertia and viscosity terms are small in deriving Eq. (4.13). If the iterative approach were used, we would find an ion velocity as in Eq. (4.13), but with the term $1/(1-b)$ expanded as $(1+b)$ and all b^2 terms neglected. This expansion is usually valid since $b \ll 1$ for fluid theory to be strictly justifiable. Watanabe and Hartman[70] have noted that there are two slightly different basic dispersion relations in the literature which may be related by expanding $1/(1-b)$ terms as they appear in the final ion equation relating only n_1 and ϕ_1. It is just the two methods of solving Eq. (4.13) for $\underset{\sim}{v}_{i\perp 1}$ which leads to this difference. Using Eq. (4.13) leads to the dispersion relations derived by Watanabe and Hartman,[70] and by

Rowberg and Wong,[47] while the iterative method of solution leads to the dispersion relations of Hendel et al.,[43] and Tsai et al.[45] In practice there is little difference in these, except perhaps in the region where b is not very small, and the fluid description is less reliable.

To find the ion parallel velocity, we add Eqs. (4.3) and (4.7), and use the relation

$$-\frac{1}{n_0 m_i}\left(\nabla \cdot \overleftrightarrow{\pi}_i\right)_z = (i\omega_D - 4C_i b\nu_{ii})v_{izl} \tag{4.14}$$

obtained from Appendix D. This yields

$$v_{izl} = \frac{T_0 k_z}{m_i}\left[\frac{2n_1/n_0 + T_{el}/T_0}{\omega_1 - i\,4C_i b\nu_{ii}}\right]. \tag{4.15}$$

We can then eliminate the velocity from the first order ion continuity equation [Eq. (4.1)] to give

$$\alpha_{11}\frac{n_1}{n_0} + \alpha_{12}\frac{e\phi_1}{T_0} + \alpha_{13}\frac{T_{el}}{T_0} = 0 \quad . \tag{4.16}$$

The α's which relate the first order variables in this equation are

$$\alpha_{11} = -\omega_1 + \frac{2T_0 k_z^2}{m_i}\,\frac{(1-b)}{(\omega_1 - i\,4C_i b\nu_{ii})} + iC_i b^2\nu_{ii} \quad ,$$

$$\alpha_{12} = -b\omega_1 + \omega_D(1-b) + iC_i b^2\nu_{ii} \quad , \tag{4.17}$$

$$\alpha_{13} = \frac{2T_0 k_z^2}{m_i}\,\frac{(1-b)}{(\omega_1 - i\,4C_i b\nu_{ii})} \quad .$$

The reason that the electron term T_{el} appears in the ion continuity equation is because the ions and electrons are coupled together by electron-ion collisions.

We now turn to consideration of the electron equations. It is straightforward to solve Eqs. (4.6) and (4.7) for the first order electron velocities, resulting in

$$\underset{\sim}{v}_{e\perp 1} = \frac{iT_0 \hat{\underset{\sim}{i}}_z \times \underset{\sim}{k}_\perp}{m_i \omega_{ci}} \left(\frac{n_1}{n_0} - \frac{e\phi_1}{T_0} + \frac{T_{e1}}{T_0} \right)$$

$$+ v_D \hat{\underset{\sim}{i}}_y \left(- \frac{n_1}{n_0} + \frac{T_{e1}}{T_0} \right) , \qquad (4.18)$$

and

$$v_{ez1} = \frac{iT_0 k_z}{m_e C_r \nu_{ei}} \left(\frac{n_1}{n_0} - \frac{e\phi_1}{T_0} + (C_t+1) \frac{T_{e1}}{T_0} \right)$$

$$+ v_{ez0} \left(- \frac{n_1}{n_0} + \frac{3}{2} \frac{T_{e1}}{T_0} \right) + v_{iz1} \quad . \qquad (4.19)$$

Upon substituting these into the perturbed electron continuity equation [Eq. (4.5)], we obtain an additional first order equation

$$\alpha_{21} \frac{n_1}{n_0} + \alpha_{22} \frac{e\phi_1}{T_0} + \alpha_{23} \frac{T_{e1}}{T_0} = 0 \quad . \qquad (4.20)$$

The new α's in this equation are given by

$$\alpha_{21} = \omega_1 - \frac{2T_0 k_z^2}{m_i} \frac{(1-b)}{(\omega_1 - i\, 4C_i b \nu_{ii})} - \frac{iT_0 k_z^2}{m_e C_r \nu_{ei}} ,$$

$$\alpha_{22} = -\omega_D + \frac{iT_0 k_z^2}{m_e C_r \nu_{ei}} , \qquad (4.21)$$

$$\alpha_{23} = - \frac{3}{2} k_z v_{ez0} - \frac{T_0 k_z^2}{m_i} \frac{(1-b)}{(\omega_1 - i\, 4C_i b \nu_{ii})} - i(C_t+1) \frac{T_0 k_z^2}{m_e C_r \nu_{ei}} .$$

A third first order equation is obtained by substituting the electron velocities into the electron heat transfer equation [Eq. (4.8)], which gives

$$\alpha_{31} \frac{n_1}{n_0} + \alpha_{32} \frac{e\phi_1}{T_0} + \alpha_{33} \frac{T_{e1}}{T_0} = 0 . \qquad (4.22)$$

This final set of the α's can be written as

$$\alpha_{31} = \omega_1 + k_z v_{ez0} + i\, C_t \frac{T_0 k_z^2}{m_e C_r \nu_{ei}} \quad ,$$

$$\alpha_{32} = -\omega_D - 2k_z v_{ez0} - i\, C_t \frac{T_0 k_z^2}{m_e C_r \nu_{ei}} \quad , \tag{4.23}$$

$$\alpha_{33} = -\frac{3}{2}\omega_1 + \frac{7}{2}(C_t+1)k_z v_{ez0} + i[C_{e\chi} C_r + C_t(C_t+1)] \frac{T_0 k_z^2}{m_e C_r \nu_{ei}} \quad .$$

Here we have neglected the zero order joule heating due to the zero order electron current.

Equations (4.16), (4.20), and (4.22) provide the three equations for the wave variables n_1, ϕ_1, and T_{e1}. The dispersion relation is obtained by requiring that the equations give non-trivial solutions for the variables. This means that the determinant of the coefficients of the equations must be zero; that is,

$$D(\omega, \underset{\sim}{k}) = \begin{vmatrix} \alpha_{11} & \alpha_{12} & \alpha_{13} \\ \alpha_{21} & \alpha_{22} & \alpha_{23} \\ \alpha_{31} & \alpha_{32} & \alpha_{33} \end{vmatrix} = 0 \quad . \tag{4.24}$$

This dispersion relation is quartic in ω and of sixth order in k_z. A number of dispersion relations have appeared in the literature which neglect some of the effects included in Eq. (4.24). Those we shall consider include ion collisional viscosity, but neglect various combinations of the following effects:

(a) first order ion axial motion;

(b) electron heat transfer (non-isothermal theory for the electrons);

(c) zero order electron axial drift (current).

These theories are summarized in Table 4.1, which also gives the order of the dispersion relations in ω and k_z.

Table 4.1

Comparison of Various Drift Wave Dispersion Relations

Effects Neglected	Authors	Order in ω	Order in k_z
a,b,c	Hendel, Chu and Politzer;[43] Rowberg and Wong[47]	2	2 (even)
a,c	Tsai, Perkins and Stix[45]	3	4 (even)
a	Tsai, Ellis and Perkins[28]	3	4 (odd)
c	Schlitt and Hendel;[71] Watanabe and Hartman[70]	4	6 (even)
none	Present work	4	6 (odd)

In Sections 4.2 - 4.4, we shall investigate the effect of these approximations, and show how they are important for interpreting experimental results. In solving the dispersion relation, we interpret the solutions in the manner described in Section 2 for an axially bounded plasma, and contrast this to the usual interpretation of the solutions.

4.1.3 Comment on the Slab Model

Before the dispersion relation is solved, some discussion is in order as to how the results of the rectangular geometry model assumed here can be applied to geometries of experimental interest; in particular, the cylindrical geometry found in plasma sources such as the Q-machine. Drift waves, as observed in Q-machines, are found to be localized to a limited radial region where χ $[= (dn_0/dx)/n_0]$ is approximately constant.[43,69] This localization can arise due to shear in either the diamagnetic velocity or the $\underset{\sim}{E}_0 \times \underset{\sim}{B}$ velocity. Shear in the diamagnetic velocity can localize the waves to a region where χ is constant, when $|\chi|$ decreases on either side of this region.[45] Perkins and Jassby[38] have shown that localization can also occur for drift waves when there is a shear in the $\underset{\sim}{E}_0 \times \underset{\sim}{B}$ velocity for a constant χ. This type of localization is analogous to that seen in Section 3.3.2

for the $m = 2$ azimuthal mode of the flute wave. In addition, Chen[63] has found from numerical solutions in cylindrical geometry that, even in a uniformly rotating plasma column (no shear), the higher order azimuthal modes for drift waves become progressively more localized. Thus, in the theory of Section 4.1.2, we take χ to be constant, which implies n_0 varies exponentially with x. The only dependence in the dispersion relation on the number density, n_0, and thus the x-position, is then through ν_{ii} and ν_{ei}. Since ν_{ii} is stabilizing and ν_{ei} is destabilizing, these effects tend to cancel out. Because the waves are assumed to vary as $\exp(-ik_x x)$ in the x-direction, we have taken only even powers of k_x in the dispersion relation, to simulate normal mode behavior of the localized waves.

In applying the rectangular slab model to cylindrical geometry, we imagine the slab of thickness Δr being bent into a cylindrical form as shown in Fig. 4.2. The x-direction then corresponds to the radial direction, and the y-direction corresponds to the azimuthal direction. The waves localized to this slab give a good representation of waves localized radially in the column, provided $\Delta r/r \ll 1$, as shown in Fig. 4.2. This latter restriction is one condition needed for cylindrical effects to be negligible. In addition, it is assumed that the radial electric field is not too large, so that centrifugal force effects may be neglected.

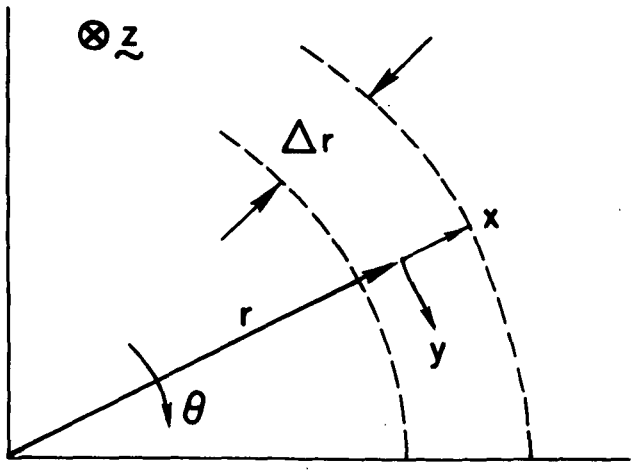

Fig. 4.2 Rectangular slab model with coordinates (x,y,z) applied to cylindrical geometry with coordinates (r,θ,z).

It should be mentioned that the rectangular geometry model may be applied directly to the ionosphere, which has the ingredients for drift waves, i.e., a density gradient, a magnetic field, and finite resistivity. We shall not pursue this study, but the general characteristics found for the drift waves may be applicable to the ionosphere.[72]

4.2 Solutions to the Isothermal Dispersion Relation

4.2.1 Basic Drift Wave Characteristics

The simplest dispersion relation for the drift waves is obtained by making the isothermal assumption for the electrons, and neglecting ion axial motion. This dispersion relation is found by neglecting all the terms in the α's which have $(\omega_1 - i\,4C_i b\nu_{ii})$ in the denominator, as these arise from ion axial motion [see Eq. (4.14)]. The upper left-hand co-factor of the determinant in Eq. (4.24) is then set equal to zero, i.e.,

$$\alpha_{11}\,\alpha_{22} - \alpha_{21}\,\alpha_{12} = 0 \quad . \tag{4.25}$$

This has the effect of letting $T_{e1} = 0$, and neglecting the electron heat transfer equation [Eq. (4.19)]. The resulting dispersion relation is

$$D(w,K) \equiv w^2 + \left\{1 - i\left[\frac{(1+b)K^2}{b\,\nu_e} + C_i b\nu_i\right]\right\} w - \left\{2\,\frac{C_i b\nu_i K^2}{\nu_e} - i\left[\frac{(1-b)K^2}{b\,\nu_e} - C_i b\nu_i\right]\right\} = 0, \tag{4.26}$$

where the normalized quantities are

$$w = \frac{\omega}{\omega_D} \quad , \quad \nu_i = \frac{\nu_{ii}}{\omega_D} \quad , \quad \nu_e = \frac{C_r \nu_{ei}}{\omega_D} \quad , \quad K^2 = \frac{T_0 k_z^2}{m_e \omega_D^2} \quad . \tag{4.27}$$

At this point we have set $E_{x0} = 0$, so that $\omega_1 = \omega - k_y v_{E0} = \omega$. The reason is that a finite E_{x0} simply produces a Doppler shift in

frequency (note that ω appears in the α's always via ω_1), so this effect can easily be accounted for after the dispersion relation has been solved for $\omega(k)$. The dispersion relation is essentially that of Hendel et al.,[43] and Rowberg and Wong,[47] the difference being that we take the ion viscosity coefficient to be $C_i = 3/10$, as given by Braginskii,[58] while they take $C_i = 1/4$. Also, that of Hendel et al. differs slightly in terms involving b, as discussed in the derivation of $\underset{\sim}{v}_{i\perp 1}$ [Eq. (4.13)].

Solutions to this dispersion relation have been of particular interest lately in order to explain instabilities which arise in Q-machines. Correlation between theory and experiment has been made in one of three ways: comparison of the onset field and frequency for self-excited unstable modes;[43] comparison of the frequency and damping rate for externally excited modes when the system is stable;[47] comparison of the frequency and growth rate for self-excited modes when the system is unstable and feedback stabilization is switched off.[73] In all cases, it is found experimentally that the system is not as unstable as theory predicts, i.e., the damping rates are larger or the growth rates smaller than predicted. This suggests an additional damping mechanism is present. In their experiment, Rowberg and Wong[47] identify this as end-plate damping for end-plates which are ion-rich. From the discussion in Section 2, this implies that we must solve the dispersion relation for complex k_z in order to construct the normal mode solutions, since the reflection coefficient, ρ, of the end-plates has $|\rho| < 1$. This approach has not been used before.

We postpone a detailed comparison with Rowberg and Wong's[47] experiment until Section 4.4. However, in order to investigate the behavior of drift waves in a parameter range which is of experimental interest, we take parameters applicable to their experiment. In applying the theory to the cylindrical geometry of the Q-machine, k_y is real and determined experimentally by identifying it with m/a, where m is the azimuthal mode, and a is the radius at which the azimuthally travelling wave has its maximum amplitude. In this connection, note that the normalized frequency, W, used in Section 3, is thus a multiple of the normalized frequency, w, used here; the relation is $W = mw$. Furthermore,

k_x is determined from the radial wave profile (often $k_x \approx k_y$), while k_z is determined from the axial profile of the wave, a matter discussed at greater length in Section 4.4. All of the other parameters are determined with reasonable precision from the experimental conditions.

A partial mapping of K into the w-plane via Eq. (4.26) for conditions corresponding to Rowberg and Wong's $m = 2$ mode is shown in Fig. 4.3. Because $D(w,K)$ is even in K, the real K-axis folds on itself, and the two sheets are shown in a single diagram. The two solutions are shown as the drift wave branch (labeled I) in the right half plane, and the flute wave branch (labeled II) in the left half plane. This flute wave is essentially the wave studied in Section 3 for propagation perpendicular to the magnetic field ($K = 0$). It is not unstable here since we are considering rectangular geometry, which neglects the destabilizing centrifugal force effects, and it will be of no particular concern in this section. The drift wave branch, on the other hand, can be unstable, and the relevant branch point of the dispersion relation, as defined in Section 2.1.2, occurs at

$$w_s = i\, C_i b \nu_i \,, \qquad K_s = 0 \quad . \tag{4.28}$$

Since $w_{si} > 0$, the system can never be absolutely unstable. The real K-axis terminates for $K = \pm \infty$ at $w = [(1-b) + i2C_i b\nu_i]/(1+b)$, which corresponds to stability in the limit of short axial wavelength. At intermediate values of K, the real K-axis may or may not dip into the lower half plane, corresponding, respectively, to convective instability or stability, depending on the parameter values. The condition for convective instability is

$$8C_i^2 \frac{(1+b)}{(1-b)^2} b^3 \nu_i^2 < 1 \quad , \tag{4.29}$$

which, for $b \ll 1$, may be approximated by

$$b^3 \lesssim (8C_i^2 \nu_i^2)^{-1} \quad . \tag{4.30}$$

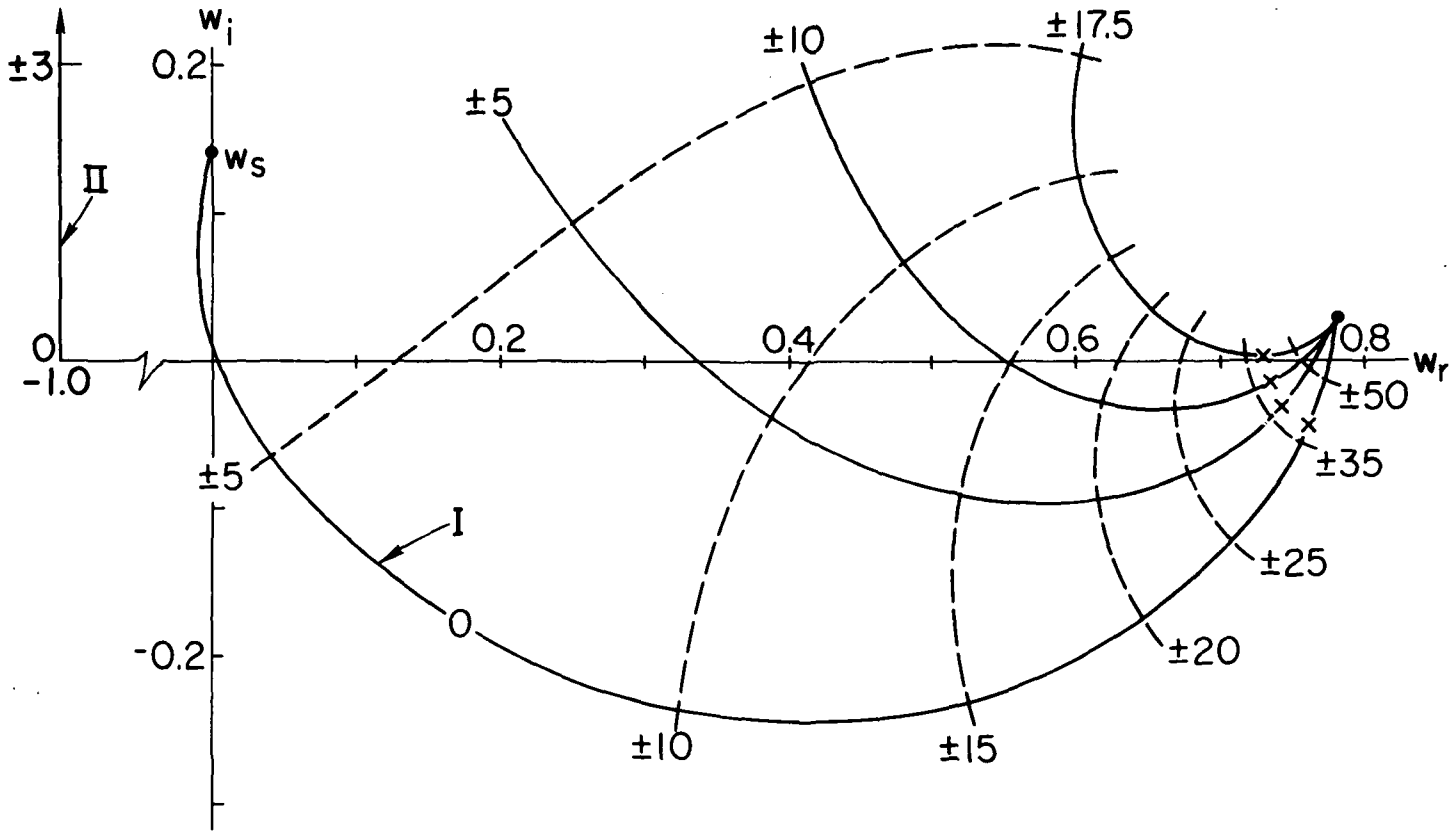

Fig. 4.3 Map of K into the w-plane via Eq. (4.26) for conditions of Rowberg and Wong's experiment: m_i = 39.1 AMU; n = 6.7 × 10^{10} cm^{-3}; T_0 = 0.19 eV; B = 1.6 kG; m = 2; $k_y = k_x$ = 1.43 cm^{-1}; χ = -0.80 cm^{-1}; ν_{ei} = 2.0 × 10^7 sec^{-1}; ν_{ii} = 5.2 × 10^4 sec^{-1}; ω_D = 1.36 × 10^4 sec^{-1}; ω_{ci} = 3.92 × 10^5 sec^{-1}; ν_e = 7.5 × 10^2; ν_i = 3.8; b = 0.124. The lowest axial mode (λ_z = 3.6L, L = 60 cm) is shown by crosses. The drift wave branch is indicated by (I) and the flute wave branch by (II). ——, K_i = constant; ---- K_r = constant.

This gives a threshold magnetic field for marginal instability, $B_c \propto \nu_i^{1/3}$.

The instability is driven by the potential energy available from the density gradient. The parallel resistivity of the electrons, as manifested by ν_e, maintains the phase difference between n_1 and ϕ_1, which is necessary for instability. Since K and ν_e always appear in the dispersion relation [Eq. (4.26)] as K^2/ν_e, the effect of varying the resistivity is seen in Fig. 4.3 by assuming K is constant and ν_e changes. Thus, the drift waves become stable as the resistivity goes to zero ($\nu_e \to 0$), the frequency going to the same limit as when $K \to \pm \infty$. In this case, the inertialess electrons may stream freely along the magnetic field lines to short out any phase difference between n_1 and ϕ_1 which might lead to instability.

For solutions with increasingly large values of K_i, corresponding to lossy end-plates ($|\rho| < 1$), the drift waves are stabilized. For reference, the value of K_r measured by Rowberg and Wong is indicated by crosses in Fig. 4.3. This demonstrates how the length of the Q-machine can restrict the normal mode frequency to be larger than the most unstable value.

It is interesting to consider the relative amplitudes and phases of the wave variables n_1/n_0 and $e\phi_1/T_0$ as K is varied. Since, for the slab model, these variables have the same ratio everywhere, we choose to normalize by n_1/n_0. Neglecting ion axial motion, we then obtain from Eqs. (4.16) and (4.17)

$$\phi_{1n} \equiv \frac{e\phi_1/T_0}{n_1/n_0} = \frac{w - i\, C_i b^2 \nu_i}{bw + (1-b) - i\, C_i b^2 \nu_i} \quad . \tag{4.31}$$

Here the w's found from solution of Eq. (4.26) must be used. In Fig. 4.4, we have plotted the phase and magnitude of this relation as a function of K_r for several values of K_i. The conditions are the same as in Fig. 4.3. When the drift wave is unstable, the phase angle is negative, corresponding to the density oscillation, n_1, leading the potential oscillation, ϕ_1. This phase angle becomes quite small ($\sim 1\text{-}2^o$) as K_r increases, but changes quite rapidly for small K_r. The phase angle is still significantly smaller than that found for the

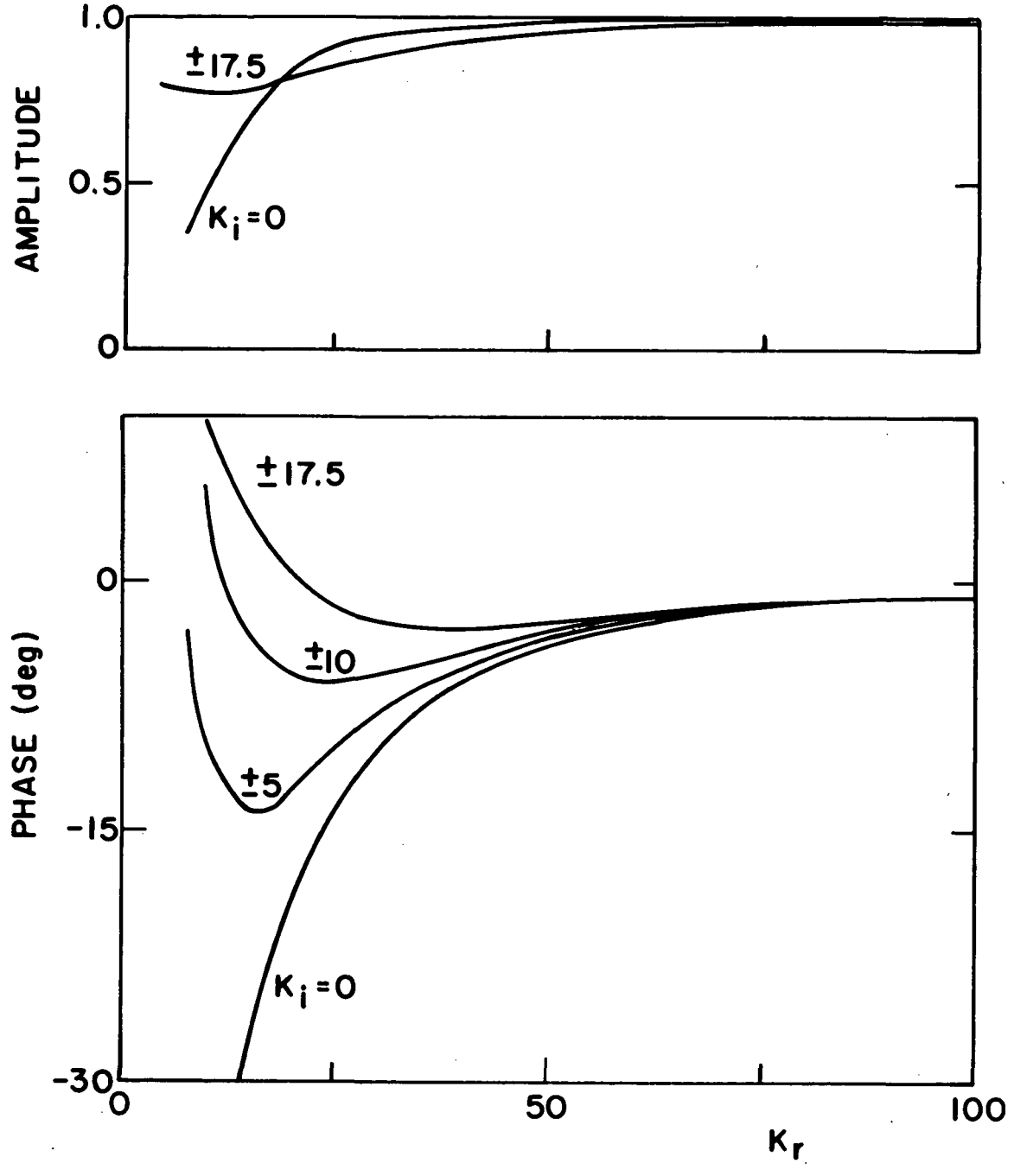

Fig. 4.4 Amplitude and phase of $\phi_{1n} = (e\phi_1/T_0)/(n_1/n_0)$ for the drift wave branch in Fig. 4.3 as K_r is varied for several K_i values.

flute wave ($\sim 180^{o}$) in Section 3. The effect of solving the dispersion relation for nonzero K_i is to decrease the phase shift and the temporal growth rate. Note that the waves are stabilized for a phase shift of about -3^{o}, while in Section 3 any phase shift between n_1 and ϕ_1 (of the proper sign) implied instability. The difference arises from the damping effect of ion collisional viscosity considered here. For the amplitudes, the normalized potential and density fluctuations are nearly equal, except for small K_r (< 20), when the potential amplitude is smaller.

4.2.2 Effect of Ion Axial Motion

To include the effect of ion axial motion in the isothermal approximation, we again use Eq. (4.25), but retain the terms of the α's with $(\omega_1 - i\, 4C_i b\nu_{ii})$ in the denominator. This gives a dispersion relation which is of third order in ω and of fourth order in k_z. It has the explicit form

$$w^3 + \beta_0 w^2 + \beta_1 w + \beta_2 = 0 \quad , \tag{4.32}$$

where the coefficients are given by

$$\beta_0 \equiv 1 - i\left[\frac{(1+b)K^2}{b\nu_e} + 5C_i b\nu_i\right] ,$$

$$\beta_1 \equiv -\left[\left(\frac{4}{b} + 6\right)\frac{K^2 C_i b\nu_i}{\nu_e} + 2\frac{m_e}{m_i}K^2 + 4(C_i b\nu_i)^2\right] + i\left[\frac{1-b}{b}\frac{K^2}{\nu_e} - 5C_i b\nu_i\right] ,$$

$$\beta_2 \equiv \left[\frac{4C_i\nu_i(1-b)K^2}{\nu_e} - 4(C_i b\nu_i)^2\right] + i\left[\left(\frac{8C_i b\nu_i}{\nu_e} + 2\frac{m_e}{m_i}\right)C_i b\nu_i K^2 + 2\frac{m_e}{m_i}\frac{1-b}{b\nu_e}K^4\right] . \tag{4.33}$$

We have used the same normalization as in Eq. (4.27). Two of the roots in ω correspond to the drift wave and the flute wave, as they are modified by ion axial motion. The third root can be labeled an ion-acoustic wave, and arises due to the axial motion. However, it is highly damped and will be of little concern here.

The modification of the drift wave is most pronounced at shorter axial wavelengths, since the new terms in the α's appear multiplied by k_z^2 (or K^2), as seen in Eqs. (4.17) and (4.21). This is physically reasonable because, for long axial wavelengths, the inertia of the ions prevents their axial motion from being significantly influenced by the wave. This effect is illustrated in Fig. 4.5, where the drift wave branch and the ion-acoustic branch (labeled III) are mapped in the w-plane for the same parameters as in Fig. 4.3. We have only included that portion of the drift wave map which is noticeably affected by the ion axial motion. The real K-axis no longer terminates at a finite w, and the growth rates of the instability are decreased. This is due to a combination of the collisional viscosity associated with the axial motion [see Eq. (4.14)] and the fact that this motion tends to short out the axial electric field. As we shall see in Section 4.4, these effects can be very important in experiments. For large values of K ($\sim 10^3$), the drift wave branch (I) and the ion-acoustic branch (III) have solutions which are related by $w_I \approx -w_{III}^*$. The axial phase velocities of the waves then approach the ion-acoustic speed [$\sim(T_0/m_i)^{\frac{1}{2}}$]. Thus, it is clear that these branches are evolving into a pair of ion-acoustic waves as the propagation becomes more nearly parallel to the magnetic field (K large). These waves are studied in Section 5.

The phase and amplitudes of the first order potential and density are not significantly affected by including ion axial motion, and one may still refer to Fig. 4.4 for these.

4.3 Solutions to the Non-Isothermal Dispersion Relation

4.3.1 Effect of Electron Heat Transfer on Drift Waves

To include electron heat transfer in the theory, we consider the electron temperature as a wave variable, and include the heat transfer equation [Eq. (4.8)]. The resulting dispersion relation is Eq. (4.24), which is now of fourth order in ω and of sixth order in k_z. At this point, we choose to leave the dispersion relation in determinant form, since it will be solved numerically. The four roots are found by constructing a fourth order equation appropriate to a given

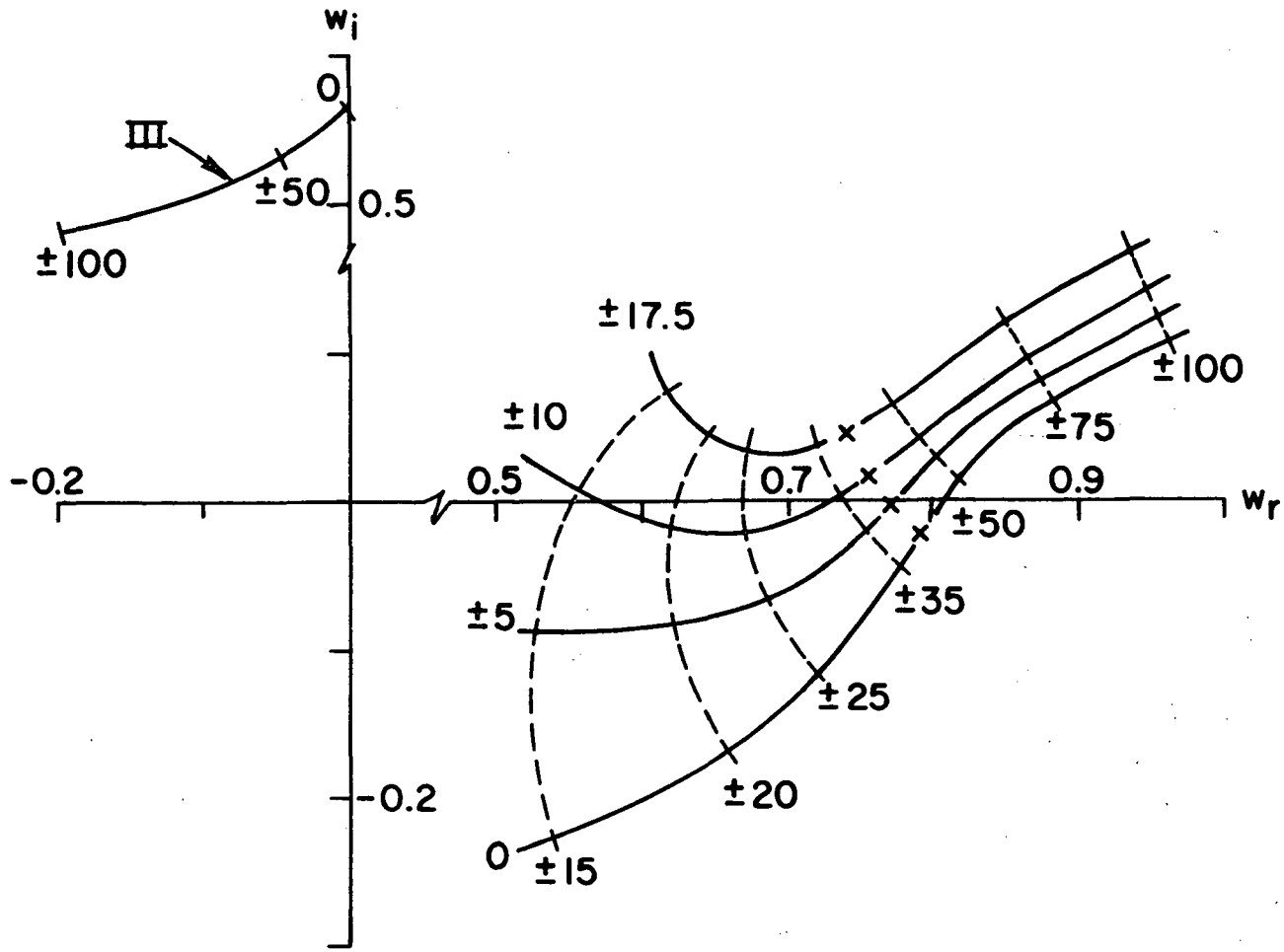

Fig. 4.5 Partial map of K into the w-plane via Eq. (4.32) which includes ion axial motion. Branch III is the ion-acoustic wave, and parameters are as in Fig. 4.3. ——— , K_i = constant; ---- , K_r = constant.

set of parameters by the Lagrangian interpolation method,[74] and then solving this equation. The interpolation method requires the determinant to be evaluated at only five points, i.e., five values of w, for each solution.

The solutions to the dispersion relation are shown in the w-plane in Fig. 4.6, with parameters as in Figs. 4.3 and 4.5. We have omitted the ion-acoustic and flute wave branches because they are damped ($w_i > 0$), but we show the new fourth root (labeled IV) because it may be unstable for very long wavelengths. This wave arises from inclusion of electron heat transfer, and has been called the entropy wave by Tsai et al.[46] It will be considered in more detail in Section 4.3.2. By comparing Figs. 4.3 and 4.5 with Fig. 4.6, we see that the growth of the drift wave may be increased or decreased by electron heat transfer, depending on the value of K. For example, with $K_i = 0$ the growth rate is larger for $K_r > 22$ and smaller otherwise. However, as K_i is increased, the growth rates decrease rapidly, and the non-isothermal theory gives larger damping rates for all K_r shown. Also, the real frequency for the non-isothermal theory is significantly lower. However, the frequency is not a good datum for distinguishing the presence of non-isothermal effects in experiments, because it must be corrected for the $\underset{\sim}{E}_0 \times \underset{\sim}{B}$ Doppler shift from measurements of $\underset{\sim}{E}_0$, which are not very precise.

The relative amplitudes and phases of the first order variables now require two sets of plots, since there are three variables. Again we normalize to n_1/n_0, and plot $\phi_{1n} \equiv (e\phi_1/T_0)/(n_1/n_0)$ and $T_{e1n} \equiv (T_{e1}/T_0)/(n_1/n_0)$ in Fig. 4.7. These relations can be found in terms of α's from Eqs. (4.16) and (4.20), and are analogous to Eq. (4.31) for the isothermal theory. In Fig. 4.7(a), we see that the phase shift between ϕ_1 and n_1 has increased over the isothermal theory (Fig. 4.4) for $K_r \gtrsim 30$, and may be more than twice as large. The shapes of the curves are very similar, however. The amplitude of ϕ_1 has decreased, the effect being most noticeable for $K_r < 40$.

The phase shift for the temperature fluctuations, shown in Fig. 4.7(b), is quite large, while the amplitude is small. In spite of this small amplitude, a knowledge of the phase and amplitude of the

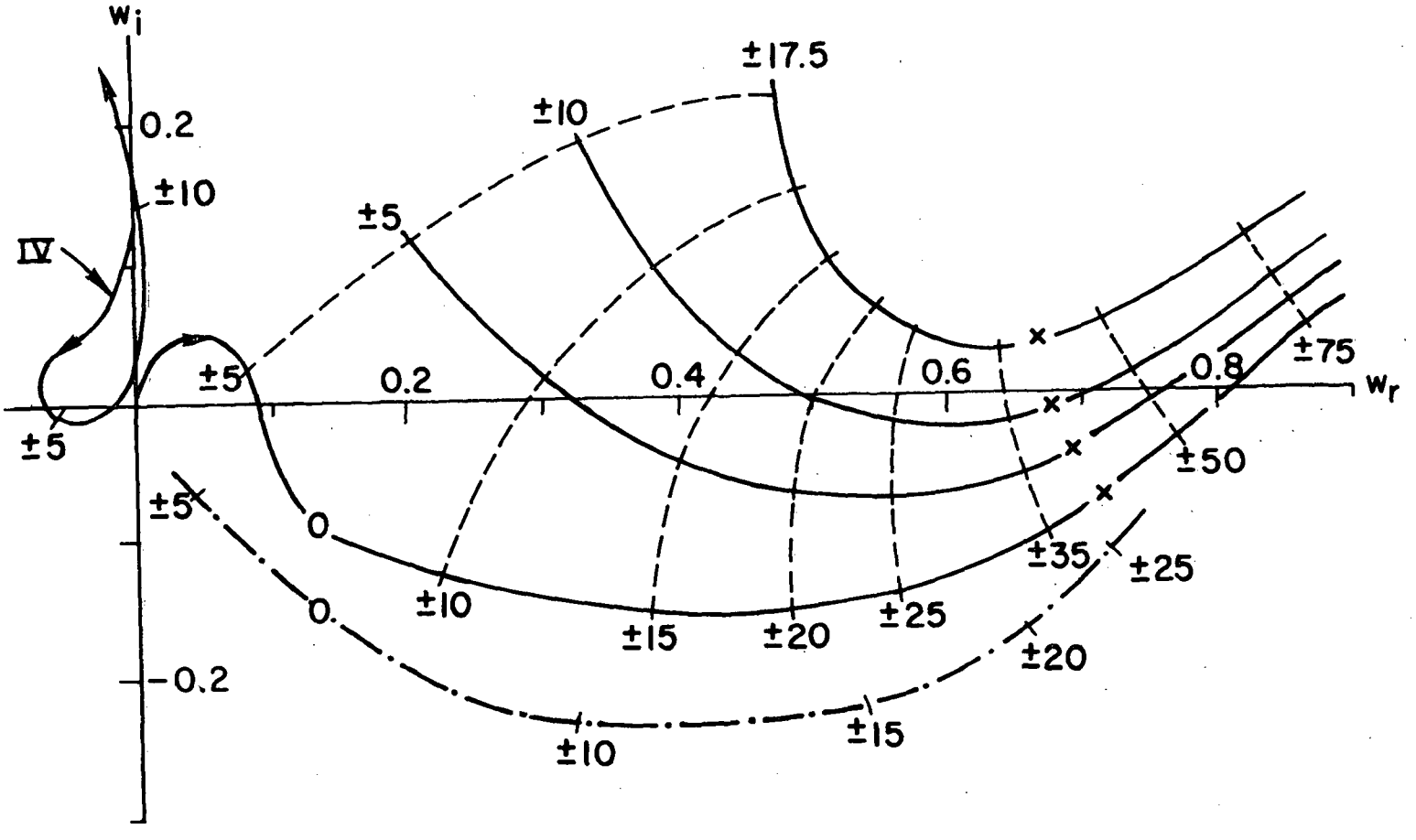

Fig. 4.6 Partial map of K into the w-plane via Eq. (4.24) for the non-isothermal theory. Branch IV is the entropy wave. Parameters as in Fig. 4.3. ——— , K_i = constant; ---- , K_r = constant; -·-·-·-· , isothermal theory as in Fig. 4.5.

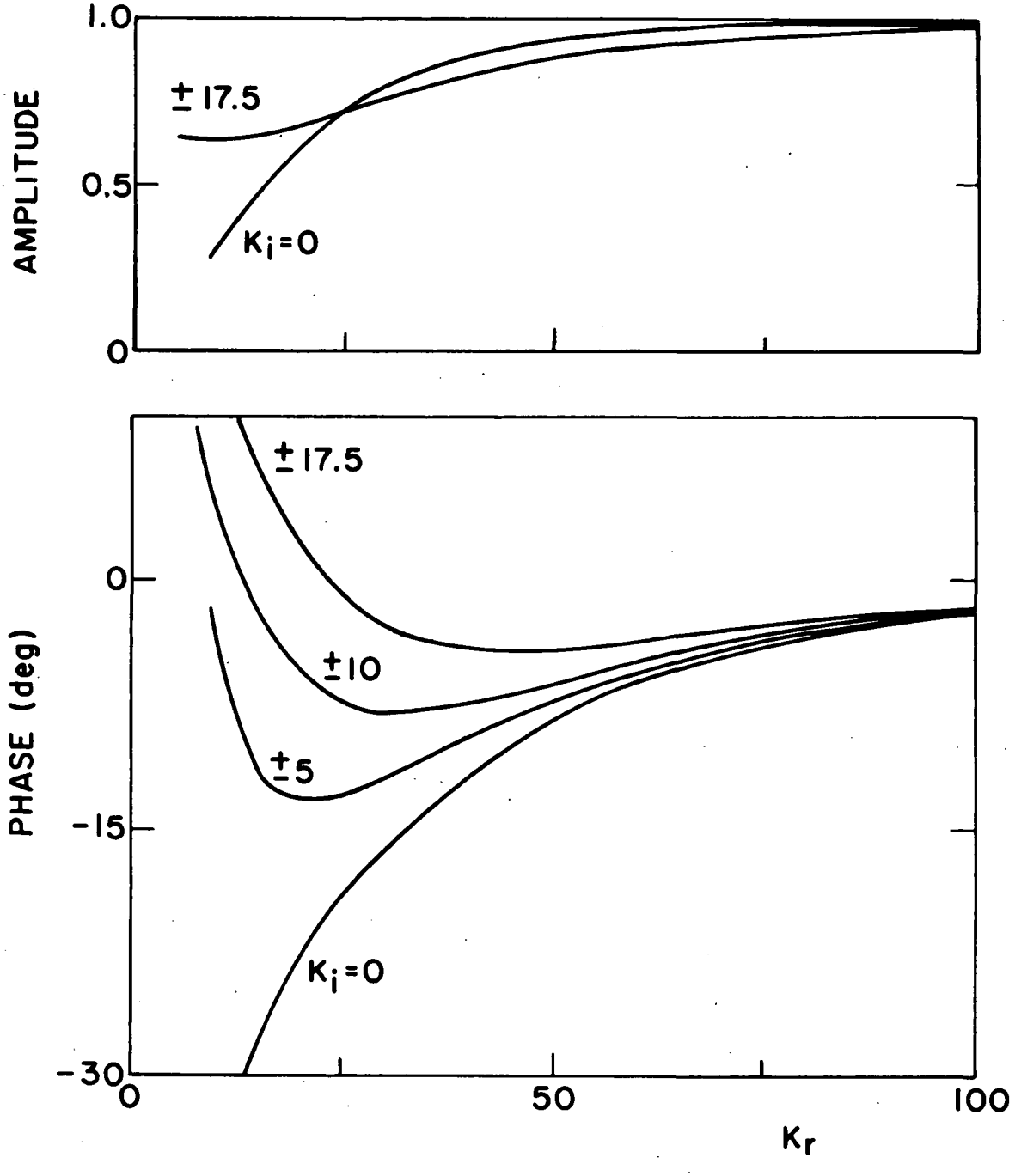

Fig. 4.7(a) Amplitude and phase of ϕ_{1n} for the drift wave branch in Fig. 4.6.

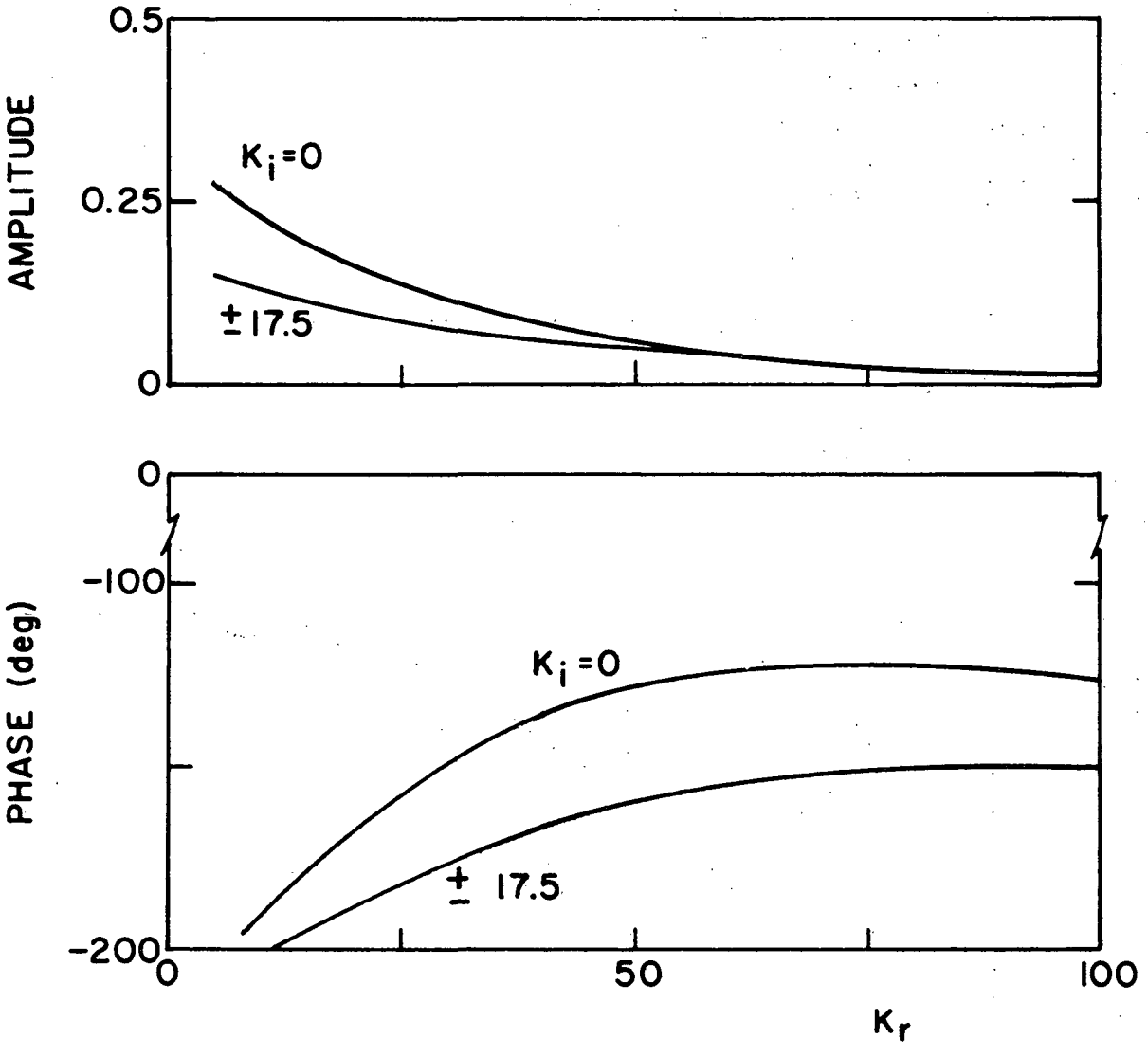

Fig. 4.7(b) Amplitude and phase of T_{eln} for the drift wave branch in Fig. 4.6.

temperature fluctuations is important in interpreting Langmuir probe measurements of the phase between n_1 and ϕ_1, as pointed out recently by Motley and Ellis.[75]

It should be noted that the temperature fluctuations do not appear to tend to zero as $K \to 0$, contrary to the proof in Appendix C that there are no temperature fluctuations for propagation perpendicular to the magnetic field if $\nabla_\perp T_{e0} = 0$. This is due to the fact that, as $K \to 0$, the drift wave branch approaches $w = 0$ (or $\omega_1 = 0$). This demands a special solution to Eqs. (4.16), (4.20), and (4.22), with $n_1 = \phi_1 = 0$, which leaves T_{e1} undetermined. The difficulty is alleviated when one considers cylindrical geometry, as in Appendix C, since the analogous special solution, $\omega - m\omega_E = 0$, does not arise in general. Even for rectangular geometry, inclusion of any small physical effect which would move the solution slightly off $w = 0$ would give $T_{e1} \to 0$ for $K \to 0$. In fact, for the entropy wave, $w \neq 0$ as $K \to 0$, so $T_{e1} \to 0$ as we shall see in the next subsection.

4.3.2 Entropy Wave

As mentioned above, the fourth root to the dispersion relation, called the entropy wave, may be unstable for very long wavelengths. For the conditions of Fig. 4.6, it becomes unstable for $5.0 \lesssim |K_r| \lesssim 6.5$, although only weakly so. It becomes stable for a small K_i value, so we will only consider the $K_i = 0$ case.

The relative amplitude and phase of the first order variables, normalized to n_1/n_0, are shown in Fig. 4.8. The potential and temperature phase shifts have opposite variations with K_r, but have approximately equal values for instability. The amplitudes are also quite different from those of the drift wave, the temperature fluctuation being much larger for the entropy wave. Note also that $T_{e1} \to 0$ as $K_r \to 0$. A similar type of entropy wave (or temperature wave) arises in the study of low-frequency instabilities in a weakly ionized gas when electron heat transfer is considered.[76] In that case, small temperature fluctuations produce large changes in the ionization rate, and the temperature waves become unstable ionization waves whose nonlinear limit is identified with the striations commonly observed in positive columns.[77]

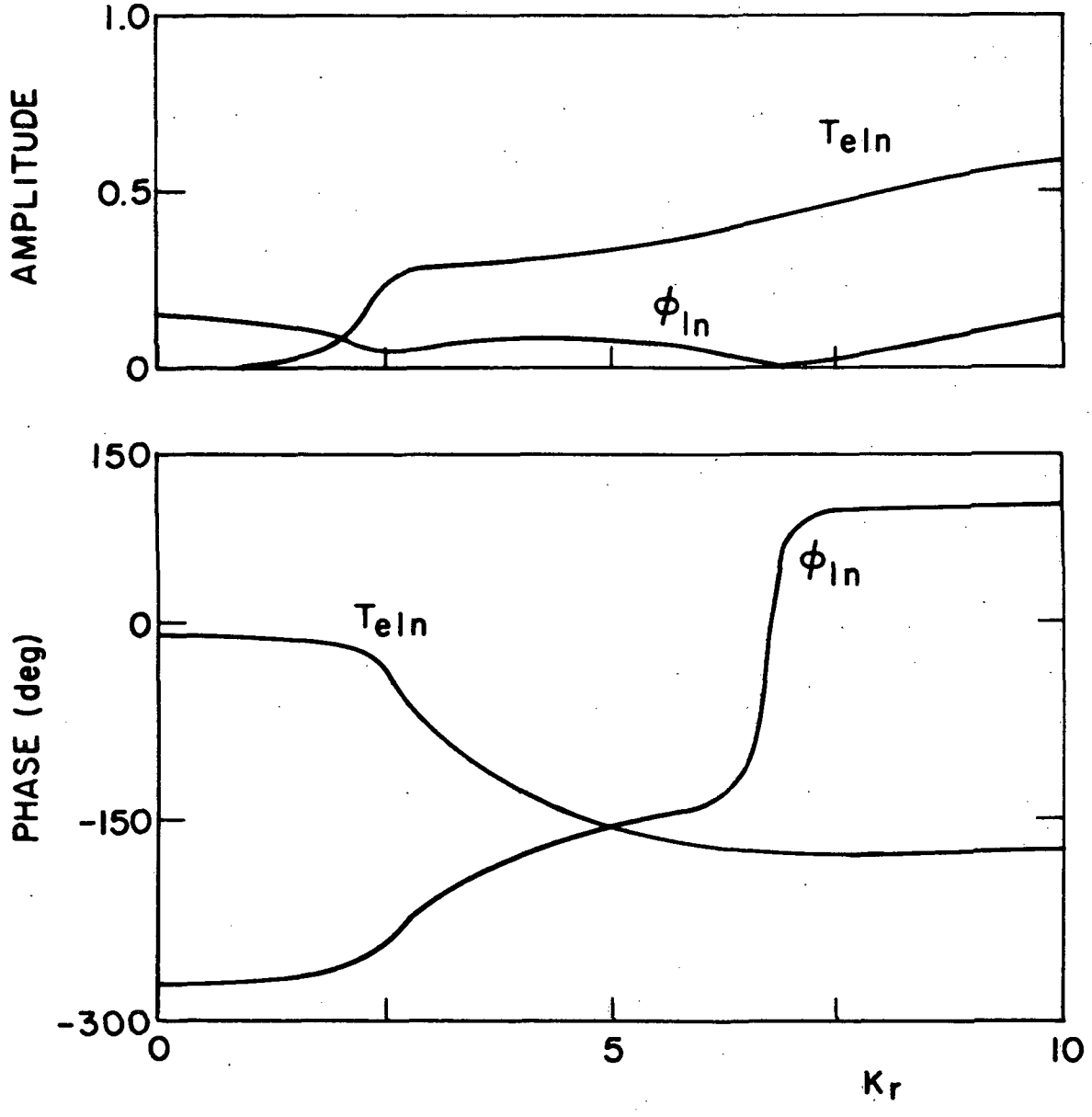

Fig. 4.8 Amplitude and phase of ϕ_{ln} and T_{eln} for the entropy wave branch in Fig. 4.6.

4.3.3 Effect of Electron Axial Drift

When there is an electron axial drift, due to an axial electric field, for example, the system is no longer symmetric, and the dispersion relation should contain odd powers of k_z (or K). The effect of this axial drift can only be determined from the non-isothermal theory, since the drift terms cancel out in the isothermal dispersion relation [see Eq. (4.26)]. Thus, we must again solve the full dispersion relation, i.e., Eq. (4.24). We illustrate the effect by solving the dispersion relation for an electron drift of $5\ C_s$, where $C_s = (T_0/m_i)^{\frac{1}{2}}$ is roughly the ion-acoustic speed. Since the dispersion relation is no longer even in K, the solutions for $\pm K$ do not coincide, and we must consider separate plots for $K \gtrless 0$. The solutions are shown in the w-plane for real K in Fig. 4.9, together with the $v_{ez0} = 0$ solutions for comparison. We see that the solutions are strongly modified by the drift, especially for small $|K|$ values. In fact, the topology has changed so that the drift wave and entropy wave branches are interconnected. For $|K| \gtrsim 10$, where the drift waves can be clearly identified, the drift is destabilizing for negatively directed waves for $K \gtrsim -22$, and stabilizing for $K \lesssim -22$. On the other hand, for the positively directed wave, the drift is stabilizing for $K \lesssim 15$, and destabilizing for $K \gtrsim 15$. Thus, for large $|K|$, the effect of the drift is destabilizing or stabilizing, according as the phase velocity is parallel or antiparallel to the electron drift. Also, the phase velocity of the wave, $(w/K)(m_i/m_e)^{\frac{1}{2}}$, is equal to the drift velocity for $K \approx 15$, and smaller than the drift velocity for $K > 15$, which is just the region that is significantly destabilized by the drift. This is reminiscent of a resonant particle type instability, where particles drifting slightly faster than the phase velocity of the wave transfer energy to the wave and cause it to grow, as in a traveling wave amplifier. However, for a collisional plasma there are no resonant particle effects, and the effect seen here arises from finite electron thermal conductivity. This mechanism will become clearer in Section 5, when we study ion-acoustic waves in the presence of an electron drift.

The amplitude and phase of ϕ_1 and T_{e1} have quite different behaviors for $K \gtrless 0$ and $K \lessgtr 0$, as shown in Fig. 4.10. For

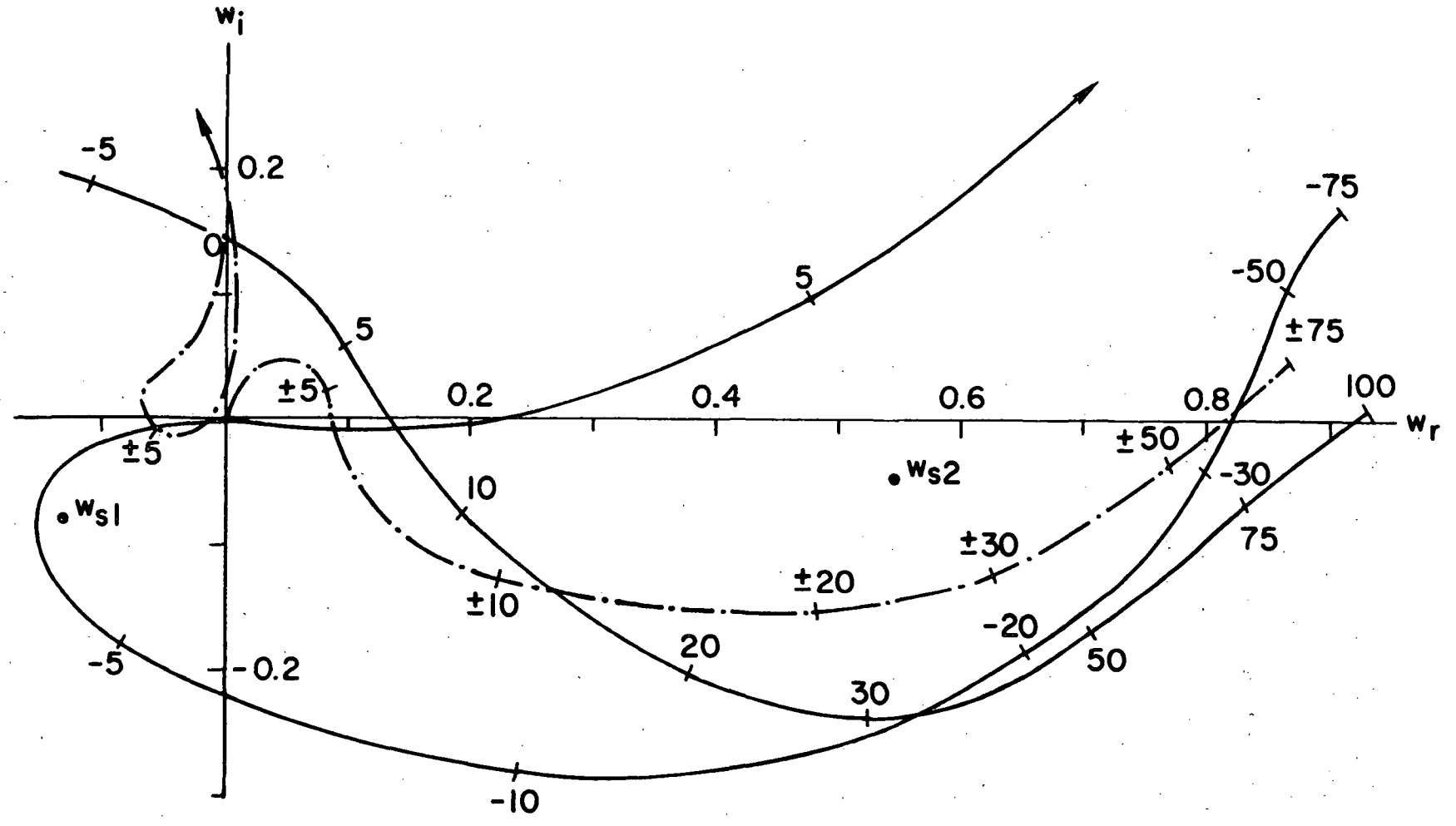

Fig. 4.9 Partial map of K into the w-plane via Eq. (4.24) with values of K_r shown on the curves ($K_i = 0$) . Parameters are as in Fig. 4.3. ——— , $v_{ez0} = 5(T_0/m_i)^{1/2}$; ---- , $v_{ez0} = 0$.

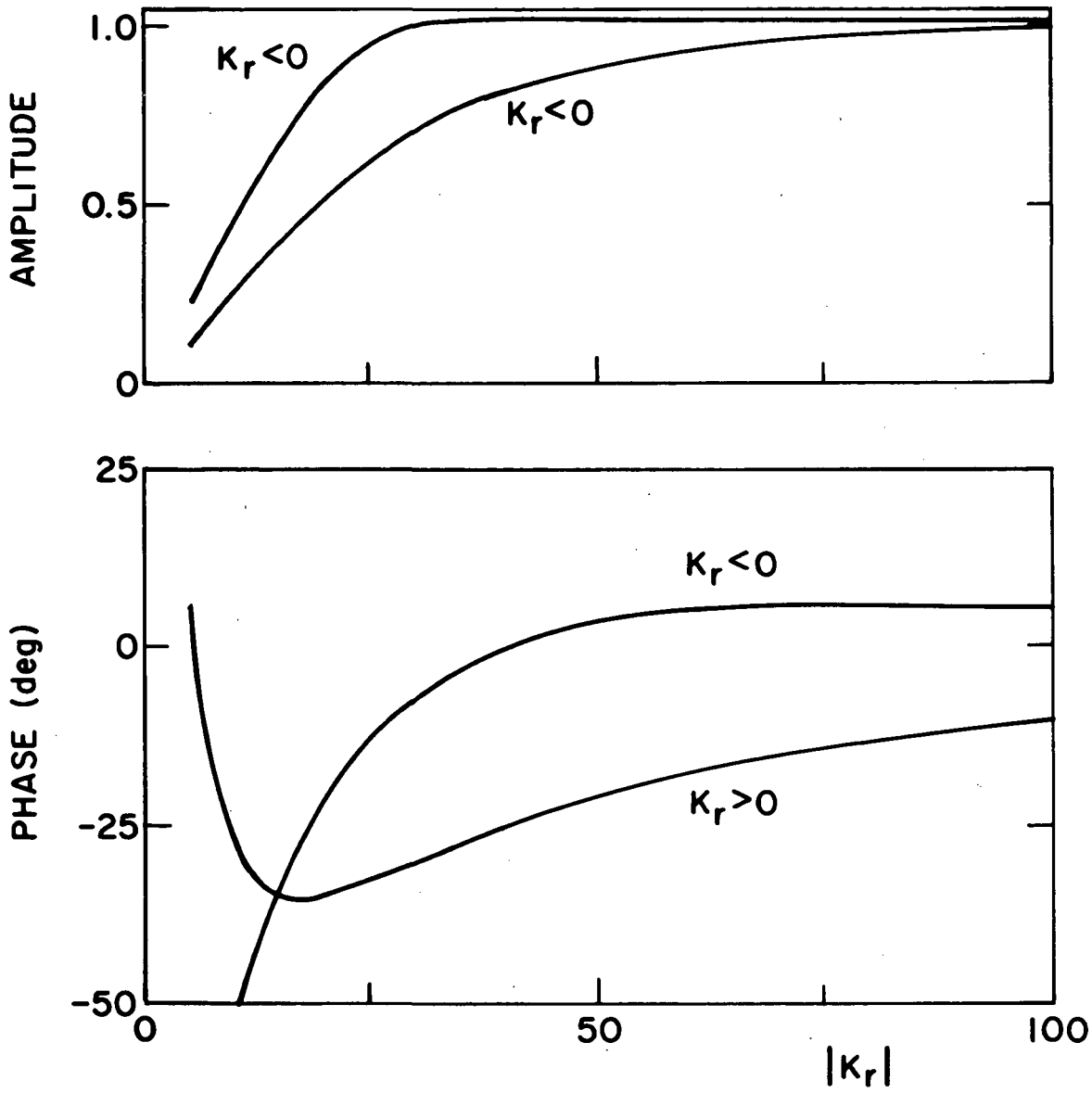

Fig. 4.10(a) Amplitude and phase of ϕ_{1n} for the drift wave branch in Fig. 4.9 with $v_{ez0} = 5(T_0/m_i)^{1/2}$

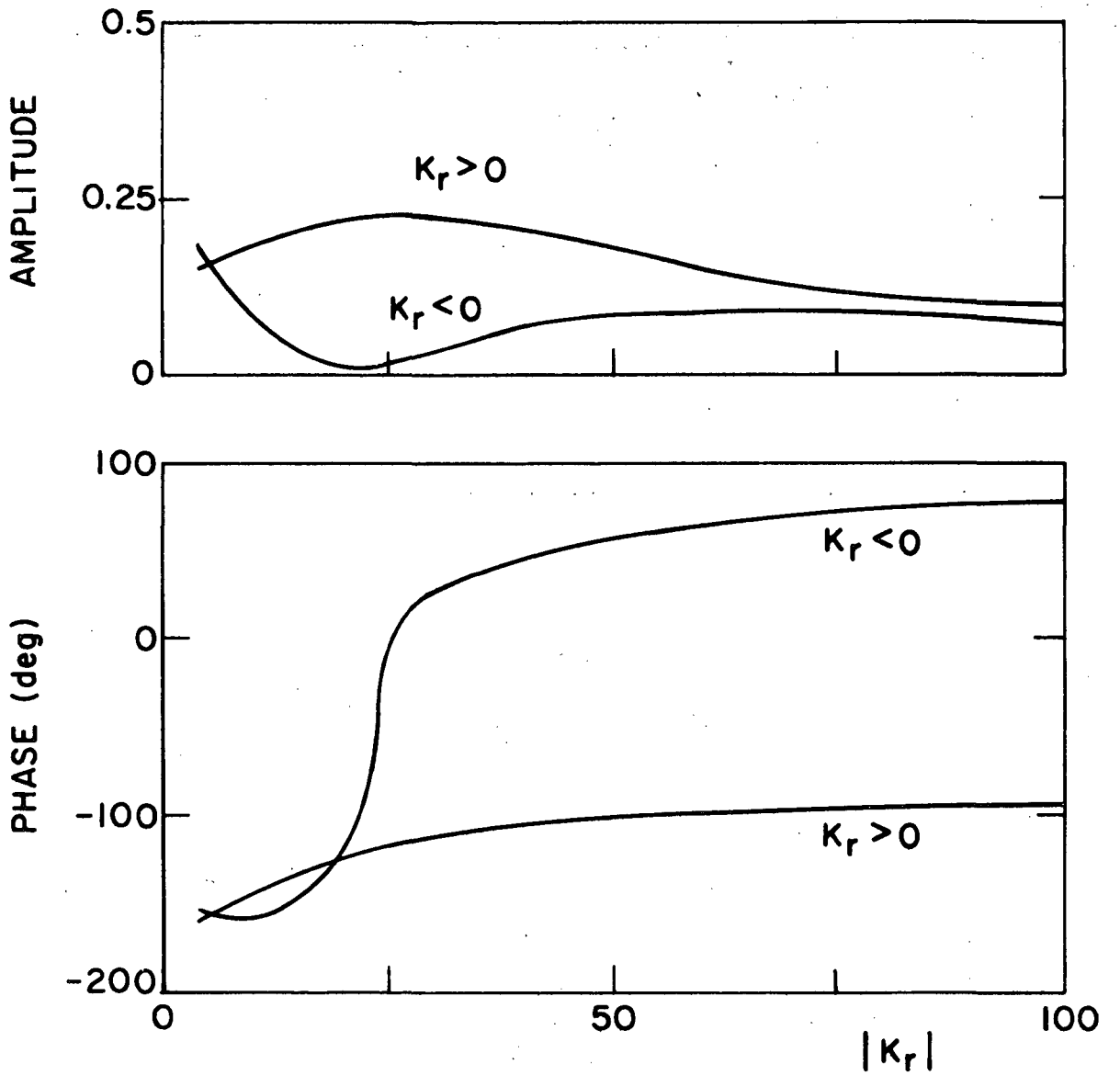

Fig. 4.10(b) Amplitude and phase of T_{eln} for the drift wave branch in Fig. 4.9 with $v_{ez0} = 5(T_0/m_i)^{1/2}$

$K > 0$, both ϕ_{1n} and T_{eln} have negative phase shifts, while for $K < 0$, the phase of each becomes positive as $|K|$ is increased. For $K > 0$, the amplitude of ϕ_{1n} is decreased, and that of T_{eln} increased, over the case when $v_{ez0} = 0$ (Fig. 4.7), so the enhanced stability is accompanied by larger temperature fluctuations. The opposite is true for $K < 0$, when ϕ_{1n} increases and T_{eln} decreases.

In addition to the solutions for real K, we find that there are now two branch points in the lower half plane when the dispersion relation is solved for complex K, one at $w_{s1} = -0.13 - i\ 0.085$, and the other at $w_{s2} = 0.54 - i\ 0.045$. Both of these are relevant branch points in the sense discussed in Section 2, so the unbounded plasma is now absolutely unstable.

To find the normal mode solutions for this asymmetric plasma, one approach is that of Tsai *et al.*,[28] who consider the boundary conditions for the end-plates of the Q-machine. These boundary conditions are derived only in the limit of strongly electron-rich sheaths, and neglect end-plate damping. In this limit, they obtain the conditions

$$\frac{n_1}{n_0} = \frac{e\phi_1}{T_{e0}} \quad , \quad \frac{T_{e1}}{T_{e0}} = 0 \quad . \tag{4.34}$$

The first condition agrees approximately with one derived by Chen[78] in the limit of electron-rich sheaths, and corresponds to a short circuit. Tsai *et al.* then construct normal axial modes from the four roots $k_z(\omega)$ of the dispersion relation satisfying these boundary conditions (they neglect ion axial motion). For conditions of interest, two drift wave roots are dominant, while two other entropy waves are heavily damped and only have significant amplitude near the end-plates. Because the medium is non-reciprocal, they find the modes are partial standing waves, even though no end-plate damping is assumed.

We discuss more generally the dependence of the normal axial modes on the terminations, when these are specified in terms of reflection coefficients for the dominant waves, by using the procedure developed in Section 2. It is now convenient to map contours of constant $(K_r^+ - K_r^-)$

and $(K_i^+ - K_i^-)$ for the dominant drift wave modes into the w-plane, as shown in Fig. 4.11 for the same parameters as Fig. 4.8. If values of the reflection coefficients, ρ_1 and ρ_2, for these dominant modes are given, either from measurements or theory, the difference $(K^+ - K^-)$ can be calculated from Eq. 2.28, and the normal mode frequencies read off Fig. 4.11. The contour $(K_i^+ - K_i^-) = 0$ is the locus of normal mode frequencies when the terminations are perfectly reflecting. Comparing this with the broken line representing the case $v_{ez0} = 0$ for perfect reflections, it is seen that the current destabilizes the normal axial modes over a wide range of $(K_r^+ - K_r^-)$ values, even though this normal mode comprises a K^+ wave and a K^- wave. However, the system can no longer be completely stabilized by decreasing the magnitude of the reflection coefficients, because of the branch points in the lower half w-plane at w_{s1} and w_{s2}.

4.4 Comparison with Experiment

4.4.1 Experiment of Rowberg and Wong

As mentioned in Section 4.2.1, we shall use the experimental results of Rowberg and Wong[47] for comparison with our theory. Their method of studying drift waves in a Q-machine is well suited for illustrating the importance of interpreting the dispersion relation for bounded systems properly, as described in Section 2. They use a double-ended Q-machine, i.e., one having identical end-plates, with no DC axial current. The drift waves are investigated by measuring the decay of externally excited normal modes when the system is stable. The modes are excited via a grid placed in the plasma, and the decay rate is measured after the excitation is switched off. This has the advantage that the waves may be kept in the linear regime by exciting them only to low amplitudes. The system is made stable by end-plate damping of the waves. This damping occurs when the end-plates have ion-rich sheaths, a point discussed at greater length below.

Rowberg and Wong, and also Hendel *et al.*,[43] measure an axial standing wave with $\lambda_z \geq 2L$ for both electron- and ion-rich sheaths, where λ_z is the axial wavelength and L the system length. The latter, who worked mostly with electron-rich sheaths, found $\lambda_z \approx 2L$ corresponding

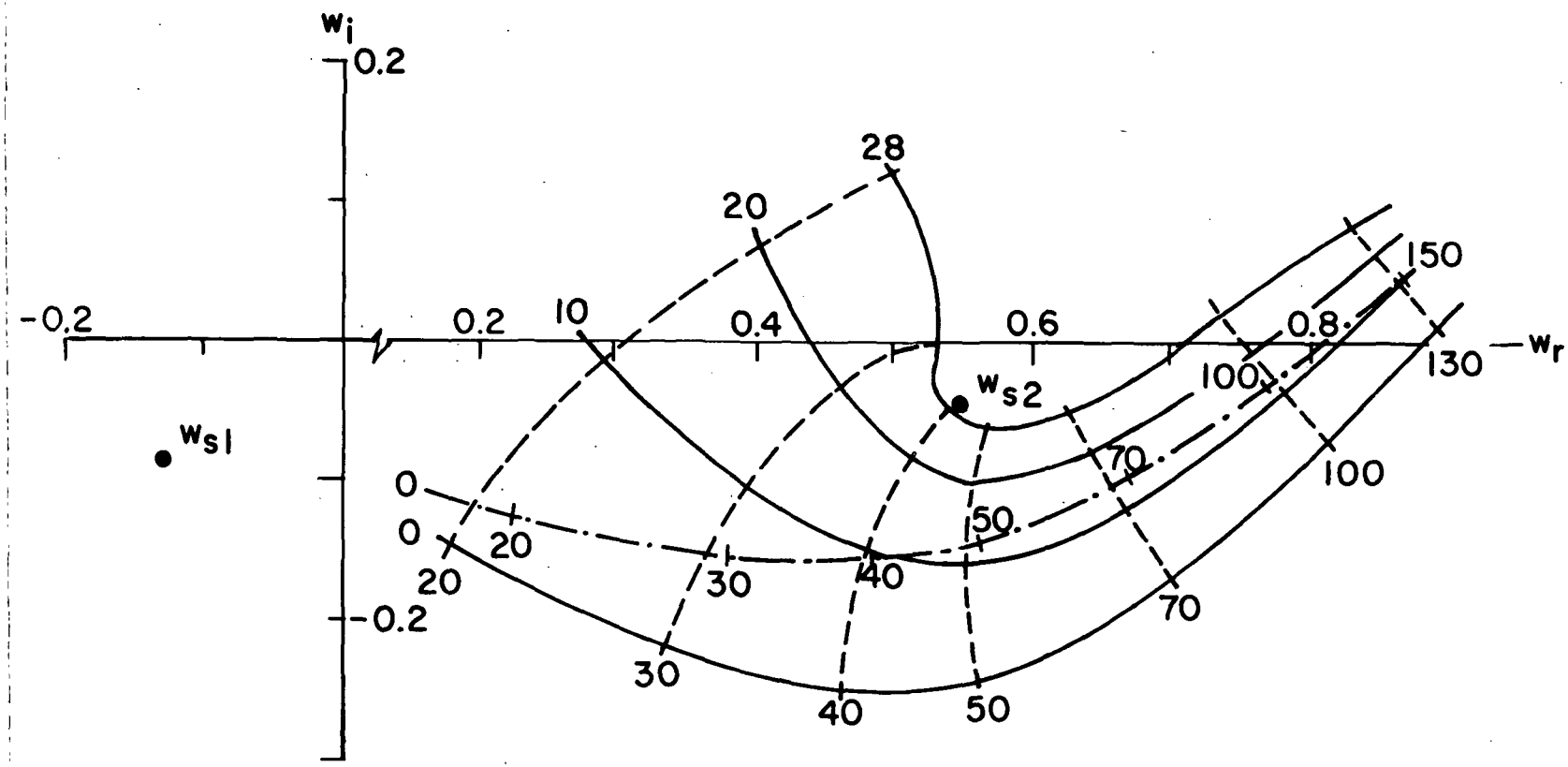

Fig. 4.11 Map of the difference $(K^+ - K^-)$ into the w-plane via Eq. (4.24) for the drift wave with $v_{ez0} = 5(T_0/m_i)^{1/2}$, as in Fig. 4.9. There are branch points at w_{s1} and w_{s2}. ——— , $(K_i^+ - K_i^-)$ = constant; ---- , $(K_r^+ - K_i^-)$ = constant; -·-·-·- , $v_{ez0} = 0$, $(K_i^+ - K_i^-) = 0$.

to a condition close to a short-circuit at the sheath edge. The former, who worked mostly with ion-rich sheaths, investigated the dependence of λ_z on the potential, U, of the plasma relative to the end-plates (Fig. 4.12). They found $\lambda_z \approx 2L$ for an electron-rich sheath ($U = -0.05V$), and $\lambda_z \approx 3.6L$ for an ion-rich sheath ($U = +0.5V$), in reasonable agreement with a formula derived by Chen[78] for the symmetric modes:

$$\frac{k_z L}{2} \tan \frac{k_z L}{2} = \frac{L}{2\rho_i} \frac{\nu_{ei}}{\omega_{ci}} \left(\frac{m_e}{2\pi m_i}\right)^{1/2} \begin{cases} 1 & U < 0 \\ \exp(-eU/T_0) & U > 0 \end{cases} , \tag{4.35}$$

where ρ_i is the ion gyroradius. For electron-rich sheaths, $U < 0$, the right-hand side of Eq. (4.35) is large, and $\lambda_z \approx 2L$ for the lowest mode. For ion-rich sheaths, $U > 0$, the right-hand side can become comparable to or less than unity, and $\lambda_z > 2L$ for the lowest mode. Due to the general shape of the solutions to the dispersion relation shown in Fig. 4.3, it is this lowest order mode which is most unstable. If the system were longer, such that a smaller k_z (or K) were admissible, the drift waves would be more unstable, and possibly a higher order axial mode could have the largest growth rate.

Equation (4.35) is derived on the assumption that k_z is real, and neglects any end-plate damping of the modes. Chen[78] discusses two damping processes connected with the end-plates. The first is due to the fact that some charged particles, carrying wave energy, escape to the end-plates and are replaced by new particles which do not have this wave energy. For ion-rich sheaths, this applies to the ions and should give rise to significant damping, whereas for electron-rich sheaths, it applies to the electrons and should give little damping. In either case, almost all the particles of the opposite charge are reflected at the sheaths. The second process is end-plate diffusion, resulting in randomization of the phase of ion gyration when ions are reflected at the end-plates.

Rowberg and Wong attribute the discrepancy between their observed and calculated growth rates for ion-rich sheaths to the loss of

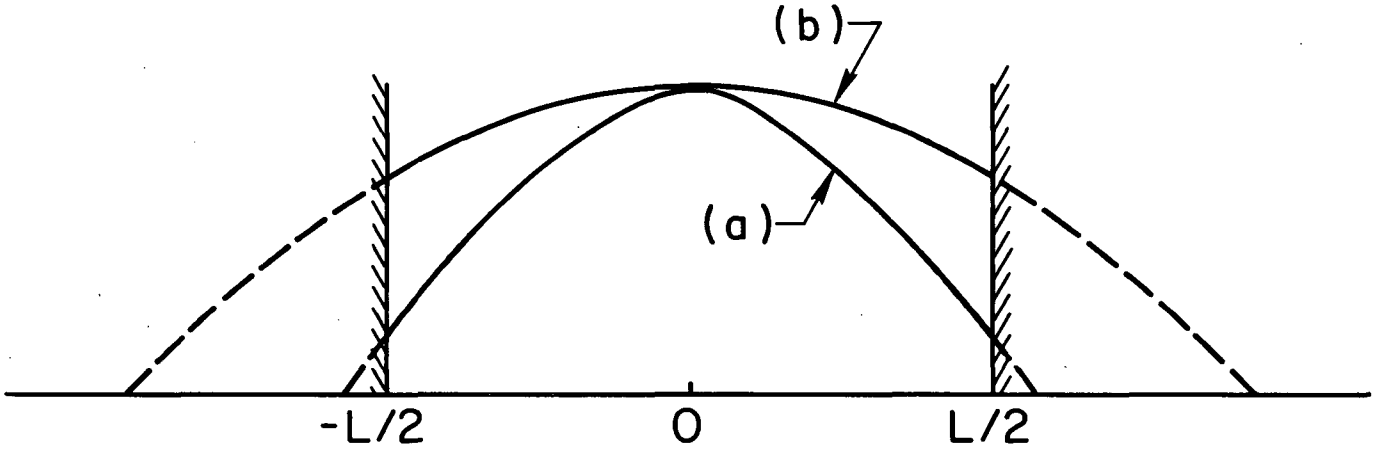

Fig. 4.12 Axial profile of wave for lowest axial mode. (a) Electron-rich sheaths, $\lambda_z \approx 2L$. (b) Ion-rich sheaths, $\lambda_z > 2L$.

ions at the end-plates. Following Chen, they calculate an associated temporal damping decrement $\omega_{iD} \equiv (\partial N_1/\partial t)/N_1$, where N_1 is the total number of perturbed ions in the column, and $\partial N_1/\partial t$ is the rate at which such ions are lost by recombination at the end-plates. For ion-rich sheaths, the decrement is evaluated as

$$\omega_{iD} = \frac{2v_{ith}}{L} \frac{1}{[1 + \exp e(U_w - U_I - U)/T_0]} , \qquad (4.36)$$

where v_{ith} is the ion thermal velocity, U_w is the end-plate work function, and U_I is the ionization potential of the neutrals. The last term in Eq. (4.36) gives the probability that an ion is lost upon striking the end-plate. The experimental damping rate is then compared with the algebraic sum of the theoretical growth (damping) rate and the end-plate damping decrement calculated from Eq. (4.36).

While Eq. (4.36) is plausible, and leads to values for ω_{iD} which agree approximately with the discrepancy between measured and calculated growth (decay) rates for the isothermal theory used by Rowberg and Wong, the agreement is poor for the non-isothermal theory, as we shall see in Section 4.4.3. Furthermore, its derivation can be criticized on several grounds. First, no account is taken of the spatial dependence of wave energy along the machine; second, it is based on collisionless concepts, and effectively distributes the damping uniformly along the system. It is clear from the viewpoint developed in Section 2 that, within a fluid model, end-plate damping should be treated as a local effect producing imperfect wave reflection ($|\rho| < 1$). Consequently, the mode is a partial standing wave constructed from roots $k_z^{\pm}(\omega)$ with complex $k_z^{\pm}$, corresponding to spatial growth toward the ends. The partial standing wave gives a flow of wave energy toward the ends, where it is dissipated, and, because of the spatial growth, the temporal growth rate is reduced.

Thus, end-plate damping is incompatible with the pure standing wave ($k_z^{\pm}$ real) assumed by Rowberg and Wong. If the observed mode was indeed a pure standing wave, then end-plate damping could not have been responsible for the discrepancy in temporal growth rate. On the other

hand, if end-plate damping was operative, then the mode could not have been a pure standing wave.

4.4.2 Normal Mode Interpretation

The theory of Section 2 should allow one to determine, from careful measurements of the axial mode pattern, the reflection coefficients and thus the values of $k_{zr}^{\pm}$ and $k_{zi}^{\pm}$. By solving the dispersion relation for these k_z values, the temporal growth rate which includes the effect of end-plate damping can be determined. One can then establish experimentally to what extent the discrepancy in temporal growth rates is attributable to end-plate damping.

For k_{zr} we have taken the value measured by Rowberg and Wong. However, due to the facts that their measurements were only over a 40 cm region of the 60 cm column, and that the wavelength was very long, their data do not allow one to determine k_{zi} directly. The difficulty is illustrated in Fig. 4.13, where the theoretical amplitude and phase of the axial normal mode are plotted with $k_{zr} = \pi/1.8L$, L = 60 cm, and with the magnitude of the reflection coefficient, $|\rho|$ [$= \exp(-k_{zi}L)$], taking on various values. The amplitude curves are very similar over the measurement region for $|\rho| > 0.3$, and the phase shifts are quite small. The measurement of this phase shift ($\sim 10^{o}$) is difficult since there is a very large azimuthal phase shift (720^{o} for the m = 2 mode); very precise tracking of the axial probe along a magnetic field line is required for the measurement. It is thus not surprising that Rowberg and Wong did not observe an axial phase shift over their measurement region.

To obtain an estimate of the value of $|\rho|$ in their experiment, we use an argument based on energy considerations. The probability that an ion is lost upon striking the end-plate for an ion-rich sheath is given by

$$\delta = [1 + \exp e(U_w - U_I - U)/T_0]^{-1} \quad , \tag{4.37}$$

as in Eq. (4.36). If we assume that most of the wave energy is carried by the ions, since the electrons have a much smaller mass, δ also

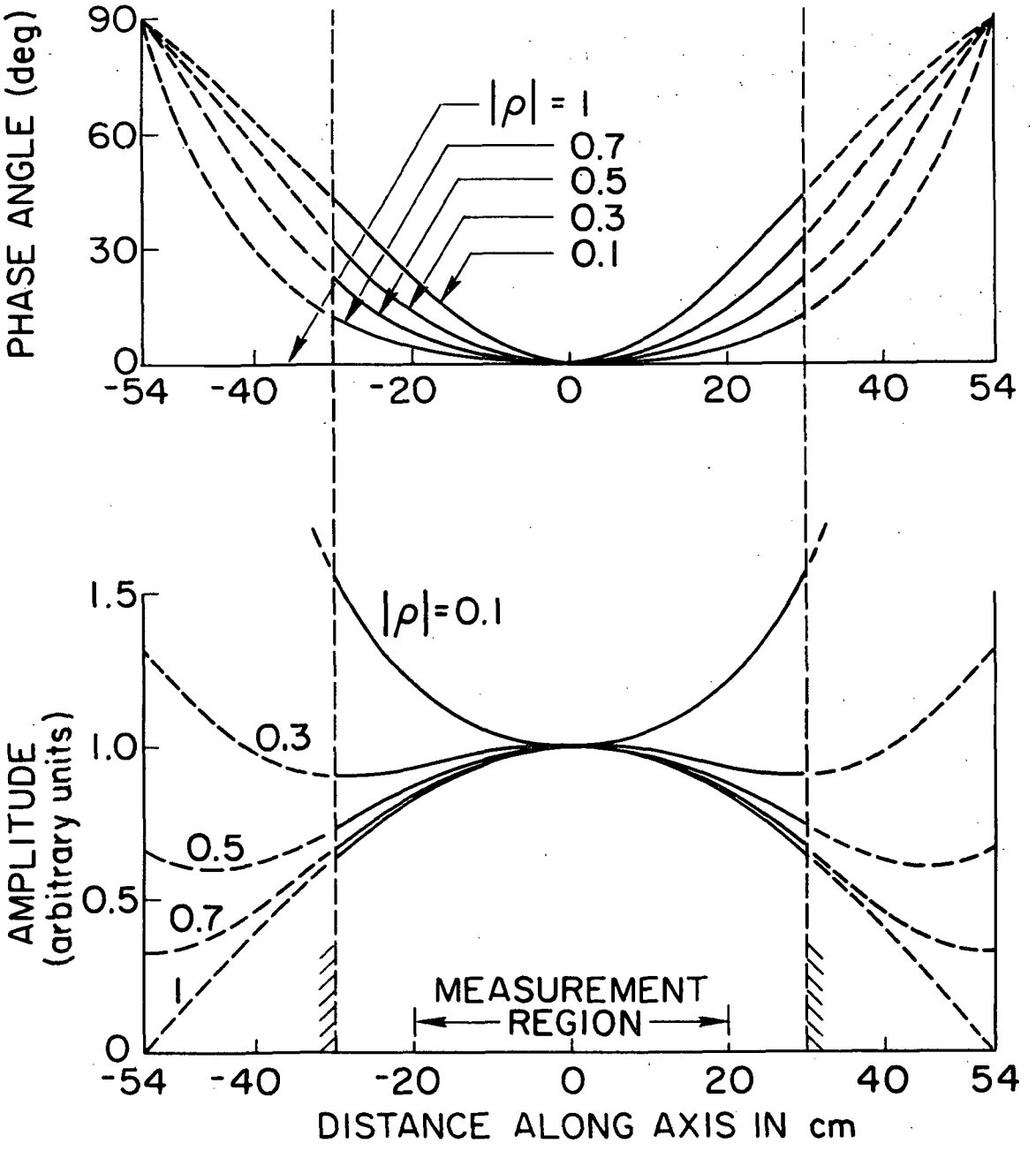

Fig. 4.13 Amplitude and phase of axial normal mode for various magnitudes of the reflection coefficient ρ, with $k_{zr} = 1.67\ cm^{-1}$.

approximates the fraction of wave energy lost at the end-plate. In terms of the reflection coefficient, the fraction of energy lost is written as $(1 - |\rho|^2)$. Using this, and Eq. (4.37), gives the result

$$|\rho| = \left[\frac{\exp e(U_w - U_I - U)/T_0}{1 + \exp e(U_w - U_I - U)/T_0}\right]^{\frac{1}{2}} . \qquad (4.38)$$

For tungsten end-plates ($U_w \approx 4.5$ eV), potassium atoms ($U_I = 4.3$ eV), ion-rich sheaths ($U = 0.5$ eV), and $T_0/e = 0.19$ eV, this yields $|\rho| \approx 0.4$. In terms of the wavenumber, we have $k_{zi} \approx 1.5 \times 10^{-2}$ cm^{-2}, or, for the normalized wave number, $K_i \approx 30$. These values should be regarded as approximate, since we have attributed all of the damping to the ion loss. Also, Eq. (4.38) is sensitive to the precise value of the work function, U_w, which is dependent on the surface conditions and lattice orientation of the end-plate.[79]

4.4.3 Comparison with Measured Results

In their experiment, Rowberg and Wong measured the damping rate of the drift waves as a function of the magnetic field. In Fig. 4.14, we have compared their experimental data with the solutions obtained from the various approximations to the full dispersion relation, as discussed in Sections 4.2 and 4.3. Note that $-\omega_i$ is plotted vertically, so that curves above the axis correspond to instability. We have taken k_{zr} to be the value measured by Rowberg and Wong, and give solutions for decreasing values of $|\rho|$, corresponding to increasing values of k_{zi}.

In Fig. 4.14(a), we show the isothermal theory results neglecting ion axial motion [Eq. (4.26)], as used by Rowberg and Wong. It is seen that reducing $|\rho|$ reduces the growth rate and leads to damping (see also Fig. 4.3), but it is clear that no single $|\rho| < 1$ curve matches the experimental results. The $|\rho| = 0.3$ curve matches at low magnetic field, but has the wrong shape at high magnetic field. On the other hand, Rowberg and Wong's procedure of subtracting a constant damping decrement of $\omega_{iD} \approx 1.4 \times 10^{-3}$ sec^{-1} from the theoretical curve for real k_z ($|\rho| = 1$) does lead to a reasonable match with the experiment.

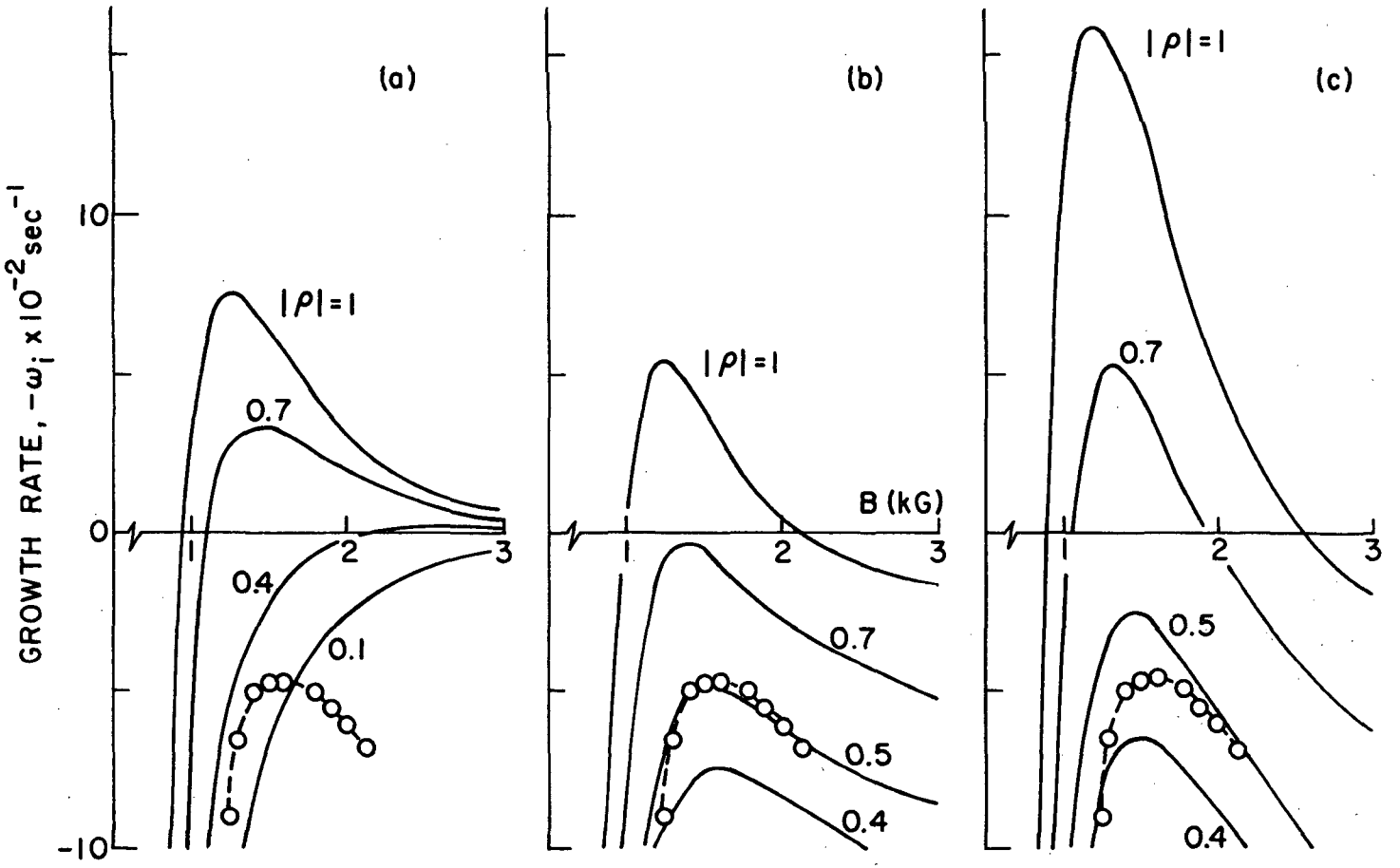

Fig. 4.14 Comparison of drift wave growth rates for (a) isothermal theory neglecting ion axial motion [Eq. (4.26)], (b) isothermal theory including ion axial motion [Eq. (4.32)], and (c) non-isothermal theory including ion axial motion [Eq. (4.24)]. Parameters as in Fig. 4.3. ——— , theory; ---- , Rowberg and Wong's experimental data.

However, in the experiment, λ_z is sufficiently small that the effect of ion axial motion is important, especially at higher magnetic fields, so we should not expect agreement with a theory neglecting ion axial motion. Thus, the apparent agreement found by Rowberg and Wong must be regarded as fortuitous.

In Fig. 4.14(b), we show the isothermal results including ion axial motion [Eq. (4.32)]. As we saw in Section 4.2.2 (Fig. 4.5), the growth rates are decreased, but more importantly the damping rates reach a minimum ($-\omega_i$ a maximum) and then decrease as the magnetic field is increased. This is just the behavior observed experimentally, and the curve for $|\rho| = 0.5$ fits the data very well. On the other hand, Rowberg and Wong's method of subtracting a damping decrement, ω_{iD}, leads to a poorer fit than before. While the agreement is quite good at this point, we shall also consider the full non-isothermal theory [Eq. (4.24)].

The non-isothermal results are shown in Fig. 4.14(c), and, for $|\rho| = 1$ (k_z real), there is a dramatic increase in the growth rate (see also Fig. 4.6) to nearly three times that of the isothermal theory. Subtracting the damping decrement, ω_{iD}, still leads to a poor fit, but this time the error is in the opposite direction to that of Fig. 4.14(b). However, the solutions for $|\rho| < 1$ continue to fit the data quite well, this time for $|\rho| \approx 0.45$. This is close to the estimated value of $|\rho| \approx 0.4$ found in the previous subsection.

We have thus shown the importance of including both ion axial motion and non-isothermal effects in interpreting the experimental data, and that the proper interpretation of these results requires solving the dispersion relation for both complex ω and complex k_z, as described in Section 2.

5. WAVES PROPAGATING PARALLEL TO THE MAGNETIC FIELD

As mentioned in Section 4.2.2, when the angle of propagation of low-frequency waves becomes more nearly parallel to the magnetic field, ion motion along the field becomes important, and two branches of the dispersion relation evolve into ion-acoustic wave branches. These waves are similar to sound waves in a neutral gas, except that there are electrostatic forces present. These forces cause the waves to be driven by a combination of the electron and ion pressures, while the inertia is due to the ions. It has been known since the early 1960's that these waves can become unstable due to electron drift in a collisionless plasma.[49-52] The resonant interaction between the drifting electrons and the wave overcomes Landau damping by the ions to produce instability. The energy for the instability comes from the kinetic energy of the drifting electrons. Later, it was shown that electron drift can also produce ion-acoustic instability in both weakly ionized[46] and fully ionized[8] collisional plasmas, where electron collisional effects cause the release of the kinetic energy.

In this section, we consider ion-acoustic waves propagating parallel to the magnetic field. We again take the case of a fully ionized collisional plasma. The basic dispersion relation for these waves is derived in Section 5.1, where we can use the Fourier transform since the plasma is assumed uniform. In Section 5.2, the dispersion relation is solved to find the characteristics of the ion-acoustic instability. The effect of an electron drift (or a current) is studied, and, in addition, it is shown that a temperature difference between the electrons and ions with $T_{e0} > T_{i0}$ can produce instability with no electron drift. This latter case is a new result,[80] and the energy for the instability is due to the lack of thermal equilibrium between the electrons and ions. We also consider the effect of axial boundaries on the solutions. These studies apply to a plasma whose steady state is maintained by some external heat sources and sinks. In Section 5.3, we consider the instability in a plasma whose "steady state" changes in time from some given initial conditions. We conclude in Section 5.4 with a discussion of situations in which ion-acoustic instability might arise.

5.1 Basic Theory: The Maintained Plasma

5.1.1 Steady State Plasma

The model, shown in Fig. 5.1, is of a uniform, fully ionized plasma immersed in a uniform magnetic field in the z-direction. There also may be an electric field, E_0, along the magnetic field. The magnetic field is included for comparison with the models of Sections 3 and 4. However, no terms due to the magnetic field will appear in the equations to follow, since we are considering quasistatic waves propagating parallel to this field. Thus, the results are equally valid for an unmagnetized plasma. The ions and electrons are allowed to have different temperatures, given by T_{i0} and T_{e0}, respectively. This is physically justifiable because the electrons and the ions each equilibrate with themselves much more quickly than with one another.[58]

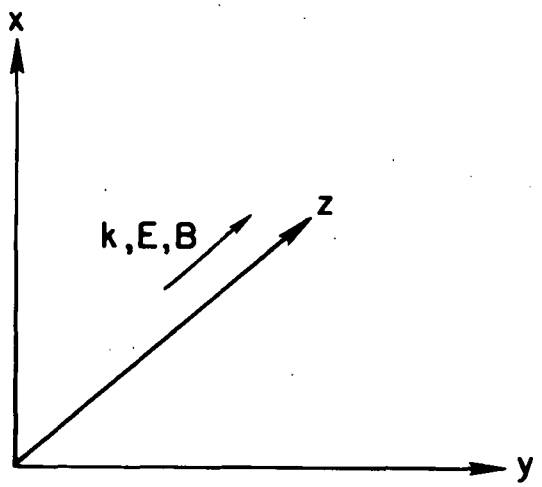

Fig. 5.1 Model of the plasma in rectangular geometry showing the DC quantities and the direction of propagation.

We again use the moment equations[58] to describe the plasma. All subscripts z are omitted, since this is the only direction in which variations are considered. In this section, the three moment equations are used for both the electrons and the ions, since heat flow along the

magnetic field may be important for each species. For the ions, the equations of continuity, momentum transfer, and heat transfer are

$$\frac{\partial n}{\partial t} + \frac{\partial (nv_i)}{\partial z} = 0 \quad , \tag{5.1}$$

$$m_i n \frac{dv_i}{dt} = - \frac{\partial (nT_i)}{\partial z} + \frac{4}{3} C_{i\eta} \frac{nT_i}{\nu_{ii}} \frac{\partial^2 v_i}{\partial z^2} + ZenE + m_e C_r \nu_{ei} nu + C_t n \frac{\partial T_e}{\partial z} \quad , \tag{5.2}$$

$$\frac{3}{2} n \frac{dT_i}{dt} + nT_i \frac{\partial v_i}{\partial z} = \frac{\partial}{\partial z} \left(\frac{C_{i\chi} nT_i}{m_i \nu_{ii}} \frac{\partial T_i}{\partial z} \right) + 3 \frac{m_e}{m_i} \nu_{ei} n(T_e - T_i) + S_i \quad . \tag{5.3}$$

Here $C_{i\eta} = 0.96$ is the ion viscosity coefficient, $C_r = 0.51$ is the resistivity coefficient, $C_t = 0.71$ is the thermal force coefficient, $C_{i\chi} = 3.9$ is the ion thermal conductivity coefficient, Ze is the charge of an ion, $u = v_e - v_i$, and S_i is a uniform external heat source or sink term which balances the heat equation in the steady state when $T_{e0} \neq T_{i0}$. From this point on, the word "source" will imply source or sink. We assume that the zero order ion velocity, v_{i0}, is zero, even in the presence of an electric field E_0. As discussed in Section 4, this is a good approximation since the ion mass is much larger than that of the electrons.

The equations for the electrons are very similar, except that we neglect electron inertia, as previously. We thus have the continuity, momentum transfer, and heat transfer equations:

$$\frac{\partial n}{\partial t} + \frac{\partial}{\partial z}(nv_e) = 0 \quad , \tag{5.4}$$

$$0 = - \frac{\partial (nT_e)}{\partial z} + \frac{4}{3} C_{e\eta} \frac{nT_e}{\nu_{ei}} \frac{\partial^2 v_e}{\partial z^2} - enE - m_e C_r \nu_{ei} nu - C_t n \frac{\partial T_e}{\partial z} \quad , \tag{5.5}$$

$$\frac{3}{2} n \frac{dT_e}{dt} + nT_e \frac{\partial v_e}{\partial t} = \frac{\partial}{\partial z} \left(\frac{C_{e\chi} nT_e}{m_e \nu_{ei}} \frac{\partial T_e}{\partial z} \right) - C_t T_e \frac{\partial}{\partial z}(nu) - 3 \frac{m_e}{m_i} \nu_{ei} n(T_e - T_i) + m_e C_r \nu_{ei} nu^2 + S_e \quad . \tag{5.6}$$

Here $C_{e\eta} = 0.73$ is the electron viscosity coefficient, $C_{e\chi}$ is the electron thermal conducitivity coefficient, and S_e is the uniform external heat source term which balances the heat equation for the electrons in the steady state.

The zero order electron velocity comes from Eq. (5.5) when we take $v_{i0} = 0$, and is given as [see also Eq. (4.10)]

$$v_{e0} = - \frac{e E_0}{m_e C_r \nu_{ei}} \quad . \tag{5.7}$$

We thus have a steady state plasma in which the ions are at rest and the electrons are drifting at a speed v_{e0}. The electrons and ions may be maintained at different temperatures by the source terms S_i and S_e. In many plasmas, it is found that the electrons have a higher temperature than the ions. This may be caused by heating of the electrons by an external source (RF heating, DC joule heating, etc.) and by the cooling of ions (occasional collisions with neutrals, for example). We do not specify the source terms S_i and S_e, but assume that they maintain the plasma in this steady state. The initial value problem for the case $S_i = S_e = 0$, when the plasma is allowed to equilibrate ($T_{e0} \rightarrow T_{i0}$) from some initial state, is studied in Section 5.3. First, however, we consider the stability of a maintained plasma for waves propagating along the magnetic field.

5.1.2 Perturbed Plasma

Since the model is of an infinite, uniform plasma, we may take the variables n, E, v_e, v_i, T_e, and T_i to have the general form

$$n(z) = n_0 + n_1 \exp i(\omega t - kz) \quad . \tag{5.8}$$

The same assumptions are made as in Sections 3 and 4, i.e., the waves are quasistatic ($E_1 = -\partial \phi_1 / \partial z$) and low frequency ($\omega \ll \omega_{pi}$), the latter implying that quasineutrality ($n_{el} = Z n_{il} \equiv n_1$) can be used. It is also assumed that sources S_i and S_e are not important in the perturbation analysis, i.e., $S_{il} = S_{el} = 0$. The effect of this assumption is discussed in Section 5.2.1.

In beginning the analysis, a simplification arises if several of the perturbed electron and ion equations are considered together. The continuity equations [Eqs. (5.1) and (5.4)] are used to find the first order velocity variables

$$v_{e1} = \left(\frac{\omega - kv_{e0}}{k}\right), \quad v_{i1} = \left(\frac{\omega}{k}\right)\frac{n_1}{n_0} \quad . \tag{5.9}$$

Next we add the momentum transfer equations [Eqs. (5.2) and (5.5)], so that the electric field and collisional terms cancel. Using Eq. (5.9), we eliminate v_{e1} and v_{i1} from this equation to give

$$\gamma_{11}\frac{n_1}{n_0} + \gamma_{12}\frac{T_{i1}}{T_{i0}} + \gamma_{13}\frac{T_{e1}}{T_{e0}} = 0 \quad . \tag{5.10}$$

The γ's which relate these first order variables are

$$\gamma_{11} = \left\{-\Omega^2 + i\,\frac{4}{3}\,\frac{\Omega\varkappa^2}{R_m}\left[2^{1/2}C_{i\eta}R_T^{5/2}/Z^2 + \frac{C_{e\eta}Z}{R_m}\left(1 - \frac{\varkappa V}{\Omega R_m}\right)\right] + \frac{(Z+R_T)}{R_m^2}\varkappa^2\right\},$$

$$\gamma_{12} = \frac{R_T\varkappa^2}{R_m^2}, \qquad \gamma_{13} = \frac{Z\varkappa^2}{R_m^2} \quad . \tag{5.11}$$

Here $\Omega \equiv \omega/\nu_{ei}$ is the normalized frequency, $\varkappa \equiv k(T_{e0}/m_e)^{1/2}/\nu_{ei} \equiv k\lambda_e$ is the normalized wavenumber, λ_e being the electron mean free path, $R_m^2 \equiv m_i/m_e$ is the mass ratio, $R_T \equiv T_{i0}/T_{e0}$ is the temperature ratio, and $V \equiv v_{e0}/(T_{e0}/m_i)^{1/2}$ is the normalized drift velocity of the electrons.

In perturbing the ion heat transfer equation [Eq. (5.3)], we find a second equation

$$\gamma_{21}\frac{n_1}{n_0} + \gamma_{22}\frac{T_{i1}}{T_{i0}} + \gamma_{23}\frac{T_{e1}}{T_{e0}} = 0 \quad . \tag{5.12}$$

The new γ's which appear in this equation can be written as

$$\gamma_{21} = \left\{ - i\Omega - \frac{6Z(1-R_T)}{R_m^2 R_T} \right\} ,$$

$$\gamma_{22} = \left\{ i \frac{3}{2} \Omega + 2^{1/2} \frac{C_{i\chi} R_T^{5/2} \kappa^2}{R_m Z^2} + \frac{3Z}{R_m^2} \right\} , \quad \gamma_{23} = \frac{3}{2} \frac{Z(1-3R_T)}{R_m^2 R_T} . \tag{5.13}$$

Similarly, the electron heat transfer equation [Eq. (5.6)] can be perturbed, which yields a third equation,

$$\gamma_{31} \frac{n_1}{n_0} + \gamma_{32} \frac{T_{i1}}{T_{i0}} + \gamma_{33} \frac{T_{e1}}{T_{e0}} = 0 . \tag{5.14}$$

This last set of γ's has the form given by

$$\gamma_{31} = \left\{ -i \left(\Omega - \frac{\kappa V}{R_m} \right) + 6 \frac{(1-R_T)}{R_m^2} \right\} , \qquad \gamma_{32} = \frac{-3R_T}{R_m^2} ,$$

$$\gamma_{33} = \left\{ i \frac{3}{2} \left(\Omega - \frac{\kappa V}{R_m} \right) + \frac{3}{2} \frac{C_r V^2}{R_m^2} + C_{e\chi} \kappa^2 - \frac{3}{2} \frac{(1-3R_T)}{R_m^2} \right\} . \tag{5.15}$$

Equations (5.10), (5.12), and (5.14) provide the three equations for the wave variables n_1, T_{i1}, and T_{e1}. We find the dispersion relation by setting the determinant of the coefficients of these equations equal to zero. The dispersion relation is thus

$$D(\Omega,\kappa) = \begin{vmatrix} \gamma_{11} & \gamma_{12} & \gamma_{13} \\ \gamma_{21} & \gamma_{22} & \gamma_{23} \\ \gamma_{31} & \gamma_{32} & \gamma_{33} \end{vmatrix} = 0 . \tag{5.16}$$

For $V = 0$, $D(\Omega,\varkappa)$ is of fourth order in Ω and of sixth order in $\varkappa$; for $V \neq 0$, it is of seventh order in $\varkappa$. The extra $\varkappa$ factor in $V \neq 0$ comes from including electron viscosity, as seen in γ_{11}. Of the roots in Ω, two correspond to electron and ion entropy (or temperature waves), and two correspond to ion-acoustic waves. It should be noted that if Ω is a solution to the dispersion relation for $\varkappa$, then $-\Omega^*$ is a solution for $-\varkappa^*$. Thus, we only need to consider solutions for $\Omega_r > 0$ or for $\varkappa_r > 0$. The stability and characteristics of these waves are studied in the next subsection.

In order to study these characteristics, we first give the relation for the perturbed potential, since it cancelled out of the equations when the momentum transfer equations were added. Using Eqs. (5.5) and (5.9), we find

$$\frac{e\phi_1}{T_{e0}} = \left[1 + i\,\frac{4}{3}\,C_{e\eta}\left(\Omega - \frac{\varkappa V}{R_m}\right)\right]\frac{n_1}{n_0} + \left[(1 + C_t) - i\,\frac{3}{2}\,\frac{C_r V}{R_m \varkappa}\right]\frac{T_{e1}}{T_{e0}} \quad . \qquad (5.17)$$

5.2 Solutions to the Dispersion Relation

5.2.1 Effect of Unequal Electron and Ion Temperatures

We consider solutions to the dispersion relation for $V = 0$, so that $D(\Omega,\varkappa)$ is even in $\varkappa$. The entropy waves are always damped ($\Omega_i > 0$), so we shall not be concerned with them. For the ion-acoustic waves, we find that instability can arise if the electrons have a higher temperature than the ions. The relevant branch point of the dispersion relation, as defined in Section 2.1.2, occurs on the real Ω-axis at

$$\Omega_s = 0, \quad \varkappa_s = 0 \; . \qquad (5.18)$$

Thus, if the waves are unstable, the system is on the boundary between convective and absolute instability.

A very convenient approximation can be made to the ion-acoustic wave dispersion relation by assuming that for these waves $\Omega/\varkappa \sim \pm\, 1/R_m$, i.e., $\omega/k \sim \pm\, C_s$. If we then restrict ourselves to $R_T < 1$

and short wavelengths with $\kappa^2 \gg R_m^{-2}$, a large number of terms in Eq. (5.16) may be neglected as small, leading to the cubic equation

$$\Omega^3 - i\left[\frac{2}{3}^{3/2}(2\,C_{i\eta} + C_{i\chi})\,\frac{R_T^{5/2}\,\kappa^2}{Z^2\,R_m^2} + \left(\frac{4}{3}\,C_{e\eta}\,\kappa^2 + \frac{1}{C_{e\chi}} + 2\right)\frac{Z}{R_m^2}\right]\Omega^2$$

$$- \left[\frac{Z + 5R_T/3}{R_m^2}\,\kappa^2\right]\Omega + i\left[\frac{2}{3}^{3/2}\,\frac{C_{i\chi}(Z + R_T)R_T^{5/2}}{Z^2\,R_m^3}\,\kappa^4 + \frac{2Z(Z + 2 - R_T)}{R_m^4}\,\kappa^2\right] = 0. \tag{5.19}$$

We now assume the ion-acoustic wave solution has the form

$$\Omega = \Omega_r + i\Omega_i, \tag{5.20}$$

where $\Omega_r \sim \pm\,\kappa/R_m$ and $|\Omega_r| \ll |\Omega_i|$. Neglecting small terms, the real part of Eq. (5.17) then gives

$$\frac{\Omega_r}{\kappa} = \pm\,\frac{(Z + 5R_T/3)^{\frac{1}{2}}}{R_m}\,, \tag{5.21}$$

which can also be written as

$$\frac{\omega_r}{k} = \pm\left(\frac{ZT_{e0} + 5T_{i0}/3}{m_i}\right)^{\frac{1}{2}}. \tag{5.22}$$

Using this result, the imaginary part of Eq. (5.19) yields the growth (damping) rate

$$\Omega_i \approx \frac{2}{3}^{3/2}\,\frac{R_T^{5/2}}{R_m Z^2}\,C_{i\eta}\kappa^2 + \frac{2}{3}\,\frac{Z}{R_m^2}\,C_{e\eta}\kappa^2 + \frac{2}{9}^{3/2}\,\frac{R_T^{7/2}\,C_{i\chi}\kappa^2}{Z^2 R_m (Z+5R_T/3)} + \frac{Z}{2R_m^2\,C_{e\chi}}$$

$$- \frac{2Z(1-4R_T/3)}{R_m^2(Z+5R_T/3)}\,. \tag{5.23}$$

For acoustic waves in a neutral gas, the dispersion relation generally has the form

$$\frac{\omega}{k} = \left(\frac{\gamma T}{m}\right)^{\frac{1}{2}}, \qquad (5.24)$$

where γ is a constant obtained from the equation of state of the gas. For an isothermal process $\gamma = 1$, while for an adiabatic process $\gamma = 5/3$. By analogy, the phase velocity of the ion-acoustic wave [Eq. (5.22)] implies that the electrons behave isothermally and the ions behave adiabatically. This suggests that we may take $C_{i\chi} = 0$ and $C_{e\chi} = \infty$, i.e., there is zero ion heat conductivity and infinite electron heat conductivity. However, while this appears true for the real frequency, we see from Eq. (5.21) that the growth (damping) rate of the wave depends on the precise values of $C_{i\chi}$ and $C_{e\chi}$.

In Eq. (5.21), the terms are, respectively, the contributions of ion viscosity, electron viscosity, ion thermal conductivity, electron thermal conductivity, and collisional energy transfer. The first four terms are all stabilizing, but the last is destabilizing for $R_T < 3/4$, i.e., for $T_{e0} > (4/3)T_{i0}$. Note that of the stabilizing terms, the fourth term has its coefficient $C_{e\chi}$ in the denominator, and thus decreases for increasing electron heat conductivity. The ion terms tend to zero as $T_{i0} \to 0$ and are proportional to R_m^{-1}, while the electron and collisional energy transfer terms, being proportional to R_m^{-2}, are smaller by a factor R_m. The first three terms contain a factor $\varkappa^2$, so that the last two terms, which do not, dominate for long wavelengths. It is clear that for long wavelengths, and R_T small enough, the destabilizing effect of the collisional energy transfer can overcome the stabilizing effects.

Figure 5.2 shows the real $\varkappa$ contour mapped into the Ω-plane for the ion-acoustic wave root for $R_m^2 = 1837$, corresponding to hydrogen, and for various temperature ratios R_T. These results were computed from the full dispersion relation, and agree very well ($< 5\%$) with the approximations given by Eqs. (5.21) and (5.23) in their range of validity. The map is symmetric about Ω_r. Except when $R_T \lesssim 1/10$, instability is confined to the region $0 < |\varkappa| \lesssim 1$, under which conditions

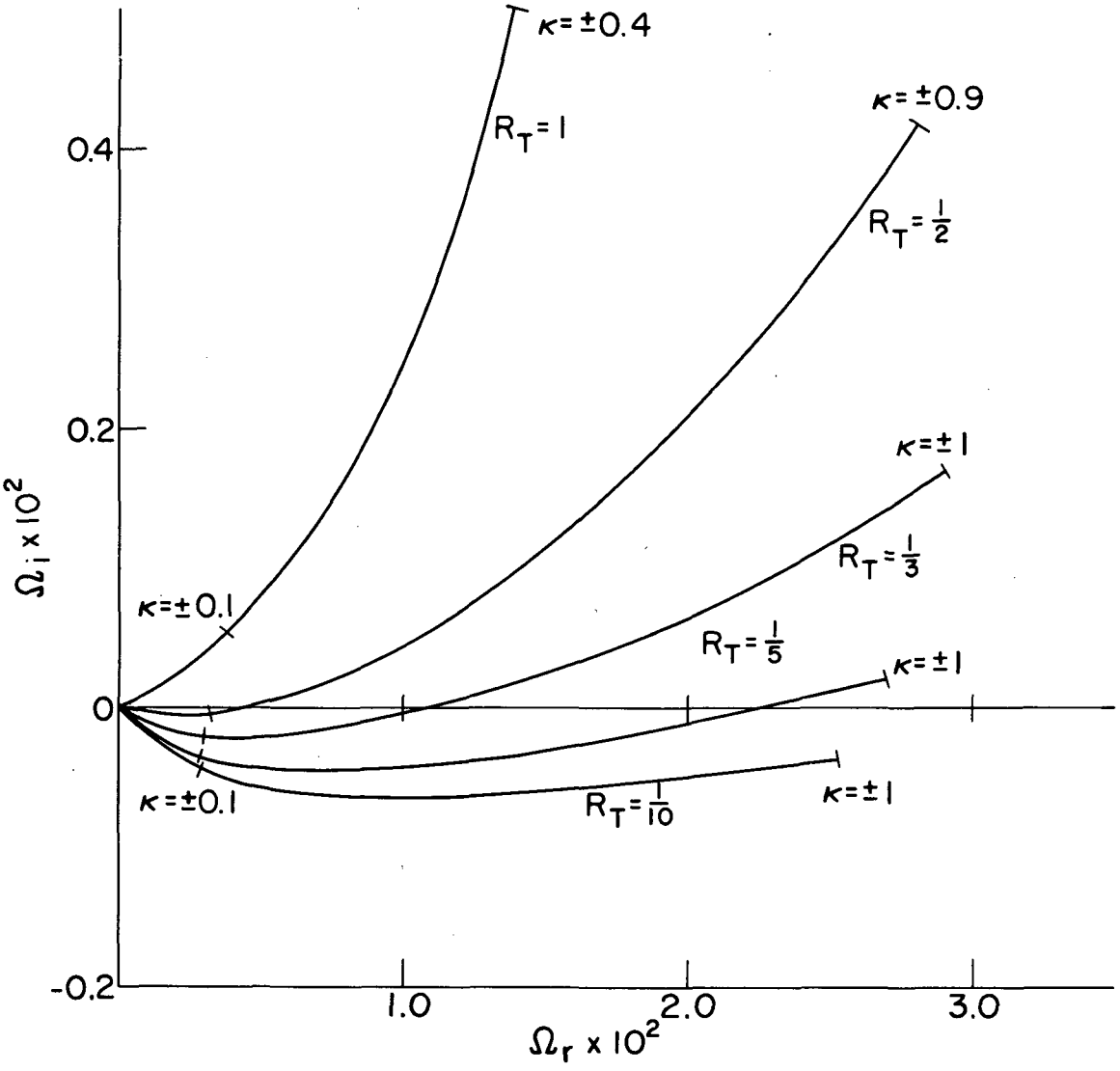

Fig. 5.2 Map of the real $\varkappa$ contour into the Ω-plane via Eq. (5.16) for the ion-acoustic wave branch with various temperature ratios, R_T, and R_m = 1837, corresponding to a hydrogen plasma.

the fluid treatment is valid. From Eq. (5.23), one finds instability for:

$$\kappa^2 < \frac{3Z^3}{2}\left\{\frac{2(1-4R_T/3) - (Z+5R_T/3)/2\ C_{e\chi}}{(2^{1/2}R_m R_T^{5/2}C_{i\eta}+Z^3C_{e\eta})(Z+5R_T/3)+(2^{1/2}/3)R_m R_T^{7/2}C_{i\chi}}\right\}. \tag{5.25}$$

The maximum growth rate occurs for $R_T \ll 1$, and is of order $(-\omega_i)_{max} \sim (m_e/m_i)\nu_{ei}$. This is comparable with the characteristic rate of energy transfer by collisions between electrons and ions. Although this growth rate may appear small, it can be as large as for other instabilities in a plasma discharge, as we shall discuss in Section 5.4.

For systems which are effectively unbounded, it is appropriate to solve for the spatial growth rates of these waves. Since the dispersion relation is nearly satisfied for real (Ω,κ) in some vicinity, say (Ω_r, κ_r), we have solutions to the dispersion relation $D(\Omega_r+i\Omega_i, \kappa_r) = D(\Omega_r, \kappa_r+\kappa_i) = 0$, where $|\Omega_i/\Omega_r| \ll 1$, $|\kappa_i/\kappa_r| \ll 1$. From this we may find the spatial growth rate for real Ω, i.e.,

$$\kappa_i = \left.\frac{-\Omega_i}{(\partial\Omega/\partial\kappa)}\right|_{\Omega_r,\kappa_r} = \mp \left.\frac{R_m\,\Omega_i}{(Z+5R_T/3)^{1/2}}\right|_{\kappa_r}. \tag{5.26}$$

Here we use the Ω_i from Eq. (5.23), and the ± sign for propagation parallel/antiparallel to the magnetic field. Thus, there is spatial growth for $\Omega_i < 0$, and the real frequency is still given by Eq. (5.21).

In order to clarify the characteristics of this instability, we have calculated the amplitude and phase of the normalized first order variables $\phi_{1n} = (e\phi_1/T_{e0})/(n_1/n_0)$, $T_{eln} = (T_{el}/T_{e0})/(n_1/n_0)$, and $T_{iln} = (T_{il}/T_{i0})/(n_1/n_0)$. These are shown in Fig. 5.3 as a function of κ for $R_T = 1/2$ and $1/10$ (note the different scales). Expressions for these quantities may be determined from the first order equations, i.e., Eqs. (5.10), (5.12), and (5.17). The potential and density oscillations are nearly equal, as would be true for a collisionless, isothermal electron gas. Here the potential oscillation leads slightly

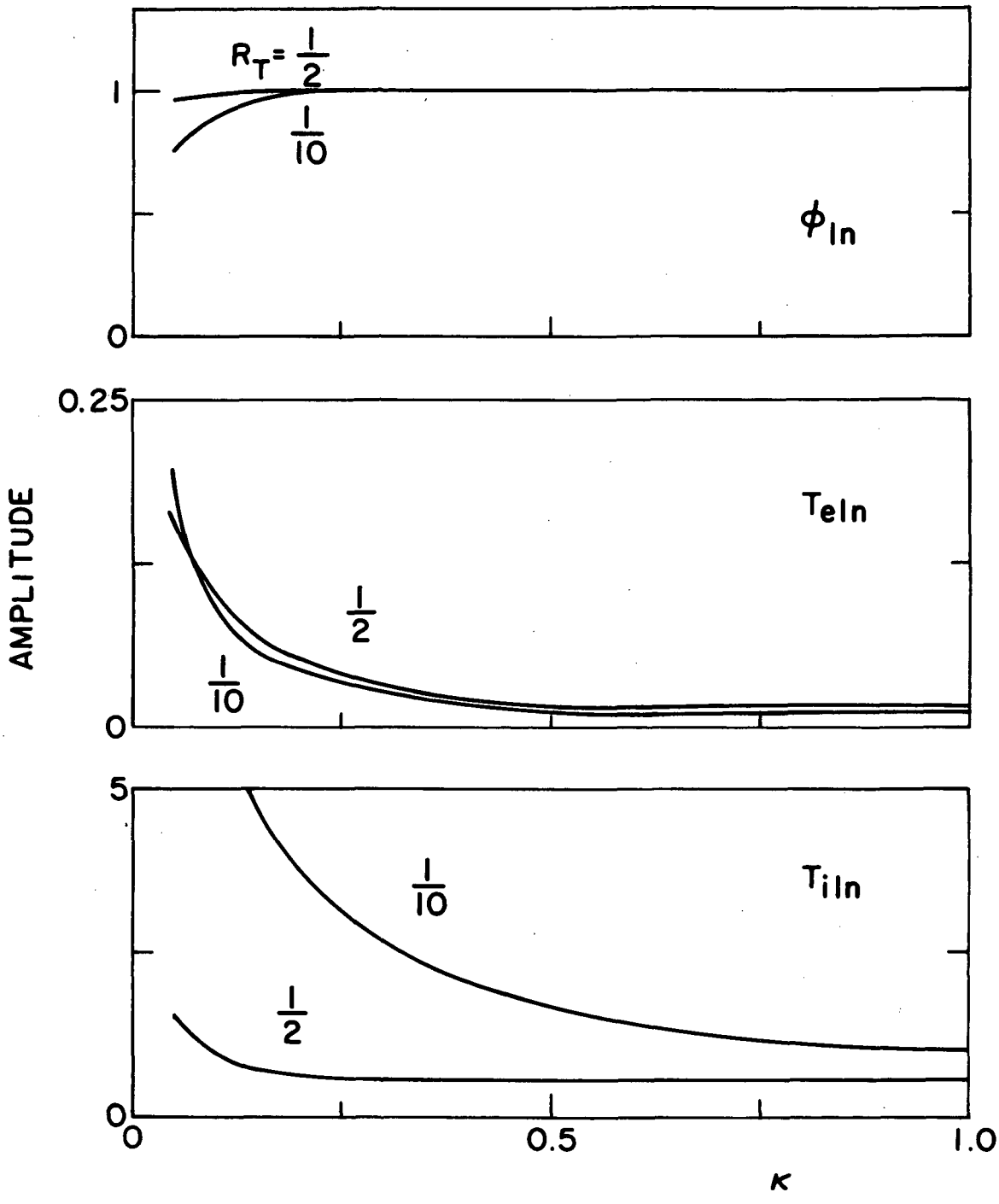

Fig. 5.3(a) Values of amplitude of the normalized variables ϕ_{1n}, T_{eln}, and T_{iln} for the conditions in Fig. 5.2 with R_T = 1/2, 1/10.

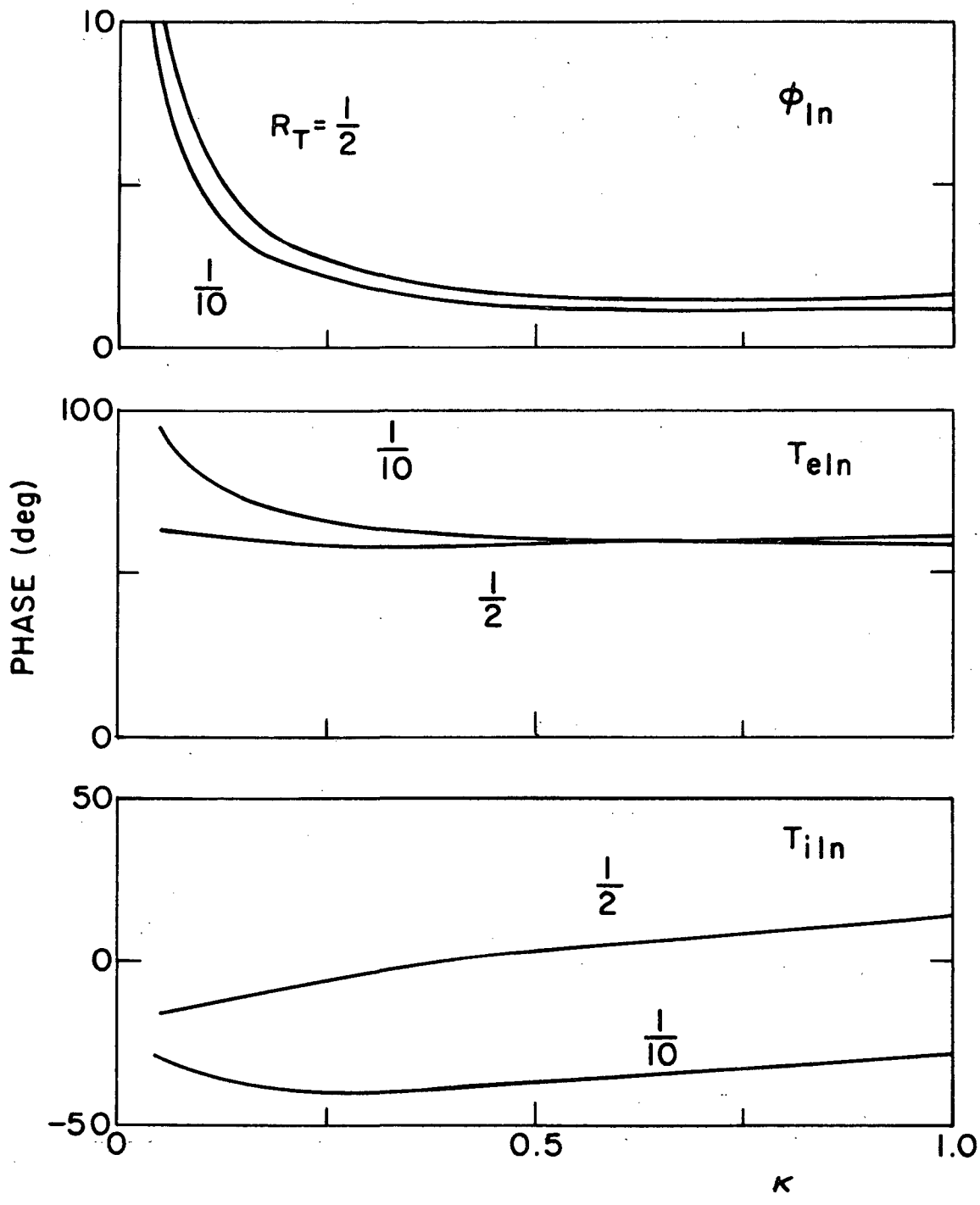

Fig. 5.3(b) Values of phase of the normalized variables ϕ_{1n}, T_{eln}, and T_{iln} for the conditions in Fig. 5.2 with $R_T = 1/2, 1/10$.

in phase, contrary to the drift wave in Section 4. The relative electron temperature oscillation is very small, as one might expect since the electrons behave nearly isothermally, and the phase is positive at $\sim 60^{\circ}$. Neither of these variables is much affected by variations in R_T. The relative ion temperature oscillation, on the other hand, is dependent on R_T; the amplitude is quite large and increases as R_T decreases, while the phase is negative for instability, but becomes positive when the plasma is stable. Thus, the characteristics of the ion temperature oscillation are the most noticeably affected by the presence of the instability.

Finally, we consider the effect of the assumption that the heat source terms S_i and S_e are not perturbed for the first order equations. For example, if we had assumed instead that these terms were proportional to the number density, n, the only change in the γ's in Section 5.1.2 would be that the factor $6(1-R_T)$ in γ_{11} [Eq. (5.13)] and γ_{31} [Eq. (5.15)] becomes $3(1-R_T)$. This affects the growth rate, in that the last term in Eq. (5.23) now becomes

$$- Z \frac{(1-5R_T/3)}{R_m^2(Z+5R_T/3)} ,$$

and the maximum growth is decreased to about half. However, the plasma can still be unstable, and the general characteristics described above are valid. Of course, to treat a specific problem rigorously, one would have to determine the explicit form of S_i and S_e by considering the physical processes which occur in the experiment being modeled. We have shown two general cases when instability can arise.

5.2.2 Effect of an Electron Drift

We now consider the stability of the ion-acoustic waves in the presence of an electron drift $V \left[= v_{e0}/(T_{e0}/m_e)^{\frac{1}{2}}\right]$. The approximation technique used in the last subsection to obtain the solution to the dispersion relation for $\varkappa^2 R_m^2 \gg 1$ and $R_T < 1$ is used again here [see Eq. (5.19)]. We find that the real frequency, Ω_r, is still given by Eq. (5.21), and that the growth (damping) rate is now

$$\Omega_i \approx \frac{2^{3/2}}{3}\frac{R_T^{5/2}}{R_m Z^2} C_{i\eta}\kappa^2 + \frac{2}{3}\frac{Z}{R_m^2} C_{e\eta}\kappa^2\left(1 - \frac{\kappa V}{\Omega_r R_m}\right)$$

$$+ \frac{2^{3/2}}{9}\frac{R_T^{7/2} C_{i\chi}\kappa^2}{Z^2 R_m (Z+5R_T/3)} + \frac{Z}{2R_m^2 C_{e\chi}}\left(1 - \frac{\kappa V}{\Omega_r R_m}\right) - \frac{2Z(1-4R_T/3)}{R_m^2(Z+5R_T/3)} \quad . \tag{5.27}$$

The drift manifests itself in the electron viscosity and thermal conductivity terms, and is destabilizing for $\kappa V/(\Omega_r R_m) > 0$, i.e., for the wave with phase velocity in the sense of v_{e0}.

Turning back for a moment to Section 4.3.3, it will be recalled that the drift waves were destabilized by an electron axial drift when the drift velocity exceeded the axial phase velocity of the wave. This effect arose when the electron heat transfer equation was included to account for finite heat flow along the magnetic field. The manner in which nonzero electron thermal conductivity can give rise to instability when an electron drift is present is illustrated in Eq. (5.27). Although this equation applies to ion-acoustic waves, we saw in Section 4.2.2 that the drift wave branch evolves into the ion-acoustic branch as the propagation becomes more nearly parallel to the magnetic field. Thus, we expect the effect of electron drift to be similar for each, as our calculations bear out. It should be mentioned that the effect of electron drift on drift waves is more involved than that implied by Eq. (5.27), in that the dispersion curves for V nonzero are not symmetrically displaced about the $V = 0$ curves (see Fig. 4.9). This difference between the drift waves and the ion-acoustic waves will also appear when we consider the normal mode solutions.

For the ion-acoustic waves, we may use Eq. (5.27) to find the drift velocity required for instability. This gives

$$\frac{v_{e0}}{[(ZT_{e0}+5T_{i0}/3)/m_i]^{1/2}} > 1 + \frac{\left\{2^{3/2} R_m R_T^{5/2}[(Z+5R_T/3)C_{i\eta}+R_T C_{i\chi}/3]\kappa^2 - 6Z^3(1-4R_T/3)\right\}}{Z^3(Z+5R_T/3)[(3/2C_{e\chi})+2C_{e\eta}\kappa^2]} \quad . \tag{5.28}$$

If we neglect electron viscosity (last term in denominator), and collisional energy exchange (last term in numerator), Eq. (5.28) reduces to Eq. (53) of Reference 8, apart from notation. It is clear that the threshold velocity is sensitive to the inclusion of the collisional energy exchange, and, as was shown in Section 5.2.1, may be zero, corresponding to instability driven purely by a temperature difference with $T_{e0} > T_{i0}$. Because of this, the threshold velocity calculated by Coppi and Mazzucato[8] may be quite inaccurate when $T_{e0} > T_{i0}$.

Figure 5.4 shows the real $\varkappa$ contour mapped into the Ω-plane, without drift and with a drift of $V = 4$, for the case of hydrogen ($R_m^2 = 1837$) with $R_T = 1/2$ and $1/10$. These results were computed from the full dispersion relation, although approximations given by Eqs. (5.21) and (5.27) give accurate results for their range of validity. It is seen that drift destabilizes the wave with phase velocity in the sense of the drift, and stabilizes the wave with phase velocity in the opposite sense. For the case $R_T = 1/10$, the drift of $V = 4$ roughly doubles the maximum growth rate predicted in the absence of drift. The spatial growth rate can be found by using Eqs. (5.26) and (5.27).

The amplitudes and phases of the normalized first order variables ϕ_{1n}, T_{e1n}, and T_{i1n} corresponding to these solutions are shown in Fig. 5.5. We have omitted some of the curves for $R_T = 1/2$ when they nearly coincide with the curves for $R_T = 1/10$. Comparing these curves with those for $V = 0$, i.e., Fig. 5.3, we see that the amplitudes of ϕ_{1n} and T_{i1n} are only slightly affected by the drift, while that of T_{e1n} increases by a factor of ~ 2 for $\varkappa > 0$, and ~ 4 for $\varkappa < 0$. Thus, as for the drift waves in Section 4.3.3, the electron drift increases the relative amplitude of the electron temperature oscillations. For the phases, both ϕ_{1n} and T_{e1n} have roughly opposite phase shifts depending on whether $\varkappa > 0$ or $\varkappa < 0$, with $\varkappa > 0$ corresponding to the negative phase shift. On the other hand, for either $\varkappa \gtrless 0$, the phase of T_{i1n} is nearly the same as when $V = 0$. Thus, while the behavior of T_{i1n} is dependent on R_T but not on V, the reverse is true for ϕ_{1n} and T_{e1n}.

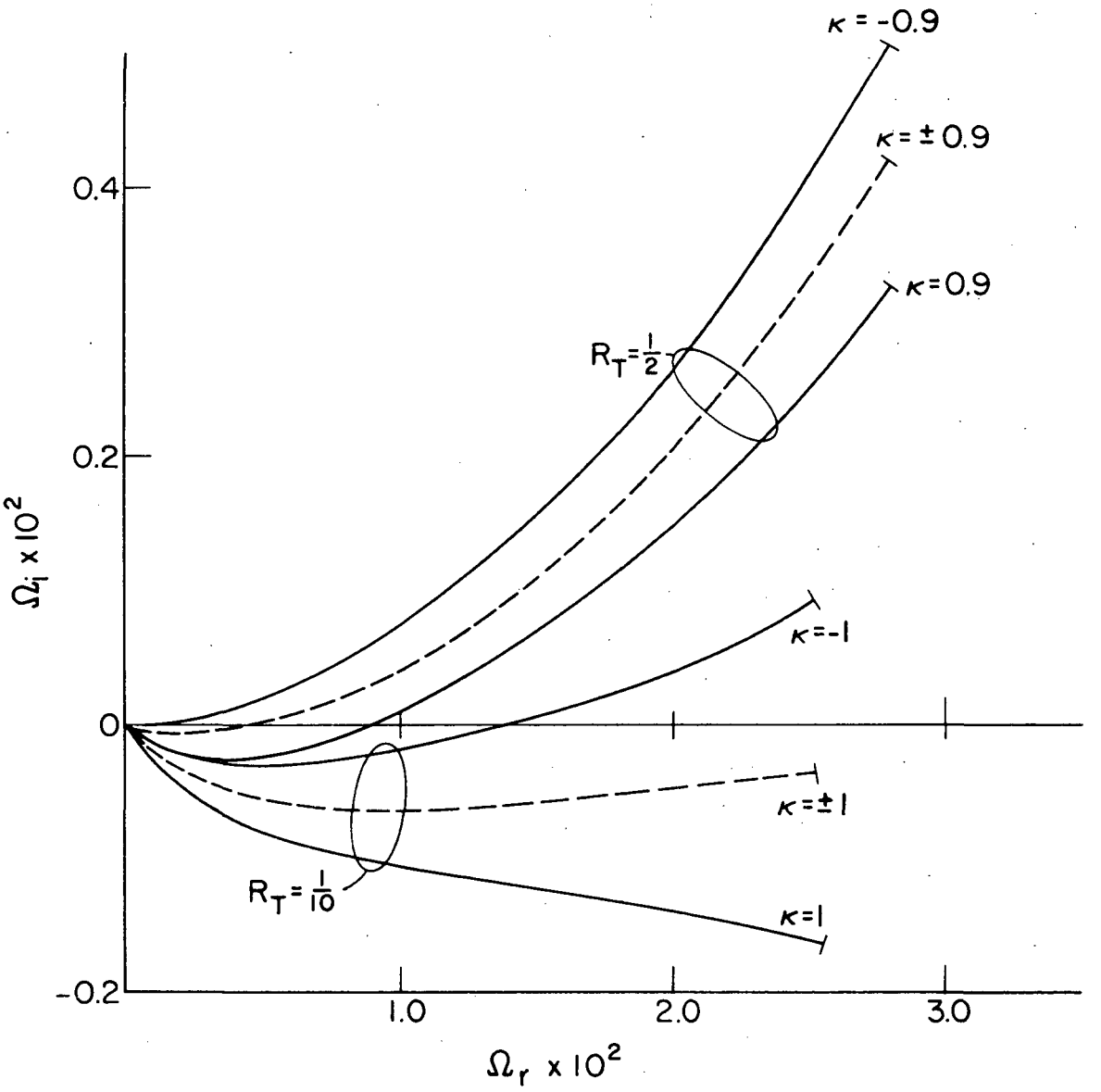

Fig. 5.4 Map of the real $\varkappa$ contour into the Ω-plane via Eq. (5.16) for the ion-acoustic wave brach with the parameters as in Fig. 5.2. ——, $v_{e0} = 4(T_{e0}/m_i)^{\frac{1}{2}}$; ----, $v_{e0} = 0$.

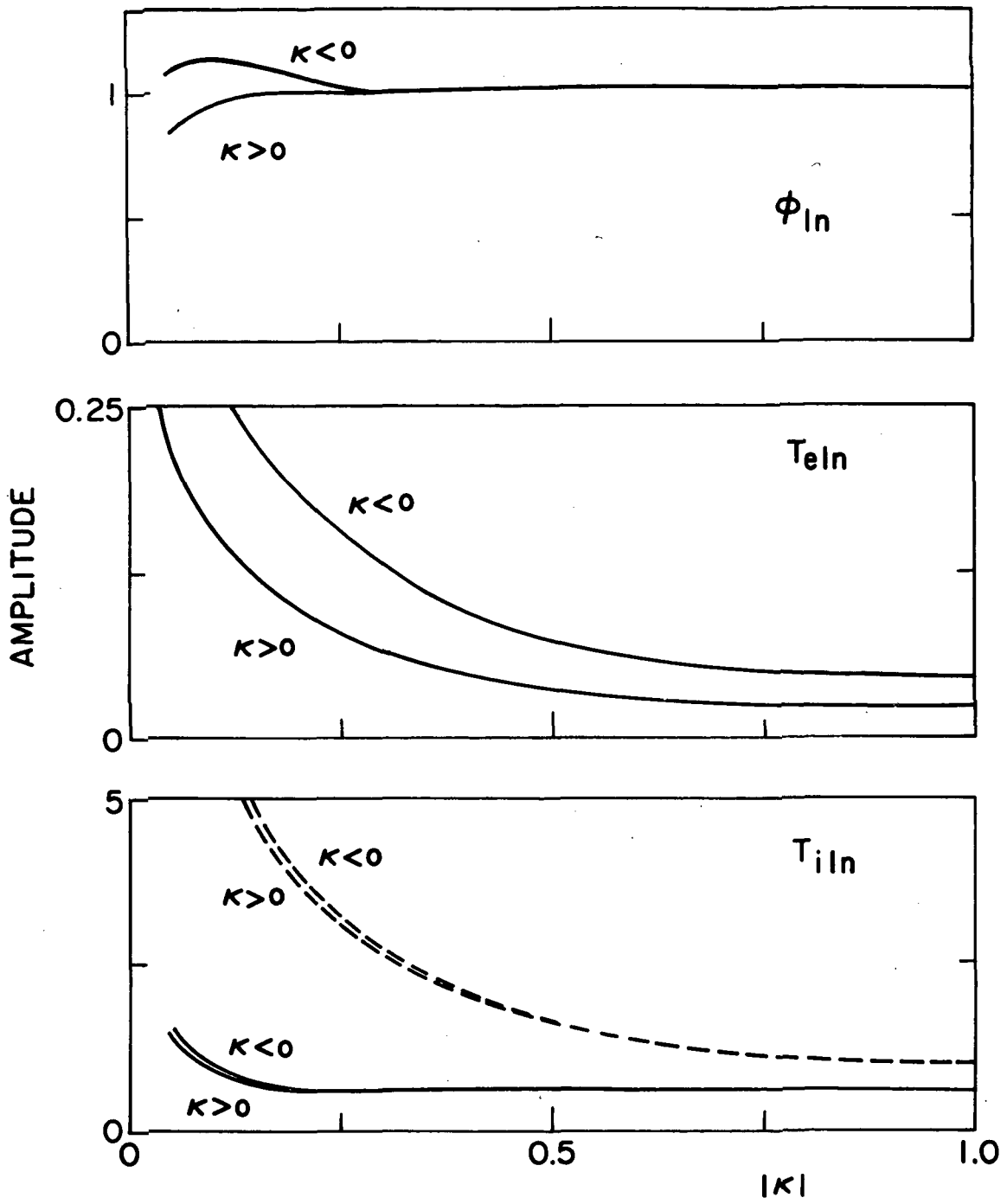

Fig. 5.5(a) Values of amplitude of the normalized variables ϕ_{1n}, T_{e1n}, and T_{i1n} for the ion-acoustic wave in Fig. 4.5 with $v_{e0} = 4(T_{e0}/m_i)^{\frac{1}{2}}$. ——, $R_T = 1/2$; ----, $R_T = 1/10$. Curves for $R_T = 1/10$ are omitted if they essentially coincide with $R_T = 1/2$ curves.

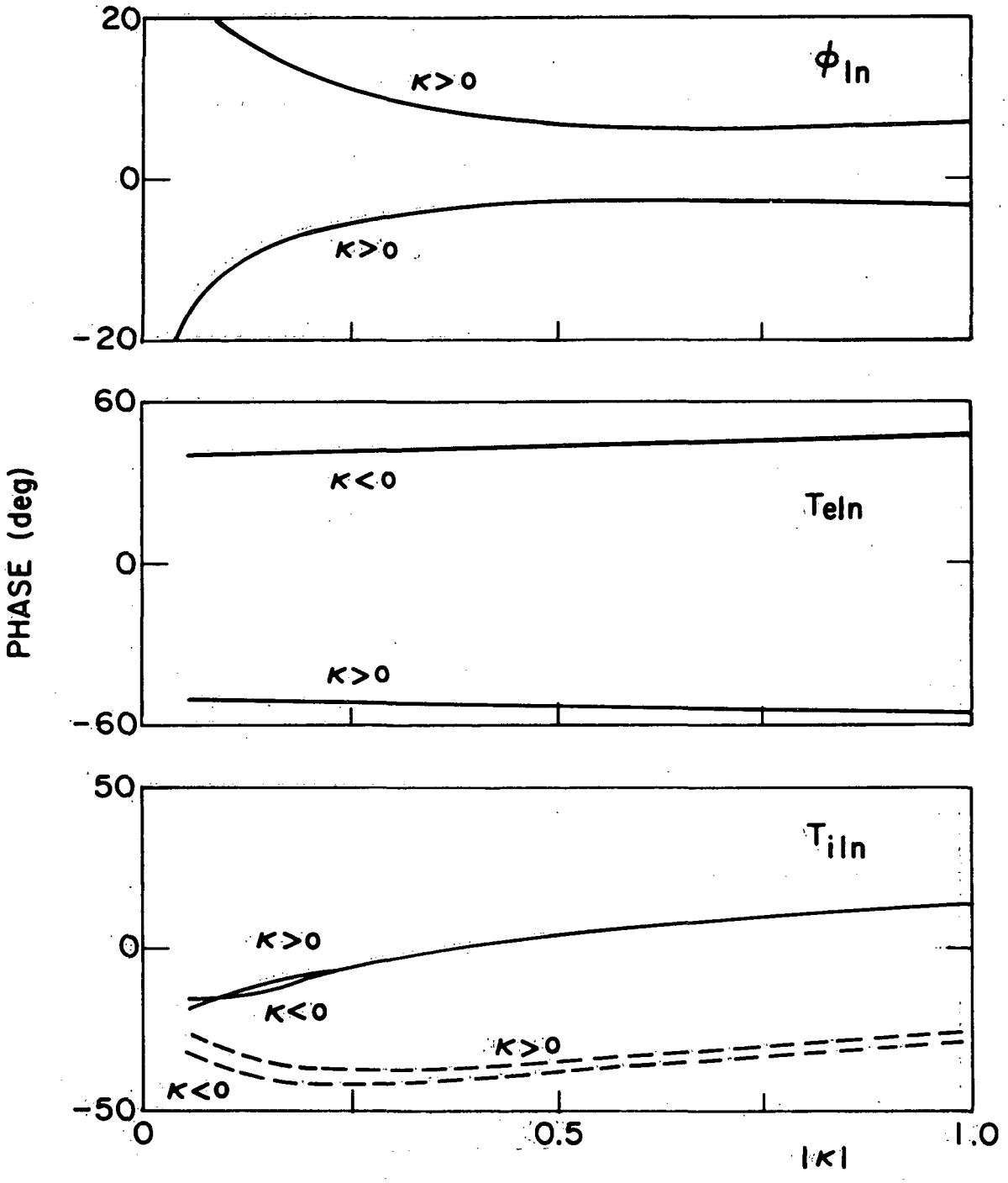

Fig. 5.5(b) Values of phase of the normalized variables ϕ_{1n}, T_{e1n}, and T_{i1n} for the conditions in Fig. 5.5(a).

5.2.3 Normal Mode Solutions

In order to describe the behavior of these ion-acoustic waves in an axially bounded system, we must solve the dispersion relation for complex Ω and complex κ, as discussed in Section 2. First, we consider the $V = 0$ case. Contours of constant $(\kappa_r^+ - \kappa_r^-)$ and constant $(\kappa_i^+ - \kappa_i^-)$ are mapped in the Ω-plane, where increasing values of $(\kappa_i^+ - \kappa_i^-)$ correspond to solutions for increasingly lossy reflections [see Eq. (2.28)]. The + or - superscript refers to waves propagating in the direction of increasing or decreasing z, respectively. This map is shown in Fig. 5.6 for $R_T = 1/10$, where the vertical scale is expanded by a factor of two over Figs. 5.2 and 5.4. We see that all the normal modes may be stabilized by increasing the reflection loss at the boundaries.

In performing this mapping for the case when an electron drift of $V = 4$ is present, we find that the effect of the electron drift appears to cancel out of the normal mode solutions. That is, the curve for $(\kappa_i^+ - \kappa_i^-) = 0$, which corresponds to lossless reflections, and $R_T = 1/10$, is the same as the curve for $V = 0$ and $R_T = 1/10$ shown in Fig. 5.6. In fact, the whole mapping is the same as found for the $V = 0$ case. This is due to the normal mode being made up of a wave propagating in each direction, one of which is amplified by the electron drift, while the other is damped by the same amount. This can be seen from Eq. (5.26) used in conjunction with Fig. 5.4. The effect of a temperature difference, on the other hand, is to amplify each wave; thus the temperature difference can contribute to the temporal growth rates of the normal modes.

The fact that the destabilization due to the electron drift disappears for the normal modes of an axially bounded system underscores the potential importance of the instability due to a temperature difference. For example, in a plasma which has an axial electric field applied (i.e., a DC current present), the electrons will heat up due to joule heating. The current driven ion-acoustic instability cannot contribute to the temporal growth rate of the normal modes because of the restrictions mentioned above, but instability will occur for the normal modes if the temperature ratio, R_T, becomes small enough. In this

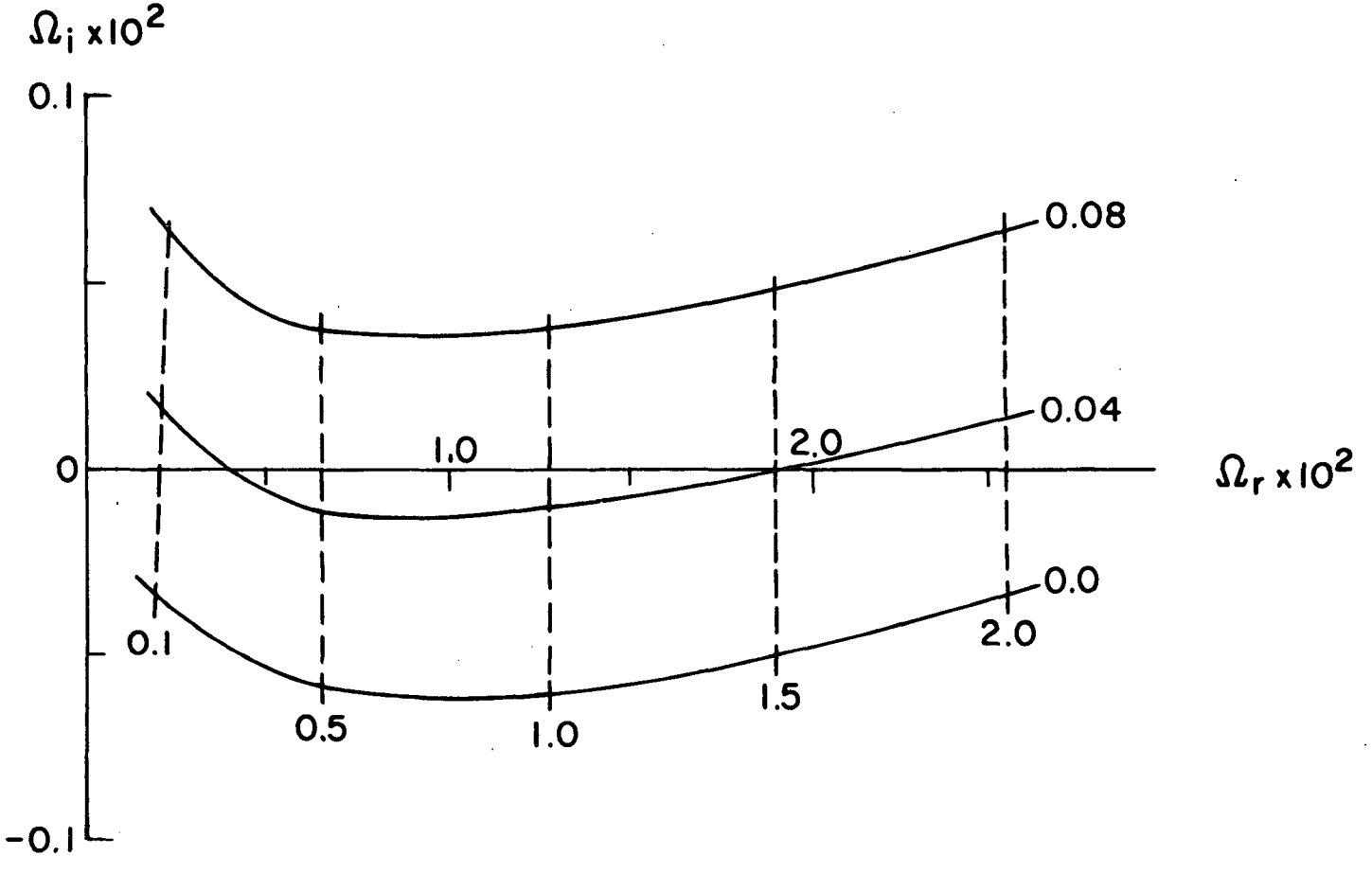

Fig. 5.6 Map of the difference $(\varkappa^+ - \varkappa^-)$ into the Ω-plane via Eq. (5.16) for $R_T = 1/10$. The curves are not dependent on V for the range considered ($0 \leq V \leq 4$).

connection, it should be noted that the wave propagating in the direction of the electron drift can exhibit spatial growth, so that there can be an enhancement of noise level along the system in the direction of this drift.

On the other hand, for toroidal systems, such as the stellarators considered by Coppi and Mazzucato,[8] periodic boundary conditions apply, and the normal modes consist of separate ion-acoustic waves propagating in either direction. In this case, the electron drift can have an effect on the stability of the normal modes as studied in Section 5.2.2.

5.3 Initial Value Problem: The Equilibrating Plasma

5.3.1 Steady State Plasma

In this subsection, we consider a plasma for which there are no external heat sources, so that $S_i = S_e = 0$. We take the system to have prescribed electron and ion temperatures at time $t = 0$. As before, we include the effect of an axial electric field which gives rise to the electron drift in Eq. (5.7) and also to joule heating of the electrons. We then allow the zero order temperatures to change in time as described by solutions to the heat transfer equations, i.e., Eqs. (5.3) and (5.6). These equations yield

$$\frac{\dot{T}_{e0}}{T_{e0}} = \frac{2}{3}\frac{C_r \nu_{ei}}{R_m^2} V^2 - 2\frac{\nu_{ei}}{R_m^2}(1-R_T), \quad \frac{\dot{T}_{i0}}{T_{i0}} = 2\frac{\nu_{ei}}{R_m^2}\frac{(1-R_T)}{R_T} \quad , \qquad (5.29)$$

where the dot denotes time differentiation. In order to obtain simple analytic solutions to these equations, we assume v_{e0} = constant, and normalize the time variable to $\tau = 2\nu_{ei}t/R_m^2$. This yields the solutions

$$T_{e0}(\tau) = \frac{T_{e0}(0)}{2}[1 + \exp(-2\tau)] + \frac{T_{i0}(0)}{2}[1 - \exp(-2\tau)]$$

$$+ \frac{C_r V^2(0)\, T_{e0}(0)}{12}[1 + 2\tau - \exp(-2\tau)] \quad ,$$

$$T_{i0}(\tau) = \frac{T_{i0}(0)}{2}[1 + \exp(-2\tau)] + \frac{T_{e0}(0)}{2}[1 - \exp(-2\tau)]$$

$$- \frac{C_r V(0) T_{e0}(0)}{12}[1 - 2\tau - \exp(-2\tau)] \quad . \qquad (5.30)$$

In Fig. 5.7, we show these solutions for $T_{e0}(0)/T_{i0}(0) = 10$, when $V = 0$ and $V(0) = 3$. For the $V = 0$ case, the temperatures relax to a common value of $[T_{e0}(0) + T_{i0}(0)]/2$ in a time $\tau \approx 2$. When $V(0) = 3$, the relaxation is slower, and both the electron and ion temperatures eventually increase due to joule heating of the electrons [the V^2 terms in Eq. (5.30)].

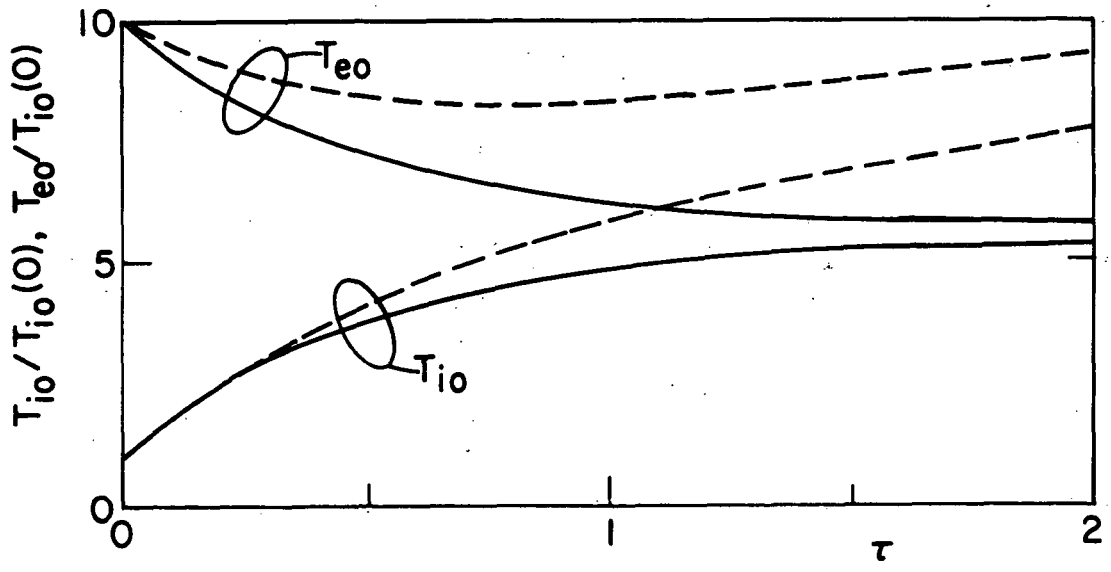

Fig. 5.7 Relaxation of electron and ion temperatures given by Eq. (5.30). ——— , $V = 0$; ---- , $V(0) = 3$.

5.3.2 Perturbed Plasma

In perturbing the basic equations to first order, we assume the variables n, E, v_e, v_i, T_e, and T_i have the form

$$n(z,t) = n_0 + n_1(t)\exp(-ikz) \quad , \tag{5.31}$$

where T_{e0} and T_{i0} are now functions of time. We make all the other assumptions quoted in Section 5.1.2, and use the same approach to derive the first order equations. By using the continuity equations [Eqs. (5.1) and (5.4)], we eliminate the velocity variables from the combined momentum transfer equations [Eqs. (5.2) and (5.5)]. This yields

$$\frac{1}{\nu_{ei}^2}\frac{\ddot{n}_1}{n_0} + \frac{4}{3}\frac{\varkappa^2}{R_m}\left[\frac{2^{1/2}C_{i\eta}R_T^{5/2}}{Z^2} + \frac{C_{e\eta}Z}{R_m}\right]\frac{1}{\nu_{ei}}\frac{\dot{n}_1}{n_0} +$$

$$\frac{\varkappa^2}{R_m^2}\left[-i\frac{4}{3}C_{e\eta}Z\frac{\varkappa V}{R_m} + (Z+R_T)\right]\frac{n_1}{n_0} + \frac{R_T\varkappa^2}{R_m^2}\frac{T_{i1}}{T_{i0}} + \frac{Z\varkappa^2}{R_m^2}\frac{T_{e1}}{T_{e0}} = 0 \quad . \tag{5.32}$$

The first order ion heat transfer equation [Eq. (5.3)] gives a second equation

$$\left[-\frac{1}{\nu_{ei}}\frac{\dot{n}_1}{n_0} - \frac{3Z(1-R_T)}{R_m^2 R_T}\frac{n_1}{n_0}\right] + \left[\frac{3}{2}\frac{1}{\nu_{ei}}\frac{\dot{T}_{i1}}{T_{i0}} + \left(\frac{2^{1/2}C_{i\chi}\varkappa^2 R_T^{5/2}}{R_m Z^2} + \frac{3Z}{R_m^2}\right)\frac{T_{i1}}{T_{i0}}\right]$$

$$+ \frac{3}{2}\frac{Z(1-3R_T)}{R_T R_m^2}\frac{T_{e1}}{T_{e0}} = 0 \quad . \tag{5.33}$$

Finally, the first order electron heat transfer equation [Eq. (5.6)] is

$$\left[-\frac{1}{\nu_{ei}}\frac{\dot{n}_1}{n_0} + \left(i\frac{\varkappa V}{R_m} + \frac{C_r V^2}{R_m^2} + \frac{3}{R_m^2}(1-R_T)\right)\frac{n_1}{n_0}\right] - \frac{3R_T}{R_m^2}\frac{T_{i1}}{T_{i0}}$$

$$+ \left[\frac{3}{2}\frac{1}{\nu_{ei}}\frac{\dot{T}_{e1}}{T_{e0}} + \left(-i\frac{3}{2}\frac{\varkappa V}{R_m} + \frac{3}{2}\frac{C_r V^2}{R_m^2} + C_{e\chi}\varkappa^2 - \frac{3}{2}\frac{(1-3R_T)}{R_m^2}\right)\frac{T_{e1}}{T_{e0}}\right] = 0 \quad . \tag{5.34}$$

If we assumed a time dependence of exp iωt, these equations would be very similar to Eqs. (5.10), (5.12), and (5.14) found in Section 5.1.2. However, we leave the time dependence unspecified for now, and find that, under the assumptions $\varkappa^2 \gg R_m^{-2}$ and $|\dot{n}_1/n_1\nu_{ei}| \sim \varkappa/R_m$, Eqs. (5.32) - (5.34) may be reduced to the single third order differential equation

$$\frac{\dddot{n}_1}{\nu_{ei}^3} + \Gamma_0 \frac{\ddot{n}_1}{\nu_{ei}^2} + \Gamma_1 \frac{\dot{n}_1}{\nu_{ei}} + \Gamma_2 n_1 = 0 \quad . \tag{5.35}$$

The coefficients of this equation are given by

$$\Gamma_0 = \frac{Z}{C_{e\chi} R_m^2} + \frac{4}{3} Z \frac{C_{e\eta}\varkappa^2}{R_m^2} + \frac{2^{5/2}}{3} \frac{C_{i\eta}\varkappa^2 R^{5/2}}{R_m} + \frac{2^{3/2}}{3} \frac{C_{i\chi}\varkappa^2}{Z^2 R_m} R_T^{5/2} + \frac{2}{R_m^2} \quad ,$$

$$\Gamma_1 = \frac{\varkappa^2}{R_m^2}(Z + 5R_T/3) - i \frac{Z\varkappa V}{C_{e\chi} R_m^3} - i \frac{4}{3} Z \frac{\varkappa V}{R_m^3} C_{e\eta}\varkappa^2 \quad ,$$

$$\Gamma_2 = \frac{2}{3} Z \frac{C_r \varkappa^2 V^2}{R_m^4} + \left(\frac{2^{3/2}}{3} \frac{C_{i\chi}\varkappa^2}{Z^2 R_m} R_T^{5/2} + \frac{2}{R_m^2} \right) \frac{\varkappa^2}{R_m^2} (Z+R_T) + \frac{2\varkappa^2(1-R_T)}{R_m^4} \quad . \tag{5.36}$$

Equation (5.35) is the counterpart of Eq. (5.19) for the maintained plasma.

5.3.3 Almost Time-harmonic Solutions

In order to solve Eq. (5.35), we assume that the time variation of the perturbed quantities is almost harmonic, and can be written as[81]

$$n_1(t) = n_1 \exp i \int \omega dt \quad , \tag{5.37}$$

where $|\omega_r| \gg |\omega_i|, |\dot{\omega}/\omega|$. We then may expand the derivatives in Eq. (5.35) to find an approximation to $\Omega_r = \omega_r/\nu_{ei}$ and $\Omega_i = \omega_i/\nu_{ei}$,

recalling that we have assumed $\kappa^2 R_m^2 \gg 1$, $R_T < 1$. This yields an Ω_r which is the same as was found for the maintained plasma [see Eq. (5.21)]

$$\frac{\Omega_r}{\kappa} = \pm \frac{(Z + 5R_T/3)^{\frac{1}{2}}}{R_m} \quad . \tag{5.38}$$

For the growth (damping) rate, we obtain

$$\Omega_i = \frac{2^{3/2}}{3} \frac{R_T^{5/2}}{R_m Z^2} C_{i\eta} \kappa^2 + \frac{2}{3} \frac{Z}{R_m^2} C_{e\eta} \kappa^2 \left(1 - \frac{\kappa V}{\Omega_r R_m}\right)$$

$$+ \frac{2^{3/2}}{9} \frac{R_T^{7/2}}{Z^2 R_m (Z+5R_T/3)} C_{i\chi} \kappa^2 + \frac{Z}{2R_m^2 C_{e\chi}} \left(1 - \frac{\kappa V}{\Omega_r R_m}\right) + \frac{2}{3} \frac{R_T}{R_m^2 (Z+5R_T/3)} \quad . \tag{5.39}$$

Here Ω_i is nearly the same as in Eq. (5.27) for a maintained plasma, except that the last term, due to collisional energy transfer, is now always positive. Thus, no instability can arise due only to an initial temperature difference in an equilibrating plasma, and one cannot expect an enhancement of the collisional equilibration by ion-acoustic waves. This conclusion is also reached in a similar analysis given recently by Kaw and Sundaram.[82] On the other hand, an electron drift can still produce instability, but, for moderate drifts, it will be quenched by the rise of the ion temperature in a time less than an e-folding period. For example, with an initial drift of $V = 3$, and $R_T = 1/10$, as in Fig. 5.7, the initial maximum growth rate is

$$\omega_i \approx - \frac{\nu_{ei}}{R_m^2} \quad . \tag{5.40}$$

At this value, the wave would e-fold in a time $\tau \approx 2$. However, as can be seen from Fig. 5.7, the ratio R_T has already increased to $1/2$ at $\tau \approx 1$; this is sufficient to quench the instability. This approach becomes less certain for larger drifts, since the zero order quantities change quite rapidly [see Eq. (5.30)]. Also, as the electron temperature increases, the electron mean free path increases as T_{e0}^2, and the plasma becomes less collisional.

5.4 Applications

To determine the importance of ion-acoustic instability for physical systems, one needs to compare its growth rate with that of other instabilities which might be present. For laboratory magnetoplasmas, there is usually a density gradient perpendicular to the magnetic field, so that drift waves can be unstable. The maximum growth rate for the drift wave is $\sim m\omega_{De}/3$, where ω_{De} is the electron diamagnetic frequency, and m is the azimuthal mode number. This maximum growth rate is valid for $T_{i0} \leq T_{e0}$. Since the ion-acoustic instability can occur due to a temperature difference for $T_{i0} < T_{e0}$, it is useful to compare the numerical values of the growth rates for realistic parameters. The diamagnetic frequency and the collision frequency ν_{ei} are both independent of mass, while the ion-acoustic growth rate is inversely proportional to mass. With this in mind, we consider a hydrogen plasma which has the same electron diamagnetic frequency and collision frequency as in the Q-machine experiment studied in Section 4.4 (for the $m = 2$ mode as in Fig. 4.3). This gives a maximum drift wave growth rate for the $m = 2$ mode of $-\omega_i \sim 5 \times 10^3$ sec^{-1}, while the ion-acoustic instability would have a maximum growth rate of $-\omega_i \sim 1 \times 10^4$ sec^{-1} for the same collision frequency and $T_{i0} \ll T_{e0}$. Higher order azimuthal modes for the drift wave have higher upper limits on the growth rate due to the dependence on m, but they are also more strongly damped by ion collisional viscosity. In any event, it is clear that the ion-acoustic waves can have growth rates comparable to or larger than those for drift waves.

Another important point is that the drift waves are stabilized by even moderate wavelengths (see Fig. 4.5), while the ion-acoustic waves can be unstable for shorter wavelengths, of the order of the electron mean free path. Thus, in short collisional plasmas, the drift waves can be stabilized or have their growth rates greatly reduced by the normal mode requirement of short axial wavelengths, while the ion-acoustic growth rate is relatively unaffected.

Since ion-acoustic waves also appear in weakly ionized plasmas,[46] it is of interest to determine if the two-temperature instability might occur there. The presence of neutrals is introduced by adding a

collision term $-nm_i\nu_{in}v_i$ to the right hand side of the ion momentum transfer equation, i.e., Eq. (5.2). Here ν_{in} is the ion-neutral momentum transfer collision frequency. We neglect electron-neutral collisions, since in adding the electron and ion momentum transfer equations in the absence of drift, the term proportional to ν_{en} is smaller than the ν_{in} in terms by a factor R_m. This is due to the relation $\nu_{en}/\nu_{in} \sim R_m$ which holds for a number of gases.[46] The effect of ion-neutral collisions is to add the term $\nu_{in}/2\nu_{ei}$ to the expression for the growth rate, i.e., Eq. (5.23). This corresponds to damping. Thus, for the ion-acoustic wave to be unstable due to a temperature difference in a plasma with neutrals present, ν_{in} must be smaller than the maximum growth rate of $\sim \nu_{ei}/R_m^2$. However, for typical weakly ionized plasmas such as the positive column, this condition is not met,[7] and, even though $T_{i0} \ll T_{e0}$, two-temperature ion-acoustic instability should not occur.

For naturally occurring plasmas, there are several possible situations in which ion-acoustic instability might arise. The daytime ionosphere does have a sufficient temperature difference between the ions and electrons[83] to produce instability. However, further investigation reveals there is enough neutral gas present[84] to cause the ion-neutral collisions to quench the instability.

In the case of the solar wind, Cuperman and Harten[13] have shown that the observed radial profiles of density and temperatures can only be explained by the two-species fluid equations if one assumes a heat transfer between electrons and protons some 30 times the collisional value. Using the collisional value gives an ion temperature near the earth which is lower than measured. It has been suggested that such an enhanced heat transfer is due to turbulence in Alfvén waves originating at the sun. Another possibility which should be investigated is that the solar wind is unstable to low-frequency ion-acoustic waves (for $T_i < T_e$), and such turbulence accounts for the enhanced heat transfer.

6. CONCLUSIONS

6.1 Review of the Research

The primary purpose of this work has been to study the characteristics of low-frequency, quasistatic instabilities of a fully ionized plasma. A moment equation description has been used for both the ions and the electrons. Before these instabilities were studied, Section 2 was devoted to developing a general method for interpreting the behavior of waves in a bounded system from solutions of the dispersion relation for the waves in an infinite medium. This was an extension of the stability analysis given by Briggs[19] for an infinite system. The result is that the dispersion relation, $D(\omega,\underset{\sim}{k}) = 0$, must be solved for complex $\underset{\sim}{k}$ in general, as determined by the reflection coefficients of the boundaries. This approach gives a very useful technique for determining the normal mode frequencies and corresponding wave profiles for bounded systems which can be described by the moment equations. The response of such a system to a steady forcing function source was also given.

In Sections 3 - 5, the low-frequency instabilities have been studied in detail. The equations describing the plasma were perturbed about zero order solutions to determine the dispersion relations for the waves. The dispersion relation given by Eq. (4.24) for rectangular geometry illustrates the basic wave types considered. For reference, the branches of this dispersion relation are plotted in Fig. 6.1, where the parameters are as in Fig. 4.3. The normalized frequency, w, and axial wavenumber, K, are given by Eq. (4.27). In Section 3, the flute wave has been studied for propagation perpendicular to the axial magnetic field (K = 0) in a cylindrical plasma column. This wave is represented by branch II in Fig. 6.1. A differential equation was derived to describe the wave, which can be driven unstable by a radial electric field. When the electric field was a linear function of radius, the column rotated uniformly due to the $\underset{\sim}{E} \times \underset{\sim}{B}$ drift. In this case, instability was due to the centrifugal force on the ions in the presence of a radial density gradient. We obtained an analytic expression for the eigenfrequency which included the effect of the column being radially bounded. This led to a generalization of some numerical results found by Chen[63] on the

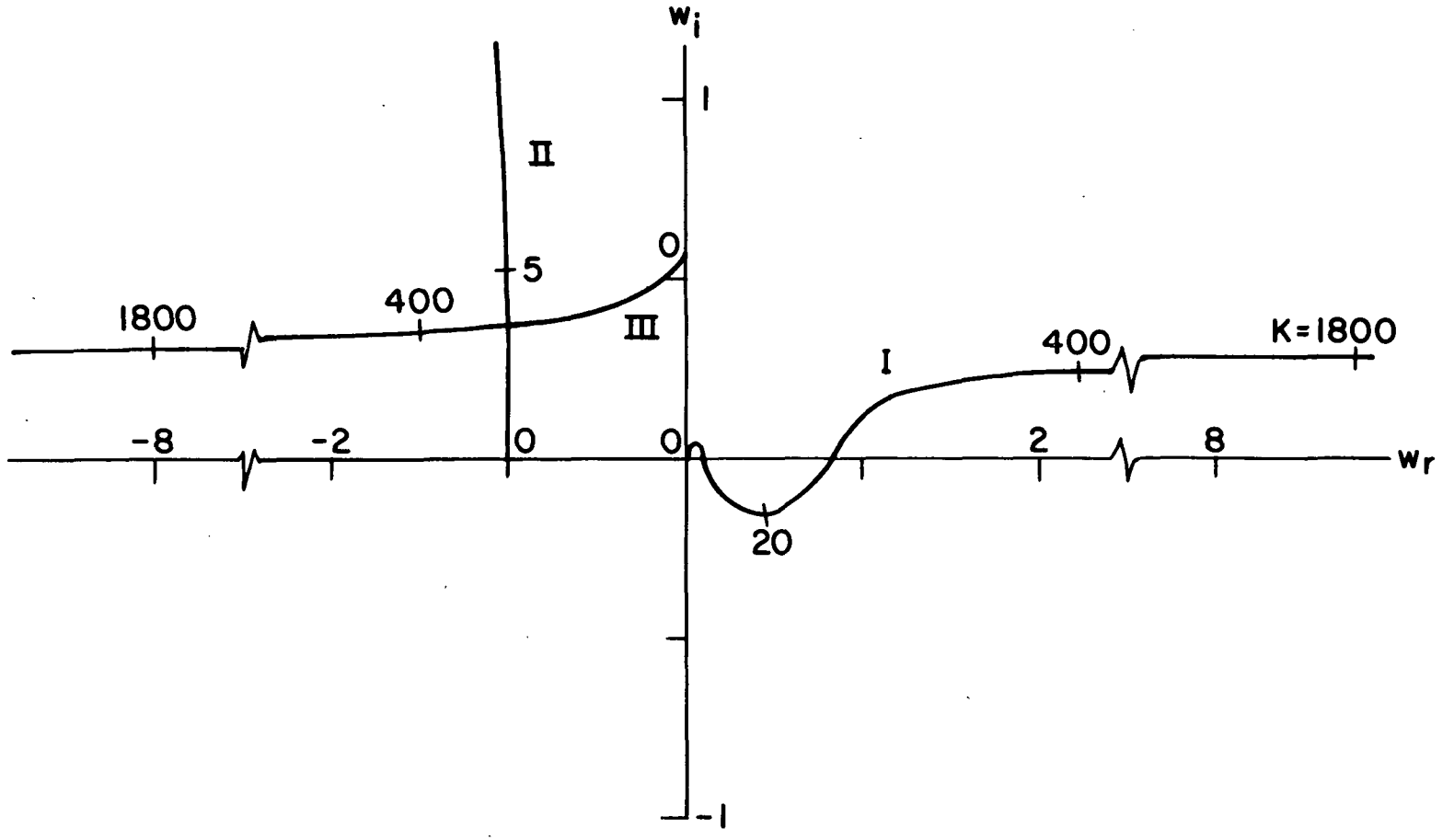

Fig. 6.1 Map of K real into the w-plane via Eq. (4.24) for the conditions in Fig. 4.3. Branch I is the drift wave for small K , while branches I and III evolve into a pair of ion-acoustic waves for large K . Branch II denotes the flute wave.

effect of the column being radially bounded. If the effect of centrifugal force were included in the solutions shown in Fig. 6.1 by including a gravitational force, branch I and branch II would couple together for small K to produce one stable wave and one unstable wave. These would correspond to the pair of eigenfrequencies given by Eq. (3.35). For nonuniform rotation of the column, a numerical procedure was used to solve the differential equation for the wave solutions. The transition to a Kelvin-Helmholtz instability[37,38] was illustrated for a sharp rotational velocity shear. These numerical solutions also gave the eigenfunctions of the waves. Finally, two instabilities in a hollow cathode arc experiment were identified as being unstable flute waves.

In Section 4, we have considered propagation at an angle to the axial magnetic field ($K \neq 0$), and concentrated on the collisional drift wave. This corresponds to branch I in Fig. 6.1 for small K (< 100). The drift wave can be unstable due only to a density gradient. A complete dispersion relation was derived in rectangular geometry, and it included the effects of ion axial motion, electron heat flow, and a zero order electron axial drift (a current). The solutions of the dispersion relation were compared to those of other authors, who neglected some of the effects included in Section 4. The relative magnitudes and phases of the first order wave variables were calculated. We also showed how the characteristics of the entropy[45] wave (see Fig. 4.6) differ from those of the drift wave. The solutions to the dispersion relation were interpreted in the manner prescribed in Section 2 for axially bounded systems. This allowed us to correctly explain the results of a drift wave experiment in a Q-machine.[47] In addition, we showed that a zero order electron drift can increase the growth rates of the normal modes of the drift wave for a bounded system.

As the angle of propagation becomes more nearly parallel to the magnetic field (K large), branches I and III in Fig. 6.1 become a pair of ion-acoustic waves. The stability of these waves has been studied in Section 5 for propagation parallel to the magnetic field. The ion-acoustic waves can be driven unstable by an electron drift in a collisional plasma if electron thermal conductivity is included, as shown by Coppi

and Mazzucato.[8] We have extended this result to show that inclusion of collisional energy exchange between the electrons and ions can significantly decrease the threshold velocity for instability when $T_i < T_e$. Additionally, we have shown that the collisional energy transfer can cause instability in the absence of an electron drift. The relative magnitudes and phases of the first order variables were also given. Further, it was found that, for an axially bounded system, the electron drift does not contribute to the temporal growth of the normal modes. These results hold for a plasma which is maintained in the steady state with $T_i < T_e$. For the case of a plasma equilibrating in time $(T_i \rightarrow T_e)$, it was shown that the collisional ion-acoustic instability should not grow to a significant level.

6.2 Suggestions for Future Work

For the linear analysis of the waves we have considered, there are several extensions which would be of interest. First, for propagation at an angle to the magnetic field, the restriction $\omega \ll \omega_{ci}$ could be relaxed. This would allow investigation of the region around ω_{ci}, where ion cyclotron waves can propagate, and would show the transition to such waves. Second, the ion-acoustic instability could be treated for specific systems, such as the solar wind or a Q-machine with a current, in which heat sink or source terms were identified. In solving the zero order and first order equations, numerical procedures would probably have to be used. It would also be useful to determine the effects on the ion-acoustic instability of propagation at an angle to the magnetic field, and the presence of a radial density gradient.

There are several suggestions which can be made about the extension to a nonlinear analysis of the instabilities studied. First, the stability analysis of Section 2 for bounded systems shows that in general the linear wave amplitude profile in a system will not be uniform in space. Thus, nonlinear analyses which assume an infinite medium with uniform wave amplitude must be viewed with caution; future nonlinear analyses should attempt to determine the effect of a nonuniform wave amplitude. Second, Horton and Varma[9] have recently suggested that small scale turbulence may cause "collisionless" plasmas to appear collisional for waves, so that a moment equation description of

instabilities would be adequate. A more quantitative evaluation of this effect would be helpful.

Appendix A

RESPONSE OF A BOUNDED SYSTEM TO AN ARBITRARILY POSITIONED SOURCE

We use the same model as in Section 2.2.1, except that now the source has the form $s(t,z) = f_0(t)\,\delta(z-z_0)$. The medium is described by Eq. (2.9) while the boundaries are described by Eq. (2.12). To evaluate the response, we use the approach developed in Section 2.2.2, and model the reflected waves by an infinite series of image sources. The resulting model is shown in Fig. A.1. The image source values are still given by Eqs. (2.14) and (2.15), but the source f_n is now located at $nL + z_0(-1)^n$. The shaded area again denotes the reciprocal medium with dispersion relation $D(\omega,-k) = 0$. The response of each source in this mixed medium can be found by the procedure described in Section 2.2.2, and illustrated in Fig. 2.7. This yields the result that any source f_n at $z = nL + z_0(-1)^n$ can be replaced by a source $\bar{f}_n$ at $z = nL/2 + (1-\Delta)z_0$, which is subject to the regular medium only. Here $\Delta = 1$ if n is odd, and $\Delta = 0$ otherwise. The $\bar{f}_n$'s are given by

$$\bar{f}_n = \exp\left[-\,ik^{\pm}(nL/2 - \Delta z_0)\right] f_n \quad , \tag{A.1}$$

where $k^{\pm}$ is used for $n \gtrless 0$. Equation (A.1) is the generalization of Eq. (2.19) for which $z_0 = 0$. The total response in the bounded region $(-L/2 \le z \le L/2)$ is obtained by using Eqs. (2.3) and (2.4) to find the responses to all of the $\bar{f}_n$ sources, and adding the results. This gives

$$\psi(t,z) = \frac{1}{2\pi}\int_{-\infty+i\sigma_0}^{\infty+i\sigma_0} \frac{-if_0(\omega)}{k^+ - k^-}\left\{\exp[-ik^{\pm}(z-z_0)] + \bar{A}(z)\sum_{m=1}^{\infty}\exp[-im(\bar{\alpha}_1+\bar{\alpha}_2)]\right\}\exp i\omega t\, d\omega \, , \tag{A.2}$$

where $k^{\pm}$ is used for $z \gtrless z_0$. The other quantities in Eq. (A.2) are

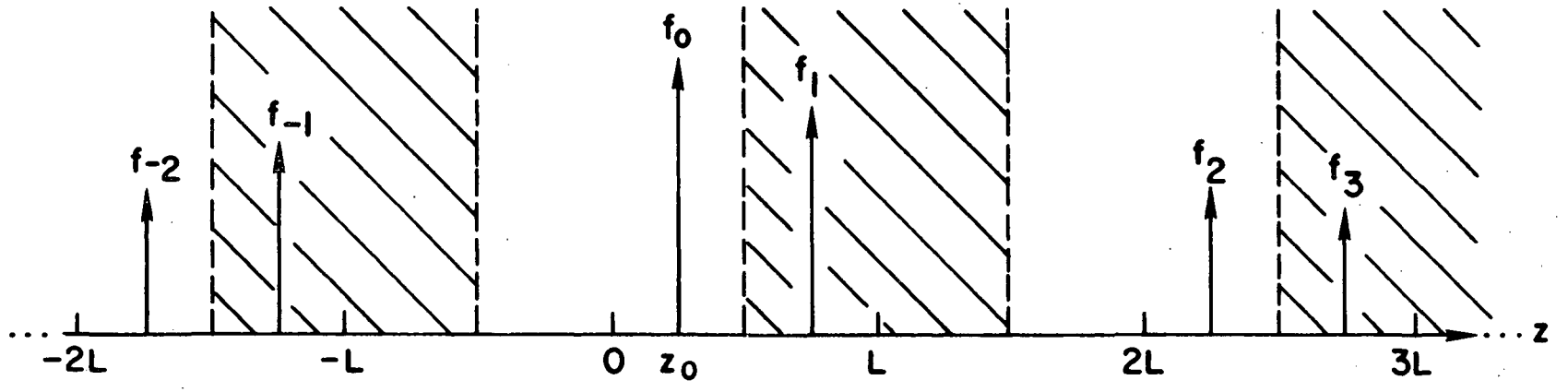

Fig. A.1 Bounded system ($-L/2 \leq z \leq L/2$) modeled as an infinite system with image sources as given in Eqs. (2.14) and (2.15). Shaded area contains the reciprocal medium.

$$\bar{\alpha}_1 = (k^+ - k^-)(\frac{L}{2} + z_0) \mp \theta_1 + i\ell n|\rho_1| , \qquad (A.3)$$

$$\bar{\alpha}_2 = (k^+ - k^-)(\frac{L}{2} - z_0) \mp \theta_2 + i\ell n|\rho_2| , \qquad (A.4)$$

and

$$\bar{A}(z) = \left\{(1+\exp i\bar{\alpha}_1)\exp[- ik^-(z-z_0)] + (1+\exp i\bar{\alpha}_2)\exp[- ik^+(z-z_0)]\right\}. \qquad (A.5)$$

Note that these equations indeed reduce to Eqs. (2.20-2.23) for the special case $z_0 = 0$.

We now prove that the form of the asymptotic natural response is independent of the source position, z_0. For the natural response, $f_0(t)$ is taken to be an impulse function, so $f_0(\omega) = 1$ in Eq. (A.2). The normal mode frequencies are defined by the relation

$$\bar{\alpha}_1 + \bar{\alpha}_2 = 2n\pi \quad , \qquad (A.6)$$

where n is an integer. This is the condition for branch points in the integrand of Eq. (A.2) due to the reflected waves, and is the counterpart to Eq. (2.25), where $z_0 = 0$. However, from Eqs. (2.21), (2.22), (A.3) and (A.4), we have

$$\alpha_1 + \alpha_2 = \bar{\alpha}_1 + \bar{\alpha}_2 \ , \qquad (A.7)$$

so Eqs. (2.25) and (A.6) are in fact identical. Thus, Eq. (2.28), which gives the restrictions on $(k^+ - k^-)$ for the normal modes, is independent of z_0, as is Eq. (2.29), which gives the normal mode frequencies, ω_n.

In addition, we show that the axial profile of the asymptotic natural response is independent of z_0. As in Eq. (2.27), the axial profile is given by $\bar{A}(z)$. Using Eqs. (A.3) - (A.6), $\bar{A}(z)$ can be reduced to

$$\bar{A}(z) = P\left\{|\rho_1|^{\frac{1}{2}} \exp i(\phi - k^+z) + |\rho_2|^{\frac{1}{2}} \exp[-i(\phi + k^-z)]\right\} , \qquad (A.8)$$

where $\phi = n\pi/2 \pm (\theta_1 - \theta_2)/4$. The constant P has the form

$$P = 2 \exp\left[(k_i^+ - k_i^-)\frac{L}{4} + i(k^+ + k^-)\frac{z_0}{2} + in\pi\right] \cos\frac{\bar{\alpha}_1}{2} \quad , \tag{A.9}$$

and contains all of the z_0 dependence, but is independent of z. Thus, the axial dependence is given by the terms within the brackets of Eq. (A.8), and can be reduced directly to the profile given by Eqs. (2.41) and (2.42).

Appendix B

ION VELOCITY DUE TO A RADIAL ELECTRIC FIELD IN CYLINDRICAL GEOMETRY

In Section 3.1.1, we found the ion fluid velocity in the approximation that the rotation frequency v_0/r is much less than ω_{ci}. We now consider the solution to the ion equation of motion for larger electric fields; first from the fluid equation [Eq. (3.3)], for an electric field which increases linearly with radius, so we may neglect viscosity; and second, from the single particle equation of motion. We neglect the density gradient as contributing only a small diamagnetic drift for these larger fields; this allows a more direct comparison between the methods. The second method will clarify the understanding of the actual orbits of the ions.

With the electric field a linear function of radius, the radial and azimuthal components of Eq. (3.3) become

$$m\left(v_r \frac{\partial v_r}{\partial r} - \frac{v_\theta^2}{r}\right) = eE + ev_\theta B, \tag{B.1}$$

and

$$m\left(v_r \frac{\partial v_\theta}{\partial r} + \frac{v_\theta v_r}{r}\right) = - ev_r B , \tag{B.2}$$

respectively. Here $\underset{\sim}{v}_i = v_r \hat{\underset{\sim}{i}}_r + v_\theta \hat{\underset{\sim}{i}}_\theta$, and we have dropped all the subscripts i. The coordinate system is shown in Fig. 3.1. Equation (B.2) can also be written as

$$v_r\left[\frac{\partial v_\theta}{\partial r} + \frac{v_\theta}{r} + \omega_c\right] = 0 , \tag{B.3}$$

where $\omega_c = eB/m$ is positive. Thus, we may have two solutions: either $v_r = 0$, or the terms in the bracket add to zero. We denote these by Solution I and Solution II, respectively. Using Eq. (B.1), Solution I becomes

$$v_r = 0 \ , \qquad v_\theta = \frac{\omega_c r}{2}\left[-1 + \left(1 - \frac{4E}{\omega_c r B}\right)^{\frac{1}{2}} \right] \ , \tag{B.4}$$

where we have required $v_\theta \to 0$ for $E \to 0$. For Solution II, we require v_θ to remain finite as $r \to 0$, and find

$$v_r = \frac{\omega_c r}{2}\left(\frac{4E}{\omega_c r B} - 1\right)^{\frac{1}{2}} \ , \qquad v_\theta = -\frac{\omega_c r}{2} \ . \tag{B.5}$$

Since the velocities must be real, we use Solution I for $4E/(\omega_c r B) < 1$, and Solution II otherwise. We show the behavior of the velocity as a function of the electric field strength in Fig. B.1. Also shown is the small electric field approximation used in Section 3.1.1 [see Eq. (3.8)]. This is obtained by expanding Eq. (B.4) to second order in E for small $4E/\omega_c r B$, to give

$$v_\theta = v_E\left(1 - \frac{v_E}{\omega_c r}\right) , \tag{B.6}$$

where $v_E = -E/B$. Figure B.1 shows the validity of this approximation, if we restrict ourselves to rotation frequencies much less than ω_c. The asymmetry of the rotation velocity for $v_E > 0$ and $v_E < 0$ is due to the centrifugal force, as mentioned in Section 3.1.1, which always acts outward, opposing or aiding the electric field force for $v_E > 0$ or $v_E < 0$, respectively. The behavior of the solutions near $v_E/\omega_c r = -1/4$, where the solutions change abruptly, becomes clear if we consider the motion of a single particle.

The equations of motion for a charged particle in cylindrical geometry with an axial magnetic field can be readily obtained using a Hamiltonian method.[85] The canonical equation for angular momentum gives

$$\frac{m}{r}\frac{d}{dt}(r^2\dot{\theta}) + eB\,\dot{r} = 0 \ , \tag{B.7}$$

where the dot denotes the time derivative. Assuming that the particle starts from rest at some position $r = a$, Eq. (B.7) can be integrated to give

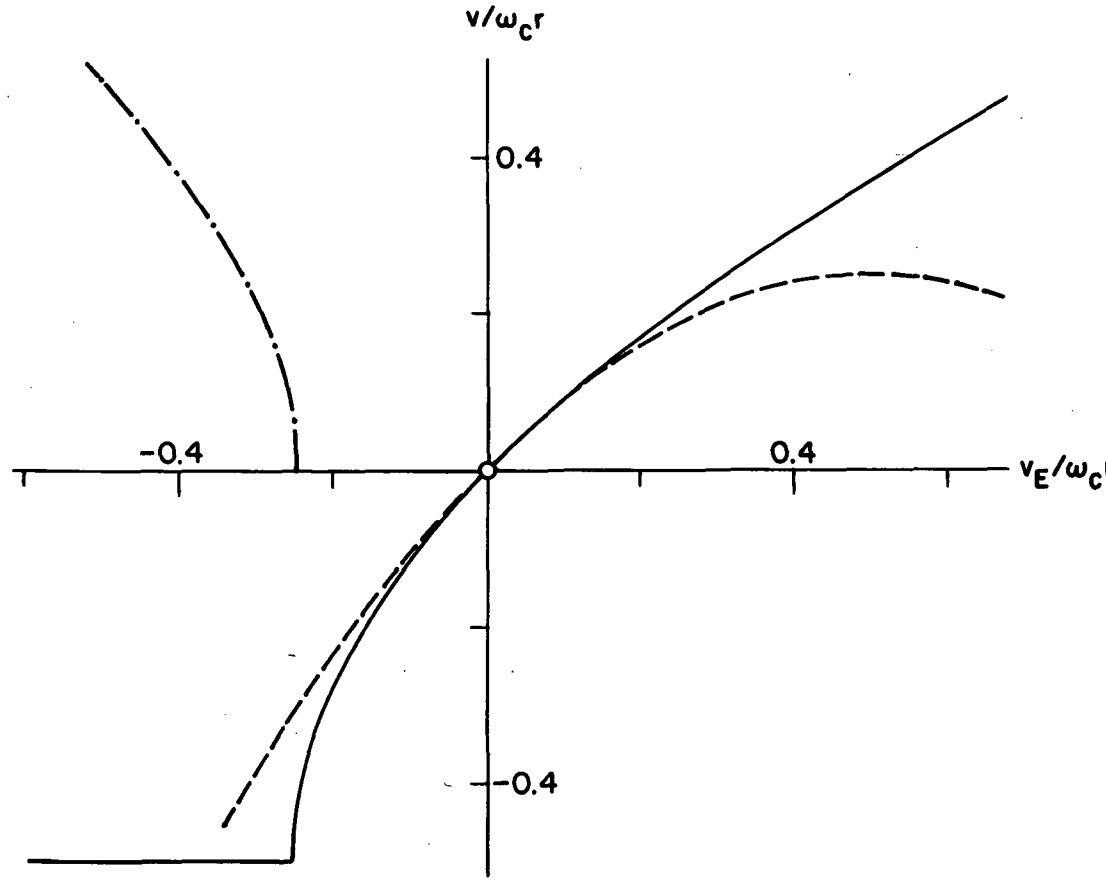

Fig. B.1 Fluid velocity components due to a radial electric field ($v_E = -E/B$) from Eqs. (B.4) and (B.5). ——, v_θ; -·-·-·, v_r; ----, v_θ from Eq. (B.6).

$$v_\theta = r\dot{\theta} = -\frac{\omega_c}{2r}(r^2 - a^2). \qquad (B.9)$$

The conservation of energy for the particle is written as

$$\frac{m\dot{r}^2}{2} + \frac{mr^2\dot{\theta}^2}{2} - \frac{eEr}{2}\left(1 - \frac{a^2}{r^2}\right) = 0 \quad , \qquad (B.10)$$

where the last term is the potential energy. Using Eqs. (B.9) and (B.10), we find

$$\dot{r}^2 = \left(1 - \frac{a^2}{r^2}\right)\left(\frac{eEr}{m} - \frac{\omega_c^2 r^2}{4}\left[1 - \frac{a^2}{r^2}\right]\right) \quad . \qquad (B.11)$$

At the turning points of the orbit, the radial velocity, $\dot{r}$, must be zero. One such point is $r = a$, but for the orbit to be closed, we must have a second zero; this occurs when the terms in the second bracket of Eq. (B.11) add to zero, i.e.,

$$\frac{E}{(\omega_c rB/4)} = 1 - \frac{a^2}{r^2} \quad . \qquad (B.12)$$

The left-hand side of Eq. (B.12) is independent of r, since $E \propto r$, and the right-hand side is always smaller than 1. Thus, the condition for a second turning point of the orbit cannot be satisfied if

$$E > \frac{\omega_c rB}{4} \quad . \qquad (B.13)$$

This is just the condition for which we use Solution II Eq. (B.5) in the fluid equation approach. Physically, this means that the particle orbits are not closed, and since this occurs for a positive electric field, the ions are accelerated outwards. As a^2/r^2 becomes small compared to 1, the angular frequency of the ion approaches $-\omega_c/2$ [see Eq. (B.9)], which is consistent with Eq. (B.5) for the fluid approach.

We have seen that the change from Solution I to Solution II in the fluid equation approach occurs just when the ion orbits become unbounded, and the radial guiding-center velocity becomes nonzero. Thus, even though the two solutions join abruptly (see Fig. B.1), the fluid

equation describes the motion of the particles qualitatively, even for large electric fields. On the other hand, the fluid approach neglects the large ion orbits for these large fields (when the electric field effect dominates over thermal motion); they might be important for determining the finite Larmor radius effects on plasma waves.

In solving the fluid equations, we have essentially assumed that the plasma density is uniform by neglecting the diamagnetic drift term. Upon closer examination, this presents some difficulties for Solution II, in that the continuity equation [Eq. (3.2)] is not satisfied. This arises from the nonzero v_r in Solution II, since $n\nabla \cdot v_r \hat{i}_r \neq 0$. To balance this term in the continuity equation, one needs a source term to make up for the radial loss of plasma. For a more rigorous treatment of this problem, one should solve the electron and the ion continuity and momentum transfer equations self-consistently, in order to determine the velocities, the density profile, and the electric field profile for a given system. This has been done, for example, for a weakly ionized plasma in a positive column.[86] We do not pursue such a study here; the purpose of this appendix has been to illustrate the type of ion motion which arises with strong electric fields.

Appendix C

EFFECT OF ELECTRON TEMPERATURE FLUCTUATIONS ON WAVES PROPAGATING PERPENDICULAR TO THE MAGNETIC FIELD

In this Appendix, we prove that the electron temperature has no effect to any order on the waves studied in Section 3. This means that Eq. (3.18), which gives the relationship between ϕ_1 and n_1 when the isothermal assumption is made, is valid even if the electron temperature is considered as a wave variable. For generality, we assume that $n_0(r)$ and $T_{e0}(r)$ are arbitrary functions of r.

From Eq. (3.13), we can solve for the electron velocity

$$\underset{\sim}{v}_e = \underset{\sim}{v}_D + \underset{\sim}{v}_E \quad , \tag{C.1}$$

where $\underset{\sim}{v}_D$ and $\underset{\sim}{v}_E$ are the diamagnetic and $\underset{\sim}{E} \times \underset{\sim}{B}$ velocities

$$\underset{\sim}{v}_D = - \frac{\hat{\underset{\sim}{i}}_z \times \nabla_\perp (nT_e)}{neB} \quad , \tag{C.2}$$

$$\underset{\sim}{v}_E = - \frac{\hat{\underset{\sim}{i}}_z \times \underset{\sim}{E}}{B} \quad , \tag{C.3}$$

and $\hat{\underset{\sim}{i}}_z$ is the unit vector in the direction of the magnetic field. If we insert the velocity from Eq. (C.1) into the continuity equation, Eq. (3.12), and use the result

$$\nabla_\perp \cdot (n\underset{\sim}{v}_D) = - \frac{\nabla_\perp \cdot \hat{\underset{\sim}{i}}_z \times \nabla_\perp (nT_e)}{eB} = 0 \quad , \tag{C.4}$$

the continuity equation becomes

$$\frac{\partial n}{\partial t} + \nabla_\perp \cdot (n\underset{\sim}{v}_E) = 0 \quad . \tag{C.5}$$

Equation (C.5) is valid to all orders, so the electron temperature drops out of the analysis. The first order version of Eq. (C.5) is

$$-\frac{mT_{i0}}{eBr}\,\frac{n_0'}{n_0}\left(\frac{e\phi_1}{T_{i0}}\right) = \left(\omega + \frac{mE_0}{rB}\right)\left(\frac{n_1}{n_0}\right). \qquad (C.6)$$

For the Gaussian number density distribution in Eq. (3.1), this reduces directly to Eq. (3.18), which we derived making the isothermal assumption. This proves that for the dispersion characteristics of these waves we may neglect even a zero order gradient in the electron temperature, and use the isothermal assumption.

On the other hand, the above result does not imply that there are no electron temperature fluctuations associated with these waves. Indeed, we find that there can be such fluctuations, and derive an expression for them below. We use the electron heat transfer equation for variations perpendicular to the magnetic field, which can be written as[58]

$$\frac{3}{2}\,n\,\frac{dT_e}{dt} - T_e\,\frac{dn}{dt} - \frac{5}{2}\,\nabla_\perp \cdot \frac{nT_e}{eB}\,(\hat{i}_z \times \nabla_\perp T_e) = 0\,, \qquad (C.7)$$

where $d/dt = \partial/\partial t + \underset{\sim}{v}_e \cdot \nabla_\perp$.

We use the identity[46]

$$\frac{5}{2}\,\nabla_\perp \cdot \frac{nT_e}{eB}\,(\hat{i}_z \times \nabla_\perp T_e) = \frac{3}{2}\,n\,\underset{\sim}{v}_D \cdot \nabla_\perp T_e - T_e \underset{\sim}{v}_D \cdot \nabla_\perp n, \qquad (C.8)$$

and Eq. (C.1), to reduce the heat transfer equation to

$$\frac{3}{2}\,n\left(\frac{\partial}{\partial t} + \underset{\sim}{v}_E \cdot \nabla_\perp\right) T_e - T_e\left(\frac{\partial}{\partial t} + \underset{\sim}{v}_E \cdot \nabla_\perp\right) n = 0\,. \qquad (C.9)$$

Also, from Eqs. (3.14) and (3.16), we have to first order

$$\underset{\sim}{v}_E = \underset{\sim}{v}_{E0} + \underset{\sim}{v}_{E1} = \left(\frac{-E_0}{B}\right)\hat{i}_\theta + \frac{T_{e0}}{eB}\left\{\frac{im}{r}\,\frac{e\phi_1}{T_{e0}}\,\hat{i}_r + \frac{e\phi_1'}{T_{e0}}\,\hat{i}_\theta\right\}, \qquad (C.10)$$

where the prime denotes differentiation with respect to r. The first order heat transfer equation then yields

$$\frac{T_{e1}}{T_{e0}} = \frac{2}{3}\left(\frac{n_1}{n_0}\right) + \frac{(2/3)(n_0'/n_0) - (T_{e0}'/T_{e0})}{\omega + mE_0/rB}\left(\frac{m\phi_1}{Br}\right). \qquad (C.11)$$

Since $\omega = - mE_0/rB$ is not, in general, an eigenfrequency as seen from Eq. (3.35), we may eliminate ϕ_1 from Eq. (C.11), by using Eq. (C.6). This gives an expression for the electron temperature fluctuations:

$$\frac{T_{e1}}{T_{e0}} = \frac{\left(T_{e0}'/T_{e0}\right)}{(n_0'/n_0)} \frac{n_1}{n_0} \quad . \qquad (C.12)$$

Thus, even though the dispersion relation for the waves is not affected by the isothermal assumption for the electrons, there will be temperature fluctuations if a zero order temperature gradient is present.

Appendix D

ION VISCOSITY TENSOR INCLUDING ION-ION COLLISIONS

We use rectangular geometry, with the magnetic field in the z-direction (see Fig. 3.2), and assume $\omega_{ci}^2 \gg \nu_{ii}^2$. The components of the viscosity tensor given by Braginskii[58] are

$$\pi_{xx} = -\frac{\eta_0}{2}(W_{xx} + W_{yy}) - \frac{\eta_1}{2}(W_{xx} - W_{yy}) - \eta_3 W_{xy} ,$$

$$\pi_{yy} = -\frac{\eta_0}{2}(W_{xx} + W_{yy}) - \frac{\eta_1}{2}(W_{xx} - W_{yy}) + \eta_3 W_{xy} ,$$

$$\pi_{zz} = -\eta_0 W_{zz}$$

$$\pi_{xy} = \pi_{yx} = -\eta_1 W_{xy} + \frac{\eta_3}{2}(W_{xx} - W_{yy}) , \qquad \text{(D.1)}$$

$$\pi_{xz} = \pi_{zx} = -\eta_2 W_{xz} - \eta_4 W_{yz} ,$$

$$\pi_{yz} = \pi_{zy} = -\eta_2 W_{yz} + \eta_4 W_{xz} .$$

We need the definition

$$W_{\ell,k} = \frac{\partial v_{i\ell}}{\partial x_k} + \frac{\partial v_{ik}}{\partial x_\ell} - \frac{2}{3}\delta_{\ell,k}\nabla \cdot \underset{\sim}{v}_i , \qquad \text{(D.2)}$$

where $v_{i\ell}$ is the velocity component in the x_ℓ-direction ($x_1, x_2, x_3 \rightarrow x, y, z$ for rectangular geometry), and $\delta_{\ell,k}$ is the Kronecker delta. Finally, we have

$$\eta_0 = 0.96\left(\frac{nT_i}{\nu_{ii}}\right), \quad \eta_1 = \frac{3}{10}\left(\frac{nT_i}{\omega_{ci}}\right)\left(\frac{\nu_{ii}}{\omega_{ci}}\right), \quad \eta_2 = 4\eta_1 , \quad \eta_3 = \frac{1}{2}\left(\frac{nT_i}{\omega_{ci}}\right), \quad \eta_4 = 2\eta_3 , \qquad \text{(D.3)}$$

where ν_{ii} is the ion-ion collision frequency. This is defined as[58]

$$\nu_{ii} = 3.3 \times 10^{-8} \lambda \left(\frac{2m_p}{m_i}\right)^{1/2} \frac{Z^3 n}{T_i^{3/2}} \quad , \tag{D.4}$$

where $\lambda = 23.4 - 1.15 \log n + 3.45 \log T_e$ is the Coulomb logarithm (for $T_e < 50$ eV), m_p and m_i are the proton and ion masses, Ze is the charge of an ion, e is the electronic charge, n is the number density in cm^{-3}, and T_i and T_e are the ion and electron temperatures in electron volts.

Likewise, the electron-ion collision frequency for momentum transfer, ν_{ei}, is given by[58]

$$\nu_{ei} = 2.9 \times 10^{-6} \lambda \frac{Zn}{T_e^{3/2}} \cdot \tag{D.5}$$

REFERENCES

1. D. J. Rose and M. Clark, Jr., Plasmas and Controlled Fusion (MIT Press, Cambridge, Mass., 1961).

2. B. Lehnert, Proc. 2nd Int. Conf. on the Peaceful Uses of Atomic Energy (United Nations, Geneva, 1958), Vol. 31, p. 349.

3. A. C. Kolb, Proc. 2nd Int. Conf. on the Peaceful Uses of Atomic Energy (United Nations, Geneva, 1958), Vol. 32, p. 328.

4. B. B. Kadomtsev and A. V. Nedospasov, J. Nucl. Energy C1, 230 (1960).

5. N. Rostoker and A. C. Kolb, Phys. Rev. 124, 965 (1961).

6. N. D'Angelo and R. W. Motley, Phys. Fluids 6, 422 (1963).

7. F. W. Crawford and G. S. Kino, Proc. IRE 49, 1767 (1961).

8. B. Coppi and E. Mazzucato, Phys. Fluids 14, 134 (1971).

9. C. W. Horton, Jr. and R. K. Varma, Phys. Fluids 15, 620 (1972).

10. H. G. Booker and H. W. Wells, Terres. Magn. 43, 249 (1938).

11. D T. Farley, B. B. Balsley, R. F. Woodman, and J. R. McClure, J. Geophys. Res. 75, 7199 (1970).

12. D. T. Farley, Jr., J. Geophys. Res. 68, 6083 (1963).

13. S. Cuperman and A. Harten, Astrophys. J. 162, 315 (1970); 163, 383 (1971).

14. J. R. Pierce, Bell System Tech. J. 30, 626 (1951).

15. R. Q. Twiss, Proc. Phys. Soc. (London) B64, 654 (1951); Phys. Rev. 88, 1392 (1952).

16. P. A. Sturrock, Phys. Rev. 112, 1488 (1958). Also in Plasma Physics J. E. Drummond Ed. (McGraw-Hill, New York, N.Y., 1961), Chap. 4.

17. H. Derfler, Proc. 5th Int. Conf. on Ionization Phenomena in Gases (North-Holland, Amsterdam, 1961) Vol. 2, p. 1423; Proc. 8th Int. Conf. on Ionization Phenomena in Gases (Springer Verlag, Vienna, 1967) p. 294; Phys. Letters 24A, 763 (1967); Phys. Rev. A1, 1467 (1970).

18. A. Bers and R. J. Briggs, MIT RLE Quarterly Progress Report Nos. 71, p. 122 (1963); 74, p. 133 (1964).

19. R. J Briggs, Electron-Stream Interaction with Plasmas (MIT Press, Cambridge, Mass., 1964), Chap. 2.

20. K. B. Dysthe, Nucl. Fusion 6, 215 (1966).

21. D. E. Baldwin and G. Rowlands, Phys. Fluids 13, 2036 (1970).

22. A. J. Duncan, J. R. Forrest, F. W Crawford, and S. A Self, Phys. Fluids 12, 316 (1969); 14, 1959 (1971).

23. D. Montgomery and D. Gorman, Phys. Fluids 5, 947 (1962).

24. M. Dobrowolny, F. Engelman and A. Sestero, Z. Naturforsch 24, 1235 (1969).

25. B. Bertotti and A. Nocentini, Plasma Phys. 12, 39 (1970).

26. C. C. Cheng and E. G. Harris, Phys. Fluids 12, 1262 (1969).

27. A. Nocentini, Proc. 4th Europ. Conf. on Controlled Fusion and Plasma Physics (CNEN, Rome, 1970), p. 147.

28. S-T. Tsai, R. F. Ellis and F. W. Perkins, Phys. Fluids 15, 345 (1972).

29. M. Kruskal and M. Schwarzschild, Proc. Roy. Soc. (London) 223A, 348 (1954).

30. M. N. Rosenbluth and C. L. Longmire, Ann. Phys. (N.Y.) 1, 120 (1957).

31. M. N. Rosenbluth, N. A. Krall, N. Rostoker, Nucl. Fusion Suppl. Pt. 1, 143 (1962).

32. K. V. Roberts and J. B. Taylor, Phys. Rev. Letters 8, 197 (1962).

33. F. F. Chen, Phys. Fluids 9, 965 (1966).

34. L. G. Kuo, E. G. Murphy, M. Petravić, and D. R. Sweetman, Phys. Fluids 7, 988 (1964).

35. T. E. Stringer and G. Schmidt, Plasma Phys. 9, 53 (1967).

36. M. N. Rosenbluth and A. Simon, Phys. Fluids 8, 1300 (1965).

37. G. I. Kent, N. C. Jen, and F. F. Chen, Phys. Fluids 12, 2140 (1969).

38. F. W. Perkins and D. L. Jassby, Phys. Fluids 14, 102 (1971); D. L. Jassby, Phys. Fluids 15, 1590 (1972).

39. S. S. Moiseev and R. Z. Sagdeev, Zh. Eksp. Teor. Fiz. 44, 763 (1963). [English translation: Sov. Phys. - JETP 17, 515 (1963).]

40. F. F. Chen, Phys. Fluids 7, 949 (1964); 8, 912 (1965).

41. F. F. Chen, Phys. Fluids 8, 1323 (1965).

42. N. A. Krall, in Advances in Plasma Physics, A. Simon and W. B. Thompson, Eds. (Interscience, New York, N. Y., 1968), Vol. 1.

43. H. W. Hendel, B. Coppi, F. Perkins, and P. A. Politzer, Phys. Rev. Letters 18, 439 (1967); H. W. Hendel, T. K. Chu, and P. A. Politzer, Phys. Fluids 11, 2426 (1968).

44. A. A. Galeev, S. S. Moiseev, and R. Z. Sagdeev, J. Nucl. Energy C6, 645 (1964).

45. S-T. Tsai, F. W. Perkins, and T. H. Stix, Phys. Fluids 13, 2108 (1970).

46. S. A. Self, J. Plasma Phys. 4, 693 (1970).

47. R. E. Rowberg and A. Y. Wong, Phys. Fluids 13, 661 (1970).

48. L. Tonks and I. Langmuir, Phys. Rev. 33, 195 (1929).

49. B. D. Fried and R. W. Gould, Phys. Fluids 4, 139 (1961).

50. J. D. Jukes, J. Nucl. Energy C3, 140 (1961).

51. T. E. Stringer, J. Nucl. Energy C6, 267 (1964).

52. I. B. Bernstein and R. M. Kulsrud, Phys. Fluids 3, 937 (1960).

53. U. Ingard and M. Schulz, Phys. Rev. 158, 106 (1967).

54. M. Schulz, Phys. Fluids 10, 244 (1967).

55. W. P. Allis, S. J. Buchsbaum, and A. Bers, Waves in Anisotropic Plasmas (MIT Press, Cambridge, Mass., 1963), Chap. 8.

56. C. K. Birdsall, G. R. Brewer, and A. V. Haeff, Proc. IRE 41, 865 (1953).

57. Waveguide Handbook, N. Marcuvitz, Ed. (MIT Radiation Lab. Ser. Vol. 10, McGraw-Hill, New York, N. Y., 1951).

58. S. I. Braginskii, in Reviews of Plasma Physics, edited by M. A. Leontovich (Consultants Bureau, New York, N.Y., 1965), Vol. I, p. 205.

59. T. K. Chu, B. Coppi, H. W. Hendel and F. W. Perkins, Phys. Fluids 12, 203 (1969).

60. G. L. J. Müller, J C. Corbin, and R. S. Palmer, in Feedback and Dynamic Control of Plasmas, A.I.P. Conference Proceedings No. 1, (Am. Inst. Phys., New York, N. Y., 1970), p. 129.

61. E. T. Whittaker and G. N. Watson, A Course of Modern Analysis (Cambridge University Press, Cambridge, 1952), 4th ed., p. 337.

62. B. Lehnert, Phys. Fluids 9, 1367 (1966).

63. F. F. Chen, Phys. Fluids 10, 1647 (1967).

64. E. Jahnke and F. Emde, Tables of Functions (Dover Publishing, New York, N. Y., 1956), 4th ed., p. 275.

65. E. L. Ince, Ordinary Differential Equations (Dover Publishing, New York, N. Y., 1956), p. 396.

66. L. M. Lidsky, S. D. Rothleder, D. J. Rose, S. Yoshikawa, C. Michelson, and R. J Mackin, Jr., J. Appl. Phys. 33, 2490 (1962).

67. D. B. Ilić, T. D. Rognlien, S. A. Self, and F. W. Crawford, Stanford University Institute for Plasma Research, Report No. 482 (July, 1972).

68. M. Hudis and L. M. Lidsky, J. Appl. Phys. 41, 5011 (1970).

69. B. Van Der Sijde and P. A. W. Tielemans, Proc. 10th Int. Conf. on Phenomena in Ionized Gases (Parsons and Co., Oxford, 1971), p. 192.

70. M. Watanabe and C. W. Hartman, Electronics Research Laboratory Plasma Research QPR No. 1, University of California, Berkeley (1 Jan. to 31 March 1970).

71. L. G. Schlitt and H. W. Hendel, Bull. Am. Phys. Soc. 15, 1439 (1970); Phys. Fluids 15, 1578 (1972).

72. Semiannual Report No. 8, NASA Research Grant NGL 05-020-176, Stanford University Institute for Plasma Research Report No. 412 (Feb., 1971).

73. A. Y. Wong and F. Hai, Phys. Rev. Letters 23, 163 (1969).

74. L. Fox and D. F. Mayers, Computing Methods for Scientists and Engineers (Oxford University Press, London, 1968), p. 146.

75. R. W. Motley and R. F. Ellis, Phys. Fluids 14, 886 (1971).

76. A. J. Duncan and J. R. Forrest, Phys. Fluids 14, 1973 (1971).

77. L. Pekarék, Proc. 10th Int. Conf. on Phenomena in Ionized Gases (Parsons and Co., Oxford, 1971), Invited paper, p. 365.

78. F. F. Chen, Plasma Phys. 7, 399 (1965).

79. See values in Handbook of Chemistry and Physics, 47th Edition, R. C. Weast, ed. (Chemical Rubber Co., Cleveland, 1966), p. E-69.

80. T. D. Rognlien and S. A. Self, Phys. Rev. Letters 27, 792 (1971).

81. P. Kaw, Phys. Rev. 188, 506 (1969).

82. P. K. Kaw and A. K. Sundaram, Phys. Letters 38A, 355 (1972).

83. J. V. Evans, J. Geophys. Res. 72, 3343 (1967).

84. H. Rishbeth and O. K. Garriott, Introduction to Ionospheric Physics (Academic Press, New York, N. Y., 1969), p. 131.

85. G. Schmidt, Physics of High Temperature Plasmas, (Academic Press New York, N. Y., 1966), p. 29.

86. H. N. Ewald, F. W. Crawford, and S. A. Self, J. Appl. Phys. 38, 2753 (1967).